



TECHNICAL REPORT 0-6922-1
TXDOT PROJECT NUMBER 0-6922

Evaluation of Long-term Strength and Durability Properties of Pre-stressed Concrete Girders with Microcracking

Dr. Raissa Ferron
Dr. Salamone Salvatore
Mr. Michael Rung
Ms. Savitha Srinivasan
Mr. Brennan Dubuc
Mr. Arvin Ebrahimkhanlou

February 2020; Published September 2020

<http://library.ctr.utexas.edu/ctr-publications/0-6922-1.pdf>



Technical Report Documentation Page

1. Report No. FHWA/TX-20/0-6922-1		2. Government Accession No.	3. Recipient's Catalog No.	
4. Title and Subtitle Evaluation of Long-term Strength and Durability Properties of Pre-stressed Concrete Girders with Microcracking		5. Report Date Submitted: February 2020 Published: September 2020		
		6. Performing Organization Code		
7. Author(s) Dr. Raissa Ferron; Dr. Salamone Salvatore; Ms. Savitha Srinivasan; Mr. Michael Rung; Mr. Brennan Dubuc; Mr. Arvin Ebrahimkhanlou		8. Performing Organization Report No. 0-6922-1		
9. Performing Organization Name and Address Center for Transportation Research The University of Texas at Austin 3925 W. Braker Lane, 4 th floor Austin, TX 78759		10. Work Unit No. (TRAIS)		
		11. Contract or Grant No. 0-6922		
12. Sponsoring Agency Name and Address Texas Department of Transportation Research and Technology Implementation Division P.O. Box 5080 Austin, TX 78763-5080		13. Type of Report and Period Covered Technical Report January 2016 – February 2020		
		14. Sponsoring Agency Code		
15. Supplementary Notes Project performed in cooperation with the Texas Department of Transportation.				
16. Abstract The presence of unexplained surface microcracks in several in-service prestressed girders across Texas led to concerns of reduced service life due to loss in long-term strength and durability. This project was designed to estimate both this potential loss in service life and the likelihood of long-term strength and durability issues that might arise due to the presence of these microcracks. Measurements of crack width, strain, stiffness and resistivity were taken from full-scale in-service and overcast or rejected girders over two years. Cores were collected from the overcast girders for further laboratory investigation of cracking, strength, stiffness, and durability properties. While the girders exhibited an increase in cracking and shrinkage, they have not shown a significant loss in strength, stiffness, and durability due to the presence and temporal growth of the microcracks. Exposure to environment and presence of pre-existing cracks were major factors affecting the rate of increase in cracking, while external loading was not. This temporal data was used to generate an empirical model to estimate the remaining service life of the girders using non-destructive test measurements as input variables. The model had a regression coefficient and reliability index in the "Good" range, and an error of 359 days. Laboratory specimens were cast to determine a critical cracking index value of 18 mm/m (0.5755 in./yd). The empirical model under-predicted service life by 4–10 years for all girders when compared to Life-365®. As these girders are designed for a service life of 75 years, the present rate of growth in microcracking can reduce the service life of the in-service girders from 2 to 13 years depending on the girder and nature of cracking. Further reduction in service life is also possible under fatigue loading as the girders age. Thus, continuous monitoring of the girders, especially in the last two decades of the girders' lives, is recommended. In addition, the behavior of these girders with surface microcracks under marine exposure was observed to determine the effect of the microcracks on chloride-induced corrosion. Exposure to the simulated marine environment led to the formation of microcracks in the low water-cement ratio concrete specimens. However, the presence of microcracks did not significantly impact corrosion potential in the timeframe of the study. A novel approach using guided ultrasonic waves and acoustic emission to monitor corrosion process in prestressing strands was explored, with encouraging results. Further research should explore the key parameters that can influence corrosion monitoring using guided ultrasonic waves and to determine the efficacy of using the guided wave ultrasonic method as part of the maintenance program.				
17. Key Words Microcracks, In-service, Pre-stressed concrete, Durability, Service life, Guided ultrasonic waves, Corrosion, Marine exposure		18. Distribution Statement No restrictions. This document is available to the public through the National Technical Information Service, Springfield, Virginia 22161; www.ntis.gov.		
19. Security Classif. (of report) Unclassified	20. Security Classif. (of this page) Unclassified	21. No. of pages 260	22. Price	



**THE UNIVERSITY OF TEXAS AT AUSTIN
CENTER FOR TRANSPORTATION RESEARCH**

Evaluating Long-term Durability and Performance of Prestressed Concrete Beam with Extensive Surface Cracking

Dr. Raissa Ferron
Dr. Salamone Salvatore
Mr. Michael Rung
Ms. Savitha Srinivasan
Mr. Brennan Dubuc
Mr. Arvin Ebrahimkhanlou

CTR Technical Report: 0-6922-1
Report Date: Submitted: February 2020; Published: September 2020
Project: 0-6922
Project Title: Evaluating Long-term Durability and Performance of Prestressed Concrete
Beam with Extensive Surface Cracking
Sponsoring Agency: Texas Department of Transportation
Performing Agency: Center for Transportation Research at The University of Texas at Austin

Project performed in cooperation with the Texas Department of Transportation and the Federal Highway Administration.

Disclaimers

Author's Disclaimer: The contents of this report reflect the views of the authors, who are responsible for the facts and the accuracy of the data presented herein. The contents do not necessarily reflect the official view or policies of the Federal Highway Administration or the Texas Department of Transportation (TxDOT). This report does not constitute a standard, specification, or regulation.

Patent Disclaimer: There was no invention or discovery conceived or first actually reduced to practice in the course of or under this contract, including any art, method, process, machine manufacture, design or composition of matter, or any new useful improvement thereof, or any variety of plant, which is or may be patentable under the patent laws of the United States of America or any foreign country.

Engineering Disclaimer

NOT INTENDED FOR CONSTRUCTION, BIDDING, OR PERMIT PURPOSES.

Research Supervisor: Dr. Raissa Ferron

Acknowledgments

Funding for this project is supported by the Texas Department of Transportation (TxDOT) Project 0-6922, Evaluating Long-Term Durability and Performance of Pre-stressed Concrete Beam with Extensive Surface Cracking. The authors would like to extend their gratitude to the Project Manager, Mr. Chris Glancy, and the TxDOT Project 0-6922 research team members, especially Mr. Andy Naranjo, Mr. Jason Tucker, Mr. Doug Dupler, Mr. Donny Davis, Mr. Abraham Ramirez, Mr. Frank Estrada III, Mr. Hector Garcia, Mr. Lianxiang Du and Mr. Todd Speck. The authors would also like to express their appreciation to the precast yards for allowing access to the girders.

Table of Contents

Chapter 1. Introduction	1
1.1. Introduction.....	1
1.2. Goal and Objectives of the Study	3
1.3. Key Tasks and Report Organization	3
1.4. Scope of Work	4
Chapter 2. Field Surveys and Specimen Selection	5
2.1. Overview of Chapter.....	5
2.2. Objectives	5
2.3. Materials and Methods.....	6
2.3.1. Selection of Girders	6
2.3.2. Field Visit Schedule.....	8
2.3.3. Tests Conducted.....	9
2.3.4. Monitoring Period.....	12
2.4. Conclusions.....	13
Chapter 3. In-situ Examination via Non-Destructive Methods	14
3.1. Overview of Chapter.....	14
3.2. Objectives	14
3.3. Background.....	14
3.4. Materials and Methods.....	16
3.4.1. Specimen Nomenclature	16
3.4.2. Selection of Testing Locations on Girders.....	17
3.4.3. Experimental Methods	19
3.5. Results and Discussions.....	22
3.5.1. Effect of External Loading.....	23
3.5.2. Effect of Exposure to the Environment.....	27
3.5.3. Effect of Pre-Existing Cracks	29
3.5.4. Effect of Direction of Measurement	31
3.6. Conclusions.....	32
Chapter 4. Evaluation of Extracted Cores.....	34
4.1. Overview of Chapter.....	34
4.2. Objective.....	34
4.3. Background.....	34
4.4. Materials and Methods.....	36

4.4.1. Visual Evaluation	37
4.4.2. Strength Tests.....	38
4.4.3. Stiffness Tests	38
4.4.4. Durability Tests.....	39
4.4.5. Accelerated Weathering Test	41
4.5. Results and Discussions	46
4.5.1. Visual Evaluation.....	46
4.5.2. Strength Test Results	51
4.5.3. Stiffness Test Results	51
4.5.4. Durability Test Results.....	52
4.5.5. Accelerated Weathering Test	53
4.5.6. Quantification of Effect of Weathering and Initial Cracking on Loss in Durability	59
4.6. Conclusions.....	61
Chapter 5. Prediction of Remaining Service Life of Girders.....	63
5.1. Overview of Chapter.....	63
5.2. Objective	63
5.3. Background.....	63
5.4. Literature Review on Service Life Prediction Models	64
5.4.1. Mechanistic Models	64
5.4.2. Simulation Models	64
5.4.3. Empirical Models.....	64
5.4.4. Commonly Used Service Life Prediction Models	66
5.4.5. Prediction of Remaining Service Life of Cracked Concrete.....	67
5.5. Materials and Methods.....	68
5.5.1. Girder Notations.....	68
5.5.2. Experimental Methods	69
5.5.3. Analytical Methods.....	82
5.6. Results and Discussions.....	85
5.6.1. Serviceability and Critical Cracking Parameters	85
5.6.2. Empirical Model	88
5.6.3. Calculation of Remaining Service Life of Girders	90
5.7. Conclusions.....	96
5.7.1. Serviceability and Critical Cracking Parameters	96
5.7.2. Prediction of Remaining Service Life of Girders	97

Chapter 6. Marine Simulation Testing.....	99
6.1. Overview of Chapter.....	99
6.2. Objective.....	99
6.3. Background.....	100
6.4. Materials and Methods.....	101
6.4.1. Block Design.....	101
6.4.2. Marine Simulation Tank.....	102
6.4.3. Experimental Methods.....	104
6.5. Results and Discussions.....	106
6.5.1. Growth of Cracking.....	106
6.5.2. Corrosion Potential.....	109
6.6. Conclusions.....	112
Chapter 7. Monitoring Corrosion of Prestressing Strands.....	115
7.1. Overview of Chapter.....	115
7.2. Objectives.....	115
7.3. Overview of Monitoring System and Testing Approach.....	115
7.4. Guided Wave Propagation in Stressed Strands.....	116
7.4.1. Background and Overview.....	116
7.4.2. Theoretical Formulation for an Axially Stressed Rod.....	118
7.4.3. Experiment.....	128
7.4.4. Experimental Results.....	131
7.5. Monitoring Corrosion-Induced Stress Redistribution in Strands using Guided Waves.....	136
7.5.1. Background and Overview.....	136
7.5.2. Stress Measurement Using Higher-Order Modes.....	138
7.5.3. Experiment.....	145
7.5.4. Corrosion Progression.....	147
7.5.5. Higher-Order Mode Stress Measurement.....	149
7.6. Corrosion Monitoring in Prestressed Concrete using Acoustic Emission.....	154
7.6.1. Background and Overview.....	154
7.6.2. Corrosion Process and Acoustic Emission.....	155
7.6.3. Topological Data Analysis.....	157
7.6.4. Experiment.....	161
7.6.5. Benchmark Corrosion Assessment.....	164

7.6.6. Topological Data Analysis of Acoustic Emission	169
7.7. Conclusions.....	174
Chapter 8. Conclusions	176
8.1. Task 1: Field Surveys and Selection of Specimens	176
8.2. Task 2: In-Situ Examination via Non-Destructive Test Methods.....	177
8.3. Task 3: Evaluation of Cores.....	177
8.4. Task 4: Prediction of Remaining Service Life.....	178
8.5. Task 5: Marine Simulation Testing	179
8.6. Task 6: Monitoring Corrosion of Pre-stressing Strands	180
8.7. Recommendations.....	180
8.8. Future Work.....	181
References	183
Appendix A. Additional Girder Information	205
Appendix B. Optical and Scanning Electron Microscopy Images	234
Appendix C. Auxiliary Guided Wave Terms	240

List of Tables

Table 2.1: Field Visit Intervals and Tests Conducted.....	8
Table 2.2: Girder Information—Cracking, Age, Exposure (Climate, Rainfall, and Temperature)	10
Table 2.3: Girder Information—Mix Proportions, Dimensions, Strength, Curing, and Pre-stressing	11
Table 2.4: Non-Destructive Tests Conducted on Girders	12
Table 4.1: Types and Causes of Cracking in Concrete	35
Table 4.2: Items of Investigation and Serviceability Values	37
Table 4.3: Accelerated Weathering Test.....	43
Table 4.4: Correlation Coefficients between Initial Cracking Index and Change in Cracking, Loss in Mass, Absorption, UPV, and Bulk Resistivity of Samples Subjected to Accelerated Weathering Test	57
Table 4.5: Quantification of Relationships between Initial Cracking and Weathering, and Change in Cracking Index, Average Crack Width, Ultrasonic Pulse Velocity, and Bulk Resistivity	59
Table 4.6: Quantification of Relationships between Cracking and Diffusion Coefficient	61
Table 5.1: Concrete Mix Proportions and Properties.....	73
Table 5.2: Concrete Equivalent Mortar Mix Proportions and Properties	74
Table 5.3: Experimental Matrix and Notations.....	76
Table 5.4: Test Methods and Serviceability Values	77
Table 5.5: Serviceability Values for Concrete and Mortar	78
Table 5.6: Summary of Tests Conducted in the Study	82
Table 5.7: Quantification of Relationships between Cracking and Strength, Stiffness, and Durability Parameters	86
Table 5.8: Calculated Serviceability Cracking Values	87
Table 5.9: Remaining Service Life of Girders Calculated Using Model.....	92
Table 5.10: Remaining Service Life Calculated using Life-365®	95
Table 5.11: Remaining Service Life Calculated using Modified Diffusion Coefficient for Cracked Concrete	95
Table 7.1: Undeformed Density [kg/m^3] and Elastic Constants [GPa] for Hecla 17 Steel, along with Uncertainties	125
Table 7.2: Combinations of Hecla 17 Steel Elastic Constants [GPa] Yielding Upper and Lower Theoretical Bounds in Phase Velocity Change, Determined using Monte Carlo Simulation.....	133

Table 7.3: Loading Frame and Strand Dimensions	146
Table 7.4: Visual Signs of Corrosion in Specimen A and the Cycle at which They Were Observed During Experiment.....	164
Table 7.5: Visual Signs of Corrosion in Specimen B and the Cycle at which They Were Observed during Experiment	166
Table A.1: Girder 1R Additional Information	205
Table A.2: Girder 2R Additional Information	208
Table A.3: Girder 3R Additional Information	211
Table A.4: Girder 4R Additional Information	214
Table A.5: Girder 5RC Additional Information	217
Table A.6: Girder 6I, 8I, 9I and 12IC Additional Information	220
Table A.7: Girders 7I, 10I, 11I, and 13IC Additional Information	224
Table A.8: Girder 14V Additional Information.....	229

List of Figures

Figure 1.1: (a) Typical microcracking observed on girders and (b) close-up of cracked section with crack ruler for scale	1
Figure 2.1: Geographic locations of girder	6
Figure 2.2: Typical regions on an (a) extensively cracked and (b) negligibly cracked (control) girder	7
Figure 2.3: (a) Cross-section and (b) longitudinal section showing prestressing strands, and (c) vertical reinforcing bars showing (d) sections of a typical overcast girder from where cores can be extracted	13
Figure 2.4: (a) Extraction of cores from girders, (b) enlarged section of flange, and (c) typical core collected	13
Figure 3.1: Typical overcast girder showing (a) exposed face and (b) sheltered face	17
Figure 3.2: (a) Pre-stressing release cracks in a (b) typical overcast girder and (c) pictorial representation of end and middle sections of girders	18
Figure 3.3: (a) Typical in-service girder showing exterior and interior girders and (b) pictorial representation of end and middle sections of girder	19
Figure 3.4 In-service girder showing (a) exposed face and (b) sheltered face	19
Figure 3.5: Sample calculations and possible crack grid scenarios	21
Figure 3.6: Magnitude and percentage change in cracking index over the one- and two-year monitoring period	23
Figure 3.7: Magnitude and percentage change in average crack width in over the one- and two-year monitoring period	24
Figure 3.8: Crack width distributions	25
Figure 3.9: Strain over the one- and two-year monitoring period	26
Figure 3.10: Magnitude and percentage change in pulse velocity over the one- and two-year monitoring period	27
Figure 3.11: Magnitude and percentage change in surface resistivity in over the one- and two-year monitoring period	27
Figure 3.12: Effect of exposure conditions on change in cracking index over the one- and two-year monitoring period	28
Figure 3.13: Effect of exposure conditions on change in average crack width over the one- and two-year monitoring period	28

Figure 3.14: Effect of exposure conditions on change in surface resistivity over the one- and two-year monitoring period.....	29
Figure 3.15: Effect of exposure conditions on change in strain over the one- and two-year monitoring period	29
Figure 3.16: Effect of pre-existing cracks over the one- and two-year monitoring period.....	31
Figure 3.17: Effect of pre-existing cracks over the one- and two-year monitoring period.....	31
Figure 3.18: Effect of direction of measurement (parallel and perpendicular to the direction of pre-stressing) on strain over the one- and two-year monitoring period.....	32
Figure 3.19: Schematic of pre-stressing strand details in (a) cross-section and (b) longitudinal section, (c) formation of cracks and (d) orientation of microcracks direction	32
Figure 4.1: Calculation of average crack width and cracking index of cores	38
Figure 4.2: (a) Preparation of specimens for rapid migration test and (b) typical test specimens	40
Figure 4.3: (a) Rapid migration test set-up and (b) measurement of depth of penetration	40
Figure 4.4: (a) Carbonation test and (b) measurement of carbonation depth.....	41
Figure 4.5: Optical microscope images of (a) surface and (b)vertical section of cores from a typical girder, and (c) highlighted microcracks	47
Figure 4.6: Typical scanning electron microscope images of surface of cores at (a) 100X and (b) 500X magnification	47
Figure 4.7: 6 μm crack (a) viewed using optical microscope and (b) 50X magnification, (c) 100X, (d) 500X magnification viewed using SEM.....	48
Figure 4.8: 25 μm crack (a) viewed using optical microscope and (b) 50X magnification, (c) 100X, (d) 500X magnification viewed using SEM.....	48
Figure 4.9: 50 μm crack (a) viewed using optical microscope and (b) 50X magnification, (c) 100X, (d) 500X magnification viewed using SEM.....	49
Figure 4.10: 100 μm crack (a) viewed using optical microscope and (b) 50X magnification, (c) 100X, (d) 500X magnification viewed using SEM	49
Figure 4.11: Change in cracking of cores over the monitoring period	50
Figure 4.12: Temporal behavior of cracks	51
Figure 4.13: Change in strength properties of cores over the monitoring period	51

Figure 4.14: Change in stiffness properties of cores over the monitoring period	52
Figure 4.15: Change in resistivity properties of cores over the monitoring period	53
Figure 4.16: Change in diffusion of cores over the monitoring period	53
Figure 4.17: Change in cracking with exposure	55
Figure 4.18: Loss in mass and change in absorption with exposure.....	55
Figure 4.19: Change in ultrasonic pulse velocity and bulk resistivity with exposure	56
Figure 4.20: Effect of initial cracking on final cracking values	57
Figure 4.21: Effect of initial cracking on cumulative loss in mass and final absorption values	57
Figure 4.22: Effect of Initial cracking on the percentage change in ultrasonic pulse velocity and bulk resistivity.....	58
Figure 4.23: Effect of cracking index and exposure on diffusion coefficient and correlation coefficients.....	58
Figure 5.1: Typical shims used and crack (a) depths and (b) widths, and (c) plan view	71
Figure 5.2: Casting of cracked mortar test specimens (a) before and (b) after vibration, (c) after removal of shims, and (d) sectional and (e) plan view of the hardened cracks.....	75
Figure 5.3: Predicted vs. observed cracking indices for Girders 3R and 4R from the fourth round of field visits.....	90
Figure 5.4: Comparison of predicted age of girders using Life-365® and empirical models.....	94
Figure 6.1: Schematics of marine exposure blocks (a) 3-d, (b) elevation and (c) plan views showing the placement of pre-stressing strands	101
Figure 6.2: (a) Marine exposure tank and (b) schematics of setup.....	103
Figure 6.3 Visual rating index vs. cracking index	105
Figure 6.4: Relationship between visual rating index and cracking index	106
Figure 6.5: Corrosion-induced microcracking in Block A in the (a) splash and (b) unexposed zones with (c) highlighted cracks, where CI is the cracking index and VRI is the Visual Rating Index	107
Figure 6.6: (a) Microcracking in block B with (b) highlighted microcracks.....	108
Figure 6.7: Surface resistivity of blocks	110
Figure 6.8: Half-cell potential of blocks.....	112

Figure 7.1: Research proposed here: (a) steel strands; (b) strands are instrumented with low profile piezoelectric transducers to generate and receive GUWs. (c) The GUW measurements are recorded and processed, providing (d) an automatic corrosion diagnosis of the strand.....	116
Figure 7.2: Undeformed and deformed configurations of stressed rod, showing density (ρ, γ), stress (σ, τ), and wavenumber (k, K) of longitudinal guided wave.....	119
Figure 7.3: Unstressed dispersion curves for (a) phase velocity, and (b) group velocity in a steel rod. Bulk longitudinal velocity cl_0 overlain as dashed line. Peak group velocity points of L(0,7), L(0,9), and L(0,12) are identified by dots in (a) and (b).....	124
Figure 7.4: Exact theoretical change in phase velocity due to 400 MPa axial stress in steel rod. Exact Δc_{pp} regions bolded for the higher-order modes L(0, n), $n > 5$. Bulk velocity change Δcl overlain as dashed line.	125
Figure 7.5: (a) Unstressed group velocity dispersion curve of L(0,9) mode, with (b) phase velocity change under 400 MPa axial stress, and (c) group velocity change under same stress. Curves bolded in peak group velocity region. Phase velocity change stabilizes to Δc_{pp} at peak group velocity, with group velocity change less stable.....	126
Figure 7.6: Radial U_r and axial U_z modeshapes over a rod cross-section for (a) L(0,7) at 22.6 MHz-mm, (b) L(0,9) at 30.2 MHz-mm, and (c) L(0,12) at 41.7 MHz-mm. Mode shapes at two stress levels overlain, showing concentration of displacements near the core.....	127
Figure 7.7: (a) Prestressing bed experimental setup and data acquisition systems for collecting guided waves measurements on stressed strand. (b) Strain gauges installed on peripheral wires. (c) Higher-order modes excited with 10 MHz transducers. (d) Schematic of strand cross-section, with core (C) and peripheral (P) wires indicated.	129
Figure 7.8: Filtered L(0,9) mode waveform at two levels of stress, illustrating time change Δt used for phase velocity change measurement	130
Figure 7.9: Power spectrum [dB] of continuous wavelet transform of unfiltered higher-order mode signal in core (C) wire under 400 MPa axial stress; theoretical group velocity dispersion curves converted to arrival times for steel rod overlain	131
Figure 7.10: Experimental phase velocity change for the L(0,9) mode in the core (C) and peripheral (P) wire at $fd = 30.2$ MHz-mm, with error bars for the variability in strain gauge readings. Theoretical change overlain for a steel rod, including bounds for uncertainty in material constants.....	132

Figure 7.11: Experimental phase velocity change in peripheral (P) wire for (a) L(0,7) mode at $fd = 22.6$ MHz-mm, (b) L(0,12) at 41.7 MHz-mm, and (c) L(0,12) at 40.0 MHz-mm, with error bars for the variability in strain gauge readings. Theoretical change for a steel rod overlain with material uncertainty bounds..... 134

Figure 7.12: Experimental phase velocity change in the peripheral (P) wire for L(0,9) mode at $fd = 30.2$ MHz-mm. Experimental points shown for exact and approximate Δcp (derived from experiment), using $cp0$ and $cl0$, respectively. Theoretical changes overlain, showing exact theory (solid line) and the approximate theory (dashed line). 135

Figure 7.13: Flow chart for stress measurement during corrosion using higher-order modes 137

Figure 7.14: (a) Phase velocity and (b) group velocity dispersion curves for longitudinal modes in a (unstressed) 5.22 mm diameter steel rod. Higher-order modes L(0, m) indicated by mode number $m = 8, 9, \dots, 14$. Plateau frequencies of higher-order modes highlighted, with bulk longitudinal velocity $cl0$ overlain as dashed line. 139

Figure 7.15: Superposition of two harmonic waves to form a modulated wave, where $\Omega = \omega' - \omega$ and $K = k' - k$. Phase velocities c, c' overlain, along with modulation velocity C . Cases overlain for no phase shift (solid) and phase shift (dashed), showing no influence from phase shift on modulation. 141

Figure 7.16: (a) Unstressed value and (b) stress dependence of modulation velocity for six higher-order mode pairs L(0, m)-L(0, $m + 1$) for $m = 8, 9, \dots, 13$. Modulation velocity values normalized against bulk velocity values, showing approximation to within 1% error. 142

Figure 7.17: (a) Experimental setup and data acquisition system for guided wave and strain monitoring of stressed strand under accelerated corrosion. Corrosion applied by impressing current in saltwater tank using power supply. (b) Schematic of loading frame, indicating relevant dimensions. Eventual peripheral wire fracture point near the tank edge shown..... 145

Figure 7.18: Post-corrosion inspection of unloaded strand: (a) unwinding of peripheral wires, (b) fractured wires, and (c) interwire buildup of corrosion products near fracture point. Core wire diameter (5.20 mm) found to be nearly the same as before corrosion (5.22 mm)..... 148

Figure 7.19: Measured axial stress in uncorroded and corroded segments of strand, computed from strain measured in uncorroded segment. Stress increase in corroding segment due to local cross-section loss, with final spike due to fracture. 149

Figure 7.20: Wavelet transform scalogram (−40 to 0 dB) in group velocity-frequency space at two corrosion cycles. Group velocity dispersion curves overlain. Higher-order modes $L(0, m)$, $m = 8, 9, \dots, 14$ generated in frequency range 5–10 MHz are indicated. Due to increasing attenuation, only the plateau frequencies remain by cycle 29.	150
Figure 7.21: Extraction of modulation waves used for stress measurement. Consecutive higher-order modes $L(0, m)$ and $L(0, m + 1)$ extracted in pairs and superposed to form modulations.....	151
Figure 7.22: Stress change estimated using velocity change for six higher-order mode pairs, shown in (a)-(f), respectively. Velocity change measured at plateau frequency for each mode. Shaded area overlain as 95% confidence interval from Gaussian process regression. Stress change measured based on strain gages overlain.....	152
Figure 7.23: Stress change estimated using data fusion of six higher-order mode pairs, ranging from $L(0, 8)$ - $L(0, 14)$. Shaded area overlain as 95% confidence interval from Gaussian process regression. Stress change measured based on strain gages is overlain.	153
Figure 7.24: Illustration of chloride-induced corrosion in prestressed concrete cross-section. (a) No corrosion before chlorides reach strand. (b) Depassivation when chlorides penetrate to strand. (c) Corrosion products have expanded into porous interface, reaching critical pressure for crack initiation. (d) End of service life when crack reaches surface.	156
Figure 7.25: Features derived from typical acoustic emission hit, including energy and peak frequency. Hit shown in (a) time domain and (b) frequency domain.	157
Figure 7.26: Example of topological data analysis for (a) randomly sampled datacloud from a 2D annulus (one component, one hole) with landmarks indicated by squares. (b)-(d) Witness complexes constructed from landmarks, corresponding to three values of ϵ (0.02, 0.20, 0.40). Barcodes for number of (e) components and (f) holes, revealing one component and one hole (the true topology of the annulus).....	158
Figure 7.27: Determining the number of holes (first Betti number) in a simplicial complex using its associated chain complexes $\mathcal{C}_0, \mathcal{C}_1, \mathcal{C}_2$. Certain mappings of the boundary operators ∂_1, ∂_2 are shown as dashed arrows. Only one of the cycles in \mathcal{C}_1 has a hole, since the other is “filled in” in \mathcal{C}_2	160
Figure 7.28: (a) Progression of microcracking in Specimen 2 and (b) microcracking highlighted (CI-Cracking Index and VRI-Visual Rating Index)	162

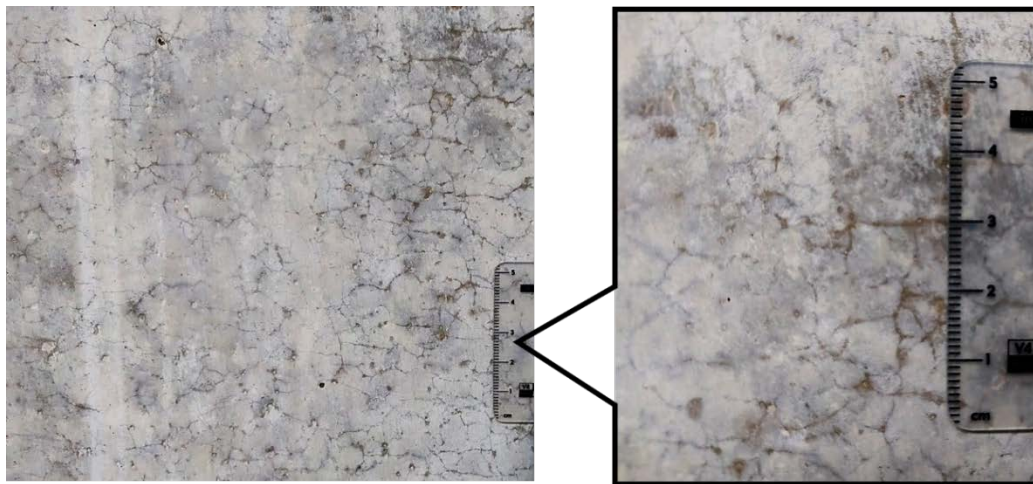
Figure 7.29: (a) Experimental setup and data acquisition system for accelerated corrosion testing. Acoustic emission sensors are highlighted, with those hidden from view also indicated. (b) Schematic of instrumented specimen, as viewed from above, with rightward and leftward ends indicated.....	163
Figure 7.30: Post-corrosion visual inspection of Specimen A. (a) Image of surface crack extending along the length of specimen, as viewed from above. (b) Right side of cross-section after being cut open, highlighting three cracks propagating radially from strand.....	165
Figure 7.31: Mass loss of strand in (a) Specimen A and (b) Specimen B, normalized against original mass embedded in concrete. Results overlain with impressed current readings.	166
Figure 7.32: Acoustic emission activity recorded over the corrosion process for (a) Specimen A and (b) Specimen B, in terms of cumulative energy and number of hits. Corrosion onset (depassivation) may be seen at cycle 15 where the first activity spike occurred.....	167
Figure 7.33: Peak frequency datacloud for AE hits over the corrosion process in (a) Specimen A and (b) Specimen B. Several frequency bands observed (indicated by arrows), suggesting the presence of various source mechanisms.....	168
Figure 7.34: Topological data analysis for datacloud of 30–110 kHz frequency band in Specimen A. (a) Datacloud with dominant holes highlighted, with data points from remaining bands overlain in light gray. (b),(c) Barcodes, indicating one component and two dominant holes.	170
Figure 7.35: Comparison of barcodes obtained from various numbers of landmarks in Specimen A. (a) Landmark selection overlain on the datacloud for 50 (top), 100 (middle), and 200 (bottom) landmarks. (b) Corresponding barcodes for 50, 100, and 200 landmarks. Converging topology of two dominant holes observed by 200 landmarks.	171
Figure 7.36: Illustration of cycle-by-cycle framework for hole measurement at two cycles based on the number of components. (a) Datacloud for 30–110 kHz frequency band highlighted. (b),(c) Selection of landmarks for cycles 30 and 50. (d),(e) Barcodes for number of components at cycles 30 and 50. Cycle 30 does not have a hole since it has only one significant component. Cycle 50 has a hole since it has at least two components which exist until $\epsilon = 0.5$	172
Figure 7.37: Topological data analysis results for hole measurement at each cycle in (a)-(b) Specimen A and (c)-(d) Specimen B.....	173

Figure 7.38: Results of cycle-by-cycle framework in Specimen A for various values of ϵ' . Only the dominant holes near cycles 1–20 and 40–60 consistently appear for each ϵ'	174
Figure A.1: Girder 1R.....	205
Figure A.2: Girder 2R.....	208
Figure A.3: Girder 3R.....	211
Figure A.4: Girder 4R.....	214
Figure A.5: Girder 5RC	217
Figure A.6: Girders 6I, 8I, 9I, and 12IC	220
Figure A.7: Girders 7I, 10I, 11I and 13IC	224
Figure A.8: Girder 14V.....	229
Figure B.1: Microscope Images of Overcast Girder 1R	234
Figure B.2: Microscope Images of Overcast Girder 2R	235
Figure B.3: Microscope Images of Overcast Girder 3R	236
Figure B.4: Microscope Images of Overcast Girder 4R	237
Figure B.5: Microscope Images of Overcast Girder 5RC.....	238
Figure B.6: Microscope Images of Overcast Girder 14V	239

Chapter 1. Introduction

1.1. Introduction

According to the 2017 ASCE infrastructure report card, Texas saw an improvement in the letter grade for Bridges from B- in 2012 to B in 2017, and 81.8% of the 53,488 bridges were classified as structurally sufficient [1]. However, over this period, microcracks have also been observed in numerous in-service pre-stressed concrete girders across Texas at relatively early ages, e.g., within thirteen to eighteen months of casting. These microcracks have shown a tendency to increase in width and number as well [2], [3]. Figure 1.1 shows the typical microcracking observed in the girders.



(a) Microcracking observed on Girders

(b) Close-up of microcracked section

Source: Images by Authors

Figure 1.1: (a) Typical microcracking observed on girders and (b) close-up of cracked section with crack ruler for scale

The pre-cast mixtures used in these pre-stressed girders exhibiting microcracking are designed for high early strength and self-consolidation. The high early strength and use of self-consolidating mixtures allows for reduced construction time and quicker release of pre-stress, thereby reducing construction costs. The mixes proportioned to have low water-cementitious material (w/cm) ratios (0.28–0.33), finer cement particle size, high cement contents, and high percentages of chemical admixtures (water reducers, superplasticizers and viscosity modifying agents). This has been shown to lead to high amounts of drying and autogenous shrinkage [2], [3]. Another factor that could lead to unwanted volumetric changes is that these girders are also subjected to limited curing periods. The typical curing period for the bridge superstructures, including bridge girders, is 8 days (for structures with

Type I and III cements) and 10 days (for structures with SCMs) [4]. Some pre-cast elements can even get only 24 hours of curing [5].

Similar surface microcracking has been seen in pre-cast pre-stressed bridge girders in other states across the United States as well. For example, Lane (1994) published a study that examined early-age cracking in a bridge in Virginia. The cracking was found to be due to plastic shrinkage and settlement [6]. Likewise, Krauss and Rogalla (1996) presented a study conducted on a bridge in Pennsylvania constructed with high-performance concrete. This bridge experienced early age cracking caused by shrinkage and creep due to the use of higher paste/aggregate volume ratios used in them [7]. Darwin et al. (2004) conducted surveys on bridges in Kansas as part of a field observational study and found microcracking in many high-performance concrete bridges caused due to high water content, cement content and total cement paste volume, in addition to increased fixity of bridge decks [8]. Subramaniam (2016) also studied early-age cracking caused by shrinkage and thermal effects in a high-performance concrete bridge girder in New York [9]. Ye et al. (2017) investigated the early-age cracking in a high performance concrete bridge in New Jersey, however these cracks were attributed to thermal stresses and live loads in a high-performance concrete bridge in New Jersey [10].

The mechanism behind the microcracks appearing in the girders of interest in this work is not fully understood yet. The cracks initially appeared in the form of a “starburst” pattern, and with continued exposure to the environment, they progressed into a map cracking pattern. The cracks appeared outside of the regular time-period of plastic shrinkage cracks, and they did not display the telltale signs of an alkali-silica reaction and corrosive products [2], [3]. Due to the low water-to-cementitious-material (w/cm) ratio of these concrete girders, the influence of autogenous shrinkage was studied and subsequently ruled out as sole driving mechanism [3]. The cause of cracking is most likely material-related and not arising from loading since for many of the girders, the microcracks developed in girders that were still sitting in the pre-cast yards (i.e., before the girders were put in-service).

While understanding the mechanism behind the microcracking would be advantageous to help prevent the formation of these microcracks, the presence of these cracks in themselves, especially in-service structures, is of concern, since it is currently unknown whether these cracks have the potential to grow wider or increase in number. Both of which, can lead to reduced service life of the bridge girders [2], [3]. With \$331.1 million dollars spent on the maintenance and replacement of bridge girders in the state of Texas in 2018 alone [11], it is important to know if the microcracks seen on the girders have the potential to cause loss in strength, stiffness, and/or durability of these girders. This information can then be used to determine if any maintenance program changes are warranted.

1.2. Goal and Objectives of the Study

The overarching goal of this research work is to develop a better understanding about the temporal behavior of microcracks seen on precast, prestressed girders in order to predict whether the presence of the microcracks would impact the long-term integrity of the girders. In order to accomplish this goal, the following research objectives were identified:

- Quantify the effect of cracking on the strength, stiffness, and durability properties of low w/cm ratio concrete mixtures generally used in the construction of pre-cast concrete girders
- Generate a reasonably reliable service life model that could be used by transportation department engineers in the field to predict the remaining service life of these girders exhibiting microcracking with easily available input variables such as age, material composition, observed cracking index/density, and ultrasonic pulse velocity.
- Observe the behavior of these girders with surface microcracks under marine exposure to determine the effect of the microcracks on chloride-induced corrosion.
- Examine the suitability of a monitoring system based on guided ultrasonic waves (GUWs) for detecting the initiation and growth of corrosion damage in prestressed concrete beams.

The results from this work would then be used as the basis to determine if any modifications should be made to maintenance program of these girders.

1.3. Key Tasks and Report Organization

To fulfill the objectives listed in Section 1.2, the study was divided into six tasks. These tasks, as well as the chapters in this report that they are associated with, are summarized below:

- Task 1: Field survey and specimen selection (see Chapter 2)
- Task 2: Girder examination (see Chapter 3)
- Task 3: Evaluation of extracted cores (see Chapter 4)
- Task 4: Prediction of remaining service life of girders (see Chapter 5)
- Task 5: Marine simulation testing (Chapter 6)
- Task 6: Corrosion monitoring of pre-stressing strands (see Chapter 7)

- Task 7: Recommendations (see Chapter 8).

1.4. Scope of Work

This study involves the observation and collection of data from full-scale girders, some of which are currently in service in bridges across roads and highways. Thus, data collection and analysis were subject to the following material, logistical, financial, and accessibility constraints:

- The bridge girders are relatively young (3 to 12 years at the time of first field visits), considering their intended service life (75 years) [12]. Thus, the effects from long-term fatigue and impact loading effects have not yet manifested and might be topics of concern later in the life of these girders. Any conclusions drawn from this research are based on the three-year monitoring period.
- Due to the presence of microcracks in sections containing large amounts of reinforcing bars and/or pre-stressing strands, it was not possible to extract samples from those sections of the girders.
- The concrete mix designs are performance-based mixes. The research team received limited information regarding the mixture proportion, pre-stressing strand design, specified strength, curing method, and curing temperature.
- The empirical models generated are for concrete mixes with w/cm ranging from 0.28 to 0.36, since these are the w/cm ratios of the girders examined in this work.
- The temporal effect of microcracks, with widths ranging from $6\mu\text{m}$ to $100\mu\text{m}$, observed on the girders are quantified in this study. Larger cracks have not been included. However, the effect of both micro and macro cracks is discussed for the lab cast concrete samples.

Chapter 2. Field Surveys and Specimen Selection

2.1. Overview of Chapter

This chapter discusses the methodology for Task 1: Field survey and specimen selection. Full-scale girders were selected for the study based on their geographical location, the extent of cracking, ease of accessibility, and mixture compositions. Some of these girders were in-service in bridges, and others were rejected/overcast girders that were being stored at pre-cast yards. These girders in the pre-cast yards were either rejected for unrelated aesthetic reasons or overcast (i.e., excess girders or girders that are not needed on a project for several years). Three rounds of field trips were performed to all girders. Non-destructive testing was conducted on all girders and cores were collected from only the overcast girders due to safety reasons and to avoid damaging to structural integrity of the in-service girders.

2.2. Objectives

The objective of Task 1 was to select appropriate full-scale girders to be used in the study and to conduct field visits to collect non-destructive test data and cores from the girders and exposure blocks exhibiting microcracking. Three types of visits were conducted by the research team:

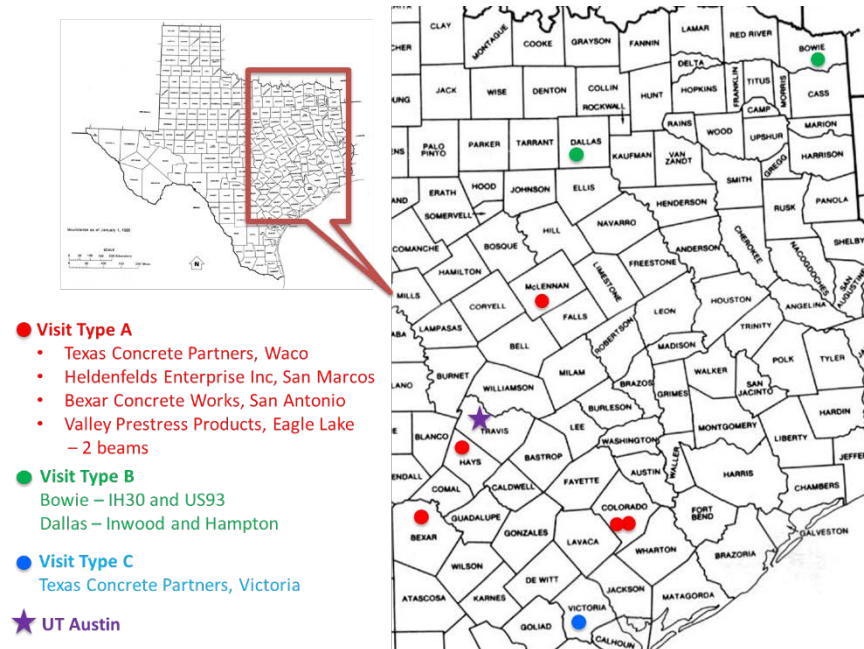
- Visit Type A: Field visits conducted at TxDOT approved precast yards. At these yards, the research team evaluated cracked girders on site. Some girders were rejected, while others were overcast and not needed on the project for several years giving the research team enough time to perform the inspection and sampling. The girders that were rejected were **not** rejected due to the presence of surface cracking visible to the naked eye. The girders were rejected due to the presence of one of two unrelated aesthetic defects (e.g., end spalling or honeycombing in the bottom flange).
- Visit Type B: Field visits conducted at in-service bridge sites. At these sites, the research team evaluated cracked girders. These cracked girders were cast at the same time (with similar materials and proportions) as the girders located at Visit Type A and/or Visit Type C.
- Visit Type C: Field visits conducted at TxDOT approved precast yards. At these sites, the research team evaluated uncracked girders. The girders were cast at the same time (and with similar materials and proportions) as those that exhibited cracking at the precast yards examined in Visit Type A.

2.3. Materials and Methods

2.3.1. Selection of Girders

Full-scale pre-stressed concrete girders that were cast by TxDOT approved producers at commercial precast plants were used in this project.

The girders were selected based on information provided by TxDOT engineers on the extent of visible microcracking on the girders; in addition, the research team took into consideration the location and accessibility of the girders when deciding on the testing matrix. As some of the girders are currently in bridge superstructures that span across rivers and busy highways, accessibility with minimal disruptions to the public played an important role in the girder selection process. Additionally, the goal was to select girders exposed to different exposure conditions and degrees of cracking across Texas, United States. The geographical locations of the selected girders, as well as whether they are located in in-service bridges (i.e., Visit Type B) or overcast/rejected beams at precast plants (i.e., Visit Type A and C) are shown in Figure 2.1.



Source: Images by Authors

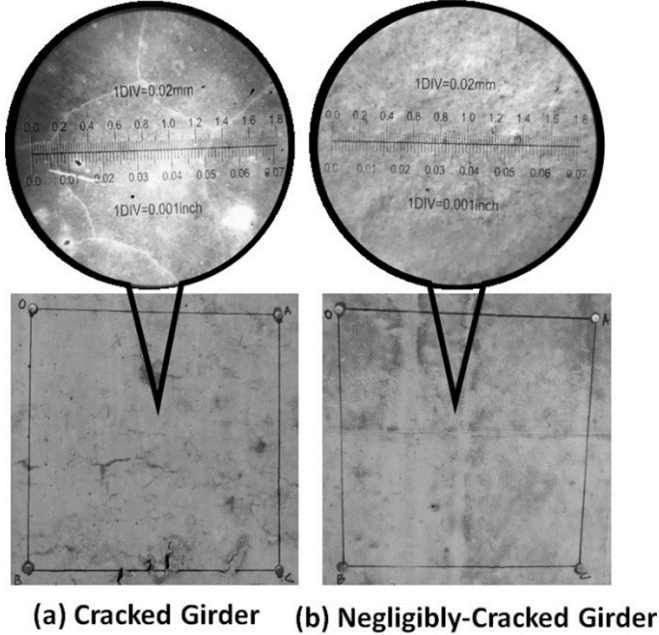
Figure 2.1: Geographic locations of girder

The following girders were selected for the study:

- Five rejected/overcast girders (1R, 2R, 3R, and 4R) were selected for observation. In this study rejected girders and overcast girders are collectively referred to as overcast. Tests on these girders were conducted

at the pre-cast yard they were cast at and stored, and the girders were not under external loads.

- Six in-service girders (6I, 7I, 8I, 9I, 10I, and 11I) that are currently in use in bridge superstructures. These girders were examined in the field at the location where they were installed. These girders had visible cracking and were under external loads. It is unknown exactly as to when the cracks appeared; however, these girders were found to exhibit microcracking during routine inspections conducted by Texas Department of Transportation engineers.
- One overcast girder (5RC) and two in-service girders (12IC and 13IC) exhibiting negligible cracking were also selected to serve as control specimens. Negligible cracking refers to cracking that is not easily visible to the naked eye (see Figure 2.2b). While these girders may display microcracks when viewed under a crack microscope, these cracks were not easily visible to the naked eye (like those see in Figure 2.2b) and hence these cracks are referred to as negligible cracks.
- One overcast girder (14V) with microcracks was used to validate the study.



Source: Images by Authors

Figure 2.2: Typical regions on an (a) extensively cracked and (b) negligibly cracked (control) girder

2.3.2. Field Visit Schedule

Three rounds of field trips were conducted to each girder approximately one year apart. Due to logistical reasons, it was not possible to collect the temporal data precisely one year apart. In addition to the three field visits, an additional round of visits was conducted to two girders to collect data for a validation study. Table 2.1 presents the dates and visit intervals.

Table 2.1: Field Visit Intervals and Tests Conducted

Girder	Location	Visit	Date of Visit	Visit Interval	Tests Conducted
1R	Valley Pre-Stress Products, Eagle Lake	1	10/06/2016	-	Non-Destructive Testing and Cores Collected
		2	06/15/2017	242	
		3	05/17/2018	336	
		4	05/22/2019	370	
2R	Texas Concrete Company, Waco	1	07/21/2016	-	
		2	06/01/2017	315	
		3	06/06/2018	370	
3R	Bexar Concrete Works, San Antonio	1	08/18/2016	-	
		2	06/29/2017	315	
		3	07/11/2018	377	
4R	Valley Pre-Stress Products, Eagle Lake	1	10/06/2016	-	
		2	06/15/2017	242	
		3	05/17/2018	336	
		4	05/22/2019	370	
5RC	Texas Concrete Company, Victoria	1	06/29/2016	-	
		2	06/08/2017	344	
		3	06/27/2018	384	
6I, 8I, 9I, 12IC	Inwood and Hampton, Dallas	1	11/07/2016	-	Non-Destructive Testing Only
		2	11/17/2017	365	
		3	12/12/2018	400	
7I, 10I, 11I, 13IC	I30 and US93, Texarkana	1	12/06/2016	-	
		2	11/16/2017	345	
		3	12/11/2018	390	
14V	Heldenfels Enterprise Inc., San Marcos	1	06/29/2017	-	Non-Destructive Testing and Cores Collected
		2	07/11/2018	377	
		3	05/30/2019	323	

To account for the difference in time intervals among the various field visits, as well as the variations in the material properties arising from different ages and compositions, the following data analysis method was used:

- The average value for each parameter was calculated.
- The average value for the parameter of interest versus time interval curve was created and the linear slope of the curve was calculated.
- The slope was then used to calculate the effective change in the parameter over the one- and two-year time periods.

2.3.3. Tests Conducted

2.3.3.1. Visual Survey

A visual survey was conducted on each girder in accordance with the American Concrete Institute's Guide for Conducting a Visual Inspection of Concrete in Service [13]. Photographs of the girders were taken during the site visits to compare significant changes in cracking magnitude and pattern. Table 2.2 and Table 2.3 summarize the results of the visual surveys for the overcast and in-service girders, respectively. Images and additional information on the girders are provided in Appendix A.

Details about each girder's exposure conditions, visual survey dates, location, type, mixture proportion, pre-stressing strand information, curing conditions, and other relevant information is provided in Table 2.2 and Table 2.3. In these tables, the extent of cracking in these girders is categorized as "extensive" or "negligible," with extensive cracking referring to girders exhibiting substantial surface cracking that is visible to the naked eye and negligible cracking indicating girders with surface cracking not easily visible to the naked eye (see Figure 2.2). Additionally, the following data were recorded for each girder:

- Description of structure: location, type, size, and loading conditions
- Environmental condition: exposure, climatic conditions, orientation, drainage, and soil conditions
- Distress indicators: cracking, staining, surface deposits, and leaks
- Cracking: location and frequency, type of cracking, crack map, width, and pattern
- Materials: strand pattern, mix design, admixtures, aggregate, and cementitious materials, strength, unit weight, and curing conditions

Table 2.2: Girder Information—Cracking, Age, Exposure (Climate, Rainfall, and Temperature)

Girder		1R	2R	3R	4R	5RC	6I, 8I, 9I, 12IC	7I, 10I, 11I, 13IC	14V
Girder Information		Overcast Girder	Overcast Girder	Overcast Girder	Overcast Girder	Overcast Control Girder	In-Service Girders 6 - Exterior 8 and 9 - Interior 12 - Control	In-Service Girders 7 - Exterior 10 and 11 - Interior 13 - Control	Overcast Validation Girder
Extent of Cracking		Extensive	Extensive	Extensive	Extensive	Negligible	6, 8 and 9 - Extensive 12 - Negligible	7, 10 and 11 - Extensive 13 - Negligible	Extensive
Age		9.6 years	7 years	5.51 years	7 years	12.2 years	11.5 years	10.8 years	3.5 years
Years in Service		-	-	-	-	-	8 years	7.8 years	-
Reason for Rejection		N/A	End Spalling	Honeycombing in the bottom flange	End Spalling	Honeycombing in the bottom flange	-	-	N/A
Climate as per NCEI Guidelines [14]	Climate at Storage Yard	Semi-Arid	Humid	Humid	Humid	Humid	Arid	Arid	Arid
	Climate at In-Service Location	-	-	-	-	-	Humid Sub-Tropical	Semi-Arid	-
Rainfall from NCEI climate data [14]	Average Annual Rainfall at Storage Yard	924 mm (36.38 in.)	836 mm (32.91 in.)	1115 mm (43.89 in.)	1115 mm (43.89 in.)	1047 mm (41.22 in.)	924 mm (36.38 in.)	924 mm (36.38 in.)	908 mm (35.75 in.)
	Average Annual Rainfall at In-Service Location	-	-	-	-	-	1041 mm (40.97 in.)	1320 mm (51.98 in.)	-
	Total Rainfall from Casting to Visit 1	6722 mm (264 in.)	4615 mm (181 in.)	10541 mm (415 in.)	6006 mm (236 in.)	13296 mm (523 in.)	8313 mm (327 in.)	9732 mm (383 in.)	4243 mm (167 in.)
	Number of Rain Days from Casting to Visit 1	312	338	686	413	423	438	391	304
Temperature from NCEI climate data [14]	Temperature on Construction Day	38-31 C (101-88 F)	25-5 C (77-42 F)	28-11 C (69-52 F)	20-11 C (69-52 F)	25-13 C (78-57 F)	25-17 C (77-62 F)	19-8 C (66-46 F)	19-(-4) C (67-25 F)
	Temperature during Construction Week	37-32 C (103-90 F)	32-5 C (80-42 F)	32-25 C (83-77 F)	32-22 C (83-71 F)	37-32 C (81-73 F)	25-12 C (77-53 F)	23-9C (73-49 F)	25-16 C (77-61 F)
	Temperature during Field Visit 1	32-31 C (100-88 F)	32-23 C (91-74 F)	35-25 C (90-72 F)	32-22 C (83-71 F)	37-22 C (99-81 F)	30-13 C (86-55 F)	12-7 C (54-44 F)	33-27 C (92-81 F)
	Temperature during Field Visit 2	32-27 C (89-90 F)	32-27 C (89-80 F)	34-25 C (95-77 F)	35-25 C (95-77 F)	34-33 C (93-91 F)	28-21 C (82-69 F)	17-13 C (63-55 F)	35-22 C (96-72 F)
	Temperature during Field Visit 3	37-32 C (99-89 F)	37-32 C (99-89 F)	31-21 C (94-70 F)	34-21 C (94-70 F)	32-31 C (90-88 F)	18-9 C (64-48 F)	16-(-2) C (60-29 F)	30-21 C (86-71 F)
	Temperature during Validation Field Visit 4	30-22 C (86-71 F)	-	-	30-22 C (86-71 F)	-	-	-	-

Table 2.3: Girder Information—Mix Proportions, Dimensions, Strength, Curing, and Pre-stressing

Girder		1R	2R	3R	4R	5RC	6I, 8I, 9I, 12IC	7I, 10I, 11I, 13IC	14V
Mix Proportions	w/cm ratio	0.28	0.30	0.28	0.30	0.28	0.36	0.36	0.31
	Coarse Aggregate	River Gravel	River Gravel	Limestone	River Gravel	River Gravel	River Gravel	River Gravel	River Gravel
	Fine Aggregate	River Sand	River Sand	River Sand	River Sand	River Sand	River Sand	River Sand	Dolomitic Limestone
	Cementitious Materials ^a	Type III Cement + Class F Fly Ash	Type III Cement + Class F Fly Ash	Type III Cement + Class F Fly Ash	Type III Cement + Class F Fly Ash	Type III Cement + Class F Fly Ash	Type III Cement	Type III Cement	Type III Cement + Class F Fly Ash
	High Range Water Reducer ^b	391 ml/100 kg of cement (6 fl. oz./100 cwt)	342 ml/100 kg of cement (5.3 fl. oz./100 cwt)	391 ml/100 kg of cement (6 fl. oz./100 cwt)	342 ml/100 kg of cement (5.3 fl. oz./100 cwt)	651 ml/100 kg of cement (10 fl. oz./100 cwt)	587 ml/100 kg of cement (9 fl. oz./100 cwt)	652 ml/100 kg of cement (10 fl. oz./100 cwt)	325 ml/100 kg of cement (5 fl. oz./100 cwt)
	Water Reducer and Retarder ^b	163 ml/100 kg of cement (2.5 fl. oz./100 cwt)	82 ml/100 kg of cement (1.3 fl. oz./100 cwt)	196 ml/100 kg of cement (3 fl. oz./100 cwt)	98 ml/100 kg of cement (1.5 fl. oz./100 cwt)	196 ml/100 kg of cement (3 fl. oz./100 cwt)	163 ml/100 kg of cement (2.5 fl. oz./100 cwt)	163 ml/100 kg of cement (2.5 fl. oz./100 cwt)	65 ml/100 kg of cement (1 fl. oz./100 cwt)
Dimensions	Girder Type ^c	Type IV	Tx70	Type IV	Type IV	Tx54	Type IV	Type IV	Tx54
	Length	30 m (100')	53 m (175')	30 m (100')	33 m (116')	33 m (115')	-	-	23 m (75')
Strength	7-day Strength	72.8 MPa (10560 psi)	67.3 MPa (9765 psi)	69.7 MPa (10110 psi)	67.3 MPa (9760 psi)	55.84 MPa (8100 psi)	58.6 MPa (8500 psi)	64.12 MPa (9300 psi)	67.6 MPa (9800 psi)
Curing	Method	Wet Mat	Q-Box	Wet Mat	Wet Mat	Wet Mat	Steam	Wet-Mat	Wet Mat
	Temperature	31.1-56.7 C (88-134 F)	N/A	23.1-59.4 C (79-139 F)	23.5-59.4 C (74-139 F)	33.9-66.1 C (92-151 F)	18.8-35.5 C (66-96 F)	N/A	32-14 C (90.2-57.5 F)
Pre-stressing	Number of Straight Strands ^c	30	40	44	40	52	38	42	28
	Number of Deflected Strands ^c	12	10	12	10	12	8	14	8
	Age at Pre-Stress Release	14 hours	N/A	16 hours	13 hours	14 hours	14 hours	15.5 hours	16 hours
<p>a - ASTM C494-2017 [15] b - ASTM C150-2017 and ASTM C618-2017 [16], [17] c - TxDOT Bridge Design Manual (2018) [18]</p>									

2.3.3.2. Non-Destructive Testing

Non-destructive tests were conducted on all girders on the field. Table 2.4 summarizes the non-destructive tests were conducted on the girders. Six locations on each overcast girder and 4 locations on each in-service girder were monitored. The test procedures and the results obtained from the study are presented in Chapter 3.

Table 2.4: Non-Destructive Tests Conducted on Girders

Test	Source for Test Method	Number of Samples Tested		
		Visit 1	Visit 2	Visit 3
Microcracking Evaluation	FHWA-HIF-09-004 Report [19]	6 overcast girders – 6 grids on each girder 8 in-service girders – 4 grids on each girder		
Strain	FHWA-HIF-09-004 Report [19]			
Ultrasonic Pulse Velocity	ASTM C597 [20]			
Surface Resistivity	AASHTO T358 – Modified for Cylinders [21]			

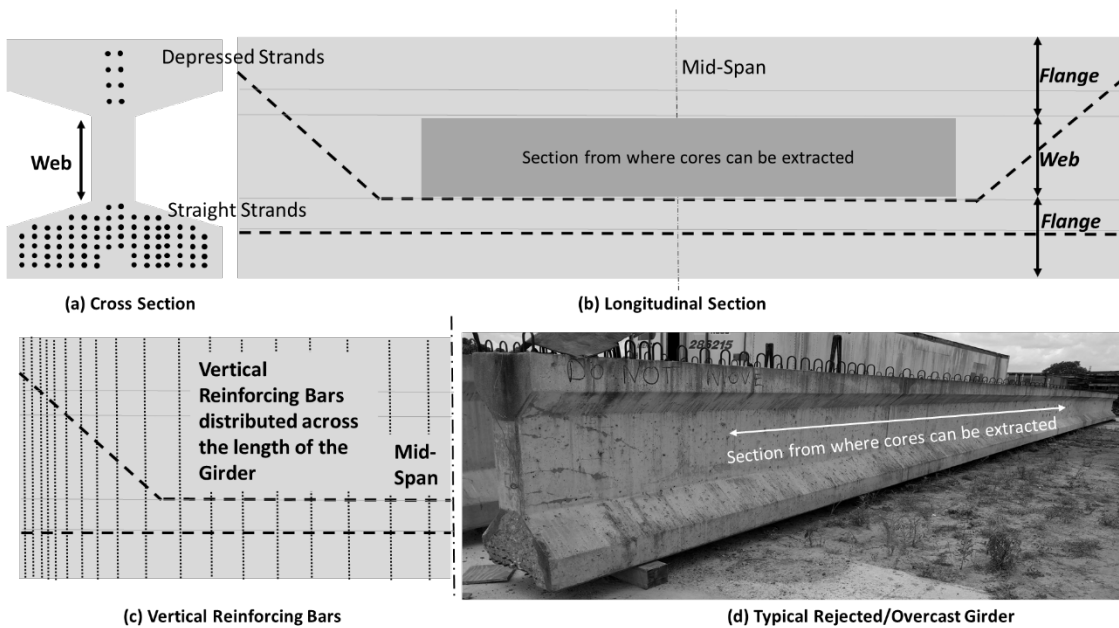
2.3.3.3. Collection of Cores

Concrete cores were collected from the web of the overcast girders from sections exhibiting microcracking (see Figure 2.3). Care was taken to avoid reinforcing bars and pre-stressing strands during coring. Thus, it was not always possible to extract specimens from areas exhibiting highest cracking densities (end sections), as the concentration of reinforcing bars and pre-stressing strands was highest there (see Figure 2.3 b and c). Samples were extracted and stored in accordance with *ASTM C823-2016 Standard Practice for Examination and Sampling of Hardened Concrete in Constructions* [22].

Figure 2.4 shows the extraction of cores from a girder. During the first visit, 15 cores were extracted from each girder. The number of cores that could be extracted from the girders was limited by the presence of vertical reinforcing bars spread across the length of the girder and the depressed pre-stressing strand; thus, 7 cores were extracted from each girder from the second and third field visits (see Figure 2.3 b and c). A total of 29 cores were extracted from each girder. Details about the laboratory testing conducted on the extracted samples and the results obtained from these tests are presented in Chapter 4.

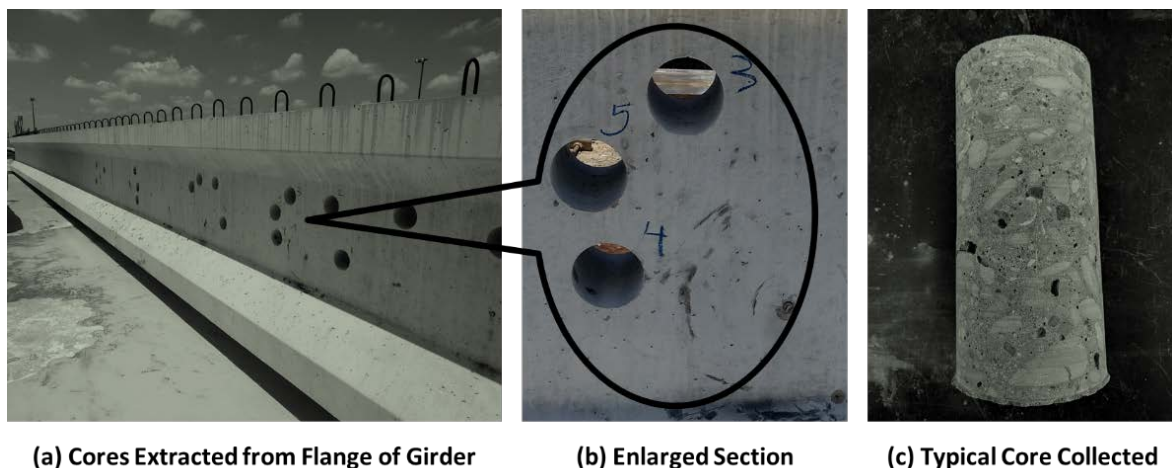
2.3.4. Monitoring Period

The girders selected were monitored for a period of 588 to 750 days by the research team, which equates to the girders were between 1275 and 5000 days (3.5 and 12.2 years) old at the beginning of the test period.



Source: Images by Authors

Figure 2.3: (a) Cross-section and (b) longitudinal section showing pre-stressing strands, and (c) vertical reinforcing bars showing (d) sections of a typical overcast girder from where cores can be extracted



Source: Images by Authors

Figure 2.4: (a) Extraction of cores from girders, (b) enlarged section of flange, and (c) typical core collected

2.4. Conclusions

Fourteen different girders displaying different degree of microcracking was selected for the research study. The girders were located across different regions of Texas and range in age from approximately 3.5 to 14 years age. Over the course of two years, non-destructive testing and cores were extracted from the girders. The data obtained from the non-destructive tests is discussed in Chapter 3, whereas the data obtained from conducting laboratory tests on the cores is discussed in Chapter 4.

Chapter 3. In-situ Examination via Non-Destructive Methods

3.1. Overview of Chapter

This chapter discusses the methodology and results for Task 2: In-situ examination via non-destructive methods. Non-destructive testing was conducted on the girders selected in Chapter 2 to monitor changes in the strength and durability. Over a two-year period, microcrack width, microcrack index, strain, ultrasonic pulse velocity, and surface resistivity of the girders were monitored. The relative change of these properties over time was used to gain insight into the microcracking behavior and potential loss in durability from these cracks. External loading, environmental exposure, and pre-existing cracks are common factors that can influence microcracking growth in concrete girders. The impact of these factors on microcracking behavior in full-scale precast concrete girders was also considered.

3.2. Objectives

The primary objective of the research conducted during this phase of the project was to investigate the rate of growth of the microcracks present on the girders and assess their potential impact on durability. A secondary objective was to determine the major factors that contribute to the growth of microcracking and to determine whether barrier coatings applied to the girders were sufficient to inhibit these microcracks.

3.3. Background

Concerns about loss in service life were raised when unexplained microcracks were found in several in-service, pre-stressed concrete bridge girders at relatively early ages, i.e., within thirteen to eighteen months of casting. Pre-stressed bridges are typically designed for a service life of fifty years [23]. In order to maximize the useful life of a bridge, maintenance and inspection are integral. It is expected that the service life of a well-maintained bridge can be extended to seventy-five years [23]. Due to the critical nature of bridge girders to the structural integrity of bridges, it is important to determine how cracks evolve over time and whether they may be a cause of concern. While it is preferable to collect and analyze data over the entire life cycle of these girders, studies conducted on in-service structures are often constrained due to resources (e.g. time, funding, and personnel). In addition, testing can be limited by availability and accessibility to the girders since critical sections may be difficult to reach without disrupting traffic flow. Due to these constraints, periodic measurements over a short period of time (e.g. 1 year) have been successfully used to provide insight into the present condition of in-service girders. For example, Cao et al. (2018) conducted a study over a 470-day period to determine the long-term deflection in cracked pre-stressed concrete box beams; Kim (2009) conducted a study on the loss of pre-stress in concrete box girders that lasted 750 days [24], [25].

Cracks, regardless of their formation mechanism, increase the ingress of deleterious material into concrete, and in turn, can accelerate the deterioration process of concrete structures. Otieno

et al. (2010) tested the influence of crack reopening on corrosion resistance. The results indicated that concrete samples with reopened cracks had higher corrosion rates when compared to the uncracked samples. The study was conducted on reinforced concrete laboratory specimens with macrocracks with widths of 400 and 700 μm and w/cm ratios of 0.40 and 0.55 [26]. Kwon et al. (2009) studied the effects of early-aged cracks due to heat of hydration and drying shrinkage in an in-service concrete wharf structure. They showed that increasing crack width led to higher diffusion coefficients. They studied the effect of a single crack, with crack widths ranging from 100 to 300 μm [27]. Wang et al. (2018) showed that laboratory samples with flexural cracks (widths ranging from 100 to 300 μm) had the highest carbonation, followed by samples with drying shrinkage cracks (widths ranging from 40 to 180 μm , while uncracked samples had the lowest carbonation [28]. Cao et al. (2013) showed that longitudinal cracks could provide a preferential path to oxygen, a crucial factor influencing corrosion propagation. They also showed that crack widening that was induced by corrosion products led to an acceleration in degradation [29].

Structures under sustained and/or cyclic loading show higher rates of deterioration than unloaded structures. Yu et al. (2015) showed that the loading of concrete played a major role in the development of chloride-induced corrosion, i.e., beams under sustained loading had higher diffusion than unloaded beams. The study was conducted on reinforced concrete laboratory specimens, some of which were subjected to a salt fog room immediately after casting and others after aging for 29 years [30]. Malumbela et al. (2010) showed that a higher rate of widening of cracks led to an increased loss of steel when reinforced laboratory specimens were subjected to loads. The rate of widening of corrosion cracks, as well as strain on uncracked faces of reinforced concrete laboratory specimens, beams, were monitored [31].

A surface crack may grow in depth and size when subjected to alternate wet and dry states and may ultimately develop into a complete structural crack. Bao and Wang (2017) conducted work on specimens with a 0.2 mm wide crack that was subjected to sustained compressive loading while also being exposed to water. They showed that higher rates of chloride penetration occurred in the samples that were exposed to water and under compressive loading when compared to unexposed loaded samples. This showed that external loading when coupled with exposure to environment could cause a loss in durability [32].

The effects of microcracks on durability have also been examined by researchers, albeit to a lesser extent. Konin et al. (1998) showed that uncracked high strength concrete (80 and 100 MPa) had lower chloride penetration than uncracked normal strength concrete (45 MPa). However, with significant microcracking, even the high strength concretes had increased chloride penetration [33]. Corina-Maria Aldea et al. (1999) studied the effect of cracks ranging between 50 to 400 μm on high strength concrete mixtures (79 MPa) and showed that the effect of a single crack smaller than 200 μm did not adversely affect the permeability [34]. However, studies conducted by Wang et al. (2016) and Poursaeed and Hansson (2008) showed that even cracks as small as 100 μm had a detrimental effect on permeability in concretes with w/cm ratios of 0.43 and 0.35 [35], [36]. Yoon and Schlangen (2014) calculated an even lower critical crack width of 13 μm for chloride diffusion by the rapid chloride penetration test. However, they also found that cracks under 40 μm width exhibited self-healing tendencies in the long term in concretes with w/cm ratios of 0.50 [37]. Alahmad et al. (2009) showed that carbon dioxide would penetrate through cracks with widths as small as 10 μm in mortars with w/cm

ratios of 0.48 [38]. Wang et al. (2018) showed that microcracks (40 to 180 μm) caused by drying shrinkage decreased carbonation resistance in reinforced concrete beam samples with w/cm ratios ranging from 0.40 to 0.55 [28].

The American Concrete Institute Building Code [39] defines structural cracks as cracks wider than 300 μm . However, it does not offer a clear definition of microcracks. Thus, various definitions for crack width ranges for microcracks have been adopted. According to the American Concrete Institute Committee 224R-01 [40] report on Control of Cracking in Concrete Structures, the term microcracking is simply used to refer to cracks that form at boundaries of coarse-aggregate (bond cracks) and propagate through the surrounding mortar (mortar cracks). Other researchers have defined microcracks as cracks with crack widths smaller than 50 μm [41], [42]. The RILEM Committee on Microcracking and Lifetime Performance of Concrete [43] suggested the use of the term microcracks for cracks with crack widths less than 10 μm . Slate (1983) defined an upper crack width limit of 100 μm and stated that the lower limit would be the smallest crack-like discontinuity that can be detected, approximately 6 μm [44]. For this study microcracks were defined as cracks with widths ranging from 6 to 100 μm .

The effects of macrocracks on durability properties of concrete have been studied extensively by the aforementioned researchers and others. However, the behavior of microcracks, particularly non-ASR related microcracks, present on in-service pre-cast concrete girders with low w/cm, have not been studied as much. In addition, a clear consensus on a critical microcrack width does not exist, and the range of the critical crack width has been stated to be as low as 13 μm [37] and as high as 200 μm [34], thus, it is important to monitor the growth of the microcracks appearing in in-service structures and determine their potential to cause loss in durability.

3.4. Materials and Methods

Full-scale pre-stressed concrete girders that were constructed at commercial precast plants were used in this project. The girder selection process and tests conducted are described in Chapter 2, Section 2.3. Additional information about the girders is provided in Appendix A. This section describes the non-destructive tests conducted and the data analysis procedures.

3.4.1. Specimen Nomenclature

Fourteen girders were included in this study:

- R: The overcast girders with visible microcracking. Four girders of this type were evaluated (1R, 2R, 3R, and 4R).
- RC: The overcast control girder with negligible visible microcracking. One girder of this type was evaluated (5RC).
- I: The in-service girders with visible microcracking. Six girders of this type were evaluated (6I, 7I, 8I, 9I, 10I, and 11I).

- IC: The in-service control girders with negligible visible microcracking. Two girders of this type were evaluated (12IC and 13IC).
- V – Overcast Girder with visible microcracking used to validate the study. One girder of this type was evaluated (14V).

3.4.2. Selection of Testing Locations on Girders

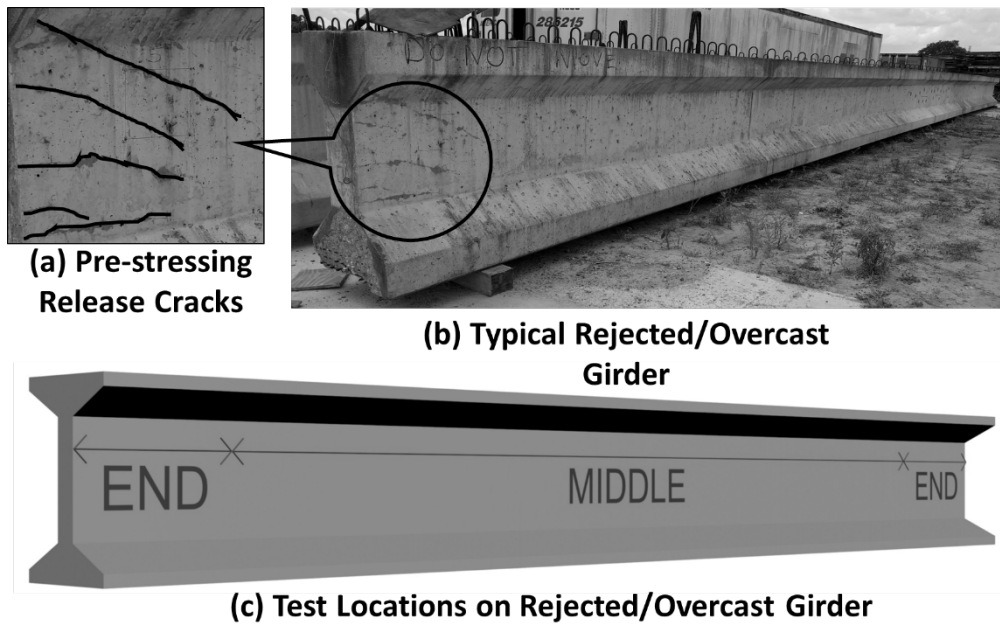
3.4.2.1. Overcast Girders

At the time of the first field visit, the youngest overcast girder was 3.5 years old while the oldest overcast girder was 12.2 years old. Upon arriving at the pre-cast yards, the girders were found to be stored in a manner with one face was exposed to the ambient environment (see Figure 3.1a), while the other face was relatively protected from the elements by neighboring elements (see Figure 3.1b). The personnel at the pre-cast yards were requested to maintain this exposure condition for all girders selected for monitoring. As such, the face exposed to the environment is referred to as “Exposed” and the other face as “Sheltered” in this work. The ends of the girders had pre-stressing release cracks (see Figure 3.2a and Figure 3.2b); pre-stressing release cracks are typically found in the end regions of precast beams (see Figure 3.2c for image showing the end and middle sections) due to the highly localized force applied to the girder during the release of the pretensioned forces [45].



Source: Images by Authors

Figure 3.1: Typical overcast girder showing (a) exposed face and (b) sheltered face



Source: Images by Authors

Figure 3.2: (a) Pre-stressing release cracks in a (b) typical overcast girder and (c) pictorial representation of end and middle sections of girders

3.4.2.2. In-Service Girders

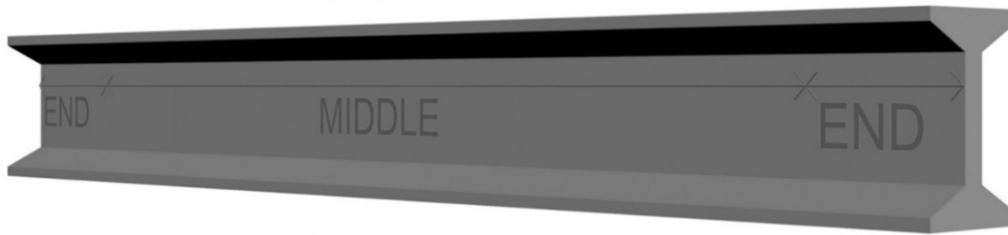
These girders are currently being used in the superstructure of in-service bridges. Thus, these girders are under dead loads as well as live “external” loads. According to Chapter 2 of the TxDOT Bridge Design Guide (2018) [46], the girders were designed based on the Federal Highway Administration's Load and Resistance Factor Design (LRFD) for Highway Bridge Superstructures for the theoretical HL-93 type vehicular loading [47].

Some of the in-service girders examined in this project were exterior girders (see Figure 3.3a) and were exposed to the elements more readily than the interior girders (see Figure 3.3b). It was found that the face of the girder exposed to the environment was painted, which can be readily seen in Figure 3.3a (notice the lighter color of the exterior girder as compared to the interior girder in Figure 3.3a). This paint is an opaque sealer, i.e., a solvent-borne stain-type coating capable of waterproofing as well as coloring finished concrete. The paint consists of a blend of acrylic and silicone resins and toning pigments suspended in solution at all times by a chemical suspension agent and solvent. The paint conformed to the Texas Department of Transportation Specification DSM8110 [48]. The paint coating on the exterior girders was provided with the intention of protecting the girders from the effects of weathering and for aesthetic reasons.

Measurements taken on the exposed face of the exterior girders (i.e., the face on the exterior side of the girder) are referred to as “Exposed” whereas the measurements that were taken on interior girders and the unexposed face of the exterior girders are referred to as “Sheltered” (see Figure 3.4b). Additionally, each girder can be considered to be comprised of “End” and “Middle” sections (see Figure 3.4b). Like the overcast girders, the ends of the in-service girders also have pre-stressing release cracks.



(a) Typical In-Service Girder



(b) Test Locations on In-Service Girder

Source: Images by Authors

Figure 3.3: (a) Typical in-service girder showing exterior and interior girders and (b) pictorial representation of end and middle sections of girder



(a) View from Left Side

(b) View from Right Side

Source: Images by Authors

Figure 3.4 In-service girder showing (a) exposed face and (b) sheltered face

3.4.3. Experimental Methods

Cracking, strain, ultrasonic pulse velocity, and surface resistivity tests were conducted on all the girders during each field visit. The temporal behavior of cracking and durability was determined using the data collected. The test methods used are described in this section.

3.4.3.1. Crack Indexing and Strain Measurement

Cracking in concrete elements is often related to the overall amount of expansion or shrinkage experienced by the affected concrete member [49]. Crack width measurements are typically used to quantify cracking severity [26], [27], [30], [31]; however, measuring only crack width may not provide a complete picture on the extent of cracking. The FHWA HIF-09004 report on ASR mitigation suggests a comprehensive method for evaluating the extent of cracking and volumetric change in concrete members by calculating the cracking index of the region of interest, determining the average crack of the cracks, and measuring strain [19].

Six locations on each overcast girder were selected. Due to limited accessibility to the in-service girders (e.g., accessing the middle of a beam is difficult when it is on a high overpass), four locations on each in-service girder were selected for evaluation. The 200 x 200 mm (8 x 8 in.) cracking index grids were set up at each test location on the girders. Figure 2.2 shows a typical crack grid on a girder. The cracking index and average crack width were calculated according to the method detailed in the FHWA HIF-09004 report [19], and is briefly summarized in this report. Specifically, the cracking index and average crack width were determined by counting the number of cracks and their respective crack widths along a perimeter square (the cracking index grid) with an illuminated Elcometer 900™ 50x crack microscope. Cracking index (I) is calculated as the summation of crack widths (W) divided by the base length (B) on the concrete surface (see Equation 3.1).

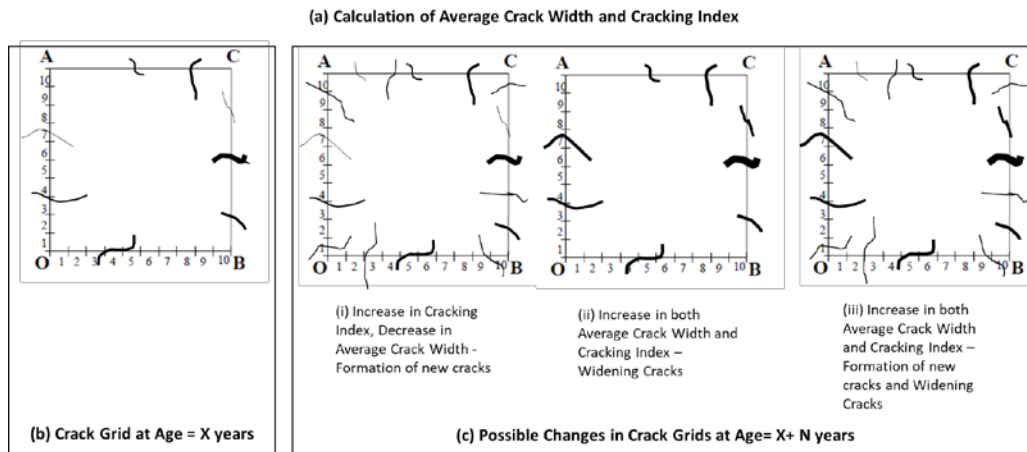
$$I = \frac{\Sigma W}{B} \quad \text{Equation 3.1}$$

Average crack width (ACW) is calculated as the summation of all crack widths (W) divided by the total number of cracks ($\#$) (see Equation 3.2).

$$ACW = \frac{\Sigma W}{\#} \quad \text{Equation 3.2}$$

Figure 3.5 shows a schematic of a typical crack grid and the calculation method for the average crack width and cracking index.

Base Length	Number of cracks	Total Crack Width (μm)	Average Crack Width (μm)	Cracking Index ($\mu\text{m}/\text{m}$)
$B = AO + OB + CB + AC$	(#)	(ΣW)	$ACW = (\Sigma W)/\#$	$CI = (\Sigma W)/B$



Source: Image by Authors

Figure 3.5: Sample calculations and possible crack grid scenarios

Strain measurements were facilitated by attaching DEMEC discs to the surface of the girders at the corners of each cracking index grid with a two-part cementing epoxy, and strain measurements were made using a Humboldt Multi-Length Strain Gauge™ set at 200 mm (8 in.) gauge length, in accordance with the FHWA HIF-09004 report [19]. The images in the squares in Figure 2.2 shows typical regions on an extensively cracked girder (see Figure 2.2a) and negligibly cracked control girder (see Figure 2.2b) as visible to the naked eye. The images shown in the circled call-out in Figure 2.2 show these girder surfaces at 50x magnification.

3.4.3.2. Ultrasonic Pulse Velocity

The in-situ condition of concrete is best determined by sampling cores and laboratory testing. However, coring is not always feasible due to safety and logistical reasons, as in this case. In such cases, UPV can be used as an indirect indicator of in-situ concrete quality. As per *ASTM C597, Standard Test Method for Pulse Velocity Through Concrete* [20], the pulse velocity of longitudinal stress waves in a concrete mass is related to the concrete's elastic properties and density. Studies have shown that UPV can be used as an indicator of modulus of elasticity and compressive strength of concrete. Researchers have showed that good correlations between UPV and elastic modulus and compressive strength [50], [51]. Researchers have also shown that UPV can also be used to accurately estimate in-field conditions of concrete structures by comparing UPV values measured in-situ and from extracted samples [52], [53].

The UPV test method can also be used to assess the uniformity and relative quality of concrete, indicate the presence of voids and cracks, identify changes in the properties of concrete and estimate the severity of deterioration or cracking. Higher pulse velocity in concrete indicates better homogeneity, i.e., higher quality concrete will have shorter wave travel time and subsequently higher velocity. The test can also be used to monitor changes in condition over time when the tests are repeated at the same locations [20]. UPV measurements were taken at the center of each cracking index grid, in accordance with *ASTM C597, Standard Test Method for Pulse Velocity Through Concrete* [20] with a C N S Farnell PUNDIT7™ portable ultrasonic pulse velocity meter.

3.4.3.3. Surface Resistivity

Electrical resistivity, an indicator of a material's ability to withstand the transfer of charge, represents the ratio between the applied voltage and resulting current multiplied by a cell constant. Higher resistivity values are associated with higher corrosion resistance [54]. Using surface resistivity measurements as an absolute value might not yield satisfactory results, due to the high scatter observed in correlation data between corrosion rate and resistivity[55]. However, the test can be used effectively to monitor changes in condition over time when test locations are marked on the element and tests are repeated at the same locations[56]. Studies have shown that surface resistivity has good correlations with both bulk resistivity and rapid chloride penetration test values [57], [58]. Surface resistivity has also successfully been used as an indicator of concrete durability for in-situ concrete members [59]–[62].

Surface resistivity was measured according to *AASHTO TP358–Standard Method of Test for Surface Resistivity Indication of Concrete’s Ability to Resist Chloride Ion Penetration* [21] with a Reispod ProceqTM Wenner probe. While the standard is prescribed for use on cylinders and cores, the method was modified in accordance with the method suggested by Gowers and Millard (2009) for the surface of the girders. Prior to each measurement, one liter of water was sprayed on the girder to saturate the surface [56].

3.5. Results and Discussions

In this study, pulse velocity is used as an indicator of the extent of deterioration in elastic properties and density of concrete, while the surface resistivity is used as an indicator of corrosion potential. The overall extent of cracking in the girder is characterized through the analysis of changes in cracking index, average crack width, and the strain. A decrease in pulse velocity and surface resistivity and an increase in cracking index, average crack width, and strain are indicative of lowering in overall quality of concrete. This section reports the temporal changes in cracking index, average crack width, strain measurements, surface resistivity, and ultrasonic pulse velocity of the test girders.

All figures in this section show the change in these parameters over the one and two-year monitoring period with the black bars indicating the change over one year and the grey bars indicating the cumulative change over two years (as seen in Figure 3.6a). In addition, values that are too small to be shown clearly on the main graphs have been magnified and shown in the insets (as seen in Figure 3.6b).

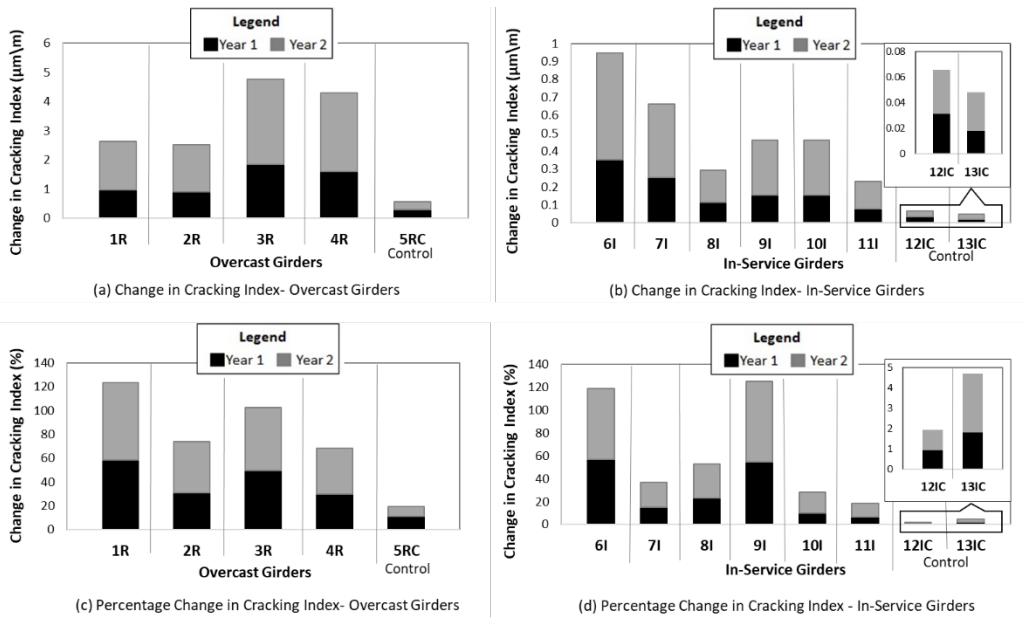


Figure 3.6: Magnitude and percentage change in cracking index over the one- and two-year monitoring period

3.5.1. Effect of External Loading

All girders show an overall increase in the cracking index (see Figure 3.6) over the two-year test period, as well as a change in the average crack width (see Figure 3.7). An increase in cracking index (see Figure 3.6) is seen in both the overcast and in-service control girders during the monitoring period. The overcast girders show a larger increase in the cracking index than the in-service girders (Note: For ease of viewing, different scales were used in Figure 3.6a and Figure 3.6b. In Figure 3.6a, the y-axis ranges from 0 to 6 $\mu\text{m}/\text{m}$; whereas in Figure 3.6b, it ranges from 0 to 1 $\mu\text{m}/\text{m}$). Like the trend exhibited by the cracked girders, the overcast control girder has a higher increase in cracking index than the in-service control girders. The negligibly cracked control girders have a lower magnitude of change when compared to their cracked counterparts (compare Overcast with Overcast Control in Figure 3.6a, and In-service with In-service Control in Figure 3.6b). As seen in Figure 3.6c and Figure 3.6d, the percentage change in cracking index shows that both overcast and in-service girders have a similar rate of increase in cracking, even though the magnitude of change is different.

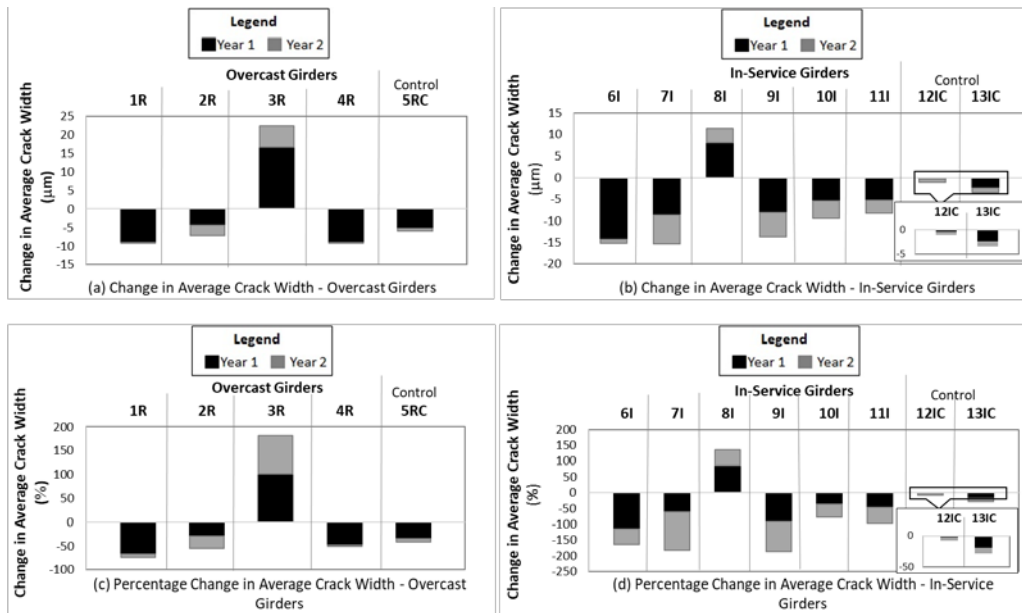


Figure 3.7: Magnitude and percentage change in average crack width in over the one- and two-year monitoring period

Figure 3.7 shows the change in average crack width values for the overcast and in-service girders. Comparing the relative change in average crack width and cracking index of girders provides insight into the formation of new cracks and the widening of existing cracks. Crack widening is observed in girders that show an increase in average crack width and cracking index. For example, Girders 3R and 8I show an increase in both average crack width (see Figure 3.8a) and cracking index (see Figure 3.8b). Analysis of the crack distribution curves provides more insight into the nature of crack growth. Girder 3R shows an increase in both the formation of new cracks and the widening of existing cracks (see Figure 3.8). The large increase in the number of cracks measured in the smallest crack width measured (i.e., 6 µm) proves that new cracks were formed. However, since there was a considerable increase in the number of cracks measured in the other width ranges as well, this shows that widening of the existing cracks also occurred. Whereas for Girder 8I, the crack growth pattern is more attributed to crack widening than the formation of new cracks, since there were fewer cracks forming in the 6 µm range and a moderate increase in the number of cracks in the other width ranges (see Figure 3.8d).

However, most girders exhibited a decrease in the average crack width (see Figure 3.7). This can lead to the erroneous conclusion that the microcracks were healing themselves, which is not the case, as indicated by the positive increase in the cracking index values (see Figure 3.6). Thus, negative values for average crack width coupled with positive cracking index values mean that the cracking behavior during the time frame of interest was dominated by the formation of thin cracks rather than by the widening of existing cracks. For example, Figure 3.8e and Figure 3.8f show crack width distributions for Girders 6I and 7I, both of which show negative values for average crack width and positive cracking index values. It can be seen that for both these girders the number of cracks measured in the 6 to 12.5 µm range increased, which means that new cracks were detected. However, since the number of cracks measured in the moderate and larger width ranges remained relatively unchanged, this indicates that overall the cracks in these size ranges are not widening. Thus, by using both average crack width and cracking index as measures of cracking, deeper insight is obtained about the growth

pattern of the microcracks. Crack width distributions for all girders is provided in Appendix A. In this work, three different crack growth patterns were observed during the monitoring period. Figure 3.5a depicts the calculation of average crack width (ACW) and cracking index (I). A schematic of a crack grid at age "X" years (see Figure 3.5b) and the temporal changes observed in the crack grid at "X+N" years is provided in Figure 3.5c. The three crack growth patterns observed in this work are summarized below:

- Figure 3.5c (i) - An increase in cracking index (I) and a decrease in average crack width (ACW) due to the formation of new cracks, as seen in the case of Girders 6I and 7I.
- Figure 3.5c (ii) - An increase in both cracking index (I) and average crack width (ACW) due to the widening of existing cracks, as seen in the case of Girder 8I.
- Figure 3.5c (iii) - An increase in both cracking index (I) and average crack width (ACW) due to the widening of existing cracks and formation of new cracks as seen in the case of girder 3R.

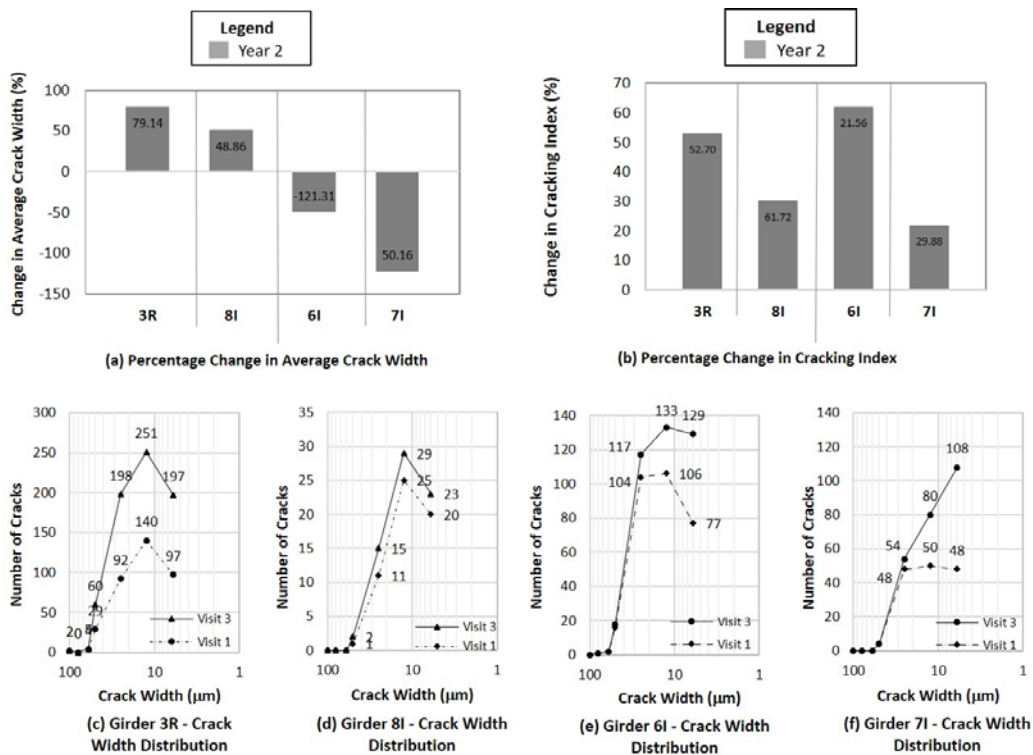


Figure 3.8: Crack width distributions

Figure 3.9a and Figure 3.9b show the strain values of the overcast and in-service girders. The strain values had standard deviations ranging between 0.00004 and 0.00006. The negative values indicate volumetric shrinkage. The expected theoretical strain value generated by the ACI Committee 209 model for prediction of creep, shrinkage, and temperature effects on concrete structures for a typical girder was calculated [63]. Strain values of 0.0003, 0.00034, and 0.0004 were calculated for typical Type IV, Tx7, and Tx54 girders [64], respectively, for a two-year period. It can be seen that all the girders, with the exception of 11I, 12IC and 13IC, have exhibited higher strain values than the predicted value. The strain values of the girders show a trend similar to the increase in cracking index with overcast girders having the highest

strain followed by the overcast control, in-service, and in-service control girders (i.e. R>RC>I>IC).

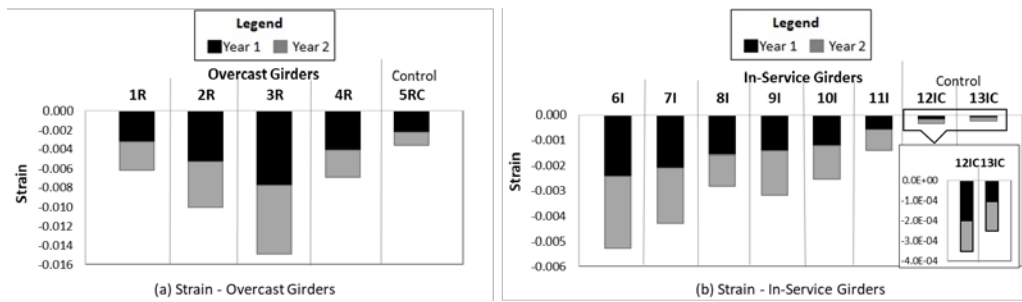


Figure 3.9: Strain over the one- and two-year monitoring period

Since the in-service girders are under the influence of external loads, they were expected to display a higher increase in microcracking and losses in durability than the overcast girders, which are not under the influence of external loads. However, the overcast cracked girders had greater reductions in pulse velocity measurements (see Figure 3.10) and surface resistivity measurements (see Figure 3.11) than the in-service cracked girders. This correlates well to the changes seen in the cracking index and strain values since the overcast girders have a larger change in cracking index (see Figure 3.6), average crack width (see Figure 3.7) and strain (see Figure 3.9) than the in-service girders. However, the magnitude of change in pulse velocity and surface resistivity is small enough that durability concerns due to this reduction are not warranted for this present state. All the concretes had an ultrasonic pulse velocity and surface resistivity values greater than 5000 m/s and 425 kΩcm, respectively. A concrete ultrasonic pulse velocity of greater than 4575 m/s is classified as "Excellent" and surface resistivity higher than 35 kΩcm is classified as having very low corrosion potential [65], [66].

The aforementioned results show that the impact of external loading on the growth of microcracks in the girders is minimal (see Figure 3.6, Figure 3.7, Figure 3.9, Figure 3.10, and Figure 3.11). To better understand the factors affecting the microcracking growth, additional data analysis was conducted to examine the role of exposure conditions (see Figure 3.1 and Figure 3.3) and the presence of pre-existing cracks (see Figure 3.2 and Figure 3.4). In addition, the effect of pre-stressing direction on strain values could also be taken into account as the girders are pre-stressed in the longitudinal direction and this can have a restraining effect on the volumetric changes.

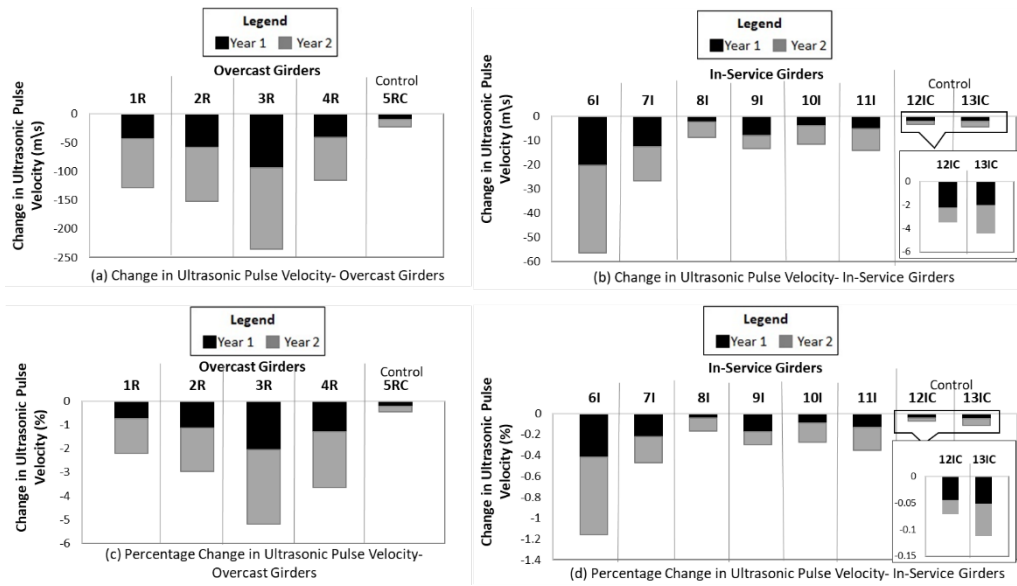


Figure 3.10: Magnitude and percentage change in pulse velocity over the one- and two-year monitoring period

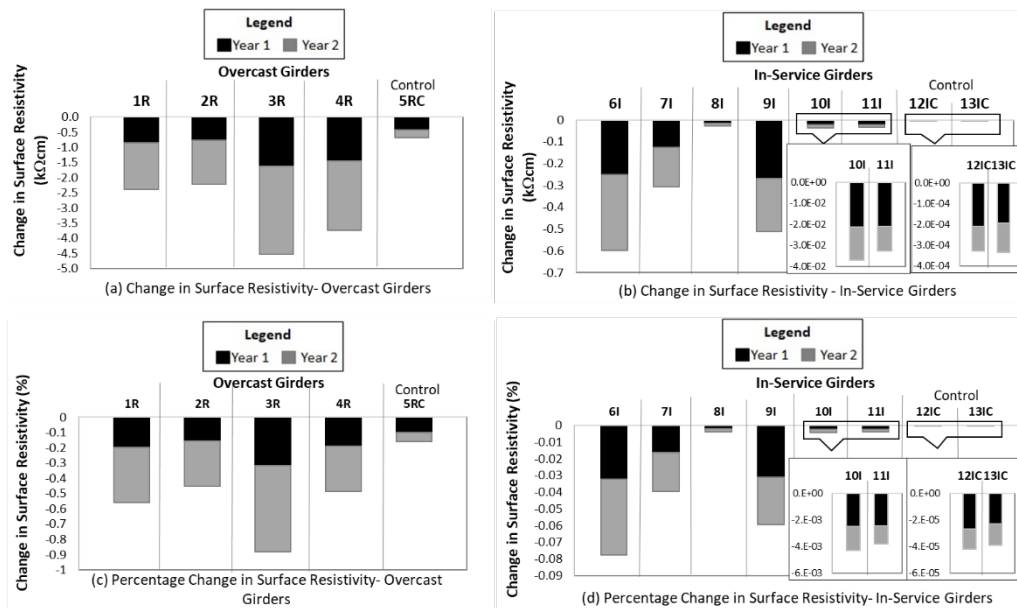


Figure 3.11: Magnitude and percentage change in surface resistivity in over the one- and two-year monitoring period

3.5.2. Effect of Exposure to the Environment

The effect of exposure conditions was analyzed to understand the factors affecting microcracking behavior. The change in cracking index, average crack width, strain, and resistivity are discussed. The change in pulse velocity is not included as it is an indicator of bulk concrete properties rather than surface properties and hence, a comparison based on exposure conditions, that would affect just one face, would not accurately be indicated by the variation in pulse velocity.

Figure 3.12 shows the change in cracking index for all girders based on the exposure conditions. The exposed faces of the overcast girders have a greater increase in cracking index than the sheltered faces (see Figure 3.1a). However, this behavior is not observed in the exposed faces of the in-service girders (see Figure 3.4b). In-service Girders 6I and 7I are exterior girders, each with one face exposed and one face sheltered, as seen in Figure 3.3. The sheltered faces of these girders display a greater change in cracking index than the exposed face of the in-service girders. This can be attributed to the paint on the exterior face of the girder (Figure 3.4a). The remaining in-service girders (8I-11I, 12IC, and 13IC) do not have exposed surfaces as they are interior girders. Figure 3.13 shows the impact of exposure conditions on the change in average crack widths for all girders. Overall, like the change in cracking index, the change in average crack width is greater for the exposed faces than the sheltered faces in the cracked overcast girders (see Figure 3.13a). The paint has the same effect on the average crack width as it does on cracking index (i.e., greater change in crack width on exposed face than the sheltered face), as seen in Figure 3.13b.

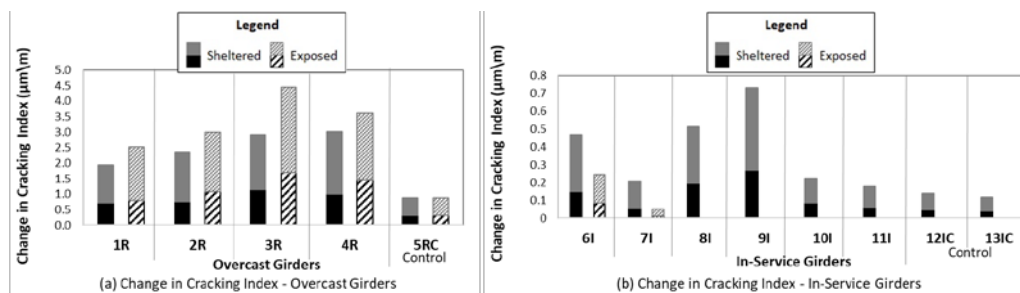


Figure 3.12: Effect of exposure conditions on change in cracking index over the one- and two-year monitoring period

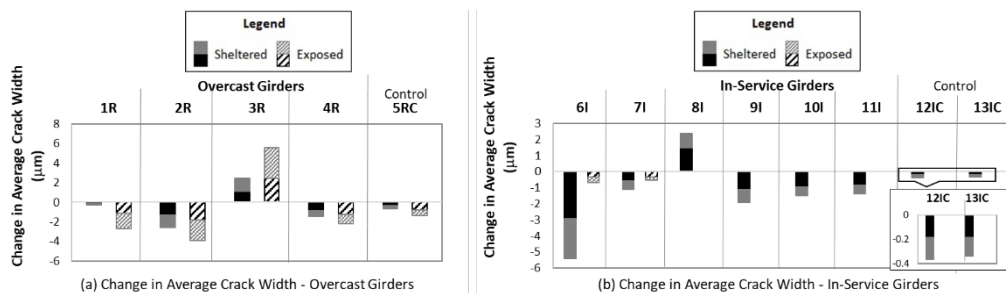


Figure 3.13: Effect of exposure conditions on change in average crack width over the one- and two-year monitoring period

Figure 3.14 shows the change in surface resistivity for all girders. The exposed faces of the girders show a greater reduction in surface resistivity than the sheltered faces in all cracked overcast girders. This suggests that the deterioration is higher in the exposed faces than the sheltered faces. In the case of the exterior in-service girders (6I and 7I), the surface resistivity of the exposed faces is higher than both the sheltered faces of the exterior girders as well as the interior in-service girders in the bridges. This indicates that the exterior faces of the in-service girders have higher deterioration than both the sheltered faces of the exterior girders and the interior girders. This contrasts with the change in cracking index and average crack width results (see Figure 3.12b and Figure 3.13b). The surface resistivity results indicate that painting the exposed face of the exterior girder does not necessarily prevent loss in corrosion resistance. Change in cracking values for the exterior faces of the in-service girders (see Figure 3.12b and Figure 3.13b) suggest that there is a lower rate of loss in durability on the exposed, exterior

faces than the sheltered face. However, the decreasing surface resistivity values for the exposed faces indicate a higher rate of loss in corrosion resistance on the exposed faces than the sheltered faces. As such, the paint appears to only prevent cracks from being observed but does not prevent the formation of cracks. If the paint truly played a significant role in decreased cracking, this would have manifested in the form of a lower decrease in the surface resistivity on the exposed faces of the in-service exterior girders as well.

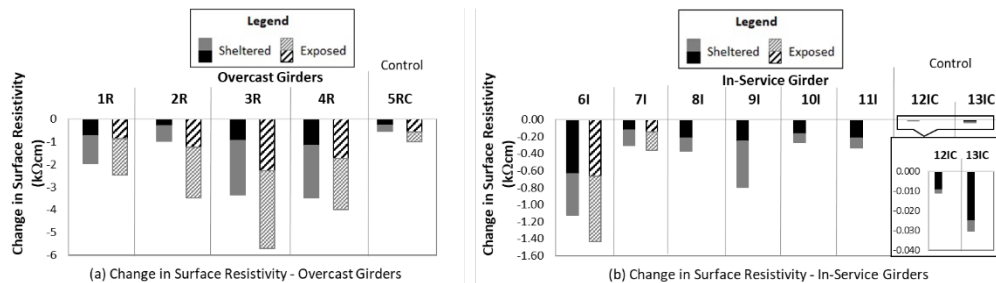


Figure 3.14: Effect of exposure conditions on change in surface resistivity over the one- and two-year monitoring period

Figure 3.15 shows the strain for all girders. The strain values are greater for the exposed faces than the sheltered faces in all the cracked overcast girders. A higher strain is also observed in the exterior faces of in-service girders (6I and 7I) when compared to the strain in the sheltered faces and the interior in-service girders. This shows that there indeed is strain in the exterior girders, further supporting the theory that the paint merely prevents the cracks from being observed and not the formation of cracks. The overcast control girder exhibits lower strain than the cracked overcast girders on the exposed face. The in-service control girders have strain values comparable to the overcast control girder, while still being lower than that of the cracked in-service girders.

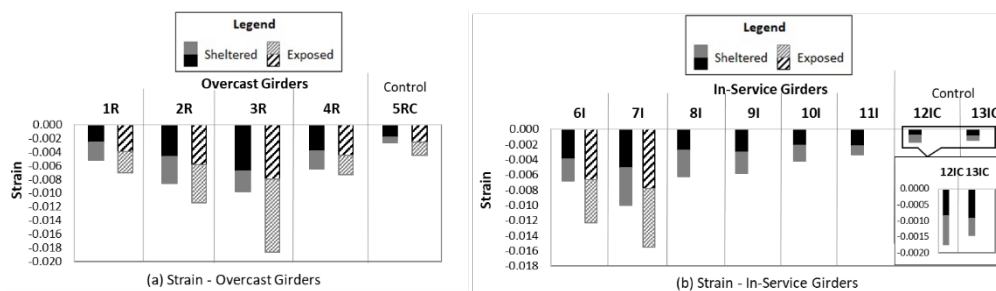


Figure 3.15: Effect of exposure conditions on change in strain over the one- and two-year monitoring period

3.5.3. Effect of Pre-Existing Cracks

Visual inspections showed that higher levels of cracking were present on the end sections of all girders than in the middle sections. This can be attributed to the presence of large pre-stress release cracks present in the end sections. These cracks generally number between 5 and 10, are wider than 100 μm , and radiate inwards from the end of the girder (as seen in Figure 3.2). As these cracks are outside the 6 to 100 μm microcrack width range, they are not included in the calculations for the average crack width and cracking index in the crack grids. Hence, the cracking parameters discussed in this study consist only of microcracks lying in the 6 to 100 μm crack width range. The impact of these larger pre-stressing release cracks on the change in

average (micro) crack width, (micro) cracking index, strain, pulse velocity, and resistivity over the monitoring period will be determined.

Figure 3.16 shows the change in three cracking parameters—(a) cracking index, (b) average crack widths, and (c) strain—for all girders examined in this work for the two-year monitoring period for the (i) overcast and (ii) in-service girders. The results corresponding to the end sections of the girders are denoted using solid bars, whereas a hatched bar with diagonal lines denotes the regions corresponding to the middle section. In both the cracked and control overcast girders, the end sections of the girders show a higher increase in the three cracking parameters than their corresponding middle sections. Similar behavior is seen in the end sections of both the cracked and control in-service girders, with the end sections exhibiting greater changes in the three cracking parameters than their middle sections. A higher change in the cracking index and average crack width values indicates an increase in the overall microcracking, while a higher change in the strain values indicates increased shrinkage. Thus, the presence of pre-existing cracks proved to be a factor that has the potential to affect the rate of change in cracking (i.e., average crack width, cracking index, and strain).

Figure 3.17 shows the change in (a) pulse velocity and (b) surface resistivity for all the (i) overcast and (ii) in-service girders. Similar trends are seen on both the pulse velocity and surface resistivity values. The decrease in pulse velocity and surface resistivity is higher in the end sections in cracked and control overcast and in-service girders than the middle sections. This behavior occurs regardless of the presence of visible cracks on the girders. The decrease in pulse velocity and surface resistivity in the end sections of all control (overcast and in-service) girders are comparable to that of the in-service cracked girders. Thus, when the rate of change in cracking parameters, ultrasonic pulse velocity, and surface resistivity between end and middle sections are compared, the end sections have a higher loss in durability in all the girders. This further supports the premise that the presence of pre-existing macrocracks play a role in reducing the integrity of the girders, and suggests that a greater reduction in modulus of elasticity (as indicated by the decrease in pulse velocity) and corrosion resistance (as shown by the decrease in surface resistivity) would occur in the end sections of the girders as compared to the middle sections.

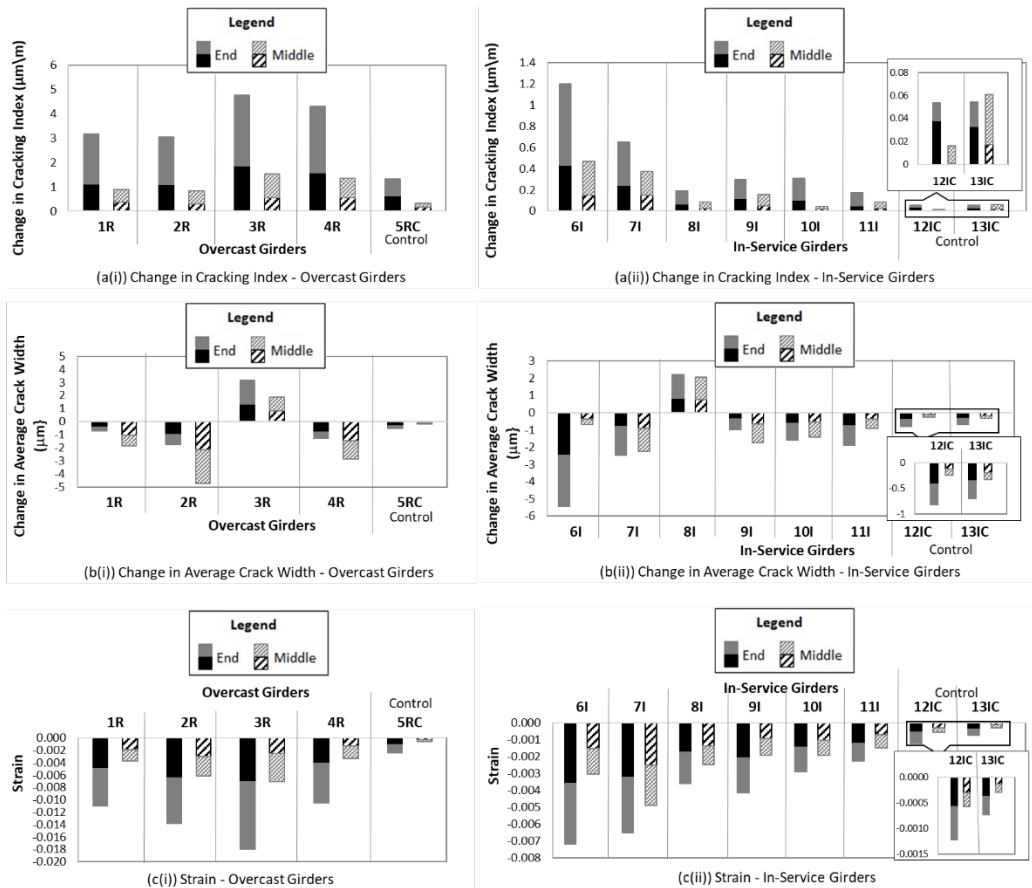


Figure 3.16: Effect of pre-existing cracks over the one- and two-year monitoring period

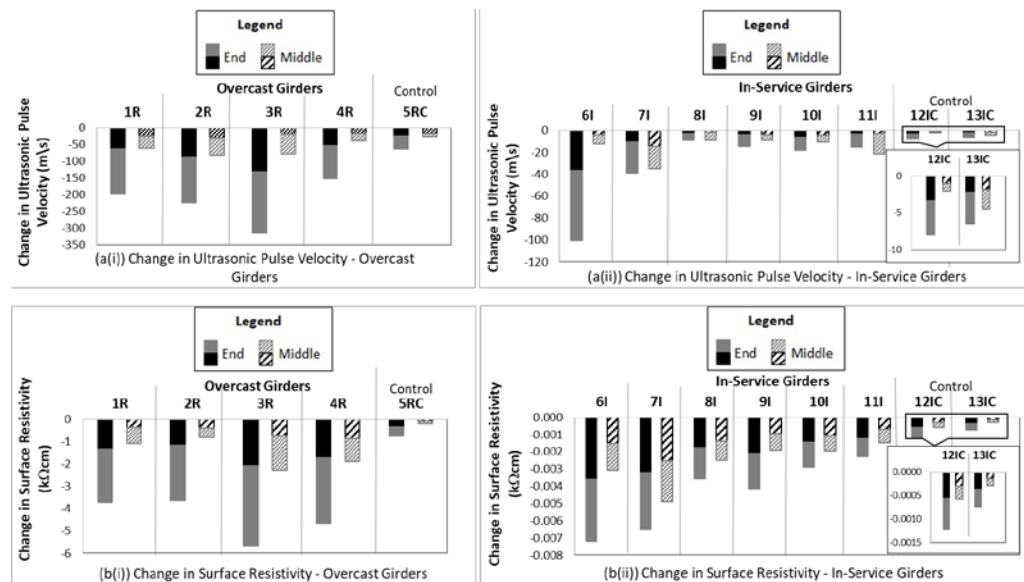


Figure 3.17: Effect of pre-existing cracks over the one- and two-year monitoring period

3.5.4. Effect of Direction of Measurement

Figure 3.18 shows that the girders exhibit shrinkage in both directions, i.e., parallel and perpendicular to direction of pre-stressing (see Figure 3.19b). However, it is seen that there is higher strain perpendicular to the pre-stressing strands than in the parallel direction. This unequal strain is reflected in the cracking behavior as well and is likely due to the pre-stressing

strands acting as restraints against shrinkage in the prestressing direction [67], [68]. This restraint results in fewer cracks opening in that direction [69], [70]. In other words, as depicted in Figure 3.19, the restraint due to the prestressing strands leads to the cracks being oriented in the direction parallel to the prestressing strands since more volumetric changes (and thus crack opening) occur in the direction in which shrinkage is unrestrained, i.e., perpendicular to the prestressing direction.

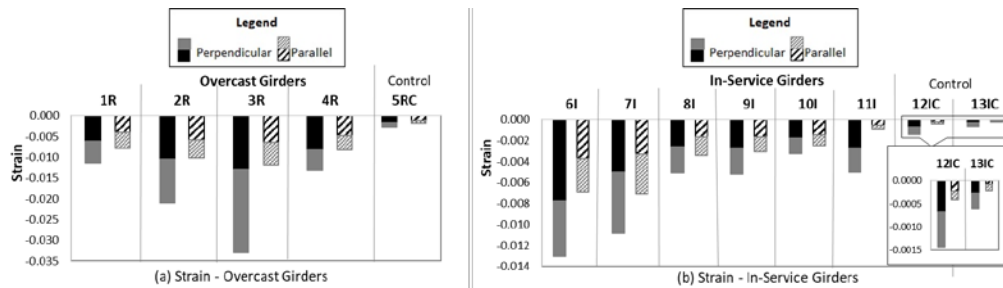
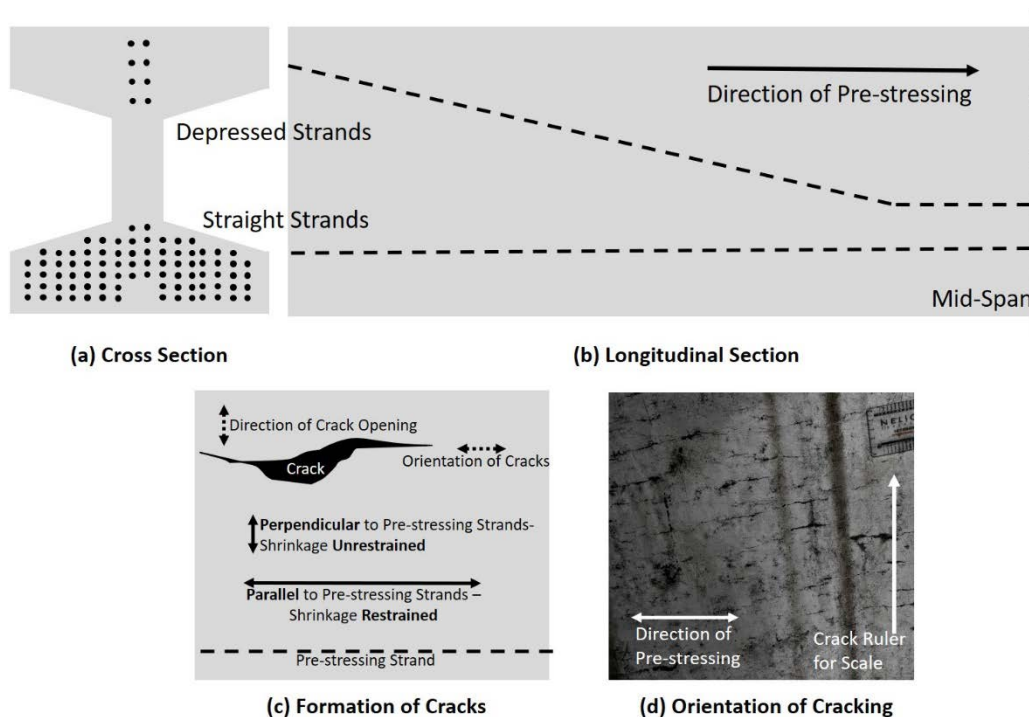


Figure 3.18: Effect of direction of measurement (parallel and perpendicular to the direction of prestressing) on strain over the one- and two-year monitoring period



Source: Image by Authors

Figure 3.19: Schematic of pre-stressing strand details in (a) cross-section and (b) longitudinal section, (c) formation of cracks and (d) orientation of microcracks direction

3.6. Conclusions

The conclusions of Task 2 are presented in this section. A temporal study to observe the cracking, ultrasonic pulse velocity, the surface resistivity of the overcast and in-service girders was conducted. It was seen that the girders exhibited an increase in cracking and shrinkage and a marginal decrease in ultrasonic pulse velocity and surface resistivity. Analysis of the temporal data showed that exposure to environment and pre-existing cracks were major factors affecting

the rate of cracking. It was also seen that external loading had not impacted the rate of growth of cracking in a negative way yet.

The following conclusions were drawn from the study:

- An increase in overall cracking, a decrease in ultrasonic pulse velocity (an indicator of stiffness properties) and decrease in surface resistivity (an indicator of corrosion resistance properties) occurred in the girders over the two-year test period. Taken holistically, this suggests that a decrease in durability occurred during the timeframe considered. However, even with these reductions, the present state of the girders should have good resistance to corrosion since the surface resistivity values, and pulse velocity values of all the girders are still in the high-quality range.
- The girders that are not in-service (i.e., overcast girders) showed a higher increase in microcracking than the in-service girders, which suggests external loading is not a major factor impacting the integrity of the beam. As the girders are relatively young (average age is under 10 years old), when one considers the intended service life of the girders (50 – 75 years), it is possible that the effects of sustained load and cyclic loading on the girders have not yet manifested.
- Exposure conditions did have an impact on the microcracking tendency in the overcast girders, and the exposed faces of the overcast girders showed the greatest increase in microcracking than the sheltered sides and interior girders. While the exposed faces of the exterior in-service girders did not exhibit an increase in average crack width and cracking index, interestingly, they exhibited a decrease in surface resistivity and higher strain. This can be attributed to the layer of paint applied to the exposed in-service girders, and the results indicate that the paint layer, intended to protect the girder surface from exposure to environment, only prevented the cracks from being visible and did not prevent their formation.
- Pre-existing cracks played a substantial role in the rate of growth of cracking, and regions that had pre-existing macrocracks exhibited a greater increase in microcracking than the regions that did not have pre-existing macrocracks.
- The direction of pre-stressing also played a role in the magnitude of strain. It is seen that there is a much higher strain perpendicular to the pre-stressing strands than in the parallel direction. This behavior may be attributed to the effects of reinforcement acting as restraints against cracking.
- The study also showed the temporal behavior of average crack width values is heavily dependent on the mechanism of increase in cracking, i.e. whether the change is due to an increase in width of existing cracks or due to the formation of new cracks. When new cracks are formed, this can lead to a decrease in average crack width over time, erroneously indicating that the cracks are growing smaller, whereas this is not the case. Hence, to accurately account for the temporal behavior of cracking, both the growth in cracking index and average crack width should be taken into consideration.

Chapter 4. Evaluation of Extracted Cores

4.1. Overview of Chapter

This chapter discusses the methodology and results for Task 3: Evaluation of extracted cores. Laboratory tests were conducted on the cores extracted from the overcast girders to determine the effect of cracking on the strength, stiffness, and durability properties of the girders. The change in cracking, compressive and split tensile strength, modulus of elasticity, ultrasonic pulse velocity, surface and bulk resistivity, chloride diffusion coefficient, and carbonation coefficient of the girders over the monitoring period is reported. In addition, accelerated weathering was conducted on a portion of the cores to study the effect of weathering and pre-existing cracks on the rate of growth of cracks. Optical and scanning electron microscope images of the surface cracks are presented to gain a better understanding of the microcracking behavior.

4.2. Objective

The primary objective of the research conducted during this phase of the project was to conduct laboratory tests on the cores collected from the Type A and Type C visits (i.e., the overcast girders) to determine the extent to which the cracking can affect strength, stiffness, and durability of the girders.

4.3. Background

Cracks are caused when concrete is subjected to stresses higher than the design value. This stress can be due to volumetric changes, loading, thermal changes, and internal pressure, among others. Table 4.1 shows the various causes that can generate cracks in concrete. However, irrespective of why they are caused, cracks exacerbate the rate of deterioration, which leads to loss of service life of in-service structures. The debilitating effect that cracks have on both strength and long-term durability of concrete structures has been quite well researched [35], [71]–[78].

Early studies on evaluating the effect of cracking in concrete were focused on large visible cracks, also known as macrocracks. These cracks are generally larger than 300 μm (0.01 in.) [39]. However, cracks several magnitudes smaller than 300 μm (0.01 in.) have been found in concrete. Thus, these cracks were called microcracks. While these microcracks were smaller in width than macrocracks, they tend to be more numerous [79].

As detailed in Table 4.1, microcracks can be caused by various methods. They also have the potential to grow into larger macrocracks over time due to chemical attacks or physical stresses [80]. Extensive microcracking is often seen in pre-cast pre-stressed bridge girders [2], [9], [10], [81]–[83]. These pre-cast mixtures are generally designed for high early strengths and self-consolidation to reduce construction time and to allow for quick release of the pre-stressing strands. Precast pre-stressed concrete mixtures typically have low w/cm (0.28–0.33), high cementitious contents (>800 lbs/yd), and contain chemical admixtures (water reducers, superplasticizers, and viscosity modifying agents) which can increase drying and autogenous

shrinkage [2], [3], [84]. Cracks formed during concrete’s plastic stage, i.e., before hardening, generally do not temporally evolve unless there are additional external stresses applied to them [85]. Structural and physio-chemical cracks are usually induced internally as microcracks that grow to external macrocracks under continued stresses [40]. Cracks formed due to volume instability tend to manifest on the concrete’s surface as microcracks and temporally evolve under increasing volumetric changes or structural loads or a combination of both [67], [86]–[88]. These cracks can be quantified in both two-dimensional as well as three-dimensional parameters. The two-dimensional surface characteristics can be quantified in terms of crack widths and crack densities. The three-dimensional characteristics can be ascertained by including crack depth/index. Other crack parameters include orientation, tortuosity, shape, and connectivity [89].

Table 4.1: Types and Causes of Cracking in Concrete

Cracking in Concrete	Time of Cracking	Cause of Cracking		Type of Cracking
	Cracking in Concrete	Before Hardening	Construction Movement	Formwork Movement
Subgrade Movement				
Plastic			Plastic Shrinkage	Microcracks
			Plastic Settlement	
			Autonomous Shrinkage	
Frost Damage			Premature Freezing	Crazing or map cracking
		Crazing and Scaling		
After Hardening		Volume Instability	Drying Shrinkage	Microcracks that grow in a map or star-burst pattern
			Thermal Shrinkage	
			Creep	
		Structural	Overloading	Compression, tension or flexure induced micro and macro cracks
			Subgrade Movement	
			Fatigue	
		Physio-chemical	Alkali Aggregate Reaction	Internal expansion induced microcracks that grow into external macrocracks
	Alkali-Silica Reaction			
	Delayed Ettringite Formation			
	Corrosion			
Freeze-thaw cycling				

The influence of crack width and depth on the strength and durability properties of concrete is well researched [38], [78], [90]–[95]. In addition, modeling the effect of a single crack on strength and durability is quite common. However, the impact of crack density/index is not studied as much due to the complexities involved in modeling multiple cracks. For example,

Kwon et al. (2009) conducted a study to estimate the service life of concrete wharves with drying shrinkage cracks. However, in their model, they decided to avoid using samples with multiple cracks to avoid the complexities of modeling multiple cracks [27]. However, some limited research has been conducted to determine the effect of cracking density/index. Jacobsen et al. (1996) used crack density, measured by counting the number of cracks traversing parallel lines, to study the effect of cracking on compressive strength and chloride ingress in concrete subjected to freezing and thawing [96]. Nemati et al. (2009) conducted an analysis of compressive stress-induced cracks in concrete. They quantified the density of microcracks and their distribution by measuring the surface area of cracks per unit volume [97]. Zhou et al. (2011) attempted to incorporate the impact of crack interconnectivity on the permeability of microcracked solids. While not focused on concrete, this study showed that increased interconnectivity in cracks led to increased permeability [98]. Akhavan et al. (2012) attempted to quantify the effects of crack geometries on the water permeability of cracked mortars. They showed that permeability coefficient was a function of the square of crack width. They also showed that tortuosity and surface roughness of cracks were factors that affected the permeability coefficient [99]. Wang and Zhang (2016) presented a numerical procedure to simulate chloride ingress into cracked concrete with different crack geometries (width ranging between 49 μm to 0.3 mm). The influences of single and multiple flexure induced cracks on chloride ingress were considered. They found that increasing crack width, depth, and the number increased the chloride ingress [100]. Wang et al. (2016) studied the effects of different cracking parameters on the potential for chloride ingress. They determined that there was a linear approximation between crack tortuosity and crack orientation. They also showed that chloride ingress increased with increasing crack density. They showed that this model could be improved by accounting for crack orientation. They also showed that chloride diffusivity was significantly affected by cracks with widths between 100 and 400 μm , but beyond this range, the influence of crack width was negligible [35].

4.4. Materials and Methods

Cores extracted from full-scale overcast girders at pre-cast yards were used in this study. Table 4.2 presents the tests conducted and the number of samples from each girder used during each study. It also presents the acceptable serviceability values from standards and literature for concretes with comparable w/cm and strengths. Some tests were non-destructive; thus, they were conducted on all the samples. These samples were later used to conduct the strength, stiffness, and durability tests since those tests are destructive tests.

Table 4.2: Items of Investigation and Serviceability Values

Test	Source for Test Methodology	28-day Serviceability Values	Source for Serviceability Values	Number of Samples Tested from each Girder		
				Visit 1	Visit 2	Visit 3
VISUAL EVALUATION						
Microcracking Evaluation	FHWA-HIF-09-004 Report [19]	-	-	15	8	8
Optical Microscopy	ASTM C1723 [101]	-	-	1	-	-
Scanning Electron Microscopy		-	-	1	-	-
STRENGTH TESTS						
Compressive Strength	ASTM C42 [102]	35 MPa (5000 psi)	TxDOT Bridge Design Manual, (2018) [18]	4	2	2
Tensile Strength	ASTM C496 [103]	3 MPa (425 psi)		2	2	2
STIFFNESS TESTS						
Ultrasonic Pulse Velocity*	ASTM C597 [20]	3660-3050 m/s	Malhotra (1976) Turgut (2006) [65], [104]	15	8	8
Elastic Modulus	ASTM C469 [105]	35 Gpa (5x10 ⁶ psi)	TxDOT Bridge Design Manual (2018) [18]	4	2	2
DURABILITY TESTS						
Bulk Resistivity*	AASHTO TP119 [54]	12–21 kΩcm	Sengul (2014) FDOT Standard (2004) [66], [106]	15	8	8
Surface Resistivity*	AASHTO T358 – Modified for Cylinders [21]	5-7.5 kΩcm		15	8	8
Chloride Diffusion Coefficient	NT Build 492 [107]	15 x 10 ⁻¹² m ² /s		4	2	2
Carbonation Coefficient	CPC-18 [108]	5.8 mm/yr ^{0.5} (0.26 in./yr ^{0.5})	50 mm (2 in.) for 75 years, i.e. Cover over expected service life [12]	6	6	6
Note: * Non-destructive test						

4.4.1. Visual Evaluation

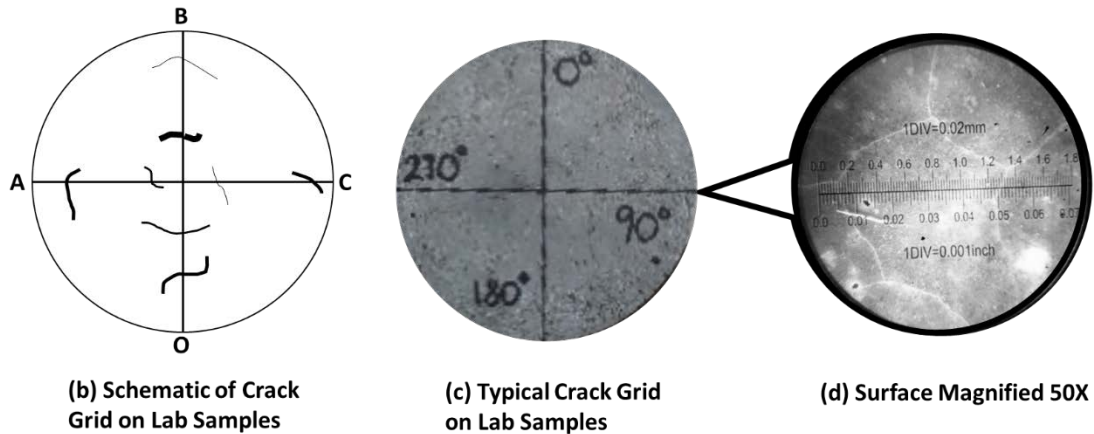
4.4.1.1. Cracking Measurements

The average crack width and cracking index of both the exposed faces of the cores were calculated. The two-dimensional severity of cracks is generally assessed using width and density/index. The average crack width and cracking density/index were calculated according to the method prescribed by the FHWA-HIF-09-004 Report [19]. Equation 3.1, Equation 3.2, and Figure 4.1 show the calculation of crack width and cracking index for in-service structures and the modified method used to measure cracking index of cores.

In addition to the surface cracking parameters, strength, stiffness, and durability tests were also conducted on the cores. Table 4.2 shows the tests conducted, the test method used, 28-day serviceability values and source, and the number of samples tested from each field visit.

Unit Length	Number of cracks	Total Crack Width (μm)	Average Crack Width (μm)	Cracking Index ($\mu\text{m}/\text{m}$)
$B=AC+OB$	(#)	(ΣW)	$ACW = (\Sigma W)/\#$	$I = (\Sigma W)/B$

(a) Calculation of Crack Width and Cracking Index



Source: Images by Authors

Figure 4.1: Calculation of average crack width and cracking index of cores

4.4.1.2. Microscopy

An optical crack microscope (50X Elcometer 900TM) and a scanning electron microscope (JEOL 6490 Low-vacuum Scanning Electron Microscope) were used to observe the cracks in cores from the first round of field visits. The surfaces of the cores were observed under an optical microscope. The cores were sliced using a lapidary saw, and the vertical sections were observed under the optical microscope to determine the crack depths. The microcracks on the surface on the cores were also observed under 100X, 500X, and 1500X under a scanning electron microscope (SEM). The crack widths from the SEM were compared to the microcracking observed under the crack microscope.

4.4.2. Strength Tests

The compressive strength of cores from each field visit was determined in accordance with *ASTM C39—Standard Test Method for Compressive Strength of Cylindrical Concrete Specimens* [109]. The tensile strength of the girders was estimated using the splitting tensile strength test (*ASTM C496—Standard Test Method for Splitting Tensile Strength of Cylindrical Concrete Specimens* [103]).

4.4.3. Stiffness Tests

The static modulus of elasticity of the cores was determined in accordance with *ASTM C469—Standard Test Method for Static Modulus of Elasticity and Poisson's Ratio of Concrete in Compression* [105]. This test involves loading a cylindrical specimen to 40% of its current

compressive strength and measuring the deformation of the central portion of the specimen. As the number of samples was limited, stress-strain curves were plotted for each sample, and the slope of the linear portion was determined to calculate the elastic modulus. In addition the ultrasonic pulse velocity of all the cores was determined in accordance with *ASTM C597-Standard Test Method for Pulse Velocity Through Concrete* [20].

4.4.4. Durability Tests

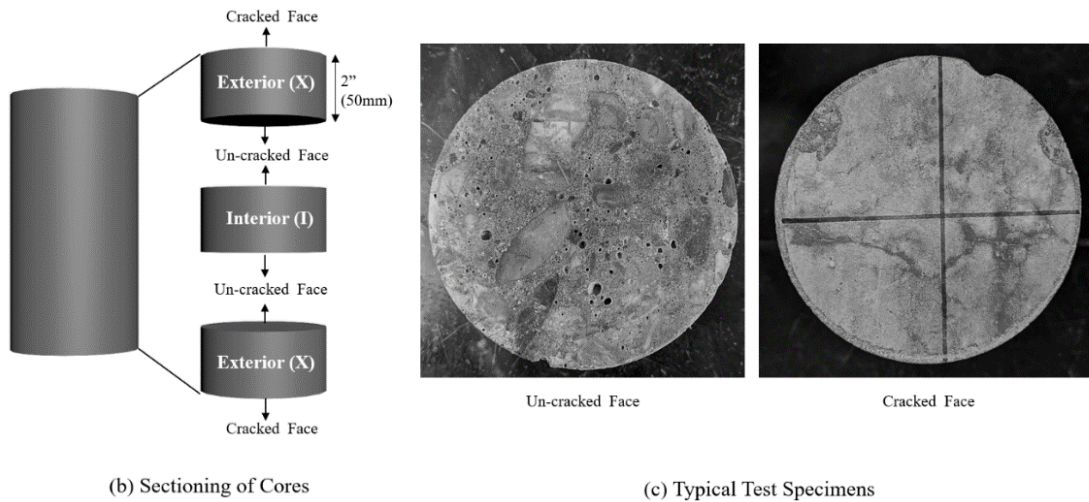
4.4.4.1. Surface and Bulk Resistivity

Surface and bulk resistivity were measured for all the cores. Surface resistivity was measured according to *AASHTO TP358-Standard Method of Test for Surface Resistivity Indication of Concrete's Ability to Resist Chloride Ion Penetration* [21]. Bulk resistivity was measured according to *ASTM C1202-Standard Test Method for Electrical Indication of Concrete's Ability to Resist Chloride Ion Penetration* [110].

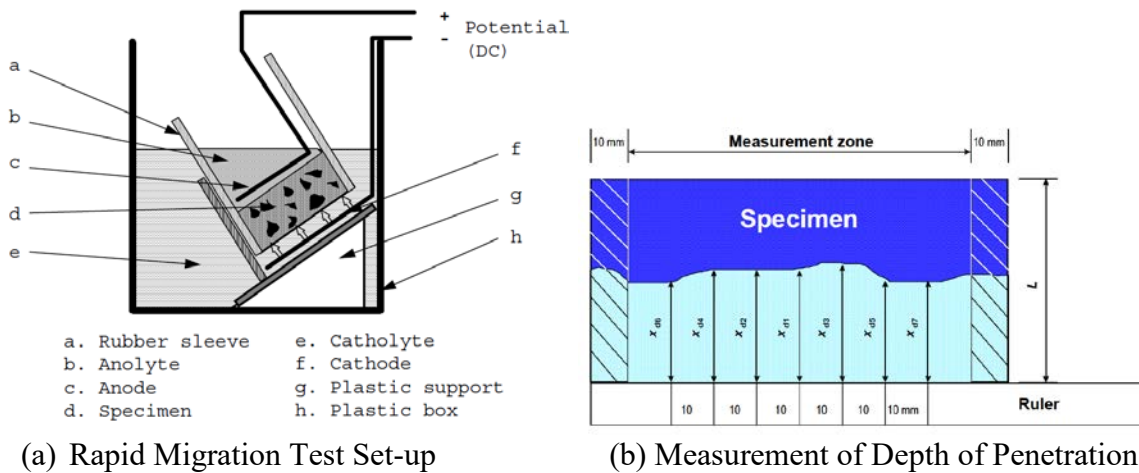
4.4.4.2. Corrosion

Chloride diffusion coefficient and carbonation coefficient were used to assess the corrosion potential of the girders.

To determine the chloride diffusion coefficient, two cores from each girder were sectioned into three 2-in. (50.8 mm) discs using a saw. Figure 4.2a shows the specimens after cutting. Two of the three specimens had cracks on one face (exterior surface of the girder, exposed to environment), while the other face was part of the interior of the girder (unexposed to environment) and did not have any cracks. Both faces of the third specimen were parts of the interior of the girder. The specimens were referred to as “Cracked” (C) and “Uncracked” (U). Figure 4.2b shows a typical cracked and interior faces of the specimens. The specimens were used to determine the chloride migration coefficient by non-steady state migration as per *NT Build 492* [107]. This test is also known as the rapid migration test (RMT). In this test, an external electrical potential is applied axially across the specimen and forces the chloride ions outside to migrate into the specimen (see Figure 4.3a). After a certain test duration, the specimen is axially split, and a silver nitrate solution is sprayed on to one of the freshly split sections. The chloride penetration depth can then be measured from the visible white silver chloride precipitation, after which the chloride migration coefficient can be calculated from this penetration depth (see Figure 4.3b). The rapid chloride penetration test (RCPT) [110] was initially used to measure the corrosion potential as this is a popular test used in the US (as noted by its inclusion in two standards: ASTM C1202 and AASHTO T277 [110]). However, due to the extremely low w/cm of the samples, no significant values were measured. Thus, the RCPT test was replaced by with the RMT, a test that is commonly used in Europe. The RMT was found to be more suitable than the RCPT to characterize the resistance to chloride ingress for the low w/cm concrete mixtures used in this work.



Source: Images by Authors
 Figure 4.2: (a) Preparation of specimens for rapid migration test and (b) typical test specimens

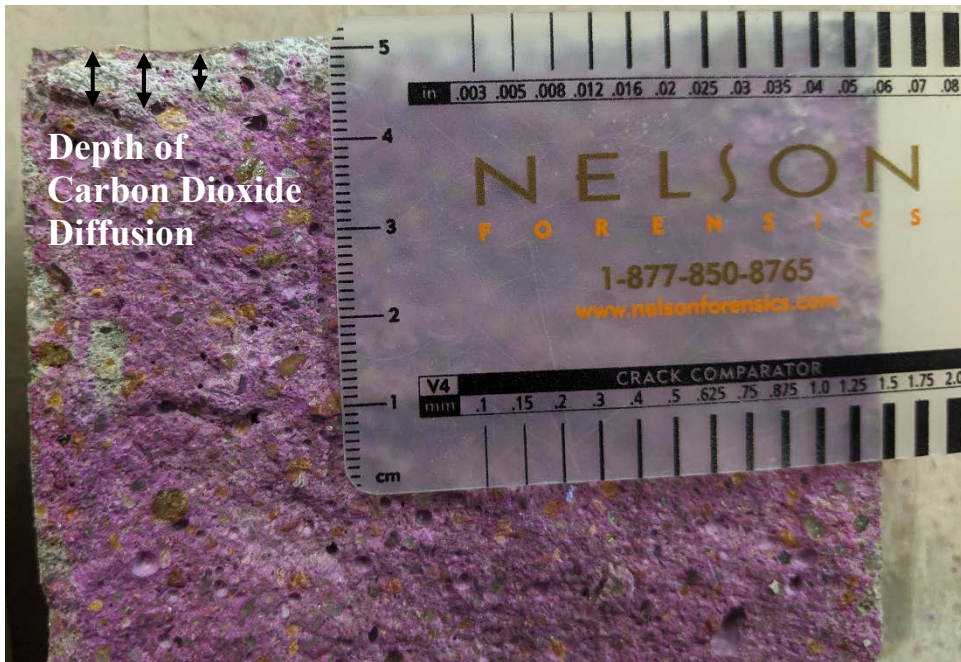


Source: NT Build 492 [107]
 Figure 4.3: (a) Rapid migration test set-up and (b) measurement of depth of penetration

Carbonation coefficient was determined in accordance with *CPC18–RILEM Concrete Permanent Committee–Measurement of hardened concrete carbonation depth* [108]. Two cores from each field visit were used. Each core had two exposed faces. Thus, four values of carbonation depth were measured from each girder from each field visit. Cores extracted from the first, second, and third round of field visits were exposed for 3 years, 2 years, and 1 year, respectively. In addition, the carbonation depth at time of extraction was also calculated by using the samples previously used for splitting tensile strength. The split surfaces of the samples were sprayed with a phenolphthalein indicator. The areas that were basic turned pink due to the basic nature of concrete while the areas that had carbon dioxide diffusion remained colorless due to the formation of carbonic acid. Thus, the depth of the colorless zone was measured to estimate the depth of carbon dioxide diffusion (see Figure 4.4).



(a) Split Specimens with Phenolphthalein Indicator Sprayed



(b) Measurement of Carbonation Depth

Source: Images by Authors

Figure 4.4: (a) Carbonation test and (b) measurement of carbonation depth

4.4.5. Accelerated Weathering Test

As stated in Section 3.6, exposure to the environment and pre-existing cracks exacerbate the rate of cracking. To further explore this behavior an accelerated weathering test was conducted.

4.4.5.1. Accelerated Weathering Test Procedure

For the accelerated weather test, two cores from each girder were sectioned into three 2-in. (50.8 mm) discs using a saw. Figure 4.2a shows the sections after cutting. Two of the three sections had cracks on one face (exterior surface of the girder, exposed to environment), while the other face was part of the interior of the girder (unexposed to environment) and did not have any cracks. Both faces of the third section were parts of the interior of the girder. The sections were referred to as “Cracked” (C) and “Uncracked” (U). Figure 4.2b shows typical cracked and interior faces of the sections.

Two cores from each girder from each of the three field visits were saw cut into 2-inch-thick specimens, and accelerated weathering was conducted by cycling the samples through 21 days of drying and 7 days of wetting. Specifically, the specimens were soaked in tap water for 1 week, air-dried for 3 weeks. This cycle was repeated throughout the project duration, with a total of 13 cycles of wetting/drying conducted in a year. This equates to 91 days a year that the concrete will be exposed to moisture if they are subjected to this cycling for an entire year; this is in line with the average annual number of days with precipitation (rain or snow) in Texas [14].

Since cores were obtained at different times, the samples extracted from cores obtained during the earlier field visits had a longer exposure period. Samples extracted from the first round of field visits had twenty-two cycles of wetting and drying, whereas the specimens from the second and third round of field visits had twelve and ten cycles of wetting and drying visits, respectively.

The following tests were conducted at the end of each cycle:

- Dry cycle
 - o Mass measurements- The specimen was weighed.
 - o Strain measurements- The diameter and height of the specimen were measured.
 - o Cracking measurements- The cracking index and average crack width were measured according to FHWA-HIF-09-004 Report [19]. The method was modified for use in cylinders by using two diameters as the base length in the place of a crack grid. Figure 4.1 shows a schematic of the modified calculations and all the possible combinations of the temporal behavior of cracking index and average crack width.
- Wet cycle:
 - o Mass measurements- The surface of the specimen was dried with a paper towel and weighed.
 - o Ultrasonic pulse velocity- The ultrasonic pulse velocity of the specimen was measured according to *ASTM C597-Standard Test Method for Pulse Velocity through Concrete* [20]. The height of the specimen used was measured from the strain measurements from the dry cycle.
 - o Bulk resistivity- The bulk resistivity of the sample was measured according to *ASTM C1202-Standard Test Method for Electrical Indication of Concrete's Ability to Resist Chloride Ion Penetration* [110]. The height of the specimen used was measured from the strain measurements from the dry cycle.

At the end of the testing period, the weathered specimens were used to determine the chloride migration coefficient by non-steady state migration as per *NT Build 492* [107] (aka rapid chloride migration test). The diffusion coefficient of the concrete samples after undergoing accelerated weathering was compared to the diffusion coefficient before undergoing

accelerated weathering. Table 4.3 summarizes the tests conducted at the end of each dry and wet cycles.

Table 4.3: Accelerated Weathering Test

Test		Number of Samples Tested from each Girder		
		Visit 1	Visit 2	Visit 3
Non-destructive test at the end of each dry cycle	Cracking Measurements	6	6	6
	Mass Measurements			
	Dimensions			
Non-destructive test at the end of each wet cycle	Mass Measurements	6	6	6
	Bulk Resistivity			
	Ultrasonic Pulse Velocity			
At the end of the Testing Period	Chloride Diffusion Coefficient	36	36	36

4.4.5.2. Analytical Investigation for Accelerated Weathering Test

At the end of each cycle of wetting and drying of the specimens collected from the first, second, and third field visits, the following values were calculated:

- **Change in cracking index:** Cracking index is a measure of the density of cracks as it is a function of the crack width spread across a fixed length of a concrete surface [19]. An increase in the cracking index shows that the concrete condition is deteriorating. The change in cracking index is calculated according to Equation 4.1.

$$\text{Change in Cracking Index} = \text{Cracking Index at cycle 'n'} - \text{Cracking Index at cycle 0}$$

Equation 4.1

- **Change in average crack width:** Average crack width is calculated according to Equation 4.2. Average crack width can increase (when there is a widening of existing cracks) or decrease (when there is formation of new cracks). Any change, i.e., positive or negative, shows that the concrete condition is deteriorating.

$$\text{Change in Average Cracking Index} = \text{Average Crack Width at cycle 'n'} - \text{Average Crack Width cycle 0}$$

Equation 4.2

- **Cumulative loss in mass:** According to the IS536 by PCA, alternate wetting and drying can cause the loss in mass due to weathering and erosion [111]. Roziere et al. also showed that cracking could impact the rate of loss in mass and vice versa [112]. The cumulative loss in mass was calculated as per Equation 4.3.

$$\text{Cumulative loss of cycle 'n'} = \text{Mass at cycle 'n'} - \text{Mass at cycle 0}$$

Equation 4.3

- **Percentage absorption:** Researchers have shown that moisture absorption is directly related to the extent of cracking in concrete. It is seen that concretes with cracks have higher absorption than uncracked concrete specimens [113], [114]. Percentage absorption was calculated as per Equation 4.4.

$$\text{Percentage absorption at cycle 'n'} = \frac{(\text{Mass of Wet Samples at cycle 'n'} - \text{Mass of Dry Sample at cycle 'n'})}{100}$$

Equation 4.4

- **Percentage reduction in ultrasonic pulse velocity:** Ultrasonic pulse velocity can be used as an indicator of concrete condition, density, and strength [115], [116]. The UPV test method can also be used to indicate the presence of voids and cracks. Higher pulse velocity in concrete indicates better homogeneity, i.e., higher quality concrete will have shorter wave travel time and subsequently higher velocity [20]. The percentage change in UPV was calculated as per Equation 4.5.

$$\text{Percentage reduction in UPV cycle 'n'} = \frac{(\text{UPV at cycle 'n'} - \text{UPV at cycle 0})}{100}$$

Equation 4.5

- **Percentage reduction in bulk resistivity:** Bulk resistivity can be used as an indicator of corrosion potential. A concrete member with higher resistivity would have a higher resistance to corrosion. Hence, a lowering in resistivity is an indicator of increased corrosion potential [56]. The percentage change in resistivity was calculated as per Equation 4.6.

$$\text{Percentage reduction in Bulk Resistivity cycle 'n'} = \frac{(\text{Bulk Resistivity at cycle 'n'} - \text{Bulk Resistivity at cycle 0})}{100}$$

Equation 4.6

4.4.5.3. Modelling Relationship between Weathering Cycles and Loss in Durability

The relationship between each test parameter and the initial cracking index and number of wetting and drying cycles was determined using multiple linear regression. This method is commonly used to model the relationship between two or more explanatory variables and a response variable by fitting a linear equation to the observed data. The equation of the best fit line is calculated by minimizing the sum of squares of the deviations from each data point to the fitted line [117].

The explanatory variables in this model are initial cracking index and number of wetting and drying cycles, and the response variable is the test parameter of interest (cracking index, average crack width, ultrasonic pulse velocity, and bulk resistivity). A model was generated with data obtained from samples from Girders 1R, 2R, 3R, 4R, and 5RC for each parameter of interest. Equation 4.7 shows an example of a model determined for a test parameter.

$$y = c + (x_n * n) + (x_i * I_i)$$

Equation 4.7

Where,

y = Test parameter of interest

c = y-intercept

x_n = Coefficient for number of cycles

n = Number of exposure cycles

x_i = Coefficient for cracking index

I_i = Initial cracking index

Regression coefficient values (R^2) for each model was also calculated. The regression coefficient provides a statistical measure of how close the experimental data is to the fitted regression line. Regression coefficient values range between 0 (no relationship) and 1 (very good relationship) [118].

The samples obtained from Girders 1R, 2R, 3R, 4R, and 5RC were used to model the relationship between the weathering and loss in durability, and the samples from Girder 14V were used to validate the model. The experimental data collected from Girder 14V was compared to the data predicted by the model. The validity of the model was assessed using the following measures of reliability:

- The reliability of the model was calculated using the inter-method reliability index method (Equation 4.8). The reliability index (see Equation 4.8) assesses the degree to which values are consistent when two methods of testing are used, i.e., by comparing the data obtained using experimental test values and predicted test values. Reliability index values range between 0 (no relationship) and 1 (very good relationship) [119]. Guidelines to interpret reliability indices are provided by statisticians. Reliability indices between 0.5 and 0.75 are considered to be “Moderate,” between 0.75 and 0.90 are considered to be “Good,” and between 0.90 and 1.00 are considered to be “Excellent” [120].

$$r = \frac{\sigma_p^2}{\sigma_p^2 + \sigma_e^2}$$

Equation 4.8

Where,

r = reliability index

σ_p = standard deviation of predicted values

σ_e = standard deviation of experimental values

- The standard error of estimate was calculated using the sum of squares method (see Equation 4.9). This value provides an estimate of the dispersion of the prediction errors, i.e., a measure of how far apart the experimental values are from the predicted test values. A lower error indicates that the predictive model has higher reliability. This value can also be compared to the standard deviations of the experimental tests. If the error values are in the same range as the standard deviation, then the model can be considered to have higher reliability [118].

$$\sigma_{est} = \sqrt{\frac{\Sigma(Y_p - Y_e)^2}{N}}$$

Equation 4.9

Where,

σ_{est} = standard error of estimate

Y_p = predicted test parameter values

Y_e = experimental test parameter values

N = number of test values

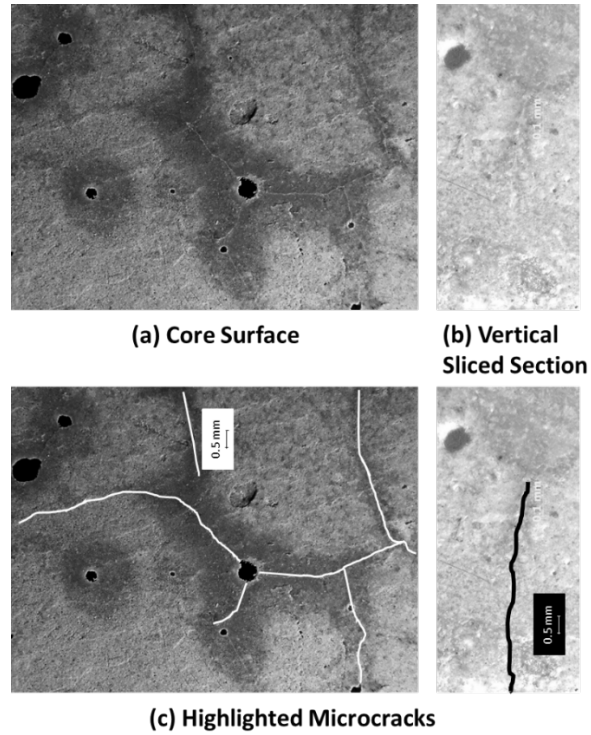
4.5. Results and Discussions

The results of tests conducted on the extracted cores is presented in this section. The change in strength, stiffness, and durability tests over the monitoring period is presented. In addition, the relationship between the growth of microcracking and exposure to the environment and pre-existing cracks is presented.

4.5.1. Visual Evaluation

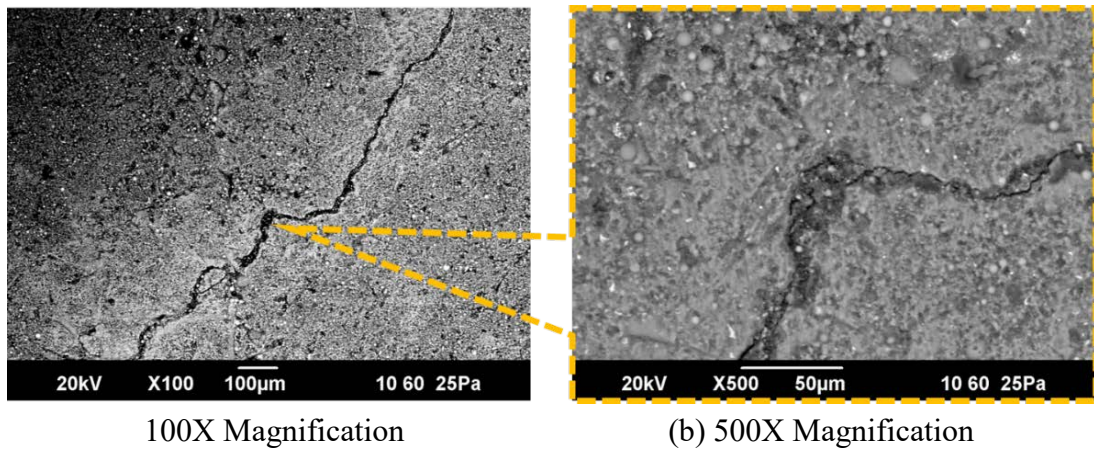
4.5.1.1. Microscopy

Figure 4.5a and Figure 4.5b show optical microscope images of the surface and vertical sections of cores from a typical girder, Figure 4.5c show these same sections with the microcracks highlighted to aid viewability. Figure 4.6 shows a typical micrograph image from the scanning electron microscope of the microcracks. These images were used to observe the features of the microcracks in greater detail. Typical crack widths observed in the field at different magnifications are shown in Figure 4.7 through Figure 4.10. The image at 50X magnification was obtained using the crack microscope, whereas the images at 100X, 500X, and 1500X were obtained using the SEM. Appendix A contains additional images and information from the visual examination.



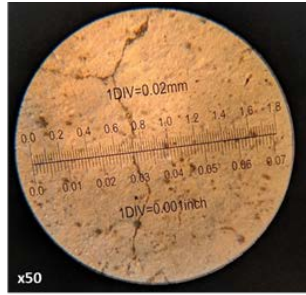
Source: Images by Authors

Figure 4.5: Optical microscope images of (a) surface and (b) vertical section of cores from a typical girder, and (c) highlighted microcracks

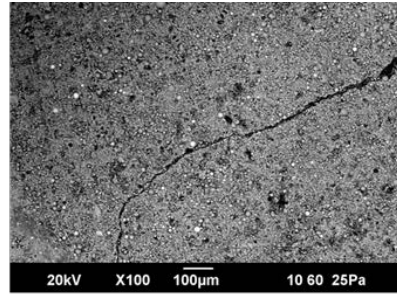


Source: Images by Authors

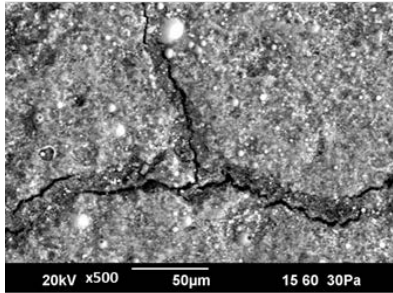
Figure 4.6: Typical scanning electron microscope images of surface of cores at (a) 100X and (b) 500X magnification



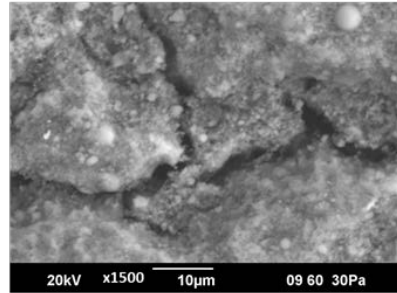
(a) 50x



(b) 100x



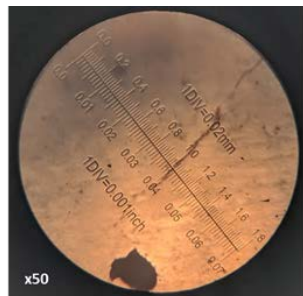
(c) 500x



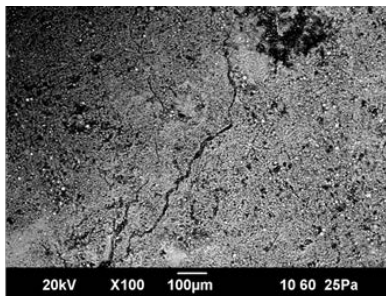
(d) 1500x

Source: Images by Authors

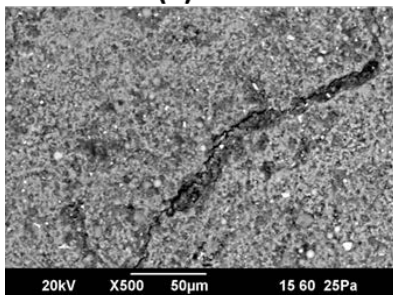
Figure 4.7: 6 μm crack (a) viewed using optical microscope and (b) 50X magnification, (c) 100X, (d) 500X magnification viewed using SEM



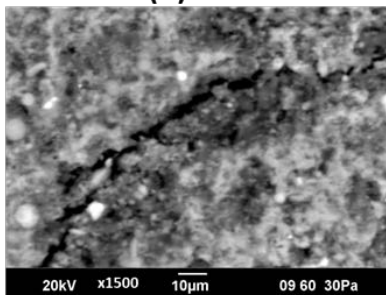
(a) 50x



(b) 100x



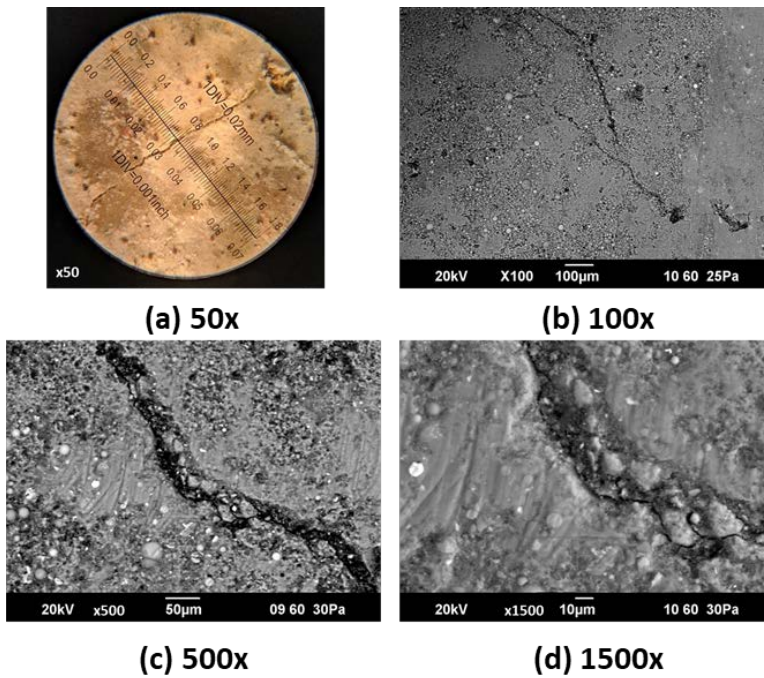
(c) 500x



(d) 1500x

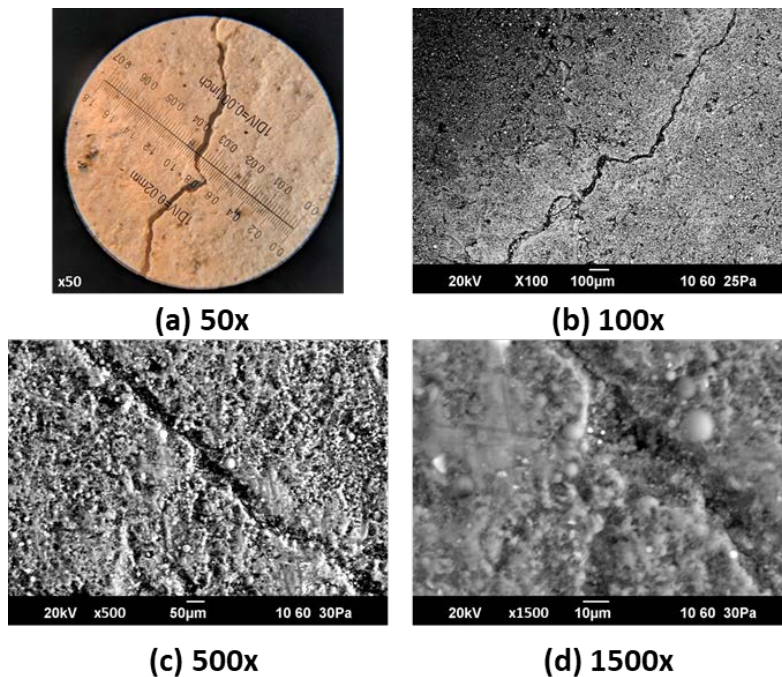
Source: Images by Authors

Figure 4.8: 25 μm crack (a) viewed using optical microscope and (b) 50X magnification, (c) 100X, (d) 500X magnification viewed using SEM



Source: Images by Authors

Figure 4.9: 50 μm crack (a) viewed using optical microscope and (b) 50X magnification, (c) 100X, (d) 500X magnification viewed using SEM



Source: Images by Authors

Figure 4.10: 100 μm crack (a) viewed using optical microscope and (b) 50X magnification, (c) 100X, (d) 500X magnification viewed using SEM

4.5.1.2. Cracking Measurements

The cracking index and average crack width of all cores were calculated using Equation 3.1 and Equation 3.2. It was seen that the cores exhibited an increase in cracking index (see Figure 4.11a). Girders 1R-4R displayed a higher increase in cracking index than the control Girder

5RC. However, it can also be seen that increasing crack index is not always associated with an increase in crack width, rather the average crack width may increase or decrease with time (see Figure 4.11b). As shown in Figure 4.11b, whether the average crack width increases or decreases depends on whether new cracks have formed. In Figure 4.12, the leftmost figure represents the initial state of cracks on the surface of a concrete specimen. However, the three figures to the right show difference scenarios that can occur with time. Crack widening is observed in girders that show an increase in average crack width and cracking index. Girders 1R, 2R, 3R and 4R in the first year, and Girders 3R and 4R in the second year show an increase in both average crack width (see Figure 4.11b) and cracking index (see Figure 4.11a). This indicates the formation of cracks (#) and widening of existing cracks (ΣW) as shown in Scenarios B and C. However, Girder 5RC in the first year and Girders 1R, 2R and 5RC in the second year show an increase in the cracking index (see Figure 4.11a), but a decrease in the average crack width (see Figure 4.11b). As shown in Scenario A in Figure 4.12, this indicates the formation of new cracks is occurring at a greater extent than the widening of existing cracks. The average crack width (ACW) is function of the number of cracks (denoted as #) in Figure 4.12)) and the sum of measured crack widths (ΣW). Thus, when # increases without a proportional increase in ΣW , ACW decreases over time.

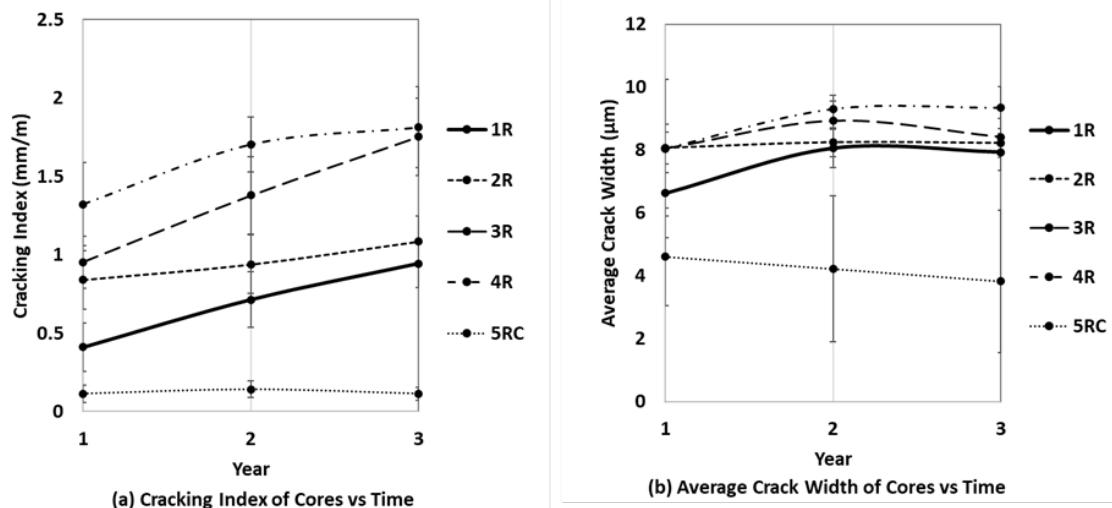
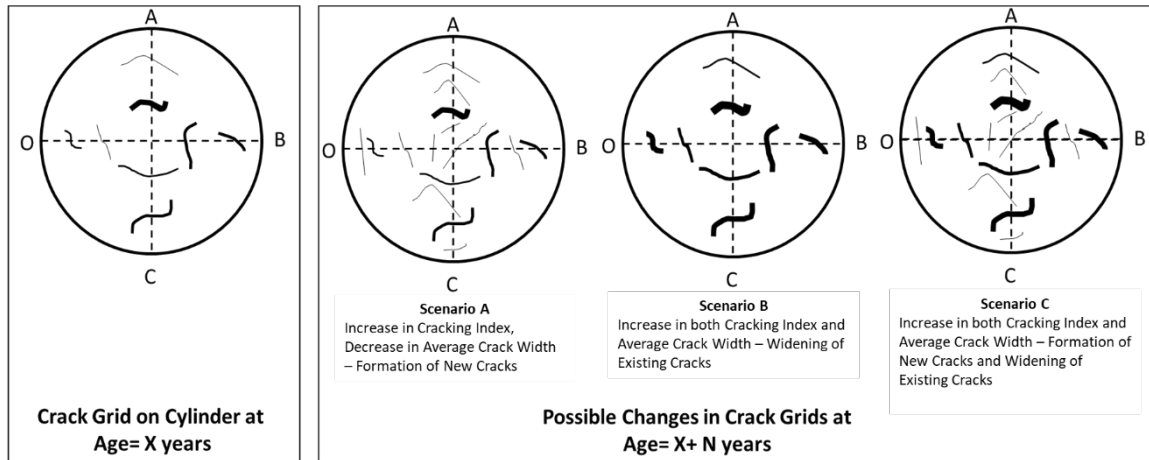


Figure 4.11: Change in cracking of cores over the monitoring period

Base Length	Number of cracks	Total Crack Width (μm)	Average Crack Width (μm)	Cracking Index ($\mu\text{m}/\text{m}$)
$B = AO + OB + CB + AC$	(#)	(ΣW)	$ACW = (\Sigma W)/\#$	$CI = (\Sigma W)/B$



Source: Images by Authors

Figure 4.12: Temporal behavior of cracks

4.5.2. Strength Test Results

Figure 4.13 shows that the girders exhibited negligible changes in strength over the testing period. Both compressive strength and tensile strength of the cores did not change in any significant manner and remained over the serviceability limits for compressive strength (35 MPa or 5000 psi) and tensile strength (3 MPa or 425 psi) as prescribed by the Texas Department of Transportation's Bridge Design Manual [18].

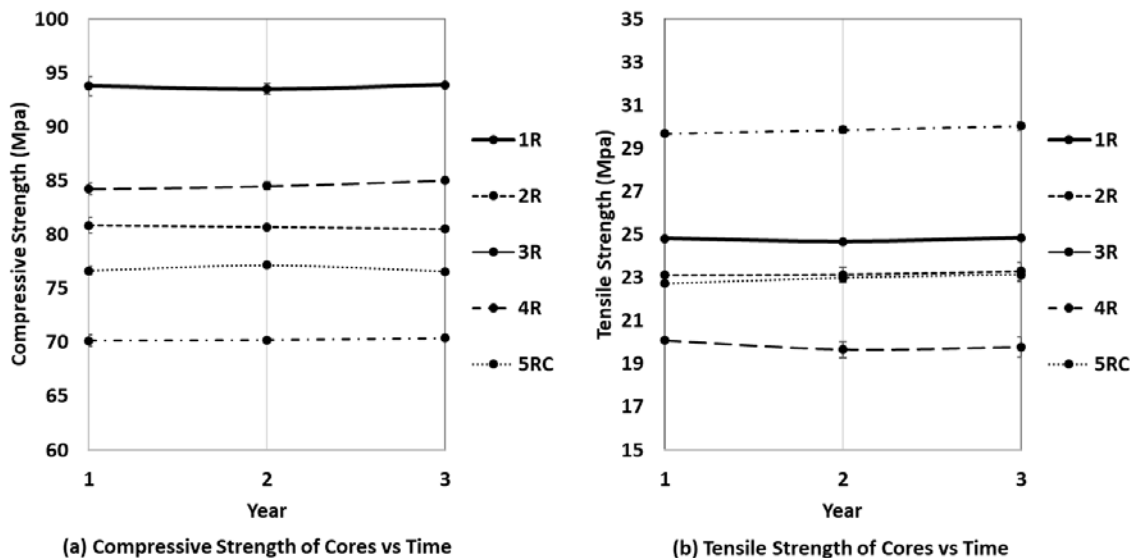


Figure 4.13: Change in strength properties of cores over the monitoring period

4.5.3. Stiffness Test Results

Figure 4.14 shows that the girders exhibited negligible changes in stiffness properties over the testing period. Both ultrasonic pulse velocity and modulus of elasticity of the cores did not change in any significant manner. Ultrasonic pulse velocity values of the samples were over

the serviceability limit of 3660 m/s [65], [104]. Modulus of elasticity values were also above the prescribed serviceability value of 35 GPa or 5×10^6 psi by the Texas Department of Transportation's Bridge Design Manual [18].

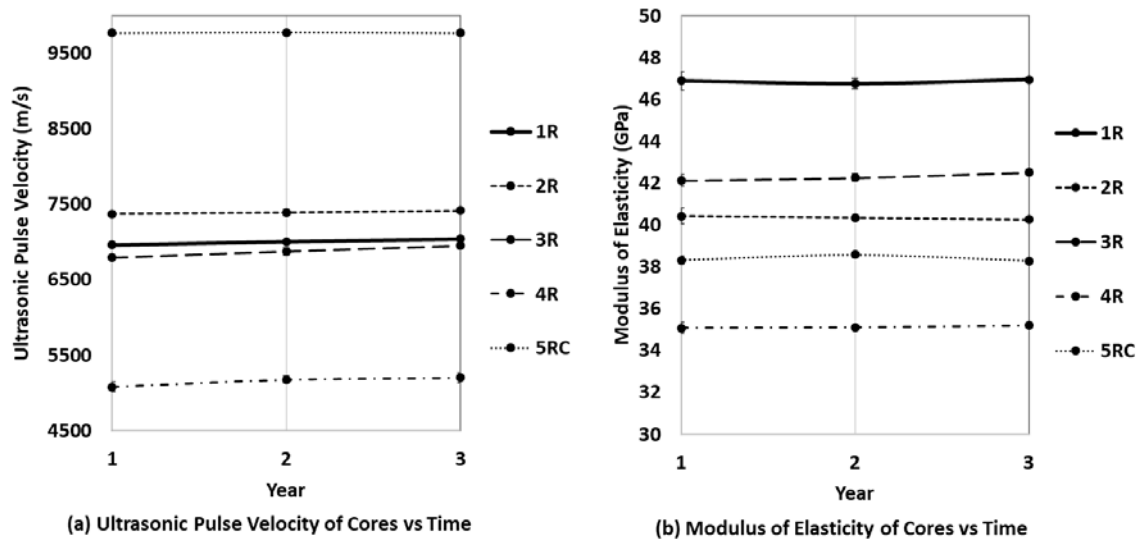


Figure 4.14: Change in stiffness properties of cores over the monitoring period

4.5.4. Durability Test Results

4.5.4.1. Resistivity

Figure 4.15 shows that the girders exhibited negligible changes in resistivity properties over the testing period. Both surface and bulk resistivity of the cores did not change in any significant manner and remained over the serviceability limits for surface resistivity (7.5 k Ω cm) and bulk resistivity (12 k Ω cm) [66], [106].

4.5.4.2. Chloride Diffusion and Carbonation Coefficient

Figure 4.16 shows that the girders exhibited an increase in the diffusion properties over the testing period. Specimens from Girders 1R-4R showed a higher increase in the chloride diffusion coefficient when compared to the control Girder 5RC. Concrete with a diffusion coefficient higher than 15×10^{-12} m²/s at 28 days is considered to have “low corrosion resistance” [66], [106]. All samples have diffusion coefficients lower than this value (see Figure 4.16a). The serviceability carbonation coefficient was calculated for these girders as 5.8 mm/yr^{0.5}, i.e., 50 mm (2 in.) for 75 years (concrete cover over expected service life) [12]. All samples have carbonation coefficient values well under this limit (see Figure 4.16b).

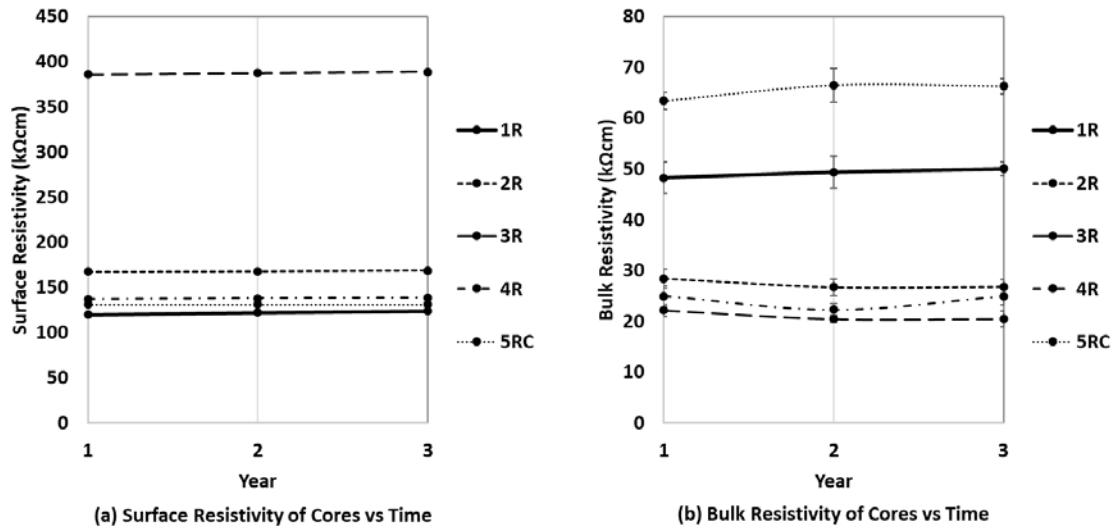


Figure 4.15: Change in resistivity properties of cores over the monitoring period

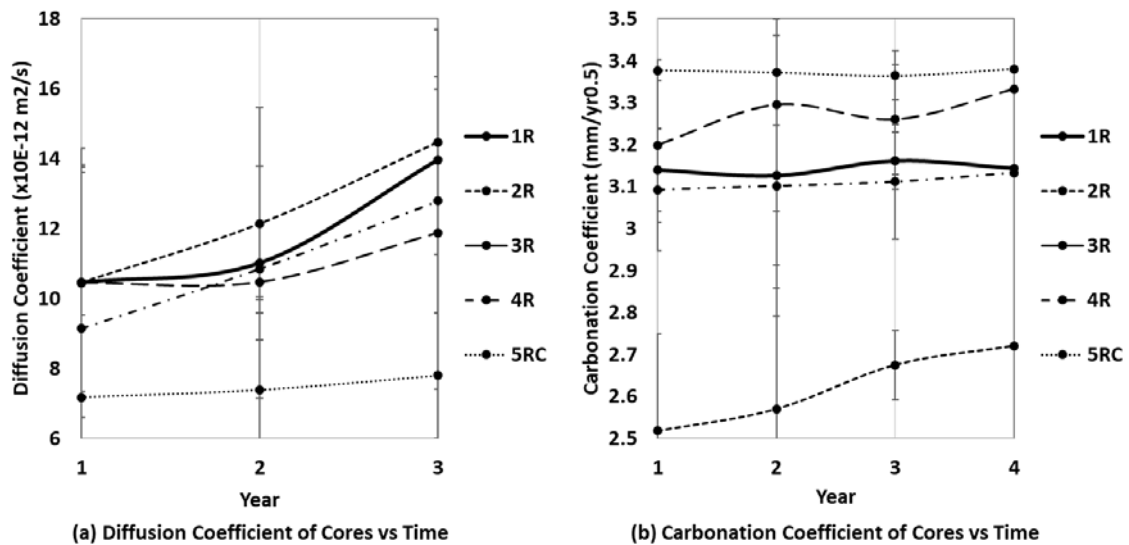


Figure 4.16: Change in diffusion of cores over the monitoring period

4.5.5. Accelerated Weathering Test

This section shows the results obtained after conducting the accelerated weathering test on the samples extracted from pre-stressed concrete girders. The results are divided into the following sub-sections:

- Effect of weathering on the non-destructive test values.
- Effect of initial cracking on the final test values.
- Effect of weathering and initial cracking on Diffusion Coefficient
- Quantification of Effect of Weathering and Initial Cracking on Loss in Durability

4.5.5.1. Effect of Weathering on Cracking, Mass, Ultrasonic Pulse Velocity, and Bulk Resistivity

The samples from the six pre-stressed girders were subjected to accelerated weathering tests. This section shows the results obtained for samples from Girder 1R from the first round of field visits, since the remaining Girders 2R, 3R, 4R, 5R, and 14V also showed similar results.

The change in cracking, mass due to water absorption, ultrasonic pulse velocity, and bulk resistivity at the end of each wetting and drying cycle for six samples from Girder 1R are shown in Figure 4.17, Figure 4.18 and Figure 4.19, respectively. Two interior (**uncracked**) samples (denoted as U1 and U2) and four exterior (**cracked**) samples (denoted as C1, C2, C3, and C4) are shown in Figure 4.17, Figure 4.18, and Figure 4.19. The number in front of the interior and exterior sample indicates the initial cracking index value of the sample. For example, the samples extracted from the interior region of the cores had an initial cracking index value of 0.0 mm/m. Thus, in Figures 4.15 through 4.17 they are denoted as 0.00 U1 and 0.00 U2. Whereas 0.81 C2 indicates that it is an exterior cracked sample that had an initial cracking index of 0.81 mm/m, respectively.

Figure 4.17a shows that increase cracking index increased as the number of wetting and drying cycles increased. It was seen that at the end of 22 cycles, the cracking index of the interior uncracked samples, U1 and U2, had lower final cracking values than the exterior cracked samples, C1, C2, C3, and C4. The exterior samples with higher initial cracking indices had higher rates of change, i.e., C4 had the highest rate of change followed by C3 and C2 and C1. This showed that initial cracking value was an important factor affecting the rate of increase in cracking. This was also similar to the behavior observed on the full-scale specimens, where sections with pre-existing cracks showed a higher rate of loss in durability when compared to sections with lesser or no previous cracking (see Section 3.5.3). It was also seen that the previously uncracked interior samples, U1 and U2, started to exhibit cracking after 12 and 11 wetting and drying cycles, respectively. Similar behavior was observed in the uncracked interior samples from the remaining girders. Figure 4.17b shows the change in average crack width with increase in number of wetting and drying cycles. It was seen that while there was an overall increase in the average crack width in all specimens, the change was not always positive (For example see line labeled 0.58 C3 in Figure 4.17b) due to the formation of a larger number of new smaller cracks rather than widening of existing cracks in the specimen.

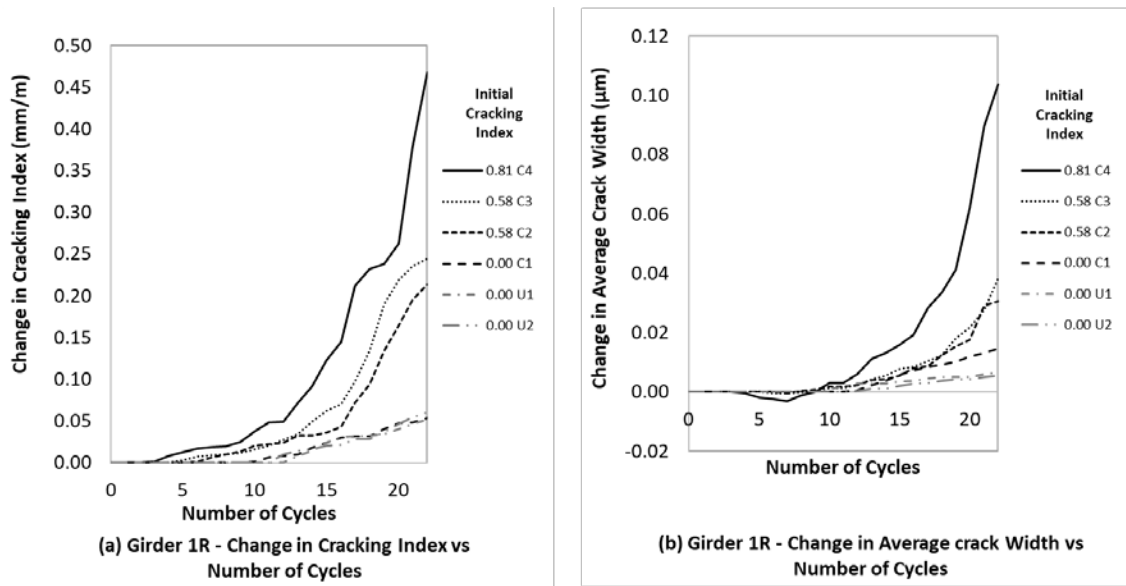


Figure 4.17: Change in cracking with exposure

Figure 4.18a and Figure 4.18b show the cumulative loss in mass and change in absorption values with weathering. Like the cracking index values, it was seen that the interior uncracked samples, U1 and U2, had a lower loss in mass and absorption when compared to the exterior cracked samples, C1–C4. Exterior cracked samples with higher initial cracking had a higher loss in mass and higher absorption than the cracked samples with lower initial cracking. This showed that microcracking had a pronounced effect on the rate at which loss in mass and an increase in absorption occurred.

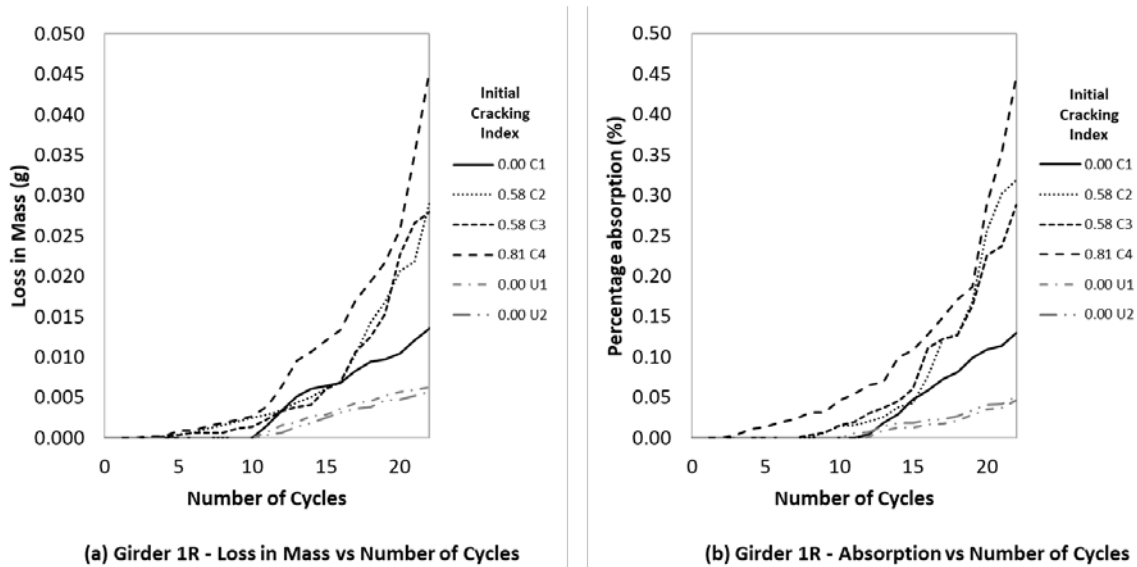


Figure 4.18: Loss in mass and change in absorption with exposure

Figure 4.19a and Figure 4.19b show the percentage change in ultrasonic pulse velocity and bulk resistivity with weathering. Reduction in ultrasonic pulse velocity is indicative of reduced overall concrete quality, i.e., increased deterioration (cracking) and reducing density [20]. Similarly, a decrease in bulk resistivity is an indicator of reduced resistance to corrosion [110]. Changes in ultrasonic pulse velocity occurred with increased weathering, with the cracked exterior samples showing greater reductions than the interior uncracked samples (~1%

reduction in the interior uncracked samples compared to 2.5 to 4% in the exterior cracked samples). This behavior is also reflected in the reduction in bulk resistivity, with the interior uncracked specimens having a loss of 0.5% and the exterior cracked specimens having a loss of 2 to 4%.

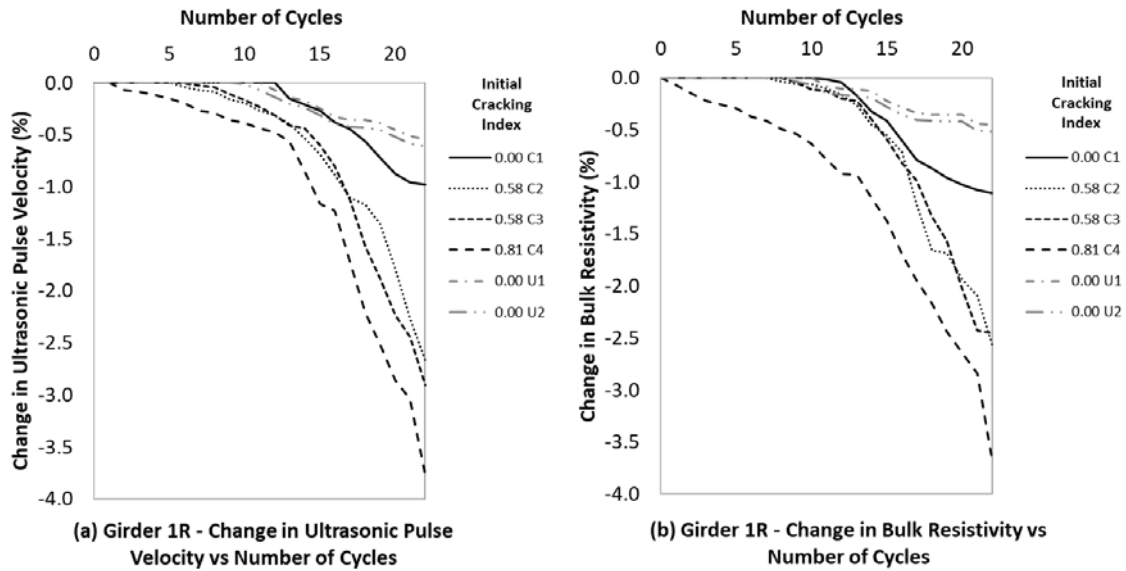


Figure 4.19: Change in ultrasonic pulse velocity and bulk resistivity with exposure

4.5.5.2. Role of Weathering and Initial Cracking on Final Cracking, Loss in Mass, Absorption, Ultrasonic Pulse Velocity, and Bulk Resistivity

Figure 4.20a and Figure 4.20b show the effect of initial cracking on the final cracking values for all samples subjected to the accelerated weathering test. It is seen that both cracking index and average crack width increase at the end of the 10, 12, and 22 cycles of alternate wetting and drying. Figure 4.21a and Figure 4.21b show the effect of initial cracking on the cumulative loss in mass and the absorption values at the end of the exposure test. Figure 4.22a and Figure 4.22b show the effect of initial cracking on the percentage change in ultrasonic pulse velocity and bulk resistivity at the end of the exposure test. Changes in cracking index, average crack width, cumulative loss in mass and absorption were higher for samples with higher initial cracking index. Change in ultrasonic pulse velocity and bulk resistivity were lower for samples with higher initial cracking index. These values were consistent with the results seen in Section 4.5.5.1.

Table 4.4 summarizes the correlation coefficients between initial cracking index and change in cracking, loss in mass, absorption, UPV and bulk resistivity of samples subjected to 22, 12 and 10 cycles of weathering. A comparison of correlation coefficients of the different tests shows that the values at the end of 22 cycles had the highest coefficient values followed by 12 and 10 cycles. This shows that the values obtained at the end of 22 cycles have higher reliability than the values obtained at the end of 12 and 10 cycles. All parameters except for average crack width and ultrasonic pulse velocity had high correlation coefficients (>0.88). The high correlation coefficient values are highlighted in Table 4.4. However, average cracking width and UPV had higher correlation coefficients at the end of 22 cycles (0.92 and 0.91 respectively).

Table 4.4: Correlation Coefficients between Initial Cracking Index and Change in Cracking, Loss in Mass, Absorption, UPV, and Bulk Resistivity of Samples Subjected to Accelerated Weathering Test

Test Parameter	Correlation Coefficients		
	10 cycles	12 cycles	22 cycles
Cracking Index	0.88	0.96	0.96
Average Cracking Index	0.74	0.78	0.92
Cumulative Loss in Mass	0.90	0.96	0.96
Absorption	0.94	0.96	0.97
Ultrasonic Pulse Velocity	0.58	0.63	0.91
Bulk Resistivity	0.94	0.95	0.97

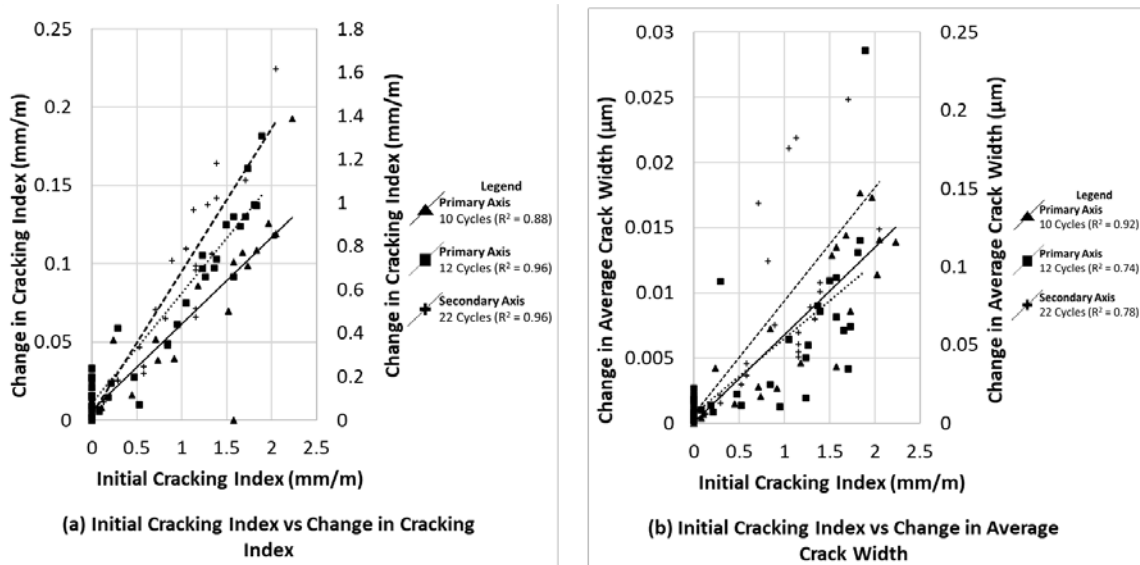


Figure 4.20: Effect of initial cracking on final cracking values

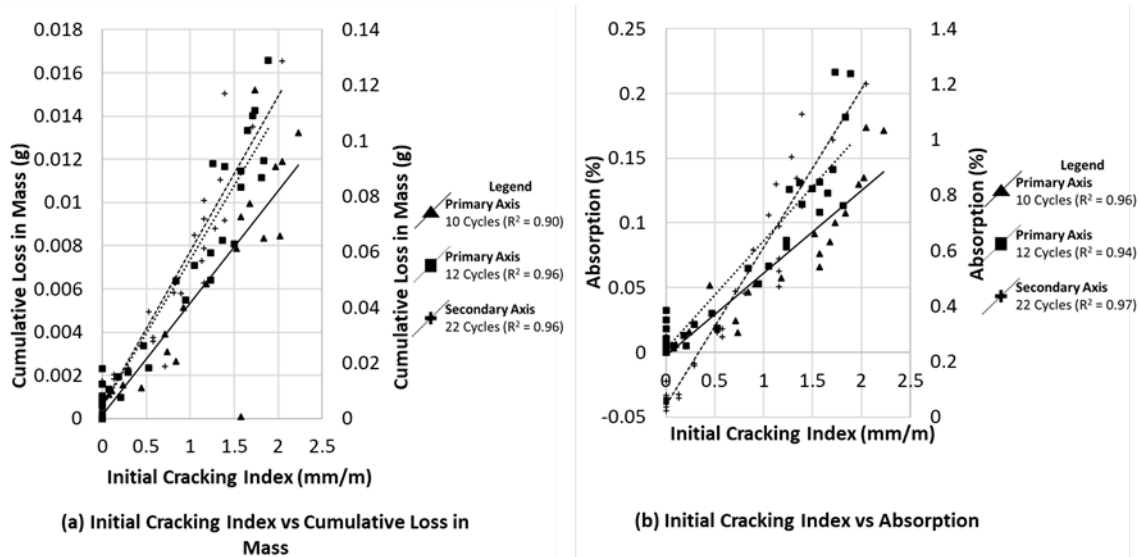


Figure 4.21: Effect of initial cracking on cumulative loss in mass and final absorption values

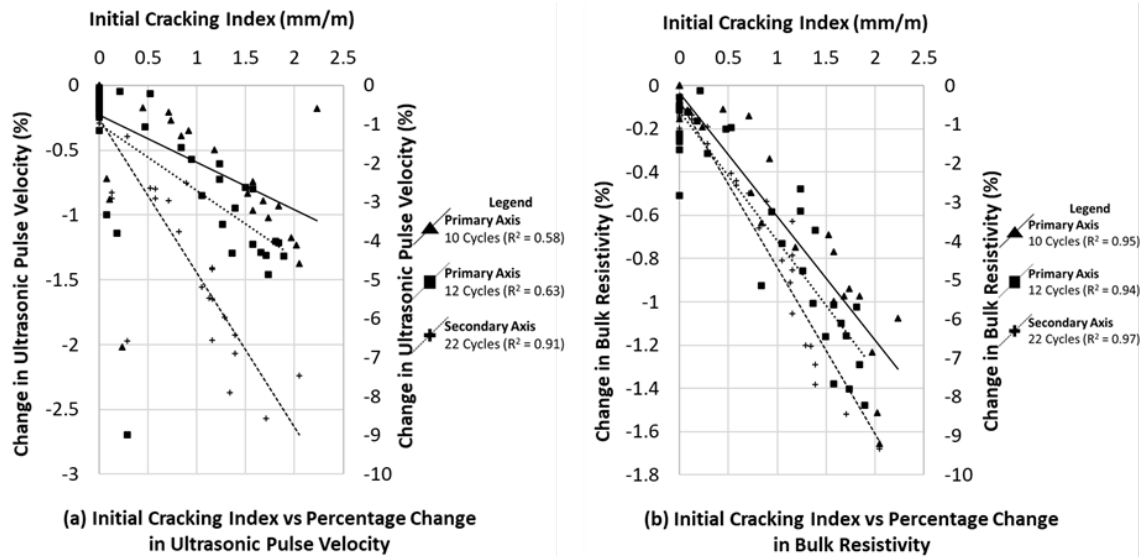


Figure 4.22: Effect of Initial cracking on the percentage change in ultrasonic pulse velocity and bulk resistivity

4.5.5.3. Effect of Weathering and Initial Cracking on Diffusion Coefficient

Figure 4.23a and Figure 4.23b show the effect of the initial cracking index and weathering on the diffusion coefficient. The figures also provide the correlation coefficients for the 0, 10, 12 and 22 cycles of weathering on the right. The specimens subjected to 22 cycles of alternate wetting and drying had the highest diffusion coefficient values when compared to the samples subjected to 12 and 10 cycles. The specimens not subjected to weathering had the lowest diffusion coefficient values. The correlation coefficient values for the specimens after 22 cycles were the highest followed by 12, 0, and 10 cycles. Specimens with higher cracking values generally showed higher diffusion coefficient values. Comparing the correlation coefficient values in Figure 4.23a and Figure 4.23b shows that considering the initial cracking index values rather than the cracking index values at the time of the test showed a marginal improvement in the correlation coefficients of specimens after 10 and 12 cycles of wetting and drying.

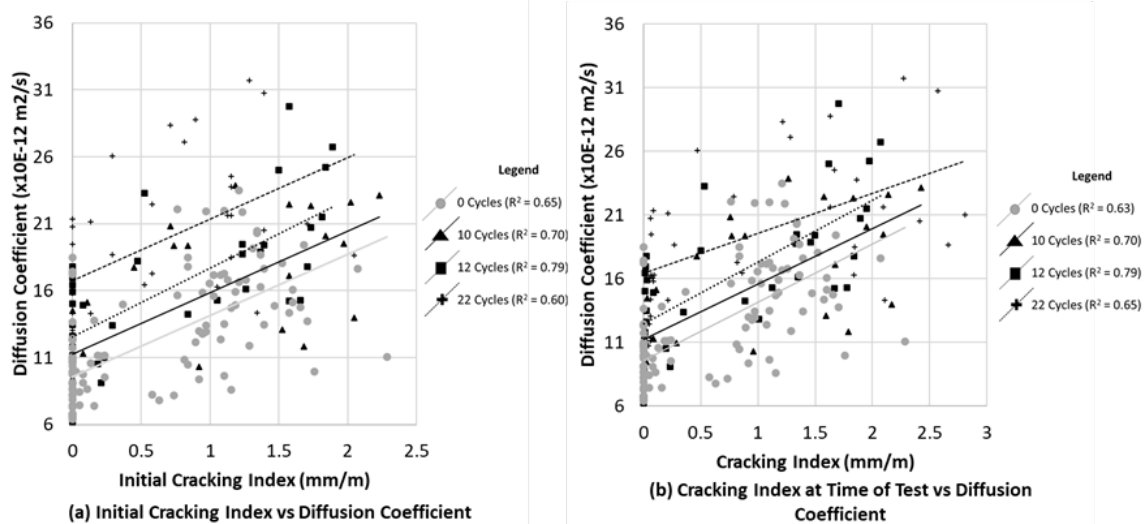


Figure 4.23: Effect of cracking index and exposure on diffusion coefficient and correlation coefficients

4.5.6. Quantification of Effect of Weathering and Initial Cracking on Loss in Durability

Table 4.5 provides the relationships obtained between initial cracking, number of weathering cycles, and the final results from the non-destructive tests. The models for change in cracking index, ultrasonic pulse velocity, and bulk resistivity had multiple regression coefficients exceeding 0.70, while the regression model for average crack had a lower coefficient value of 0.63. The reliability indices of the predicted and experimental values showed similar values. The standard errors of estimate were also comparable to the standard deviations of test values. The procedure for quantification of relationships between initial cracking and weathering, and change in cracking index, average crack width, ultrasonic pulse velocity and bulk resistivity is provided in Section 4.4.5.3. For example, the first row in Table 4.5 provides the relationship between change in cracking index and the number of cycles and initial cracking index (Equation 4.10).

$$\text{Change in Cracking Index} = -0.062 + 0.009 n + 0.049 I_i \quad \text{Equation 4.10}$$

Where,

n = number of weathering cycles

I_i = Initial Cracking Index

Table 4.5: Quantification of Relationships between Initial Cracking and Weathering, and Change in Cracking Index, Average Crack Width, Ultrasonic Pulse Velocity, and Bulk Resistivity

Parameter (y)	Coefficients for Equation 4.7 $y = c + x_n * n + x_i * I_i$			R ²	r	σ _{est}	SD _{avg}
	c	Number of Cycles (x _n)	Initial Cracking Index (x _i)				
Change in Cracking Index (mm/m)	-0.062	0.009	0.049	0.71	0.79	0.06 mm/m	0.02 mm/m
Change in Average Crack Width (μm)	-0.005	0.001	0.004	0.62	0.68	0.03 μm	0.05 μm
Change in Ultrasonic Pulse Velocity (%)	0.530	-0.090	-0.406	0.70	0.88	0.49 %	0.22 %
Change in Bulk Resistivity (%)	0.535	-0.079	-0.441	0.73	0.90	0.39 %	0.23 %

Notes:

- Input Variables: n = number of cycles
I_i = Initial Cracking Index
- c, x_n, and x_i are coefficients
- Reliability Indicators: R² = Multiple Regression Coefficient
r = Reliability Index
σ_{est} = Standard Error of Estimate
SD = Average Standard Deviation of Experimental Test Values

Similarly, Table 4.6 shows the models generated for the chloride diffusion coefficient. The first model used the initial cracking index (before the accelerated weathering test was started) as an input variable, which the second model used the final cracking index (at the end of accelerated weathering test) as an input variable. Equation 4.9 was modified to suit the chloride diffusion

coefficient as it was found that the w/cm was an additional factor influencing chloride diffusion coefficient (Equation 4.11).

$$y = c + (x_n * n) + (x_{wc} * WC) + (x_i * I_i) \quad \text{Equation 4.11}$$

Where,

y = Test parameter

c = y-intercept

x_n = Coefficient for number of cycles

n = Number of exposure cycles

x_{wc} = Coefficient for w/cm

WC = w/cm ratio

x_i = Coefficient for cracking index

I = Cracking index

The models for the diffusion coefficient had a multiple regression coefficient of 0.73 when initial cracking index was used and 0.63 when final cracking index was used. The reliability indices of the predicted and experimental values showed similar values. The standard errors of estimate for the model using cracking index at time of test were much higher when compared to the standard deviations of test values. However, the error lowers when initial cracking index is used.

Table 4.6: Quantification of Relationships between Cracking and Diffusion Coefficient

Parameter (y)	Coefficients for Equation 4.11 $y = c + x_n * n + x_{wc} * WC + x_i * I$				R ²	r	σ_{est}	SD _{avg}
	c	Number of Cycles (x _n)	Water Cement Ratio (x _{wc})	Cracking Index (x _i)				
Diffusion Coefficient (x 10 ⁻¹² m ² /s) (Initial Cracking Index)	-5.40	50.84	0.31	4.51	0.73	0.78	3.88 x 10 ⁻¹² m ² /s	2.35 x 10 ⁻¹² m ² /s
Diffusion Coefficient (x 10 ⁻¹² m ² /s) (Final Cracking Index)	-4.78	50.02	0.25	4.08	0.63	0.67	11.6 x 10 ⁻¹² m ² /s	2.35 x 10 ⁻¹² m ² /s

Notes:

- Input Variables: n = Number of Cycles
WC = Water-cement Ratio
I_i = Initial Cracking Index
- c, x_n, x_{wc}, and x_i are coefficients
- Reliability Indicators: R² = Multiple Regression Coefficient
r = Reliability Index
 σ_{est} = Standard Error of Estimate
SD = Average Standard Deviation of Experimental Test Values

4.6. Conclusions

Cores were extracted from four girders exhibiting extensive surface microcracking and one girder exhibiting negligible microcracking over a three-year monitoring period. The cracking, strength, stiffness, and durability properties of the cores were determined. It was seen that there was not a significant loss in strength, stiffness, and resistivity in the cores, however the cores exhibited an increase in the chloride diffusion and carbonation coefficients. Samples subjected to accelerated weathering showed increasing deterioration with exposure to the environment, and the samples with higher initial cracking exhibited a higher rate of deterioration.

Based on the results obtained the following conclusions can be drawn:

- The cores exhibited an increase in cracking and chloride diffusion coefficient over the monitoring period.
- The cores exhibited negligible changes in strength, stiffness, and resistivity properties over this period.
- The strength, stiffness, and durability parameters were above serviceability values during the monitoring period.
- The girders have not exhibited a major loss in strength or durability as a result of the microcracking over the monitoring period. While the coefficients for chloride diffusion and carbonation have shown increases, the values have not exceeded permissible limits.

- Based on the results of the accelerated weathering test conducted on extracted specimens from full-scale pre-cast and pre-stressed concrete girders, the following conclusions were drawn:
 - At the end of the testing period, the specimens had higher cracking index, average crack width, loss in mass, and absorption. The specimens also exhibited lower ultrasonic pulse velocity and bulk resistivity values. This indicated reduction in overall durability.
 - The samples undergoing more alternate wetting and drying cycles exhibited a higher loss in durability.
 - The samples with a higher initial cracking index exhibited higher loss in durability.
 - The relationships between the results from the non-destructive tests and the initial cracking index and number of weathering cycles were determined using data from specimens from five girders. The models had high multiple regression coefficients ranging from 0.85 to 0.97 (see Table 4.5).
 - Each model was validated by comparing experimental test values to the predicted test values using data from specimens from one girder. The reliability index of the models ranged from moderate to excellent, with values from 0.63 to 0.90 (see Table 4.5).
 - The standard error of estimate for each test parameter was also calculated and determined to be under permissible limits (see Table 4.5).
 - The relationship between diffusion coefficient, initial cracking index, and the number of wetting and drying cycles was determined (see Table 4.6). The model had a multiple regression coefficient of 0.73. The reliability index of the model was 0.78, and a standard error of estimate comparable to the standard deviation of the test values.

Chapter 5. Prediction of Remaining Service Life of Girders

5.1. Overview of Chapter

This chapter discusses the results undertaken to accomplish Task 4: Prediction of Remaining Service Life of the Girders. To support this task, additional laboratory specimens with varying degrees of cracking were cast in order to determine the critical crack width, depth and density/index for these low w/cm concretes. Using these specimens and the data collected in Task 1 (Chapter 2), Task 2 (Chapter 3), and Task 3 (Chapter 4) an empirical model to estimate the remaining service life of concrete girders with surface microcracking was developed. The model was validated using a time-delay study, and the results of the model were compared to the service lives calculated using Life-365® and two other models for cracked concretes.

5.2. Objective

The objective of the research conducted during this phase of the project was to analyze and synthesize the data collected in Tasks 1–3 to determine whether any **long-term** issue is likely to develop from the extensive surface microcracking.

5.3. Background

Concrete is a functional and cost-efficient construction material with high durability. However, it can deteriorate when exposed to the severe environment, excessive loads, and chemical attack or when it undergoes corrosion of embedded steel, aggregate reactions, and volumetric changes. This can lead to a reduction in the remaining service life of structures built with concrete. This reduction in service life leads to an increase in the cost of repair, rehabilitation, and rebuilding of infrastructure. The service life of a concrete structure can be defined as the time period for which a structure can be used for its intended purpose with maintenance, but without major repair is necessary. Service life can relate to strength or a durability serviceability limit state condition. Limit state is the condition (strength or durability) beyond which the structure no longer fulfills its design criteria. With infrastructure having longer service lives, accurate prediction of service life becomes harder due to the natural complexity involved with trying to predict the future. This challenge is further complicated by the varying environmental conditions, new materials (e.g. low w/cm concretes used in bridge girders), lack of historical data, and inadequate knowledge of deterioration mechanisms (e.g. unexplained microcracking appearing in in-service bridge girders) involved in concrete structures that makes it difficult to estimate and verify long-term reliability of the generated models [88]. However, studies have shown that there are several factors that can affect the service life of concrete structures, or in this case, bridges specifically [121]–[123]:

- Age – hydration and fatigue loading
- Exposure conditions - precipitation and temperature
- Loading – dead, live, and traffic

- Dimensions – length, span, and type of girder
- Material composition - w/cm ratio, cement type, mineral, and chemical admixtures, type, and size of aggregates, air-entrainment, diffusion coefficient, and curing
- Pre-stressing – strand size and number
- Reinforcement bars – size, spacing, depth of concrete cover, and resistivity

5.4. Literature Review on Service Life Prediction Models

Most state transportation agencies have adopted performance-based design methods to meet their infrastructure needs. Performance-based constructions are required to meet certain measurable or predictable performance requirements, without a specifically prescribed method by which to attain those requirements in contrast to traditional prescriptive building code designs [124]. Thus, service life prediction and planning are essential elements of performance-based construction. Models to estimate the discrete number of years of service of infrastructure and infrastructure components are vital in designing repair, rehabilitation, and repair programs. Researchers have used empirical, mechanistic, and simulation models for estimating the life expectancy of a concrete bridge [125].

5.4.1. Mechanistic Models

Mechanistic models measure the rate of individual deterioration mechanisms to estimate the service life. These models are commonly used when the deterioration mechanism is known. Commonly observed deterioration mechanisms are corrosion (chloride and carbonation diffusion), alkali-aggregate reaction, sulfate attack, freeze-thaw damage, and loading (compressive, tensile, shear, flexural, and fatigue) among others [126].

5.4.2. Simulation Models

Simulation models create and analyze theoretical digital prototypes to predict real-world behavior. These models are commonly used when the theory behind the deterioration mechanism and the factors affecting it are well defined. Artificial intelligence or machine learning models use systems such as artificial neural networks and case-based reasoning [127].

5.4.3. Empirical Models

Empirical models use observable data to generate and validate regression equations. These models are commonly used when historical temporal data is available. Empirical models have been successfully used to estimate the service life of bridges using a visual damage/condition rating index. The following types of empirical models have been used.

5.4.3.1. Regression Models

Regression models are commonly used for modeling the performance of infrastructure as they are easy to use and apply. They are also ideal when external validation of the data is not possible, as the data can be validated using a time-delay to check the forecasting power [128]. Regression models can be linear (straight-line extrapolation) or non-linear (polynomial,

logistic, or exponential or a combination thereof). A typical linear regression model is described in Equation 5.1 [117].

$$y = a_0 + x_{a1} * a_1 + x_{a2} * a_2 + \dots \tag{Equation 5.1}$$

Where,

y = condition of the bridge

a_0 = constant

x_a = x-coefficient for variable a

a = variables affecting the condition of bridge (Ex: age, material, traffic, environment, etc.)

Stukhart et al. (1991) used a combination of regression equations to estimate the condition rating and thus service life of bridges in Texas. They used a non-linear exponential model using age and average daily traffic as variables [129]. Bolukbasi et al. (2004) used data from 2,601 Illinois bridges over 20 years to calculate service life based on condition ratings of the deck, superstructure, and substructures of the bridges. A third-degree polynomial equation was developed [130]. Agrawal and Kawaguchi (2009) developed regression equations using bridge type, material type, climate type, snow and other precipitation, exposure to deicing salts, and location as variables to predict damage and thus service life of bridges in New York [131]. Lu et al. (2019) used a multilevel logistic regression model to estimate condition ratings of the deck, superstructure, and substructures of the bridges like the model developed by Bolukbasi et al. (2004) [132].

5.4.3.2. Time-series Models

These models are used to predict the future condition of the structure based on the previously observed conditions. These models are validated using a time-delay to check its forecasting power [128]. A typical time-series model is described in Equation 5.2 .

$$y_t = b_0 + y_{t-1} * b_1 + y_{t-2} * b_2 + \dots \tag{Equation 5.2}$$

Where,

y_t = condition of the bridge at time t

b_0 = constant

y_{t-1} = condition of bridge at time (t-1) and so on

b_1 = coefficient at time (t-1) and so on

Enright and Frangopol (1998) used a time-series model to find the probability of system failure of an in-service concrete bridge. The effects of dead and live loads, live load occurrence rate, rate of loss of strength, degradation, and resistance on the bridge damage rating were

investigated [133]. Omenzetter and Brownjohn (2006) used time histories of static strain from in-service girders retrofitted with structural health monitoring systems to predict structural changes and damage sustained [134]. Dinh et al. (2013) used time-series data from ground-penetrating radar for inspection of in-service concrete bridge decks to map the deterioration progression [135].

5.4.3.3. Markov Models

Markov models are the most commonly used regression models in bridge deterioration modeling. They are used to model the transition between discrete states for fixed time, i.e. they estimate the probability of degradation over a given period. In these models, the condition of the bridge depends on the current condition of the structure and not on the historical condition. The deterioration progress is divided into discrete states which are derived from periodical inspection information. This method is ideal when the historical data is not available, and the data is collected from periodical inspection rather than continuous observation [136]. Thus, the condition of the bridge is represented in terms of probability (see Equation 5.3).

$$X_t = X_{1t}, X_{2t}, \dots, X_{nt}$$

Equation 5.3

Where,

X_t = Probability of bridge condition at time t

X_{nt} = Probability of bridge condition at time n_t

Jiang and Sinha (1989) used geographic location, traffic volume, and bridge age and type to generate a polynomial model to estimate the damage rating at the end of service life [137]. Ng and Moses (1998) used Markov models to estimate bridge deterioration from existing historical data [138]. Yang (2004) and Thomas and Sobanjo (2012) calculated damage rating in terms of cracking in asphalt pavements to model pavement distress parameters such as ride quality and rutting [139], [140].

5.4.4. Commonly Used Service Life Prediction Models

Several service life prediction models for concrete are available. These models are generally based on the kind of degradation mechanism that the structure is expected to undergo. This degradation mechanism can be freeze-thaw damage, thermal stresses, sulfate attack, alkali-silica reaction, carbonation, or, more commonly, chloride diffusion. The damage rating index method uses petrographic examination-based data to determine the remaining service life of dam structures affected by the alkali-silica reaction. DuraCrete, ClinConc, and the Durability Index Approach use a probabilistic diffusion model for carbon dioxide and chloride ingress [141]–[143]. LIFEPROD and DuraCon are based on Fick’s law for chloride diffusion, with DuraCon also utilizing data from rapid chloride migration test [144], [145]. Stadium® is a proprietary software utilizes a multi-ionic probabilistic model based on the Nernst-Planck equation to calculate chloride, carbon dioxide, and sulfate ingress rate and corrosion initiation time [146]. The fib Bulletin 34 probabilistic model is based on Fick’s 2nd law to calculate

chloride ingress and carbonation [147]. Probabilistic service life prediction models use probability of failure due to the degradation mechanism to estimate service life.

5.4.4.1. Life-365®

Life-365® is a free software that uses semi-probabilistic chloride diffusion coefficient model based on Fick's law to predict remaining service life of concrete structures. Life-365® utilizes specimen dimensions, exposure conditions, w/cm, concrete cover, and location as input parameters to calculate service life. It uses historical experimental data to generate service life models. Concrete Works is a variant of Life-365® and predicts strength and thermal cracking along with chloride ingress [148].

5.4.5. Prediction of Remaining Service Life of Cracked Concrete

Service life prediction models for concrete with cracks also exist. These models account for the exacerbating effect that cracks have on the loss in service life, as cracks can exacerbate the rate at which deterioration occurs as they allow easier access to deleterious materials. Ann et al. (2010) developed a probabilistic service life model for a cracked bridge structure exposed to carbonation. The crack widths ranged between 0.1 to 0.2 mm. They used carbonation depth, cover depth, carbonation rate, and concrete condition (sound, cracked, and joint-section) as input variables [149]. However, it is seen that more studies focus on chloride ingress as a limit state rather than carbonation. Otieno et al. (2016) presented a resistivity and chloride diffusion-based empirical model for cracked reinforced concrete beam specimens. Surface resistivity was measured using a non-destructive method with a Wenner probe. The cracks had widths of 0.4 and 0.7 mm. They used the water-binder ratio, mineral admixtures, concrete cover depth, and crack width as input variables [150]. Kwon et al. (2009) and Pacheco (2019) provided equations to calculate chloride diffusion coefficients and hence service life models for cracked concretes [27], [151].

5.4.5.1. Kwon et al. (2009)

Kwon et al. (2009) developed a probabilistic model to estimate the service life of a concrete wharf with chloride diffusion as the limit state. A single crack was used to model the increase in diffusion coefficient. The crack width ranged from 0.1 to 0.3 mm. They used concrete cover, chloride ion concentration, chloride diffusion coefficient, and crack width as input variables [27].

$$D_{cr} = \gamma_c D_k + \left(\frac{w}{l}\right) \left(\frac{w}{w_a}\right)^2 D_0 \quad \text{Equation 5.4}$$

Where,

D_{cr} = Diffusion Coefficient with crack

γ_c = Material constant

D_k = Diffusion coefficient of sound concrete

D_0 = Crack parameter affecting diffusion

w = Predicted crack width

w_a = Allowable crack width

w/l = Crack density

5.4.5.2. Pacheco (2019)

Pacheco (2019) developed a probabilistic model based on crack width to estimate the service life of cracked concrete structures. They used migration coefficient, age, hydration, temperature, initial chloride concentration, cover, and crack width as input parameters [151].

$$D_{cr} = \frac{D_0}{1 - \frac{w_k}{w_{limit}}} \quad \text{Equation 5.5}$$

Where,

D_{cr} = Diffusion Coefficient with crack

D_0 = Diffusion Coefficient of sound concrete

w_k = Measured crack width

w_{limit} = Allowable crack width

5.5. Materials and Methods

Full-scale pre-stressed concrete girders that were constructed at commercial precast plants were used in this study. The girders selected were monitored for a period of 588 to 959 days, and the girders were between 2000 and 4500 days (5.5 to 12.2 years) old at the beginning of the test period. Non-destructive tests were conducted on six in-service girders and five overcast girders (see Chapter 3). In addition to the non-destructive tests, cores were also extracted from overcast girders (see Chapter 4). Three rounds of field visits were conducted to each girder. A fourth field visit was conducted to two overcast girders as part of a validation study. In addition, three field visits were conducted to a sixth overcast girder, and non-destructive tests were conducted, and cores were collected. The data from this girder was also used to validate the model generated. The experimental and analytical methods used to generate the model are described in this section.

5.5.1. Girder Notations

The girders are described below. (Additional information on the girders is provided in Table 2.2, Table 2.3, and Appendix A.)

- Four overcast girders (1R, 2R, 3R, and 4R) with visible surface cracking.
- Six in-service girders (6I, 7I, 8I, 9I, 10I, and 11I) with visible surface cracking.
- One overcast girder (5RC) and two in-service girders (12IC and 13IC) exhibiting negligible cracking were also selected to serve as control specimens.

- One overcast validation girder (14V) with extensive surface cracking, that was used to validate the generated model.

5.5.2. Experimental Methods

The following data was required to generate the empirical service life model:

- The present condition of the girders
- The rate of increase in cracking and decrease in strength, stiffness, and durability over time
- The relationship between the increase in cracking and decrease in strength, stiffness, and durability
- Serviceability conditions for cracking, strength, stiffness, and durability.

5.5.2.1. Present Condition of Girders

An initial field visit was conducted to all overcast and in-service girders. In-situ cracking, strain, ultrasonic pulse velocity, and surface resistivity data were collected from all girders. In addition, cores were collected from all overcast girders, and the strength, stiffness, resistivity, and chloride diffusion and carbonation coefficients were determined (see Section 2.4).

5.5.2.2. Rate of Growth of Cracking

In-situ observation and collection of cracking, strain, ultrasonic pulse velocity, and surface resistivity data from in-service and overcast full-scale girders over two years showed that the girders with surface microcracking exhibited an increase in cracking and shrinkage, and a marginal reduction in the pulse velocity and surface resistivity. The data showed that exposure to environment and presence of pre-existing cracks were major factors affecting the rate of increase in cracking, while external loading has not yet manifested any impact (see Section 3.6).

Laboratory testing of extracted cores from overcast girders showed that the strength, stiffness, and resistivity of the girders did not reduce in a significant manner, while there was a marginal increase in the diffusion coefficients. The increase in diffusion coefficient values was still under serviceability limits (see Section 4.6).

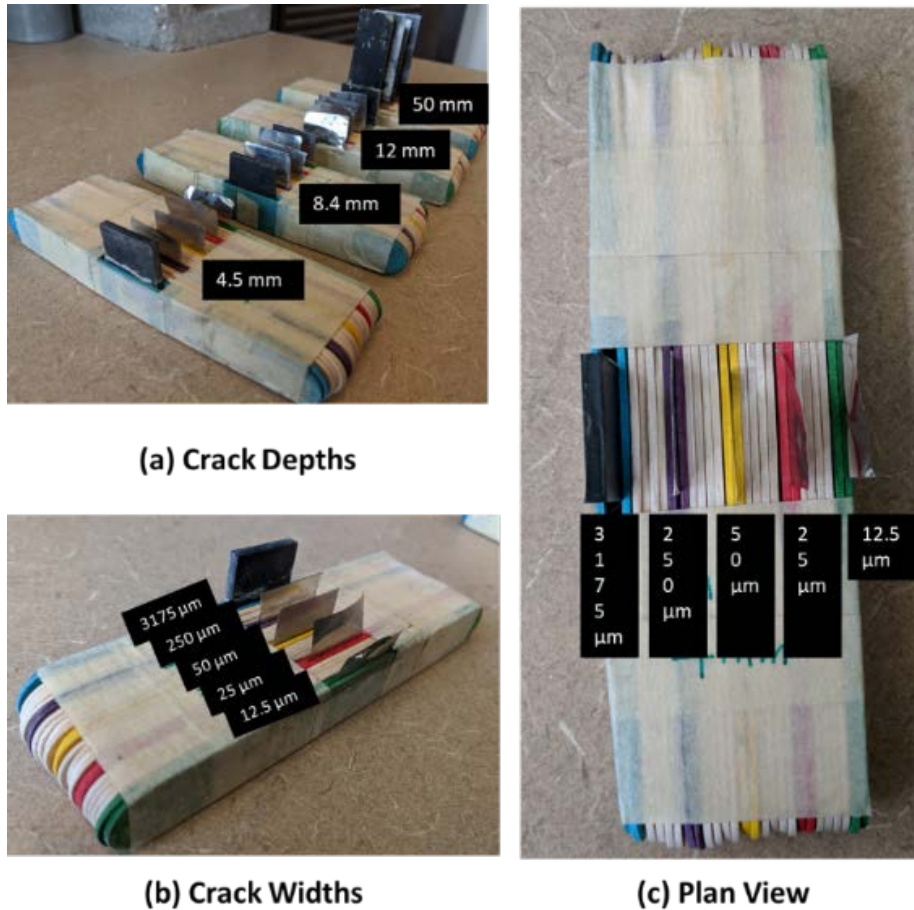
The effect of exposure and presence of pre-existing cracks was investigated by conducting accelerated weathering tests on the extracted cores and measuring the change in cracking, absorption, ultrasonic pulse velocity, bulk resistivity, and chloride diffusion coefficient. The relationship between the number of weathering cycles and initial cracking and the increase in cracking and decrease durability were quantified (see Section 4.6).

5.5.2.3. Relationship Between Cracking and Loss in Strength, Stiffness, and Durability

It was initially proposed that cores extracted from overcast girders would be used to determine the relationship between the increase in cracking and the resulting decrease in strength, stiffness, and durability. However, the following limitations were found, and it was not possible to accurately quantify the effect of cracking:

- Cracking parameters (width, depth, and density) of the microcracks could not be controlled or replicated with any accuracy, i.e., repeatability of the tests on the specimens with the same cracking values was not possible.
- Determination of the depth of the microcracks could not be done with non-destructive tests, i.e., measurement of depth and strength/stiffness/durability tests could not be performed on the same specimen.
- The range and width of cracks do not reach high levels of severity, i.e., the effect of cracks that could potentially reach serviceability could not be tested.
- The number of cores that could be extracted was limited; i.e. sample size was limited.

Thus, samples with embedded cracks were cast using stainless steel and plastic shims (see Figure 5.1). This allowed for precise control of width, depth, and density of the generated cracks.



Source: Images by Authors

Figure 5.1: Typical shims used and crack (a) depths and (b) widths, and (c) plan view

Embedded cracks have been used with success by researchers studying the effect of cracks on the diffusion properties of concrete. A study conducted by the Virginia Department of Transportation concluded that removable shims could be used to study the effects of chloride intrusion into a single microcrack with crack width 0.1–0.2 mm (0.004–0.008 in.) [152]. Šavija et al. used copper plates to embed a single microcrack with crack width 0.3 mm (0.012 in.) and depth 20 mm (0.8 in.) and conducted rapid migration tests on the samples to successfully study chloride diffusion [153], [154]. Du et al. showed that the chloride diffusion models exhibited similar behavior for both natural (tortuous) and artificial (embedded) cracks [155]. Marsavina et al. studied the influence of a single embedded microcrack of crack width 0.2 to 0.5 mm (in.) and 5 to 20 mm deep (in.) on the chloride diffusion coefficient as measured by rapid migration test [156]. Salehi et al. studied the effect of embedded cracks with widths 0.3 mm (0.01 in.), 1 mm (0.04 in.), and 2 mm (0.08 in.) to successfully study concrete surface resistivity values [157].

5.5.2.3.1. Lab Cast Specimens

The severity of cracks is generally assessed using width, depth, and density/index [19]. For this study, the range of these cracking parameters was determined after collecting data from field specimens. The data was acquired from fourteen full scale pre-stressed pre-cast girders that were exhibiting microcracking. The ranges of cracking parameters observed in this study are shown below:

- Crack Width
 - o Average Crack Width – 12.5 μm (0.0005 in.)
 - o Largest Microcrack – 50 μm (0.002 in.)
 - o ACI 224.1R Corrosion Serviceability Condition – 250 μm (0.01 in.) [40]
 - o ACI 318 Serviceability Condition for Structural Cracks – 3175 μm (0.125 in.) [39]
- Crack Depth
 - o Average Crack Depth – 4.2 mm (0.168 in.)
 - o Largest Crack Depth – 8.2 mm (0.331 in.)
 - o Assumed Serviceability Crack Depth for Corrosion – 12.9 mm (0.508 in.)
 - o Assumed Serviceability Crack Depth (Depth of Cover) – 50.8 mm (2 in.)
- Cracking Index
 - o Average Cracking Index – 0.05 mm/m (0.0019 in./yd)
 - o Largest Cracking Index – 3.5 mm/m (0.1250 in./yd)
 - o Assumed Serviceability Cracking Index for microcracks – 8 mm/m (0.2878 in./yd)
 - o Assumed Serviceability Cracking Index for macrocracks – 156.25 mm/m (5.625 in./yd)

As there are no existing serviceability limits for cracking index, the serviceability cracking indices assumed in the study are the expected worst-case scenarios based on laboratory trial and error.

5.5.2.3.2. Mix Proportions

The mix design selected for this study was adopted from the standard mix proportions suggested by the Texas Department of Transportation for pre-stressed pre-cast girders [18]. Table 5.1 shows the concrete mix proportions selected for the study.

Table 5.1: Concrete Mix Proportions and Properties

Material	Description	Quantity	
Cement	Type III	418 kg/m ³	705 lbs/cu.yd.
Fine Aggregate (FA)	SSD River Sand (AC = 1.14%)	835 kg/m ³	1407 lbs/cu.yd.
Coarse Aggregate (CA)	SSD River Gravel (AC = 1.31%)	1043 kg/m ³	1758 lbs/cu.yd.
Water	-	117 kg/m ³	252 lbs/cu.yd.
Chemical Admixture	Superplasticizer	2298 ml/m ³	8.46 fl.oz./cwt
	Retarder	766 ml/m ³	2.82 fl.oz./cwt
All materials as per ASTM C150, ASTM C33 and ASTM C494 [15], [16], [158]			
Water/Cement Mass Ratio		0.28	
Paste/Aggregate Mass Ratio		0.285	
CA/FA Mass Ratio		1.25	

Initially, the embedding the shims into the concrete mixture and then removing the shims prior to setting was tried. However, it was found that embedding cracks in concrete led to the following issues:

- The shims for the smaller crack widths 12.5 μm (0.0005 in.) and 25 μm (0.001 in.) would bend due to large-sized coarse aggregate during placement.
- The shims for larger crack widths 50 to 3175 μm (0.002 to 0.125 in.) would prevent the coarse aggregate from filling in between the embedded cracks leading to a paste rich top layer.

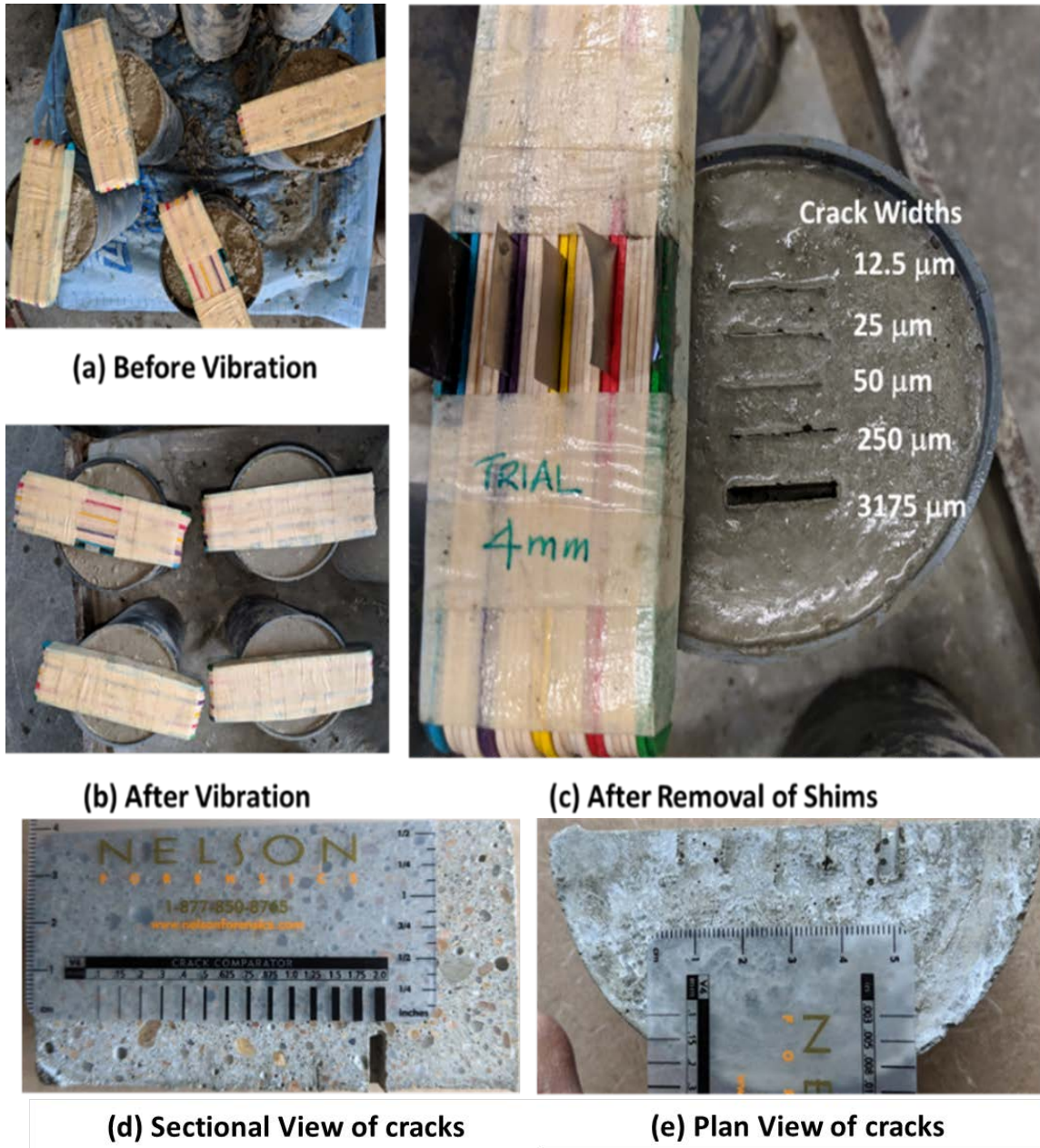
Thus, a concrete equivalent mix (CEM) was designed according to the method prescribed by Schwartzenuber and Catherine [159]. This method was chosen to allow the w/cm to remain unchanged, by keeping the total aggregate surface area the same and thus not changing the aggregate water-demand. CEM mixtures possess the same concrete composition regarding the cement nature and dosage, effective water content, mineral additives, chemical admixture types and concentrations, and sand [159]. Table 5.2 shows the modified mix design.

Table 5.2: Concrete Equivalent Mortar Mix Proportions and Properties

Material	Description	Quantity	
Cement	Type III	432 kg/m ³	728 lbs/cu.yd.
Fine Aggregate (FA)	SSD River Sand (AC = 1.14%)	1887 kg/m ³	3180 lbs/cu.yd.
Coarse Aggregate (CA)	-	-	-
Water	-	121 kg/m ³	204 lbs/cu.yd.
Chemical Admixture	Superplasticizer	2298 ml/m ³	8.46 fl.oz./cwt
	Retarder	766 ml/m ³	2.82 fl.oz./cwt
All materials as per ASTM C150, ASTM C33 and ASTM C494 [15], [16], [158]			
Water/Cement Mass Ratio		0.28	
Paste/Aggregate Mass Ratio		0.293	
CA/FA Mass Ratio		0	

Standard 100x200 mm (4x8 in.) cylinders were cast using the CEM proportions. Micro and macro cracks were embedded in the wet mixture using lubricated stainless steel (12.5 µm [0.0005 in.], 25 µm [0.001 in.], 50 µm [0.002 in.], 250 µm [0.01 in.]) and plastic (3175 µm [0.125 in.]) shims (see Figure 5.1). The cylindrical molds were half filled with mortar and shims were placed. Mortar was carefully filled through the gaps between the shims (see Figure 5.2a). The molds were placed on a vibrating table to allow the mortar to fill the gaps between shims (see Figure 5.2b). Trials were conducted to determine the best time to remove the shims. It was found that removing the shims just before the final set occurred (8 hours) allowed for easy extraction of the shims without disturbing the cracks (see Figure 5.2c). Figure 5.2d and Figure 5.2e show the cross-sectional and plan views of the embedded cracks in the hardened samples respectively.

Table 5.3 shows the experimental matrix and notations. Additional samples were cast with crack width 25 µm (0.001 in.) to validate the study



Source: Images by Authors

Figure 5.2: Casting of cracked mortar test specimens (a) before and (b) after vibration, (c) after removal of shims, and (d) sectional and (e) plan view of the hardened cracks

Table 5.3: Experimental Matrix and Notations

Notation	Crack Width (W)	Crack Depth (D)	Cracking Index (I)
(Width-Depth-Index)	μm (in.)	mm (in.)	mm/m (in\yd)
Control	0	0	0
W _a D _a I _a	12.5 (0.0005) Average-(a)	4.5 (0.18) Average (a)	0.36 (0.013) Average (a)
W _a D _a I _l			1.11 (0.040) Largest (l)
W _a D _a I _s			1.75 (0.063) Serviceability (s)
W _a D _l I _a		8.4 (0.33) Largest (l)	0.36 (0.013)
W _a D _l I _l			1.11 (0.040)
W _a D _l I _s			1.75 (0.063)
W _a D _{sc} I _a		12 (0.51) Service-ability Corrosion (sc)	0.36 (0.013)
W _a D _{sc} I _l			1.11 (0.040)
W _a D _{sc} I _s			1.75 (0.063)
W _a D _{ss} I _a		50 (2) Service-ability Strength (ss)	0.36 (0.013)
W _a D _{ss} I _l			1.11 (0.040)
W _a D _{ss} I _s			1.75 (0.063)
W _l D _a I _a	50 (0.002) Largest (l)	4.5 (0.18)	0.5 (0.018)
W _l D _a I _l			2.5 (0.090)
W _l D _a I _s			5.5 (0.198)
W _l D _l I _a		8.4 (0.33)	0.5 (0.018)
W _l D _l I _l			2.5 (0.090)
W _l D _l I _s			5.5 (0.198)
W _l D _{sc} I _a		12 (0.51)	0.5 (0.018)
W _l D _{sc} I _l			2.5 (0.090)
W _l D _{sc} I _s			5.5 (0.198)
W _l D _{ss} I _a		50 (2)	0.5 (0.018)
W _l D _{ss} I _l			2.5 (0.090)
W _l D _{ss} I _s			5.5 (0.198)

Notation	Crack Width (W)	Crack Depth (D)	Cracking Index (I)
(Width-Depth-Index)	μm (in.)	mm (in.)	mm/m (in\yd)
W _{sc} D _a I _a	250 (0.01) Serviceability Corrosion (sc)	4.5 (0.18) Average (a)	2.5 (0.090) Average (a)
W _{sc} D _a I _l			12.5 (0.450) Largest (l)
W _{sc} D _a I _s			2.78 (0.100) Serviceability (s)
W _{sc} D _l I _a		8.4 (0.33) Largest (l)	2.5 (0.090)
W _{sc} D _l I _l			12.5 (0.450)
W _{sc} D _l I _s			2.78 (0.100)
W _{sc} D _{sc} I _a		12 (0.51) Service-ability Corrosion (sc)	2.5 (0.090)
W _{sc} D _{sc} I _l			12.5 (0.450)
W _{sc} D _{sc} I _s			2.78 (0.100)
W _{sc} D _{ss} I _a		50 (2) Service-ability Strength (ss)	2.5 (0.090)
W _{sc} D _{ss} I _l			12.5 (0.450)
W _{sc} D _{ss} I _s			2.78 (0.100)
W _{ss} D _a I _a	3175 (0.125) Service-ability Strength (ss)	4.5 (0.18)	31.25 (1.125)
W _{ss} D _a I _l			93.75 (3.375)
W _{ss} D _a I _s			156.2 (5.625)
W _{ss} D _l I _a		8.4 (0.33)	31.25 (1.125)
W _{ss} D _l I _l			93.75 (3.375)
W _{ss} D _l I _s			156.2 (5.625)
W _{ss} D _{sc} I _a		12 (0.51)	31.25 (1.125)
W _{ss} D _{sc} I _l			93.75 (3.375)
W _{ss} D _{sc} I _s			156.2 (5.625)
W _{ss} D _{ss} I _a		50 (2)	31.25 (1.125)
W _{ss} D _{ss} I _l			93.75 (3.375)
W _{ss} D _{ss} I _s			156.2 (5.625)

Notation	Crack Width (W)	Crack Depth (D)	Cracking Index (I)
(Width-Depth-Index)	μm (in.)	mm (in.)	mm/m (in\yd)
W _v D _a I _a	25 (0.001) Validation (v)	4.5 (0.18) Average (a)	0.75 (0.027) Average (a)
W _v D _a I _l			2.25 (0.081) Largest (l)
W _v D _a I _s			3.5 (0.126) Serviceability (s)
W _v D _l I _a		8.4 (0.33) Largest (l)	0.75 (0.027)
W _v D _l I _l			2.25 (0.081)
W _v D _l I _s			3.5 (0.126)
W _v D _{sc} I _a		12 (0.51) Service-ability Corrosion (sc)	0.75 (0.027)
W _v D _{sc} I _l			2.25 (0.081)
W _v D _{sc} I _s			3.5 (0.126)
W _v D _{ss} I _a		50 (2) Service-ability Strength (ss)	0.75 (0.027)
W _v D _{ss} I _l			2.25 (0.081)
W _v D _{ss} I _s			3.5 (0.126)

5.5.2.3.3. Items of Investigation

The average of three specimens was used to determine the test results. Table 5.4 shows the tests conducted, and the test method followed. The serviceability values from standards and relevant studies undertaken by researchers are also included. The serviceability conditions were selected from studies using concretes with similar mix proportions.

Table 5.4: Test Methods and Serviceability Values

Test	Standard/Test Method	Concrete Serviceability Values (28 days)	Source for Test Methodology	Material Properties
STRENGTH TESTS				
Compressive Strength	ASTM C42 [102]	35 MPa (5000 psi) 3 MPa (425 psi)	TxDOT Bridge Design Manual, (2018) [18]	Pre-stressed I girders
Tensile Strength	ASTM C496 [103]			
STIFFNESS TESTS				
Ultrasonic Pulse Velocity*	ASTM C597 [20]	3660-3050 m/s	Malhotra (1976) Turgut (2006) [65], [104]	w/c ratios 0.29–0.95 3000-11500 m/s
Modulus of Elasticity	ASTM C469 [105]	35 GPa (5×10^6 psi)	TxDOT Bridge Design Manual (2018) [18]	Pre-stressed I girders
DURABILITY TESTS				
Bulk Resistivity*	AASHTO TP119 [54]	12-21 kΩcm	Sengul (2014) FDOT Standard (2004) [66], [106]	w/c ratios 0.28–0.49; 48–75 MPa (7000-11000 psi)
Surface Resistivity*	AASHTO T358 – Modified for Cylinders [21]	5-7.5 kΩcm		
Chloride Diffusion	NT Build 492 [107]	$5-10 \times 10^{-12}$ m ² /s		
Carbonation Coefficient	CPC-18 [108]	85.7 mm/yr ^{0.5} (0.26 in./yr ^{0.5})	50 mm (2 in.) over 75 years, i.e., concrete cover over expected service life [12]	Concrete I-Girders TxDOT Bridge Design Manual (2018) [18]
Note: * Non-destructive test				

5.5.2.3.4. Serviceability Values for Concrete and Mortar

The serviceability values in Table 5.4 are for concrete at 28 days. However, in this study, a concrete equivalent mortar was used. Thus, the serviceability values for mortars were determined by comparing values of uncracked concrete and concrete equivalent mortar specimens. In addition, a literature review was conducted to determine the effect of coarse aggregate on the strength, stiffness and durability

properties of concrete and mortar. Table 5.5 summarizes the serviceability values for strength, stiffness, and durability values obtained from the concrete and mortar specimen, along with a summary of the literature review conducted to determine the relationship between mortar and concrete.

Table 5.5: Serviceability Values for Concrete and Mortar

Test	Concrete Test Values (28 days)	Concrete Serviceability Values (28 days)	Mortar Test Values (28 days)	Mortar Serviceability Values (28 days)	Relationship Source
STRENGTH TESTS					
Compressive Strength	64 MPa (9298 psi)	96 MPa (13924 psi)	38 MPa (5568 psi)	57 MPa (8267 psi)	<i>Inverse Linear Correlation</i> Assad et. al (2009) [160]
Tensile Strength	6.4 MPa (925 psi)	3 MPa (425 psi)	4.5 MPa (648 psi)	2 MPa (298 psi)	<i>Inverse Linear Correlation</i> Ross et al. (1990) John and Shah (1987) Mellinger and Birkimer (1966) [161]–[163]
STIFFNESS TESTS					
Ultrasonic Pulse Velocity	10430 m/s	3050 m/s	11189 m/s	4907 m/s	<i>Inverse Logarithmic Correlation</i> Swamy and Rigby (1971) Popovics et al. (1990) [164], [165]
Modulus of Elasticity	35.9 GPa (5.2×10^6 psi)	35 GPa (5×10^6 psi)	38.6 GPa (5.6×10^6 psi)	37.6 GPa (5.4×10^6 psi)	<i>Inverse Logarithmic Correlation</i> Swamy and Rigby (1971), Yang (1998), Chen et al. (2013) [164], [166], [167]
DURABILITY TESTS					
Bulk Resistivity	26.2 kΩcm	14 kΩcm	34.0 kΩcm	18.2 kΩcm	<i>Inverse Linear Correlation</i> Hou et al. (2017), Sengul (2014) [66], [168]
Surface Resistivity	35.6 kΩcm	5 kΩcm	14 kΩcm	6.23 kΩcm	
Chloride Diffusion	$3.2 \times 10^{-12} \frac{m^2}{s}$	$10 \times 10^{-12} \frac{m^2}{s}$	$5.7 \times 10^{-12} \frac{m^2}{s}$	$17.8 \times 10^{-12} \frac{m^2}{s}$	<i>Direct Linear Correlation</i> Shi et al. (2011), Caré (2003) [169], [170]
Carbonation Coefficient	4 mm/yr ^{0.5} (0.16 in./yr ^{0.5})	7 mm/yr ^{0.5} (0.27 in./yr ^{0.5})	5 mm/yr ^{0.5} (0.20 in./yr ^{0.5})	8.3 mm/yr ^{0.5} (0.33 in./yr ^{0.5})	<i>Direct Linear Correlation</i> Khunthongkeaw et al. (2006) [171]

Researchers have shown that compressive strength has an inverse linear correlation with the percentage of the coarse aggregate present. A study conducted by Assad et al. (2009) on the comparative strength and stiffness behavior of concrete and

concrete equivalent mortars showed a strong inverse linear correlation ($R^2=0.92$) between the compressive strength of concrete and concrete equivalent mortars [160]. Tensile strength has a direct linear correlation with the percentage of coarse aggregate present. Ross et al. (1990) showed that split tensile strength of concrete was 1.5 times that of mortar [161]. Similar results were obtained by John and Shah (1987) and Mellinger and Birkimer (1966) [162], [163].

Researchers have shown that stiffness of concrete has an inverse logarithmic correlation with the percentage of coarse aggregate present in the concrete mix. A seminal study conducted by Swamy and Rigby (1970) on the dynamic properties of concrete and mortar showed that concretes have a higher modulus of elasticity when compared to mortars [164]. A study was conducted on the effect of the transition zone on the modulus of elasticity of mortars by Yang (1998) and showed that modulus of elasticity increased with increasing aggregate fraction [166]. In a study conducted to compare the dynamic properties of paste, mortar, and concrete, Chen et al. (2013) showed that the modulus of elasticity of concrete was higher by about 1.33 when compared to mortars [167]. The presence of coarse aggregate also reduces the ultrasonic pulse velocity through concrete when compared to mortar. Coarse aggregate reduces homogeneity, thereby increasing the time required by the ultrasonic wave to pass through concrete. Thus, mortars have higher ultrasonic pulse velocity [165]. This relationship is inverse logarithmic, like the modulus of elasticity [164].

Studies have shown that an inverse linear relationship exists between the volume of coarse aggregate and electrical resistivity. A study by Sengul (2014) showed that a higher fraction of coarse aggregate results in higher resistivity, i.e., concrete samples had lower resistivity when compared to mortar samples [66]. A study conducted by Hou et al. (2017) further showed that a well correlated ($R^2=0.98$) linear relationship exists between the volume of coarse aggregates and the resistivity of concrete and mortar samples [168].

Studies have shown that a direct linear relationship exists between the volume of coarse aggregate and diffusion coefficients. Shi et al. (2011) obtained a correlation coefficient of 0.99 between the chloride diffusion coefficient of concrete versus mortar. Concretes had a chloride diffusion coefficient about 1.5 times that of mortar [170]. Caré (2003) obtained a correlation coefficient value of 0.94 when comparing the coarse aggregate volume and chloride diffusion coefficient. The study accounted for the effect of interfacial transition zone and tortuosity due to the inclusion of coarse aggregates [169]. The carbonation coefficient also has a direct linear correlation with coarse aggregate. Khunthongkeaw et al. (2006) showed that concrete has slightly lower carbonation coefficient value when compared to mortars [171].

5.5.2.3.5. Quantification of Relationships between Increase in Cracking and Decrease in Strength, Stiffness, and Durability

The relationship between each test parameter and the three cracking parameters (width, depth, and index) was determined using multiple linear regression. This method is commonly used to model the relationship between two or more explanatory variables and a response variable by fitting a linear equation to the observed data. The equation of the best fit line is calculated by minimizing the sum of squares of the deviations from each data point to the fitted line [117]. The explanatory variables in this model are crack width, depth, and index, and the response variable is the test parameter (compressive strength, tensile strength, ultrasonic pulse velocity, modulus of elasticity, bulk resistivity, surface resistivity, chloride diffusion coefficient, and carbonation coefficient). The model was generated with data obtained by testing the samples cast with all crack depths and indices and 12.5 μm , 50 μm , 250 μm , and 3175 μm crack widths (see Table 5.3). The multiple regression coefficients (R^2) for each model were also calculated. The regression coefficient is a statistical measure of how close the experimental data is to the fitted regression line. The coefficient values range between 0 (no relationship) and 1 (very good relationship) [118]. Equation 5.6 is a sample of the model generated for each test parameter.

$$y = c + x_w * W + x_d * D + x_i * I$$

Equation 5.6

Where,

y = Test parameter

c = y-intercept

x_w = Coefficient for crack width

W = Crack width

x_d = Coefficient for crack depth

D = Crack depth

x_i = Coefficient for cracking index

I = Cracking Index

5.5.2.3.6. Validation of Model

Samples were cast with 25 μm crack width (see Table 5.3) and tested. This experimental data was compared to the data predicted by the model. The validity

of the model was assessed using the reliability index and standard error of estimates (see Section 4.4.5.3).

5.5.2.4. Serviceability and Critical Cracking Parameters

The effect of increasing degree of cracking (width, depth, and density/index) on the strength, stiffness, and durability properties of concrete was quantified. Compressive and tensile strength, ultrasonic pulse velocity, modulus of elasticity, bulk, and surface resistivity decreased with increased cracking. Carbonation and chloride diffusion coefficient increased with increased cracking. Table 5.5 contains the serviceability values for strength, stiffness, and durability parameters for mortars at 28 days. The serviceability cracking values for each test parameter are calculated by optimizing the crack width, depth, and index values in Equation 5.6 by substituting the serviceability values for “y” (test parameter).

The test parameter with the lowest serviceability crack values was the critical test parameter. The critical width, depth, and index were determined by selecting the cracking values corresponding to the critical test parameter.

5.5.2.5. Summary of Tests Conducted

Conclusions drawn from the non-destructive tests on girders (see Section 3.6) and laboratory tests on extracted cores and accelerated weathering tests (see Section 4.6) conducted on extracted cores were used to generate the model. Lab specimens with varying degrees of cracking were cast, and critical cracking values were estimated (see Section 5.5.2.4). The tests conducted on the samples are summarized in Table 5.6.

Table 5.6: Summary of Tests Conducted in the Study

Test	Source for Test Method	Number of Samples Tested		
		Visit 1	Visit 2	Visit 3
NON-DESTRUCTIVE TESTS ON FULL-SCALE GIRDERS				
Microcracking Evaluation	FHWA-HIF-09-004 Report [19]	6 overcast girders – 6 grids on each girder 8 in-service girders – 4 grids on each girder		
Strain	FHWA-HIF-09-004 Report [19]			
Ultrasonic Pulse Velocity	ASTM C597 [20]			
Surface Resistivity	AASHTO T358 – Modified for Cylinders [21]			
TESTS ON CORES AND EMBEDDED CRACK CYLINDER SPECIMENS				
VISUAL EVALUATION				
Microcracking Evaluation	FHWA-HIF-09-004 Report [19]	15	8	8
Optical Microscopy	ASTM C1723 [101]	1	-	-
Scanning Electron Microscopy	ASTM C1723 [101]	1	-	-
STRENGTH TESTS				
Compressive Strength	ASTM C42 [102]	4	2	2
Tensile Strength	ASTM C496 [103]	2	2	2
STIFFNESS TESTS				
Ultrasonic Pulse Velocity	ASTM C597 [20]	15	8	8
Elastic Modulus	ASTM C469 [105]	4	2	2
DURABILITY TESTS				
Bulk Resistivity	AASHTO TP119 [54]	15	8	8
Surface Resistivity	AASHTO T358 – Modified for Cylinders [21]	15	8	8
Chloride Diffusion Coefficient	NT Build 492 [107]	4	2	2
Carbonation Coefficient	CPC-18 [108]	6	6	6
ACCELERATED WEATHERING TESTS ON EXTRACTED CORES				
Microcracking Evaluation	FHWA-HIF-09-004 Report [19]	36 specimens undergoing 22 weathering cycles each. 36 specimens undergoing 12 cycles weathering each. 36 specimens undergoing 10 weathering cycles each.		
Bulk Resistivity	AASHTO TP119 [54]			
Ultrasonic Pulse Velocity	ASTM C597 [20]			
Mass Measurements	-			
Chloride Diffusion Coefficient	NT Build 492 [107]	108 specimens before undergoing accelerated weathering 108 specimens at the end of the accelerated weathering test		

5.5.3. Analytical Methods

As described in Section 5.4, estimating the remaining service life of the cracked concrete girders can be done using various methods. This study utilizes a

combination of regression and time-series models to predict the remaining service life of the low w/cm concrete pre-cast girders with microcracking.

As the mechanism causing these microcracks is not fully understood, developing a theoretical model was not possible. However, as the microcracks did exhibit an increase over the monitoring period, this change could be recorded and quantified. It was found that exposure to the environment and extent of pre-existing cracks had an effect on the rate of growth of microcracks (see Section 3.5.2 and Section 3.5.3). As discussed earlier, time-series models are ideal when historical data can be collected at time intervals (see Section 5.4.3.2). In addition, regression models can be successfully used in predicting service life of concrete infrastructure elements (see Section 5.4.3.1). Cracking, strength, stiffness, and durability data was collected from the girders by conducting three field trips, approximately one year apart. These field trips served two purposes, establishing the present condition of the girders and quantifying the rate at which these changes occur. An additional fourth field trip was conducted to two girders to serve as a time-delay study to validate the reliability of the model generated. The empirical service life model was generated using the following method:

- **Determine the present condition of the girders:** Cracking, strength, stiffness, and durability data were collected from 5 overcast and 8 in-service full-scale girders.
- **Determine the rate of increase in cracking and decrease in strength, stiffness, and durability:** Change in cracking, strength, stiffness, and durability over time was determined by collecting data from the girders two more times one-year apart. Cracking was estimated by calculating the average crack width and cracking index. Strength was estimated by measuring the compressive and tensile strength. Stiffness was estimated by measuring the ultrasonic pulse velocity and modulus of elasticity. Durability was estimated by measuring surface and bulk resistivity, chloride diffusion coefficient and carbonation coefficient.
- **Quantify the relationship between the increase in cracking and decrease in strength and durability:** Specimens with different degrees of cracking were cast, and their strength, stiffness, and durability were determined, and the relationships quantified.
- **Determining the serviceability conditions for cracking:** Chloride diffusion coefficient was determined to be the limit state value for durability. A critical crack width of 100 μm and a critical cracking index of 18 mm/m was calculated.

- **Determine factors affecting the rate of cracking:** The effect of external loading, exposure to the environment, the presence of pre-existing cracks, and the direction of pre-stressing were determined. It was found that exposure to environment, presence of pre-existing cracks, and direction of pre-stressing had the biggest impact on the rate of change of cracking when compared to external loading.
- **Modeling the rate of growth of cracking:** While direction of pre-stressing was a factor affecting the rate of growth of cracking, the direction of pre-stressing is the same for all girders and hence has not been considered as a factor in the model. Data from the non-destructive tests conducted on the girders and accelerated weathering test on extracted cores were used to model the remaining service life (see Equation 5.7). Multiple regression coefficient using sum-of-least-squares was also calculated for the model.

$$y = c + x_{a1} * a_1 + x_{a2} * a_2 + x_{a3} * a_3 + x_{a4} * a_4 + x_{a5} * a_5 \quad \text{Equation 5.7}$$

Where,

y = Age of specimens in days

c = empirical constant

a₁ = Effect of exposure expressed using a binary code. 0 for samples that were not exposed to the environment and 1 for samples exposed to the environment.

a₂ = Effect of pre-existing cracks expressed using the cracking index of girders during the first field visit and the cracking index of accelerated weathering tests before the start of the test.

a₃ = w/cm used to account for variation in material composition.

a₄ = Ultrasonic pulse velocity used to account for variation in material composition.

a₅ = The cracking index observed during subsequent field visits, and at the end of each accelerated weathering test cycle was used.

x_{a1} – x_{a5} = coefficients for a₁ - a₅

- **Validation of model:** The model was validated using the data collected from the fourth round of field visits from two overcast girders (3R and 4R), i.e., time-delay validation. The model was also validated using data from one overcast girder (14V). The validity of the model was assessed using the reliability index and standard error of estimates (see Section 4.4.5.3).

5.6. Results and Discussions

The results of the laboratory tests performed on embedded crack cylinders to determine the critical cracking values are presented in this section. The model generated is presented along with the results of the validation study performed. The remaining service life of the girders was estimated using the generated empirical model and compared to the service life predicted using Life-365® and the modified chloride diffusion coefficient for cracked concretes.

5.6.1. Serviceability and Critical Cracking Parameters

5.6.1.1. Relationship between Cracking and Concrete Parameters

The relationship between cracking, strength, stiffness, and durability parameters, as well as the critical cracking values, are presented in this section. The methodology for generating regression equation coefficients is presented in Section 5.5.2.3.5. The methodology for validation of models is presented in Section 5.5.2.3.6.

Table 5.7 summarizes the mathematical relationships between strength, stiffness, and durability tests, and cracking parameters. For example, the first row in Table 4.5 provides the relationship between compressive strength and crack width, depth and index (Equation 5.8) and chloride diffusion coefficient and crack width, depth and index (Equation 5.9). The compressive strength reduces with an increase in crack width, depth and index as indicated by the negative coefficient values, while chloride diffusion coefficient increases as indicated by the positive coefficient values. The coefficients are empirically based on crack width (0–3175 µm), depth (0–50 mm), and index (0–156 mm/m), which have differing magnitudes; thus the magnitude of the coefficients does not indicate their relative importance in the model.

$$\text{Compressive Strength} = 93.64 - 0.0035 * W - 0.54 * D - 0.163 * I \quad \text{Equation 5.8}$$

$$\text{Chloride Diffusion Coefficient} = 5.29 + 0.0002 * W + 1.89 * D + 0.393 * I \quad \text{Equation 5.9}$$

Where,

W = Crack Width

D = Crack Depth

I = Cracking Index

Table 5.7: Quantification of Relationships between Cracking and Strength, Stiffness, and Durability Parameters

Parameter (y)	Coefficients for Equation 5.6 $y = c + x_w * W + x_d * D + x_i * I$				R ²	r	σ_{est}	SD _{avg}
	c	x _w	x _d	x _i				
Compressive Strength (CS)	93.64	-0.0035	-0.54	-0.163	0.86	0.71	3.70 MPa	0.41 MPa
Tensile Strength (TS)	4.38	-0.0002	-0.03	-0.006	0.88	0.70	0.23 MPa	0.10 MPa
Ultrasonic Pulse Velocity (UPV)*	11236	-0.3813	-62.43	-23.23	0.85	0.68	833 m/s	169 m/s
Modulus of Elasticity (MOE)	41.59	-0.0006	-0.04	-0.012	0.88	0.67	0.36 GPa	0.05 GPa
Bulk Resistivity (BR)*	32.06	-0.0028	-0.04	-0.017	0.93	0.73	1.05 kΩcm	0.52 kΩcm
Surface Resistivity (SR)*	12.63	-0.0009	-0.04	-0.013	0.93	0.76	0.87 kΩcm	0.39 kΩcm
Chloride Diffusion Coefficient (D _{nssm})	5.29	0.0002	1.89	0.0393	0.96	0.94	1.82 x 10 ⁻¹² m/s ²	0.93 x 10 ⁻¹² m/s ²
Carbonation Coefficient (K)	3.45	-0.0008	0.34	0.042	0.86	0.60	3.69 mm/yr ^{0.5}	0.54 mm/yr ^{0.5}
Notes:								
<ul style="list-style-type: none"> • Input Variables: W = Crack Width D = Crack Depth I = Cracking Index • c, x_w, x_d, and x_i are coefficients • Reliability Indicators: R² = Multiple Regression Coefficient r = Reliability Index σ_{est} = Standard Error of Estimate SD = Average Standard Deviation of experimental test values 								

5.6.1.2. Critical Cracking Values

Table 5.8 summarizes the serviceability cracking values. The table also shows the critical test parameter and the critical cracking values for the test parameter. Section 5.5.2.4 presents the methodology for calculating the serviceability cracking values. It also presents the methodology for determining the critical cracking parameter and the critical cracking values.

The chloride diffusion coefficient was determined to be the critical test parameter for cracking, as it had the lowest serviceability cracking values. The critical cracking values were determined as 100 μm for crack width, 7 mm for crack depth, and 0.018 mm/m for cracking index. The ACI 224R report on Control of Cracking in Concrete Structures provides an upper crack width limit of 250 μm (0.01 in.) for corrosion resistance and 0.41 mm (0.016 in.) for strength in dry conditions under service loads [21]. Other researchers have also calculated critical crack widths for corrosion resistance. Corina-Maria Aldea et al. (1999), Wang et al. (2016), Poursaeed and Hansson (2008), and Sahmaran (2007) calculated critical crack widths of 200 μm , 100 μm , 100 μm , and 135 μm for chloride permeability in high strength concretes respectively [34]–[36], [172].

A cracking index of 18 mm/m translates to 180 cracks with 100 μm width per meter length of concrete or four cracks with 0.004 in. width per inch of concrete.

Table 5.8: Calculated Serviceability Cracking Values

Test	Serviceability Test Values	Serviceability Cracking Values		
		Crack Width (μm)	Crack Depth (mm)	Cracking Index (mm/m)
STRENGTH TESTS				
Compressive Strength (CS)	57 MPa (8267 psi)	300	23	142
Tensile Strength (TS)	2 MPa (298 psi)	500	45	150
STIFFNESS TESTS				
Ultrasonic Pulse Velocity (UPV)*	4907 m/s	320	25	200
Modulus of Elasticity (MOE)	37.6 GPa (5.4×10^6 psi)	340	34	200
DURABILITY TESTS				
Bulk Resistivity (BR)*	18.2 k Ωcm	3000	50	202
Surface Resistivity (SR)*	6.23 k Ωcm	2650	40	202
Chloride Diffusion Coefficient (D_{nssm}) ⁺⁺	$17.8 \times 10^{-12} \text{ m}^2/\text{s}$	100 ⁺	7 ⁺	18 ⁺
Carbonation Coefficient (K)	8.3 mm/yr ^{0.5} (0.33 in./yr ^{0.5})	350	10	42
Notes: * Non-destructive test ++ Critical Test Parameter + Critical Cracking Values				

5.6.2. Empirical Model

An empirical model that can be used to predict the remaining service life of the low w/cm concrete girders with microcracking is presented in this section. The reliability of the model has also been presented using a time-delay study as well as data from an additional girder. The service life predicted by Life-365® has been reported. In addition, the service life predicted by chloride diffusion coefficient based model for cracked concrete developed by Kwon et al. (2009) and Pacheco (2019) was also calculated and reported [27], [151].

5.6.2.1. Generation of Empirical Model

The empirical model was generated with temporal data collected from 5 overcast girders and 8 in-service girders. This was supplemented with data from the accelerated weathering test conducted on specimens extracted from the overcast girders. The regression model generated is shown in Equation 5.10. The model had a regression coefficient of 0.77, which lies in the “Good” range.

$$y = - 8403 - 912 * a_1 - 1441 * a_2 + 29848 * a_3 + 0.20 * a_4 + 1330 * a_5$$

Equation 5.10

Where,

y = Age of specimens in days

a₁ = Effect of exposure expressed using a binary code. 0 for samples that were not exposed to the environment and 1 for samples exposed to environment.

a₂ = Effect of pre-existing cracks expressed using the cracking index of girders during the first field visit and the cracking index of accelerated weathering tests before the start of the test.

a₃ = w/cm used to account for variation in material composition.

a₄ = Ultrasonic pulse velocity used to account for variation in material composition.

a₅ = The cracking index observed during subsequent field visits, and at the end of each accelerated weathering test cycle was used.

5.6.2.2. Validation of Empirical Model

The generated model was validated using two sets of data, a time-delay study on two girders and observed data from an additional girder.

5.6.2.2.1. Time-Delay Study

The model was validated using a time-delay study by collecting data from two overcast girders. The model was used to calculate the predicted cracking index using Equation 5.11. Figure 5.3 shows the predicted vs. observed cracking indices from the fourth round of field visits conducted on girder 3R and 4R. The predicted and observed values had a high correlation coefficient of 0.92. The reliability index of the model was calculated to be 0.69 which lies in the “Moderate” range. The standard error of estimates was calculated to be 0.72 mm/m. The standard deviation of observed cracking index values was 0.82 mm/m. Thus, the model was found to have moderate to good reliability.

$$a_{5 \text{ predicted}} = \frac{y + 8403 + 912 * a_1 + 1441 * a_2 - 29848 * a_3 - 0.20 * a_4}{1330}$$

Equation 5.11

Where,

$a_{5 \text{ predicted}}$ = The predicted cracking index.

y = Age of specimens during the fourth field visit in days.

a_1 = Effect of exposure expressed using a binary code. 0 for samples that were not exposed to the environment and 1 for samples exposed to environment.

a_2 = Effect of pre-existing cracks expressed using the cracking index of girders during the first field visit.

a_3 = w/cm used to account for variation in material composition.

a_4 = Ultrasonic pulse velocity used to account for variation in material composition.

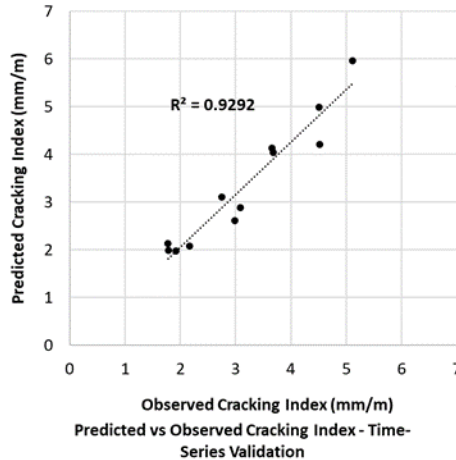


Figure 5.3: Predicted vs. observed cracking indices for Girders 3R and 4R from the fourth round of field visits

5.6.2.2.2. Validation Study on Additional Girder

A sixth overcast girder was selected to validate the study, and three field visits were conducted one year apart. The age of the girder during each field visit is known, and these values were compared to the values predicted using Equation 5.10. The observed values of exposure conditions, w/cm, ultrasonic pulse velocity, cracking index during the first field visit, and cracking index during the subsequent field visits were used to predict the age of the girder during each field visit. The reliability index of the model was calculated to be 0.76 which lies in the “Moderate” range. The standard error of estimates was calculated to be 359 days, a little less than one year. Thus, the model was found to have moderate to good reliability.

5.6.3. Calculation of Remaining Service Life of Girders

The service lives of the low w/cm concrete girders were calculated using the generated model. The service life was also calculated using Life-365® and two models for cracked concretes based on the chloride diffusion coefficient proposed by Kwon et al. (2009) and Pacheco (2019) [27], [151].

5.6.3.1. Empirical Model

The remaining service life of the girders monitored was calculated using the model generated. Equation 5.10 was used to calculate the expected service life of the girders, i.e., the amount of time taken to reach a critical cracking index value of 18 mm/m. Two exposure conditions were evaluated for each girder, exposed to environment and unexposed to environment. The average cracking index and ultrasonic pulse velocity of the girders measured during the first field visit were used as input variables, along with the w/cm. The results are presented in Table 5.9.

It is seen that the girders have between 50 and 62 years of service life remaining. It is also observed that a girder, when not exposed to the environment, will have around two and a half additional years of service life when compared to the same girder when exposed to the environment. As these girders are designed for a service life of 75 years, the present rate of growth in microcracking can reduce the service life of the in-service girders from 2 to 13 years depending on the girder and nature of cracking. On average, the service life reduction was 5 years considering all the girders examined in this study [12].

5.6.3.2. Life-365®

Table 5.10 presents the remaining service life as calculated using Life-365®. The input parameters were w/cm, girder dimensions, cover depth, and location. The remaining service life of girders ranged between 79 and 98 years. The remaining service life reduced to 54.1–64.3 years when the calculated diffusion coefficient was used as the input parameter instead of the default location.

Table 5.9: Remaining Service Life of Girders Calculated Using Model

Girder	Age (Days)	Exposure [#]	Pre-Existing Cracks (mm/m)	w/c	UPV (m/s)	Critical Cracking Index (mm/m) ⁺	Service Life*		Remaining Service Life**		Average Remaining Service Life (Years)
							Days	Years	Days	Years	
1R	2613	1	1.35	0.28	4736	18	22015	60.3	19402	53.2	54.45
		0					22927	62.8	20314	55.7	
2R	2554	1	1.62	0.28	5120	18	21705	59.5	19151	52.5	53.75
		0					22617	62	20063	55	
3R	2012	1	3.04	0.3	3147	18	19852	54.4	17840	48.9	50.15
		0					20764	56.9	18752	51.4	
4R	2498	1	1.93	0.3	5793	18	21993	60.3	19495	53.4	54.65
		0					22905	62.8	20407	55.9	
5RC	3512	1	0.74	0.28	4527	18	22852	62.6	19340	53	54.25
		0					23764	65.1	20252	55.5	
6I	3508	1	0.35	0.36	4883	18	25874	70.9	22366	61.3	62.55
		0					26786	73.4	23278	63.8	
7I	4357	1	0.18	0.36	4496	18	26040	71.3	21683	59.4	60.65
		0					26952	73.8	22595	61.9	
8I	3508	1	1.1	0.36	5686	18	24958	68.4	21450	58.8	60.05
		0					25870	70.9	22362	61.3	
9I	3508	1	0.33	0.36	5131	18	25954	71.1	22446	61.5	62.75
		0					26866	73.6	23358	64	
10I	4357	1	1.11	0.36	4234	18	24646	67.5	20289	55.6	56.85
		0					25558	70	21201	58.1	
11I	4357	1	0.86	0.36	4068	18	24973	68.4	20616	56.5	57.75

Girder	Age (Days)	Exposure [#]	Pre-Existing Cracks (mm/m)	w/c	UPV (m/s)	Critical Cracking Index (mm/m) ⁺	Service Life*		Remaining Service Life**		Average Remaining Service Life (Years)
							Days	Years	Days	Years	
		0									
12IC	3508	1	2.37	0.36	4913	18	22970	62.9	19462	53.3	54.55
		0					23882	65.4	20374	55.8	
13IC	4357	1	0.75	0.36	3944	18	25106	68.8	20749	56.8	58.05
		0					26018	71.3	21661	59.3	
14V	1291	1	1.62	0.31	3454	18	22259	61	20968	57.4	58.65
		0					23172	63.5	21881	59.9	

Note:
#1 = Exposed, 0=Unexposed
+ Critical Cracking Index based on chloride diffusion coefficient (See Section 5.5.2.3.5)
* Service life predicted using Equation 5.10
** Remaining Service Life = Service Life – Age of Girders

Kwon et al. (2009) and Pacheco (2019) proposed models for calculating service life using a modified diffusion coefficient for cracked concrete. The diffusion coefficients obtained were used to calculate the service life using Life-365®. Table 5.11 presents the remaining service life predicted using the modified diffusion coefficient. Equation 5.4 shows the model proposed by Kwon et al. (2009). The model uses observed crack width and serviceability crack width to account for the effect of cracking [27]. The observed average crack width and diffusion coefficient during the first field visit was used. The serviceability crack width was calculated as 100 µm (0.1mm). The remaining service life ranged between 54.1 and 64.3 years. Equation 5.5 shows the model proposed by Pacheco (2019). The model uses observed crack width and serviceability crack width to account for the effect of cracking [151]. The observed average crack width and diffusion coefficient during the first field visit were used. The serviceability crack width was calculated as 100 µm (0.1mm). The remaining service life ranged between 54.0 and 64.2 years.

The remaining service life of the girders as predicted by Life-365® was similar to that predicted by the Kwon et al. (2009) and the Pacheco (2019) models, with Kwon’s model predicting the same service life and Pacheco’s model showing only a slight reduction. This showed that both modified diffusion coefficient models proposed by Kwon et al. (2009) and Pacheco (2019) were not sensitive enough to reflect the behavior of microcracks.

The empirical model under-predicted service life for all the girders by about 4 to 10 years, when compared to the Life-365®. This behavior is shown in Figure 5.4

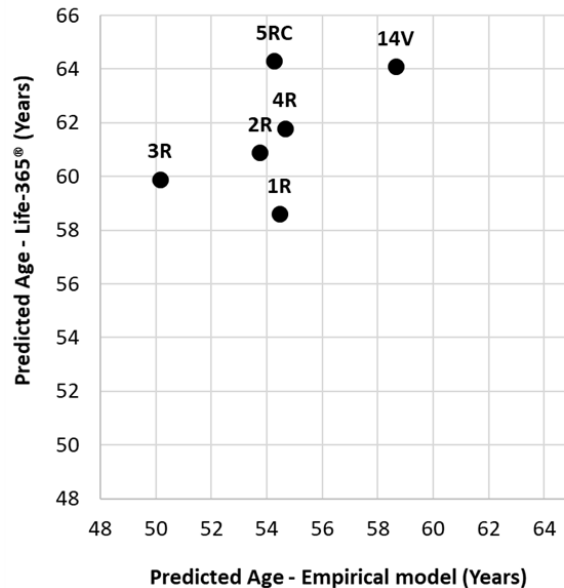


Figure 5.4: Comparison of predicted age of girders using Life-365® and empirical models

Table 5.10: Remaining Service Life Calculated using Life-365®

Girder	w/cm ratio	Dimensions mm (in.)	Cover mm (in.)	Age (years)	Actual Location	Location (Rural Bridge)	Life-365® - Location		Diffusion Coefficient x10-12 m2/s (x10-9 in2/s)	Life-365® - Diffusion	
							Service Life (Years)	Remaining Service Life (years)*		Service Life (Years)	Remaining Service Life (years)*
1R	0.28	200 (8)	50 (2)	7.2	Eagle Lake	Houston	102	94.8	10.47 (16.2)	65.8	58.6
2R	0.28	200 (8)	50 (2)	7	Waco	Dallas	105.7	98.7	10.45 (16.2)	67.9	60.9
3R	0.3	175 (7)	50 (2)	5.5	San Antonio	San Antonio	97.6	92.1	10.43 (16.2)	65.4	59.9
4R	0.3	200 (8)	50 (2)	6.8	Eagle lake	Houston	98.5	91.7	9.14 (14.2)	68.6	61.8
5RC	0.28	175 (7)	50 (2)	9.6	Victoria	Houston	102	92.4	7.18 (11.1)	73.9	64.3
6I, 8I, 9I, 12IC	0.36	200 (8)	50 (2)	11.9	Dallas	Dallas	91.8	79.9	-	-	-
7I, 10I, 11I, 13IC	0.36	200 (8)	50 (2)	9.6	Texarkana	Dallas	91.8	82.2	-	-	-
14V	0.31	200 (8)	50 (2)	3.5	San Marcos	Austin	95.8	92.3	10.89 (16.8)	67.6	64.1

Note:
* Remaining Service Life = Service Life – Age of Girders

Table 5.11: Remaining Service Life Calculated using Modified Diffusion Coefficient for Cracked Concrete

Girder	Age (years)	D ₀ x10-12 m2/s (x10-9 in2/s)	Kwon et al. (2009)					Pacheco (2019)			
			w (mm)	Crack Density (w/l)	D _{cr} x10-12 m2/s (x10-9 in2/s) +	Service Life (Years)	Remaining Service Life (years)*	w _k (mm)	D _{cr} x10-12 m2/s (x10-9 in2/s) ++	Service Life (Years)	Remaining Service Life (years)*
1R	7.2	10.47 (16.2)	0.0006	10.3E-5	10.47 (16.2)	65.8	58.6	0.0006	10.54 (16.34)	65.7	58.5
2R	7	10.45 (16.2)	0.0006	8.0E-5	10.45 (16.2)	67.9	60.9	0.0006	10.51 (16.29)	67.8	60.8
3R	5.5	10.43 (16.2)	0.0007	15E-5	10.43 (16.2)	65.4	59.9	0.0007	10.51 (16.29)	65.3	59.8
4R	6.8	9.14 (14.2)	0.0005	4.5E-05	9.14 (14.2)	68.6	61.8	0.0005	9.19 (14.24)	68.5	61.7
5RC	9.6	7.18 (11.1)	0.0006	7.5E-05	7.18 (11.1)	73.9	64.3	0.0006	7.22 (11.19)	73.8	64.2
14V	3.5	10.89 (16.8)	0.0006	6.7E-05	10.89 (16.8)	67.6	64.1	0.0006	10.99 (16.83)	67.5	63.9

Note:
* Remaining Service Life = Service Life – Age of Girders
+ Diffusion Coefficient as calculated by Equation 5.4, w_a = 0.1 mm, D₀ = Diffusion coefficient of sound concrete
++ Diffusion Coefficient as calculated by Equation 5.5, w_{limit} = 0.1 mm, D₀ = Diffusion coefficient of sound concrete

5.7. Conclusions

The conclusions of Task 4 are presented in the following sections. The first section summarizes the conclusions of the study conducted on the embedded crack specimens to estimate the serviceability and critical cracking parameters. The second section summarizes the conclusions drawn from the model generated and the results of the validation study.

5.7.1. Serviceability and Critical Cracking Parameters

This research work was conducted to empirically quantify the relationship between cracking parameters (width, depth, and index/density) on the strength, stiffness, and durability properties of low w/cm concrete mixes and determine the critical cracking values. The following conclusions were drawn:

- Strength, as calculated by compressive and tensile strength, reduced with increasing crack width, depth, and index.
- Stiffness, as calculated by ultrasonic pulse velocity and modulus of elasticity, reduced with increasing crack width, depth, and index.
- Durability reduced with increasing crack width, depth, and index as indicated by.
 - o Decreased bulk and surface resistivity
 - o Increased chloride diffusion coefficient and carbonation coefficient
- The relationship between each test parameter and the cracking parameters was modeled using multiple linear regression. The models had high multiple regression coefficients ranging from 0.85 to 0.96.
- Each model was validated by comparing experimental test values to the predicted test values. The reliability index of the models ranged from moderate to excellent, with values from 0.60 to 0.94.
- The standard error of estimate for each test parameter was also calculated and determined to be under permissible limits (see Table 5.7).
- The serviceability cracking parameters for each strength, stiffness, and durability test parameter were calculated (see Table 5.8).
- The critical test parameter was determined to be the chloride diffusion coefficient, and the critical cracking values were calculated as:
 - o Critical Crack Width = 100 μm

- o Critical Crack Depth = 5 mm
- o Critical Cracking Index = 18 mm/m
- A cracking index of 0.018 mm/m translates to 180 cracks with 100 μm width per meter length of concrete or four cracks with 0.004 in. width per inch of concrete

5.7.2. Prediction of Remaining Service Life of Girders

This research work was conducted to generate an empirical model that can be used to predict the remaining service life of the low w/cm concrete girders with microcracking. The following conclusions were drawn:

- An empirical model was generated with temporal data collected from 5 overcast girders and 8 in-service girders. This was supplemented with data from the accelerated weathering test conducted on specimens extracted from the overcast girders. The model had a regression coefficient of 0.77, which lies in the “Good” range.
- The model was validated and found to have moderate to good reliability:
 - o A time-delay study by collecting data from two overcast girders. The predicted and observed values had a high correlation coefficient of 0.92. The reliability index of the model was calculated to be 0.76, which lies in the “Moderate” range. The standard error of estimates was calculated to be 0.72 mm/m. The standard deviation of observed cracking index values was 0.82 mm/m.
 - o A sixth overcast girder was selected to validate the study, and three field visits were conducted one year apart. The reliability index of the model was calculated to be 0.74, which lies in the “Moderate” range. The standard error of estimates was calculated to be 359 days, a little less than one year.
- The service lives of the low w/cm concrete girders were calculated using the generated model. The service life was also calculated using Life-365® and two models for cracked concretes based on the chloride diffusion coefficient proposed by Kwon et al. (2009) and Pacheco (2019) [27], [151].
 - o The remaining service life of the girders, i.e., the amount of time taken to reach a critical cracking index value of 18 mm/m, was calculated using the model generated. It was seen that the girders have between 50 and 62 years of service life remaining. It was also observed that, on average, a girder, when not exposed to the environment, would have around two

additional years of service life when compared to the same girder when exposed to the environment.

- o The remaining service life of the girders as calculated using Life-365® ranged between 54.1 and 64.3 years.
- o Kwon et al. (2009) and Pacheco (2019) proposed models for calculating service life using a modified diffusion coefficient for cracked concrete. The diffusion coefficients obtained were used to calculate the service life using Life-365®.
 - Kwon et al. (2009): 54.1 and 64.3 years.
 - Pacheco (2019): 54.0 and 64.2 years.
- o The remaining service life of the girders as predicted by the Life-365® was similar to that predicted by the Kwon et al. (2009) and Pacheco (2019) models. This showed that the two modified models were not sensitive enough to account for the behavior of microcracking. The empirical model under-predicted service life for all girders by 4 to 10 years when compared to Life-365®.

As these girders are designed for a service life of 75 years, the present rate of growth in microcracking can reduce the service life of the in-service girders from 2 to 13 years depending on the girder and nature of cracking. On average, the service life reduction was 5 years considering all the girders examined in this study. Further reduction in service life is also possible under fatigue loading as the girders age. Thus, continuous monitoring of the girders, especially in the last two decades of the girder's lives is recommended.

Chapter 6. Marine Simulation Testing

6.1. Overview of Chapter

This chapter discusses the activities undertaken under Task 5: Marine Simulation Testing. To accomplish this task, a marine simulation tank was set-up to simulate in-service marine exposure conditions. Three concrete blocks with embedded prestressing strands were cast with a mixture that exhibited cracking at a relatively early age. Each block had three distinct exposure zones- submerged, splash and unexposed zones. One block (A) was placed in the simulation tank after 28 days of curing, the second block (B) was exposed to the environment until it exhibited adequate cracking and was then placed in the marine simulation tank, and the last block (C) will perform as a control specimen and was placed indoor and not exposed to the environment. Weekly half-cell potential and monthly surface resistivity measurements were taken. Block A underwent 2000 cycles of wetting and drying, and Block B underwent 348 cycles.

Block A exhibited corrosion-induced cracking in the splash zone (cracking index of 0.047 in./yd) after 7 months of exposure. At the end of 14 months, the block began to exhibit corrosion-induced microcracking in the region between the splash zone and unexposed zone (cracking index of 0.015 in./yd). Block B exhibited a cracking index of 0.01 in./yd (visual rating of 1.5) at the end of 24 months of environmental exposure. Block C did not exhibit any cracking over the testing period.

Block A exhibited corrosion-induced cracking in the splash zone within 7 months of marine simulation and in the region between splash and unexposed zones within 24 months of marine simulation. Block B was showed adequate surface microcracking after 24 months of exposure to the environment and was placed in the marine simulation tank. Both blocks showed a greater change in resistivity and half-cell potential in the splash zone, followed by the unexposed zone. The submerged zone did not show any significant changes. Block C did not show any significant change in resistivity or half-cell potential. None of the blocks have reached serviceability conditions for surface resistivity yet. Block A showed increasing levels of corrosion potential after 8.2 months of marine simulation and higher than 90% corrosion potential after 24 months of marine exposure. Block B showed increasing levels of corrosion potential after 1.7 months of marine simulation. Block C has shown corrosion potential of under 10%.

6.2. Objective

The goal of this task was to study the effects of marine exposure on low w/cm concretes with surface microcracks.

6.3. Background

Corrosion of embedded steel in concrete is prevented by a passive layer that is formed around the steel when in the presence of an alkaline environment. This passive layer can break down in the presence of chlorides or acidic environments. Thus, exposure to the marine environment can increase the rate of corrosion and thereby reduce the service life. To prevent the chloride ions or acidic environment from reaching the steel adequate concrete cover is provided. This, loss in service life can be further exacerbated when the concrete cover is cracked as cracks allow easier access to chlorides and other deleterious materials [40].

The effect of aggressive environments on corrosion of cracked concrete has been studied by researchers extensively. Ramezani pour et al. (2018) reported critical crack widths between 0.03 mm to 0.3 mm for concrete exposed to a marine environment for a single crack. They also showed that increasing the crack width to cover ratio increased the probability of rebar corrosion. It was observed that the increase of crack width to cover ratio led to a reduction in electrical resistivity and half-cell potential [173]. Shao and Li (2014) showed that the growth rate of chloride concentration increased with an increase in the width of a single crack, indicating that increasing crack width from 0 μm to 300 μm reduced the service life of reinforced concrete pipes in a marine environment reduced from 70.6 years to 52.5 years [174]. Jaffer and Hansson (2008) showed that in over 18 months of exposure to salt solution, corrosion occurred only at the cracks in reinforced concrete specimens. Further loss in re-bar cross-section was expected at the cracks before corrosion initiated in the uncracked regions. The corrosion was twice as high in the cracked unexposed areas of the test beam when compared to the uncracked submerged regions. A significantly greater loss of the cross-section of rebars occurred at the cracks than that predicted by calculation from the current densities based on either the polarized area or the areas covered by corrosion products [175].

The effect of finer microcracks on the behavior of concretes under marine exposure has also been studied by researchers. Yoon and Schlangen (2013) also showed that critical crack widths for chloride exposure were lower than previously estimated values of 0.04 mm, with specimens with a single crack exhibiting higher chloride diffusion coefficients when compared to uncracked specimens [37]. Kobayashi and Kojima (2017) also showed that concrete specimens with multiple fine cracks with widths ranging from 0.01 to 0.6 mm and higher crack densities had higher chloride ingress and rebar corrosion when compared to sound concrete specimens [176]. Lopez-Calvo et al. (2018) showed that cracking was found to be an influencing factor in promoting corrosion of the steel in concrete. In samples with 25 mm concrete cover, even a single crack with width as small as 90 μm , showed corrosion activity after only one year of exposure. Specimens with a wider crack showed higher levels of corrosion activity. In concrete specimens with a cover of 45 mm

cracks with width of 200 μm and wider showed certain corrosion activity along the testing period [177].

6.4. Materials and Methods

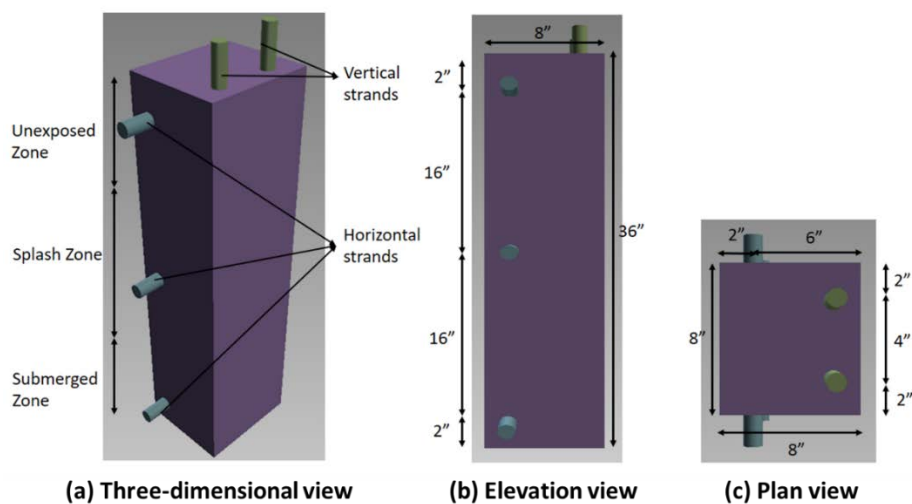
A specimen was designed to determine the effect of microcracking on the corrosion behavior of the low water cement ratio concrete girders under marine conditions. The specimen was subjected to marine simulation, and weekly measurements were taken to determine the change in cracking and corrosion potential.

6.4.1. Block Design

A marine block was designed with the goal of mimicking a girder specimen undergoing marine exposure. This was done by creating clearly defined zones on the concrete block to accurately simulate in-service marine exposure conditions. Figure 6.1 shows the schematics of the reinforced concrete block. The block was divided into three distinct exposure zones:

- Submerged zone
- Splash zone (alternate wetting and drying)
- Unexposed zones.

The block was reinforced with five pre-stressing strands, two vertical bars running across the entire height of the blocks, and three horizontal bars with a 2-inch cover, one in each exposure zone. The selection of mix proportions is discussed in Section 5.5.2.3.2. The mixture proportions are provided in Table 5.1.



Source: Images by Authors

Figure 6.1: Schematics of marine exposure blocks (a) 3-d, (b) elevation and (c) plan views showing the placement of pre-stressing strands

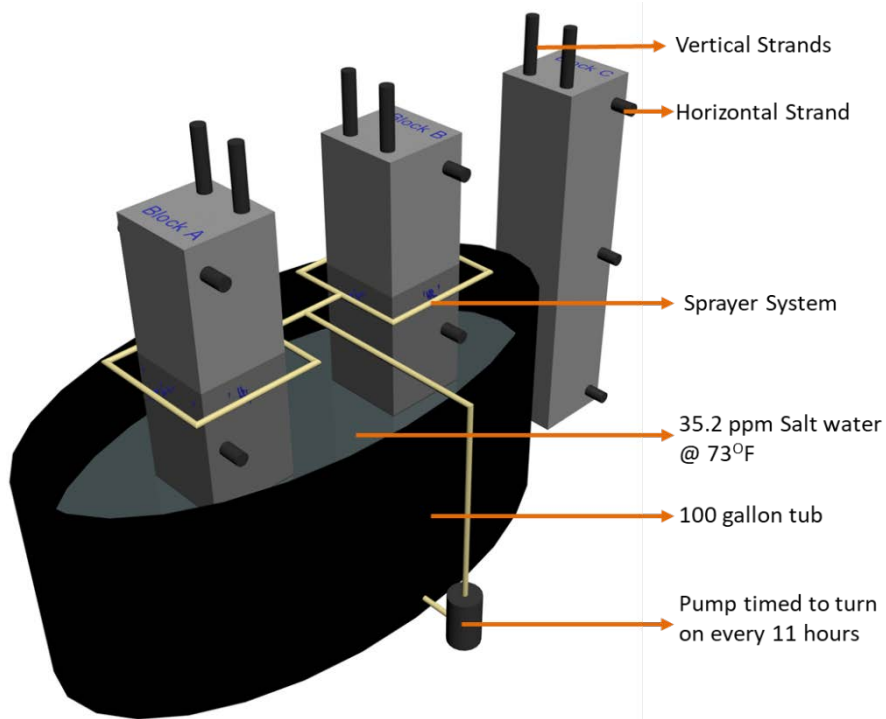
6.4.2. Marine Simulation Tank

Figure 6.2 shows the marine simulation tank set-up. A 100-gallon plastic tub was filled with 50 gallons of saltwater at 35.2 ppm concentration (simulating salt-water concentration at UT marine exposure site at Port Aransas [178]). A PVC piping system was designed and set-up to spray the salt-water over the surface of the concrete block. The spray system was placed on a timer to spray saltwater on the surface of the block intermittently. Experimental tests were conducted to determine the time for surface drying, as this would allow for increased salt saturation. Surface drying was found to occur at 11 hours. Thus, the timer was set to spray the surface of the block for thirty minutes every twelve hours. Three identical blocks were cast and subjected to the following exposure conditions (see Figure 6.2):

- Block A - Placed in the marine simulation tank after 28 days of curing.
- Block B - Exposed to the atmosphere after 28 days of curing until the block exhibited surface microcracking. The block did not show signs of adequate surface microcracking with just exposure to the environment. Thus, to accelerate the cracking, the block was exposed to accelerated weathering by subjecting the block to four cycles of surface wetting and drying each day. The surface of the block was saturated with water for five minutes and allowed to dry for six hours.
- Block C – Placed indoors at 73°F to perform as a control specimen.



(a) Marine Exposure Tank



(b) Schematics of Marine Exposure Tank

Source: Images by Authors

Figure 6.2: (a) Marine exposure tank and (b) schematics of setup

6.4.3. Experimental Methods

Cracking and corrosion potential of all three blocks was measured. Cracking measurements were observed each week visually, and the cracking index was measured each month. The corrosion potential was measured each week.

6.4.3.1. Measurement of Cracking

Cracking was monitored by placing a 100 x 100 mm (4x4 in.) crack grid and measuring the growth in cracking. The cracking index and average crack width were calculated according to the method detailed in the FHWA HIF-09004 report [19]. In addition, visual observation was used. A visual scale developed by the performing agency in a previous study was also used to observe the change in cracking (see Figure 6.3).

This visual scale was converted to an equivalent cracking index value (see Figure 6.4). This scale was used to determine the time at which Block B exhibited adequate surface microcracking, so it could be placed in marine simulation and to monitor the growth in the splash zone cracking in Block A.

6.4.3.2. Measurement of Corrosion Potential

Change in corrosion potential was measured by half-cell potential and resistivity measurements. A copper-copper sulfate standard electrode was used to measure the half-cell potential in accordance with the *ASTM C876 - Standard test method for half-cell potentials of uncoated reinforcing steel in concrete* [179].

Surface resistivity was measured according to *AASHTO TP358– Standard Method of Test for Surface Resistivity Indication of Concrete’s Ability to Resist Chloride Ion Penetration* [21] with a Reispod Proceq™ Wenner probe.



Visual Rating - 0



Cracking Index - 0



Visual Rating - 1



Cracking Index - 0.003 in/yd



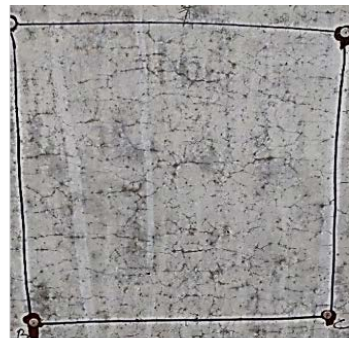
Visual Rating - 2



Cracking Index - 0.025 in/yd



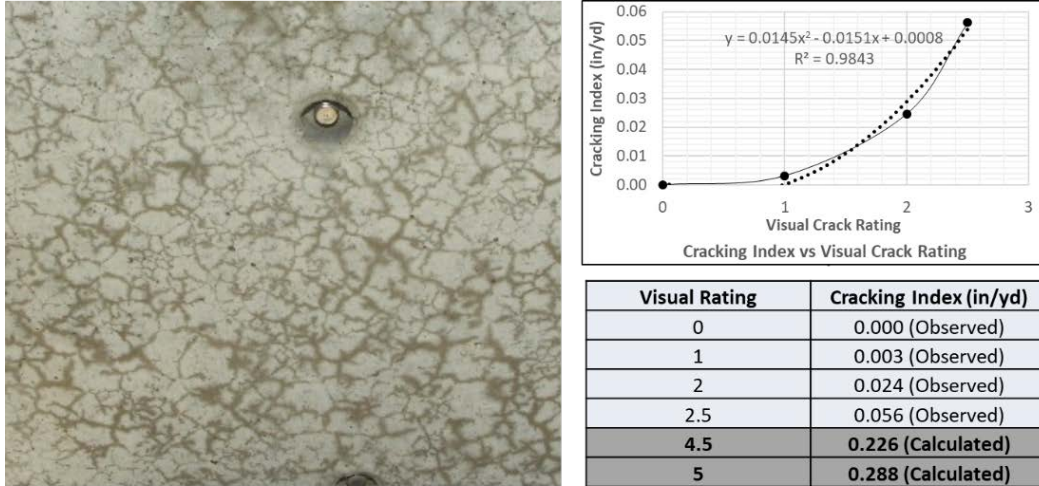
Visual Rating - 2.5



Cracking Index - 0.056 in/yd

Source: Images by Authors

Figure 6.3 Visual rating index vs. cracking index



Visual Rating – 4.5

Calculated Cracking Index – 0.23 in/yd

Source: Images by Authors

Figure 6.4: Relationship between visual rating index and cracking index

6.5. Results and Discussions

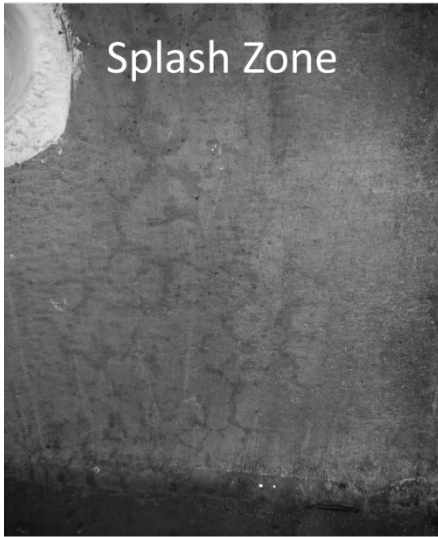
The change in cracking and corrosion potential of the three blocks is reported in this section. Block A underwent 2000 cycles of wetting and drying, Block B underwent 348 cycles, and Block C underwent 0 cycles.

6.5.1. Growth of Cracking

Block A exhibited corrosion-induced microcracking in the splash zone after 7 months of exposure. At the end of 14 months, the block began to exhibit corrosion-induced microcracking in the region between the splash zone (cracking index of 0.047 in./yd) and unexposed zone (cracking index of 0.015 in./yd) as well (see Figure 6.5a and Figure 6.5b). Figure 6.5c shows the same figures with the microcracks highlighted to aid viewability. An additional set of readings were taken in this intermediate zone as well for the remainder of the testing period.

Block B exhibited initial signs of surface microcracking after exposure to the environment for 10 months. To accelerate the rate of cracking, the block was subjected to accelerated weathering for 14 months. At the end of 24 months, Block B had a cracking index of 0.01 in./yd (visual rating of 1.5) (see Figure 6.6). This was deemed as adequate surface microcracking, and the block was placed in the marine simulation tank.

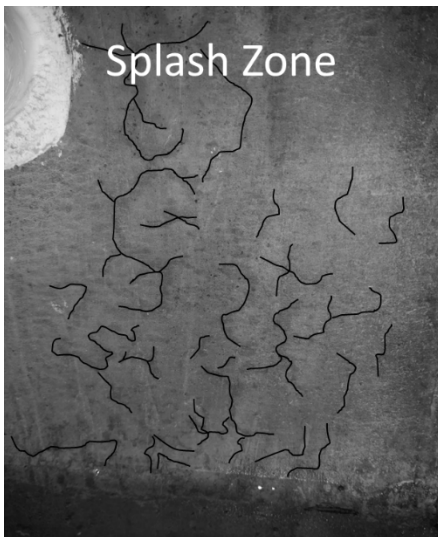
Block C, the block that was not placed in the marine environment, did not display any significant cracking over the testing period.



CI-0.047 in/yd, VRI-2
(a) Splash Zone



CI-0.015 in/yd, VRI- 1.5)
(b) Cracking in area between Unexposed and Splash Zones



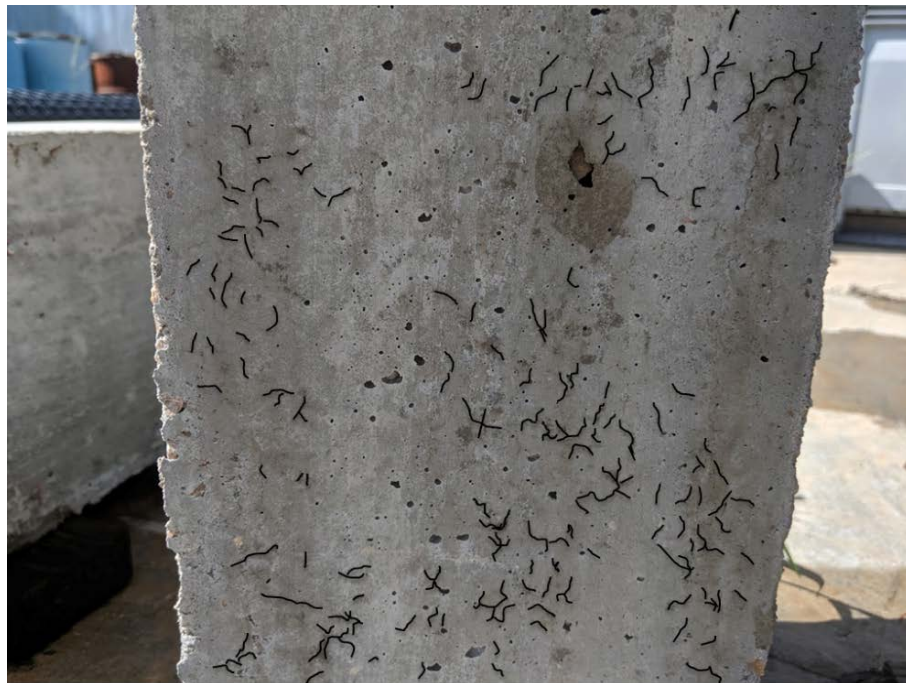
(c) Highlighted Microcracks

Source: Images by Authors

Figure 6.5: Corrosion-induced microcracking in Block A in the (a) splash and (b) unexposed zones with (c) highlighted cracks, where CI is the cracking index and VRI is the Visual Rating Index



(a) Cracking Index - 0.01 in/yd (Visual Rating – 1.5)



(b) Highlighted Microcracks

Source: Images by Authors

Figure 6.6: (a) Microcracking in block B with (b) highlighted microcracks

6.5.2. Corrosion Potential

The change in corrosion potential was determined from monthly surface resistivity readings and weekly half-cell potential measurements for each pre-stressing strand in each zone.

6.5.2.1. Change in Surface Resistivity

The surface resistivity of the blocks was measured every month in the exposed and splash zones. As the submerged zone was underwater, the measurement of surface resistivity was not possible as the salt-water interfere with the resistivity values.

Blocks A and B showed an almost immediate loss in resistivity as soon as marine simulation started, as shown in Figure 6.7a and Figure 6.7b. Block A showed a steady loss in resistivity after exposure began in both the unexposed and splash zones. The splash zone showed a greater loss in resistivity when compared to the unexposed zone. This can be attributed to the higher degree of saturation. It was seen that the onset of the surface microcracking in the splash and the unexposed zones of the block did not show any significant effect on the loss in resistivity (see Figure 6.7a).

Block B showed a gradual loss in resistivity with exposure to the external environment. The rate of loss increased under accelerated weathering. The appearance of surface microcracks did not show a noticeable effect on the loss in resistivity. When placed in the marine tank, the block exhibited an immediate drop in the surface resistivity, followed by a gradual loss with further exposure (see Figure 6.7b).

Block C did not show any significant changes in the surface resistivity over the monitoring period (see Figure 6.7c).

None of the blocks have reached serviceability of the surface resistivity value of 5 to 7.5 k Ω cm [66], [106] yet. The unexposed zone and splash zone of Block A has surface resistivity values of 43 k Ω cm and 21 k Ω cm at the end of the test. Figure 6.7c shows the serviceability value for surface resistivity.

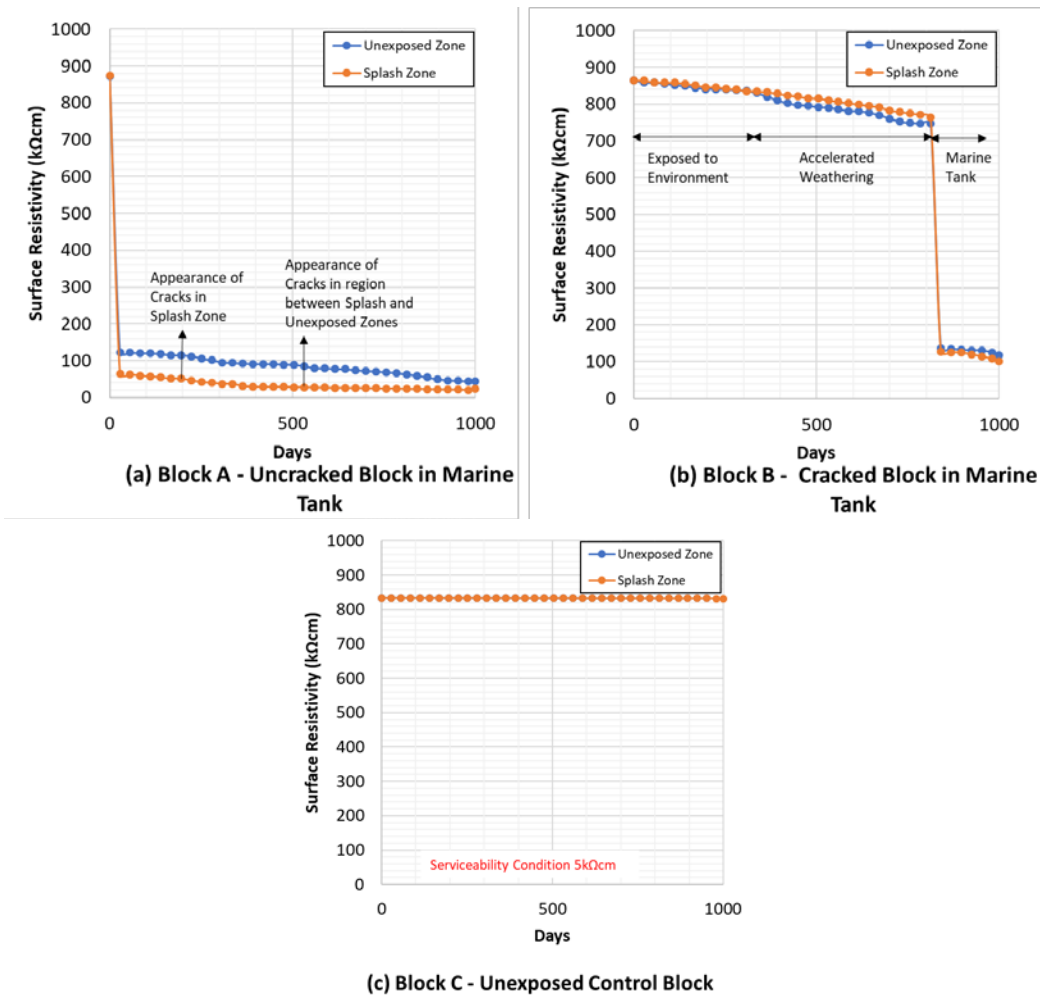


Figure 6.7: Surface resistivity of blocks

6.5.2.2. Change in Half-Cell Potential

Half-cell potential measurements were taken each week for all five pre-stressing strands, 2 vertical strands, and 3 horizontal strands in each zone in each girder. The surface of the blocks was sprayed with water before the measurements were taken. The three zones on the vertical strands displayed similar behavior when compared to the three horizontal strands in each block. Thus, the results of the horizontal strands are provided to avoid redundancies.

Block A showed an immediate change in the half-cell potential values after being exposed to marine simulation. The splash zone showed the greatest change, followed by the unexposed zone. The submerged zone did not show a significant change during the monitoring period. The splash zone showed an increase in the rate of change of half-cell potential values after the appearance of surface microcracks and an even greater rate of loss after the appearance of microcracks in the intermediate region between splash and unexposed zones. The effect of the microcracks in the intermediate zone are also observed in the rate of change of half-

cell potential values of the unexposed zone (see Figure 6.8a). This showed that the corrosion-induced microcracks were increasing the corrosion potential of the blocks.

Block B exhibited a change in half-cell potential when exposed to the environment. The rate of change increased when the block was subjected to accelerated weathering. The block was placed in the marine tank, and the rate of change increased and was comparable to the values seen in Block A at the same amount of exposure (see Figure 6.8a and Figure 6.8b). This showed that the presence of initial microcracking in the block did not significantly impact the initial rate of change of the corrosion potential. This can, however, change as the corrosion-induced cracking can be exacerbated by the presence of the initial microcracking. Comparing the final levels of cracking and the change in half-cell potential of the two blocks will provide a greater understanding of the effect of microcracking on the loss in corrosion potential.

Block C did not exhibit a significant change in the half-cell potential over the monitoring period (see Figure 6.8c).

The unexposed and splash zones of Block A have half-cell potential values less than -350mV, which corresponds to 90% likelihood of corrosion. The unexposed and splash zones on Block B have half-cell potential values between -200 and -350 mV which indicates that corrosion is increasing. Block C has half-cell potential values over -200 mV, which indicates that the chances of corrosion are under 10% [179]. Figure 6.8c shows the serviceability values for half-cell potential.

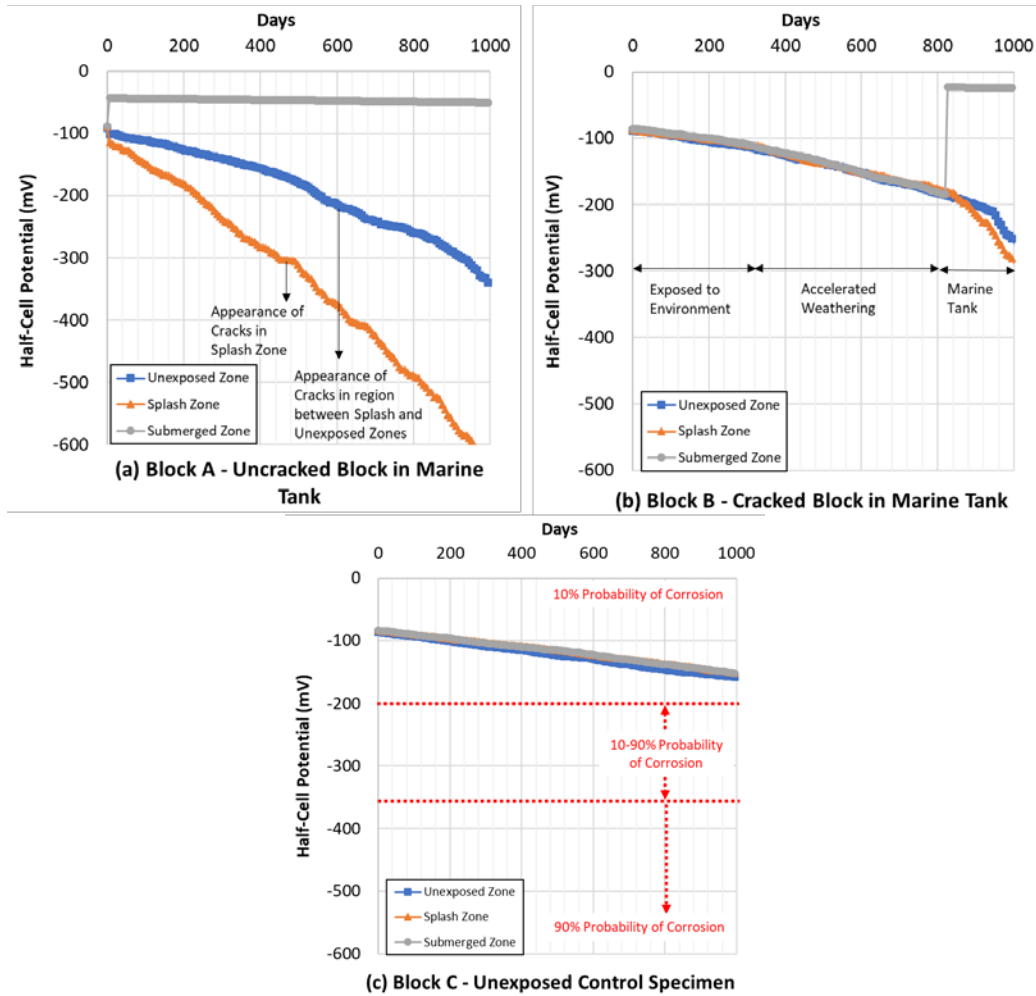


Figure 6.8: Half-cell potential of blocks

6.6. Conclusions

The conclusions of Task 5 are presented in this section. The change in cracking and corrosion potential of low w/cm concretes with surface microcracking under marine exposure was observed. Three blocks were cast with embedded pre-stressing strands to mimic the real-world conditions of a typical girder. Block A was exposed to the marine environment 28 days after casting, Block B was exposed to marine environment after it exhibited adequate surface microcracking, and Block C performed as a control specimen and was not exposed to the environment. Marine simulation consisted of one unexposed zone, one splash zone that underwent two cycles of exposure to salt-water each day followed by drying, and a submerged zone that was permanently under the waterline. As of December 31st, 2019, Block A underwent 2000 cycles of wetting and drying, and Block B underwent 348 cycles. The following conclusions were drawn from the study:

- Growth in cracking:

- o Block A exhibited corrosion-induced cracking in the splash zone (cracking index of 0.047 in./yd) after 7 months of exposure. At the end of 14 months, the block began to exhibit corrosion-induced microcracking in the region between the splash zone and unexposed zone (cracking index of 0.015 in./yd).
- o Block B exhibited a cracking index of 0.01 in./yd (visual rating of 1.5) at the end of 24 months of environmental exposure, 14 of which were under accelerated weathering conditions.
- o Block C did not exhibit any cracking over the testing period.
- Change in surface resistivity:
 - o Block A showed a steady loss in resistivity after exposure began in both the unexposed and splash zones. The splash zone showed a greater loss in resistivity when compared to the unexposed zone.
 - o Block B showed a gradual loss in resistivity with exposure to the external environment. The rate of loss increased under accelerated weathering. When placed in the marine tank, the block exhibited an immediate drop in the surface resistivity, followed by a gradual loss with further exposure.
 - o Block C did not show any significant changes in the surface resistivity over the monitoring period.
 - o It was seen that the onset of the corrosion-induced microcracking in the splash and the unexposed zones of Block A and the presence of microcracks in Block B did not show any significant effect on the loss in resistivity.
 - o None of the blocks have reached serviceability for surface resistivity, i.e., a value of 5 to 7.5 k Ω cm [66], [106] yet.
- Change in half cell potential
 - o Block A showed an immediate change in the half-cell potential values after being exposed to marine simulation. The splash zone showed the greatest change, followed by the unexposed zone. The submerged zone did not show a significant change during the monitoring period.
 - o Block B exhibited a change in half-cell potential when exposed to the environment. The rate of change increased when the block was subjected to accelerated weathering. The block was placed in the marine tank, and

the rate of change increased and was comparable to the values seen in Block A at the same amount of exposure

- o Block C did not exhibit a significant change in the half-cell potential over the monitoring period.
- o The corrosion-induced microcracks were increasing the corrosion potential of Block A. However, the presence of initial microcracking in Block B did not significantly impact the initial rate of change of the corrosion potential. This can, however, change as the corrosion-induced cracking can be exacerbated by the presence of the initial microcracking. Comparing the final levels of cracking and the change in half-cell potential of the two blocks will provide a greater understanding of the effect of microcracking on the loss in corrosion potential.

Chapter 7. Monitoring Corrosion of Prestressing Strands

7.1. Overview of Chapter

This chapter presents the activities conducted under Task 6: Monitoring Corrosion of Prestressing Strands. In this task, the research team examined the suitability of a monitoring system based on guided ultrasonic waves (GUWs) for detecting the initiation and growth of corrosion damage in prestressed concrete beams. The proposed monitoring system was based on low profile piezoelectric transducers, which have the capability of transmitting and receiving GUWs to interrogate corrosion progression. The research team designed and constructed experimental setups to investigate the relationship between GUV signals and corrosion damage characteristics, such as loss of prestress and fractured wires. The monitoring system can operate in two modes: (1) In its first (passive) mode, the system continuously monitors the strand and the progress of corrosion; (2) In the second (active) mode, the system is activated for periodically scheduled inspections. After developing the setup, the research team carried out a set of experiments that focused on testing the corrosion damage in strands embedded in concrete, as well as un-embedded strands.

7.2. Objectives

The main objective of Task 6 was to develop a diagnostic technique to capture initiation and growth of corrosion damage in prestressed concrete beams.

7.3. Overview of Monitoring System and Testing Approach

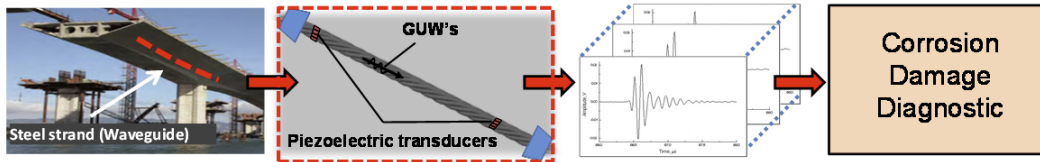
The overall procedure that the research team followed is summarized in Figure 7.1. Piezoelectric transducers were embedded on prestressed strand and concrete specimens to generate and receive GUWs. The research team developed analytical models and data processing techniques to process the GUV measurements and eventually diagnose the corrosion damage.

After developing the GUV based monitoring system setup, the research team carried out three sets of experiments:

1. The first set of experiments consisted of active GUV measurements performed on a pristine strand at different prestress levels.
2. For the second set, accelerated corrosion tests were carried out on a free prestressed strand (i.e., unbonded strand) while collecting active GUV measurements.

- Finally, for the third set, the research team carried out accelerated corrosion tests on a prestressed strand embedded in a concrete block (i.e., bonded strand) while collecting passive ultrasonic measurements. The first block was tested before the appearance of microcracks and the second block was tested after being subjected to accelerated weathering to induce microcracks.

The research team applied the accelerated corrosion tests in Experiments #2 and 3 through an electrochemical process based on *ASTM F2832—Standard Guide for Accelerated Corrosion Testing for Mechanical Fasteners* [180].



Source: Images by Authors

Figure 7.1: Research proposed here: (a) steel strands; (b) strands are instrumented with low profile piezoelectric transducers to generate and receive GUWs. (c) The GUW measurements are recorded and processed, providing (d) an automatic corrosion diagnosis of the strand

7.4. Guided Wave Propagation in Stressed Strands

7.4.1. Background and Overview

Seven-wire prestressing strands serve as load bearing elements in civil infrastructure, prestressed/post-tensioned concrete structures. The level of stress in a strand (and within individual wires) is therefore critical to the performance of the structure. As such, the ability to monitor this stress using guided waves may yield valuable structural information. Aside from stress measurement [181]–[184], guided ultrasonic waves have received attention for damage detection as well [185]–[189]. A recent study [190] has also addressed the issue of attenuation in strands and identified the potential for large inspection distances (> 100 m). In damage detection applications, however, the effect of stress may need to be compensated for. This is because false indicators of damage (e.g., changes in wave velocity) may be caused by stress as opposed to damage.

The effect of stress on wave propagation is referred to as acoustoelasticity [191]. To date, the effect of stress on guided waves has been studied in a wide range of structures, including plates [184], [192], pipes [193]–[195], and rails [196], [197]. For rods in particular, theoretical studies have been carried out on longitudinal [198], flexural [199], and torsional [200] modes, dating back to the early years of acoustoelasticity in the 1960-70s. Due to the complex interaction of wires in a seven-wire strand, the first studies on the effect of stress in this waveguide were

experimental, and did not come until roughly 30 years later. Kwun et al. [201] experimentally studied guided waves generated by magnetostrictive sensors, which excite all of the wires at once within a strand. In their study, missing frequency content (termed the notch frequency) was linearly correlated with the logarithm of the stress level. Chen and Wissawapaisal [202], [203] also performed experimental studies on the fundamental longitudinal mode $L(0,1)$ in stressed strands. In their work, they proposed an approximate acoustoelastic rod theory to predict the stress dependence of waves propagating within individual wires. Washer et al. [204] performed experiments with magnetostrictive sensors, demonstrating a linear dependence of velocity with respect to large levels of stress ($> 50\%$ ultimate tensile strength, or UTS). Rizzo [205] experimentally studied the effect of stress on the transmission energy of the $L(0,1)$ mode in both the core wire and entire strand. One of the main conclusions of this study was that the core wire has better potential for stress measurement than the entire strand. Chaki and Bourse [182] studied the $L(0,1)$ mode excited in the core wire of a strand for the purpose of stress measurement. The approximate acoustoelastic theory developed in [181], [202] was applied to predict the stress dependence in an individual wire, although there was some disagreement with the experimental results. In particular, a nonlinear stress dependence was found at lower stress levels ($< 35\%$ UTS), which diverged from the theory and has not yet been definitively explained. Nonlinear and divergent results were also found earlier by Lanza di Scalea et al. [181] using magnetostrictive sensors. More recently, the semi-analytical finite element (SAFE) method has been used to study guided waves propagating within seven-wire strands as a whole. In particular, Treysede and Laguerre [206] presented the first SAFE study applied to seven-wire strands, which explained the notch frequency discovered by Kwun et al. Nucera and Lanza di Scalea [207] studied the effect of stress on higher harmonics, where the generation of a second harmonic from a primary excitation was correlated with stress. Lastly, Schaal et al. [208] and Treysede [209] studied the energy leakage between adjacent wires in a stressed strand. The work by Treysede provided numerical validation for the stress dependence of the notch frequency.

Although studies have been made on the fundamental mode $L(0,1)$ for stress measurement, higher-order modes $L(0, n)$, $n > 1$ have seen little attention for this purpose. In addition to the unexplained nonlinear dependence of the fundamental mode at lower stress, there has also been reasonable disagreement ($> 50\%$) between theory and experiment at higher stress [182]. Aside from the fundamental mode, higher-order modes have also been studied for potential damage detection in strands [210]–[212]. However, the effect of stress on these modes has seen little attention. Furthermore, although the exact guided wave theory for an axially stressed rod was presented in the 1960s, it has seen little applications to strands. Instead, only approximate rod theories have been used [181], [182]. One of the attractive characteristics of higher-order modes (particularly $n > 5$) is that their mode shapes

are concentrated near the core of a rod in certain frequency ranges [213], [214]. This translates into minimal energy leakage and attenuation when there is another medium bordering the rod. In this report, the term higher-order modes is used to refer to those with $n > 5$, where their behavior becomes increasingly similar [213].

This section studies the effect of stress on higher-order modes propagating in individual wires of seven-wire strands. The main idea is to use acoustoelastic rod theory to predict the effect of stress on these modes, while idealizing each wire as a rod with free boundaries. To this end, the exact acoustoelastic rod theory developed by Suhubi is adapted for small deformations. Expressions for the mode shapes are then derived, from which the concentration of higher-order modes near the core of a stressed rod may be verified. In this section, an approximate theory for higher-order modes is also proposed. This is presented in the form of an explicit function of stress, as opposed to an implicit dispersion equation. In order to validate the application of acoustoelastic rod theories to strands, a custom-built prestressing bed was designed for recording higher-order mode measurements on a stressed strand. The stress-induced phase velocity change is used to characterize the influence of stress on these modes. In combination with the approximate theory, another approximation is also proposed for higher-order modes. This approximation allows for the phase velocity change to be computed from time change measurements in a simpler manner. Together, the two approximations may be used to compare theoretical and measured velocity changes of higher-order modes without solving for dispersion curves.

This section is organized as follows: First, in Sec. 7.4.2, the adaptation of the exact acoustoelastic theory and the proposed approximate theory are presented. In addition, theoretical results are presented based on these formulations. In Sec. 7.4.3, the higher-order mode experiments on a stressed strand are described, as well as the approximate phase velocity change derived from experiment. Experimental results for higher-order modes are then presented in Sec. 7.4.4.

7.4.2. Theoretical Formulation for an Axially Stressed Rod

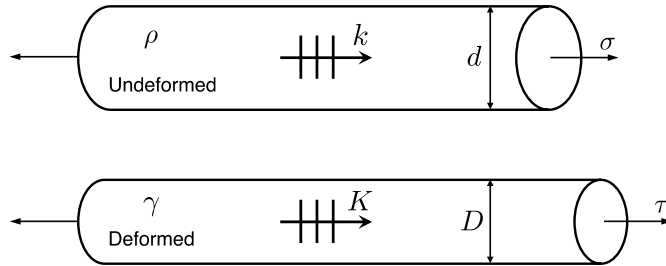
This subsection presents the exact acoustoelastic theory for an axially stressed steel rod, and derives expressions for the mode shapes of the guided wave solutions. The proposed approximate theory for higher-order modes is then presented. In addition, theoretical results for the effect of stress on guided waves in a steel rod are demonstrated. Since a tensioned strand generates predominantly axial stresses within individual wires, the waveguide of each wire is idealized as an axially stressed rod [181], [182].

7.4.2.1. Exact Acoustoelastic Theory for Longitudinal Modes

Suhubi [198] has solved for the exact dispersion equation of longitudinal modes in an axially stressed elastic rod of arbitrary strain energy function (and therefore arbitrary stress-strain relation). This theory is adapted here for a strain energy function that is applicable to steels and other stiff materials under small deformations [215].

Let us consider a rod subjected to an axial stress τ , which is illustrated in Figure 7.2. The variable τ is used to indicate that the stress is referenced to the deformed configuration (Cauchy stress). It produces the principal extensions λ_r, λ_z in the radial and axial directions, respectively. The deformed diameter of the rod is therefore expressed in terms of the undeformed diameter d as

$$D = \lambda_r d$$



Source: Images by Authors

Figure 7.2: Undeformed and deformed configurations of stressed rod, showing density (ρ, γ), stress (σ, τ), and wavenumber (k, K) of longitudinal guided wave

Small amplitude guided wave motion, with wavenumber K and angular frequency ω , is then superimposed on the deformed configuration. The radial and axial displacement components of guided waves are described in terms of the deformed configuration of the rod as [198]

$$u_r = U_r(R) \exp[i(KZ - \omega t)]$$

$$u_z = U_z(R) \exp[i(KZ - \omega t)]$$

where R and Z are the radial and axial position in the deformed configuration. From the equation of motion in [198], the displacement mode shapes U_r, U_z can be written as

$$U_r = C_1 J_1(\chi_3 R) + C_2 J_1(\chi_4 R)$$

$$U_z = C_1 \frac{\chi_1^2 - \chi_3^2}{\beta_1 \chi_3} J_0(\chi_3 R) + C_2 \frac{\chi_1^2 - \chi_4^2}{\beta_1 \chi_4} J_0(\chi_4 R)$$

Equation 7.1

where C_1, C_2 are constants, $J_0(\cdot), J_1(\cdot)$ are the zero and first order Bessel functions of the first kind, respectively, and β_i and χ_i terms are contained in the Appendix. From [198], the boundary conditions for vanishing stress along the surface of the rod $R = D/2$ reduce to

$$\left[iK U_r + \frac{\partial U_z}{\partial R} \right]_{R=D/2} = 0$$

$$\left[(\alpha_1 - 2\Phi_3) \frac{\partial U_r}{\partial R} + (\alpha_1 + 2\lambda_r^4 \Phi_2) \frac{U_r}{R} + iK \alpha_2 U_z \right]_{R=D/2} = 0$$

Equation 7.2

where α_i and Φ_i terms are contained in the Appendix. Satisfying the above conditions for nontrivial values of C_1, C_2 yields the dispersion equation relating ω and K [198],

$$(iK\beta_1 + \chi_3^2 - \chi_1^2) \left[(\alpha_1 - 2\Phi_3)\chi_4 + iK\alpha_2 \frac{\chi_1^2 - \chi_4^2}{\beta_1\chi_4} \right] J_1\left(\frac{\chi_3 D}{2}\right) J_0\left(\frac{\chi_4 D}{2}\right)$$

$$- (iK\beta_1 + \chi_4^2 - \chi_1^2) \left[(\alpha_1 - 2\Phi_3)\chi_3 + iK\alpha_2 \frac{\chi_1^2 - \chi_3^2}{\beta_1\chi_3} \right] J_0\left(\frac{\chi_3 D}{2}\right) J_1\left(\frac{\chi_4 D}{2}\right)$$

$$+ 4D^{-1}(\Phi_3 + \lambda_r^4 \Phi_2)(\chi_3^2 - \chi_4^2) J_1\left(\frac{\chi_3 D}{2}\right) J_1\left(\frac{\chi_4 D}{2}\right) = 0$$

Equation 7.3

The work in [198] does not develop expressions for the modeshapes of longitudinal modes. To this end, the constants C_1, C_2 may be determined using the first boundary condition. Assuming $C_1 = 1$, the second constant may be found as

$$C_2 = - \frac{iK\beta_1 - \chi_1^2 + \chi_3^2 J_1(\chi_3 D/2)}{iK\beta_1 - \chi_1^2 + \chi_4^2 J_1(\chi_4 D/2)}$$

Equation 7.4

7.4.2.1.1. Adaptation to Small Deformations

Entering into the above equations (as seen from the Appendix) are the deformed density of the medium γ , and derivatives of the strain energy function U with respect to strain invariants I_i . These invariants are defined [198]

$$I_1 = 2\lambda_r^2 + \lambda_z^2$$

$$I_2 = \lambda_r^4 + 2\lambda_r^2 \lambda_z^2$$

$$I_3 = \lambda_r^4 \lambda_z^2$$

Here, the required partial derivatives $\partial U/\partial I_i, \partial^2 U/(\partial I_i \partial I_j)$ and extensions λ_r, λ_z are found for a particular form of strain energy function. Specifically, the strain energy function proposed by Murnaghan [216] is used, which is expanded up to the third order in strain. This is an appropriate assumption in the acoustoelasticity of relatively stiff materials, such as metals [215]. The strain energy function is defined in terms of the strain invariants I_E, II_E, III_E [216],

$$U = \frac{1}{2}(\lambda + 2\mu)I_E^2 - 2\mu II_E + \frac{1}{3}(l + 2m)I_E^3 - 2mI_E II_E + nIII_E$$

where l, m, n are the Murnaghan third order elastic constants. The above invariants may be expressed in terms of the invariants I_i [217],

$$I_E = \frac{1}{2}(I_1 - 3)$$

$$II_E = \frac{1}{4}(I_2 - 2I_1 + 3)$$

$$III_E = \frac{1}{8}(I_3 - I_2 + I_1 - 1)$$

From here onward it is assumed that the stress induced deformation is small, which is appropriate for the stiff material under consideration [215]. This reduces the partial derivatives of U , as mentioned in [218], to

$$\frac{\partial U}{\partial I_1} = \mu + \frac{1}{8}n + \frac{1}{2}(\lambda + 2\mu + 2m)I_E$$

$$\frac{\partial U}{\partial I_2} = -\frac{1}{2}\mu - \frac{1}{8}n - \frac{1}{2}mI_E$$

$$\frac{\partial U}{\partial I_3} = \frac{1}{8}n$$

$$\frac{\partial^2 U}{\partial I_1^2} = \frac{1}{4}(\lambda + 2\mu) + m + \frac{1}{2}(l + 2m)I_E$$

$$\frac{\partial^2 U}{\partial I_1 \partial I_2} = -\frac{1}{4}m$$

where all other $\partial^2 U/(\partial I_i \partial I_j) = 0$, $II_E = III_E = 0$, since they are entirely composed of higher-order strain terms, and

$$I_E = 2e_r + e_z$$

The extensions may then be expressed in terms of the radial and axial small strains e_r, e_z as

$$\lambda_r = 1 + e_r$$

$$\lambda_z = 1 + e_z$$

In addition, the Cauchy stress τ reduces to the second Piola-Kirchhoff stress σ , which is referenced to the undeformed configuration (see Figure 7.2). The small strains are related to this stress according to linear elasticity,

$$e_r = -\frac{\lambda}{2\mu(3\lambda + 2\mu)}\sigma$$

$$e_z = \frac{\lambda + \mu}{\mu(3\lambda + 2\mu)}\sigma$$

Equation 7.5

The deformed density of the medium may also be related to the undeformed density ρ as [216]

$$\gamma = (1 - I_E)\rho$$

Solution pairs (ω, K) of the dispersion equation describe the longitudinal modes referenced to the deformed configuration of a stressed rod. Pairs (ω, k) , referenced to the undeformed configuration, may then be found through the wavenumber transformation [194], [219]

$$k = \lambda_z K$$

The phase and group velocity, referenced to the undeformed configuration, may then be computed from the solutions as $c_p = \omega/k$ and $c_g = d\omega/dk$, respectively. In addition, from here onward in this chapter, a superscript 0 notation is used to denote velocities in the absence of stress, as in c_p^0 and c_g^0 . The mode shapes in Equation 7.1 may also be expressed in terms of the undeformed radial position $r = R/\lambda_r$ as

$$U_r = C_1 J_1(\chi_3 \lambda_r r) + C_2 J_1(\chi_4 \lambda_r r)$$

$$U_z = \frac{C_1(\chi_1^2 - \chi_3^2)}{\beta_1 \chi_3} J_0(\chi_3 \lambda_r r) + \frac{C_2(\chi_1^2 - \chi_4^2)}{\beta_1 \chi_4} J_0(\chi_4 \lambda_r r)$$

Equation 7.6

The phase velocity change $\Delta c_p = c_p - c_p^0$ is used to quantify the effect of stress on wave propagation. The velocity change may be related to a time change in a narrowband waveform [220],

$$\Delta c_p = -\frac{(c_p^0)^2}{\ell} \Delta t$$

Equation 7.7

where c_p^0 is the unstressed phase velocity at the center frequency of the waveform, ℓ is the propagation length subjected to stress, and Δt is the time change of a zero-crossing point in the waveform.

7.4.2.2. Theoretical Results for a Steel Rod

As a point of reference, the phase and group velocity dispersion curves for an unstressed steel rod may be seen in Figure 7.3. The curves were computed using Equation 7.3, with $\sigma = 0$ MPa, and the material properties for Hecla 17 steel listed in Table 7.1 [221]. This particular steel is selected to represent the high Carbon steel strand due to the unavailability of its third order elastic constants l, m, n . Hecla 17 is chosen due to its high Carbon content of 0.6%, which has been shown to play a significant role in the third order constants of steel [222]. In addition to the guided modes, the velocity of a bulk longitudinal wave is also overlain in Figure 7.3.

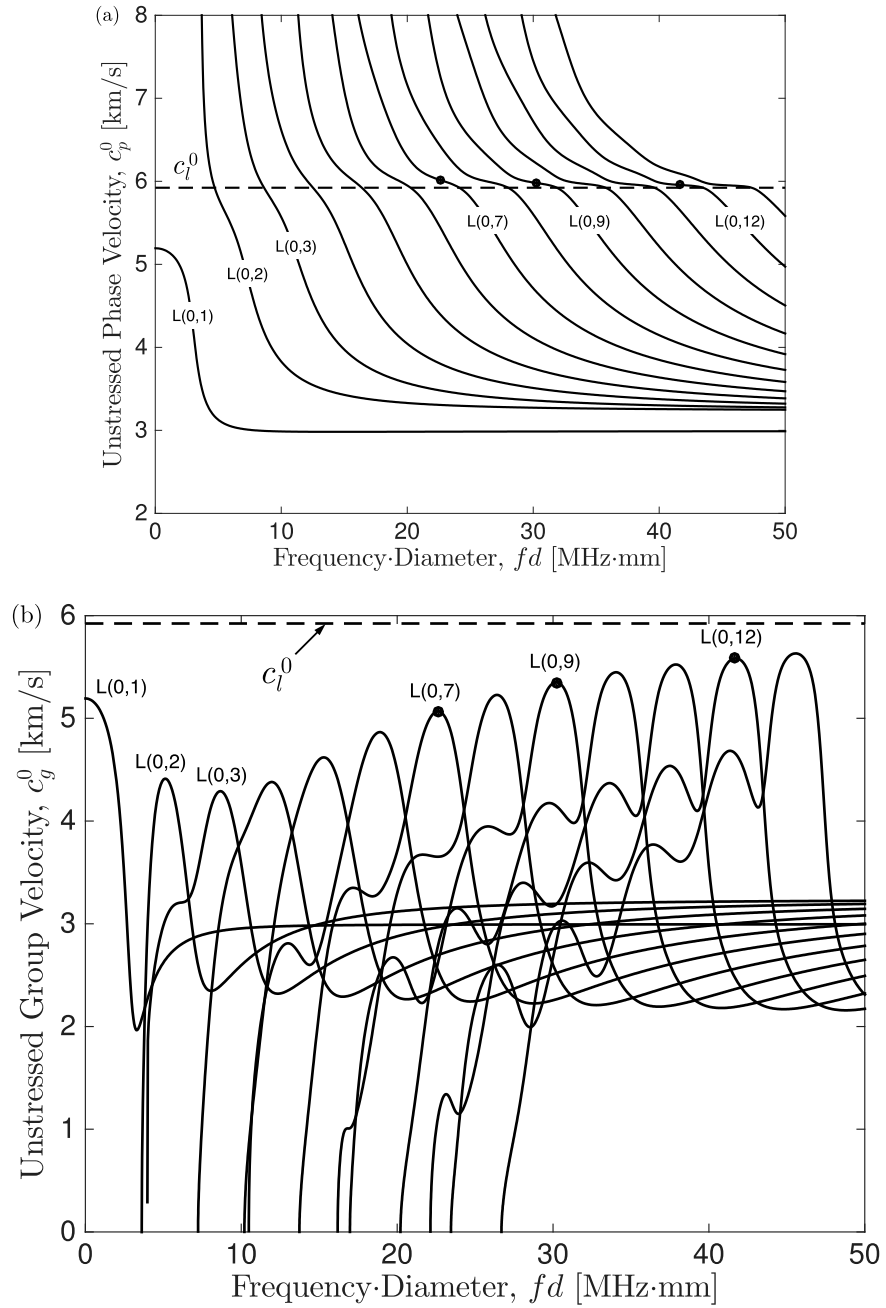


Figure 7.3: Unstressed dispersion curves for (a) phase velocity, and (b) group velocity in a steel rod. Bulk longitudinal velocity c_l^0 overlain as dashed line. Peak group velocity points of L(0,7), L(0,9), and L(0,12) are identified by dots in (a) and (b).

Table 7.1: Undeformed Density [kg/m³] and Elastic Constants [GPa] for Hecla 17 Steel, along with Uncertainties

Parameter	Value
ρ	7825
λ	110.5 ± 1
μ	82.0 ± 0.5
l	-328 ± 30
m	-595 ± 32
n	-668 ± 24

The change in phase velocity based on Equation 7.3 is shown in Figure 7.4, due to an axial stress of $\sigma = 400$ MPa. Plateaus in the phase velocity change may be seen for the higher-order modes near $\Delta c_p = -40$ m/s (bold lines), where the change is relatively stable across both mode and frequency. The bolded plateau region, denoted $\Delta c_p|_p$, is defined as the region where the change of the guided wave phase velocity Δc_p is within 1% from its value at the peak group velocity point. For reference, the bulk longitudinal wave velocity change Δc_l (which is constant across frequency) has also been overlain in the figure. It may be seen that the plateaus of higher-order modes in this figure asymptote to Δc_l . For this type of steel, there is roughly a 2% difference between the exact value of $\Delta c_p|_p$ (bold region) and its approximation (dashed line).

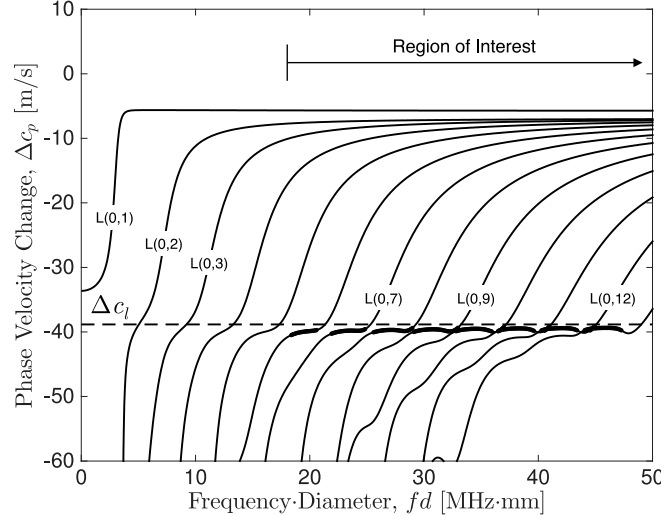


Figure 7.4: Exact theoretical change in phase velocity due to 400 MPa axial stress in steel rod. Exact $\Delta c_p|_p$ regions bolded for the higher-order modes $L(0,n)$, $n > 5$. Bulk velocity change Δc_l overlain as dashed line.

For interest, Figure 7.5 shows the changes in phase velocity Δc_p and group velocity Δc_g of the $L(0,9)$ mode in particular. The plateau region in Δc_p is indicated by a bold line in each of the plots. The unstressed group velocity of the mode is also shown, where it may be seen that the plateau coincides with the peak group velocity

region. In addition to the mode having the fastest group velocity (i.e., first arrival time) at these frequencies, it also has relatively little dispersion. It may be noted that this is the same region that has been identified for damage detection applications [210], [213]. Compensation for stress in this region may therefore be necessary, due to the high levels of stress experienced by strands. Comparing the two velocities, it may be seen that Δc_p is more stable than Δc_g across frequency. The phase velocity may therefore be more reliable for stress measurement applications.

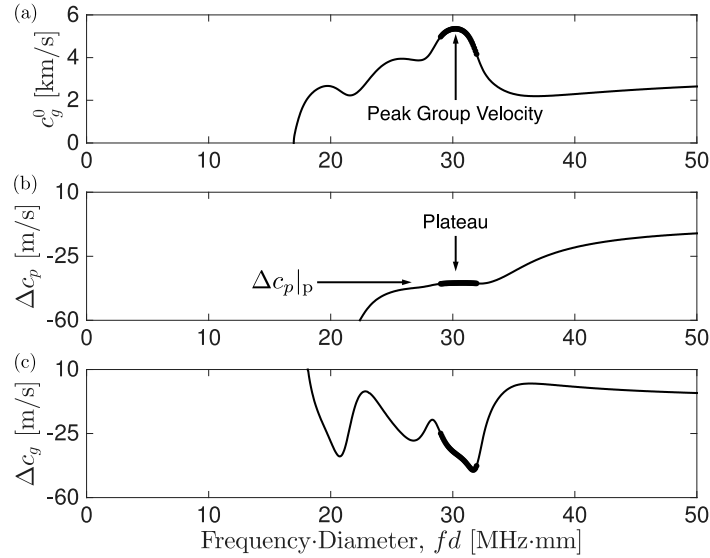


Figure 7.5: (a) Unstressed group velocity dispersion curve of L(0,9) mode, with (b) phase velocity change under 400 MPa axial stress, and (c) group velocity change under same stress. Curves bolded in peak group velocity region. Phase velocity change stabilizes to $\Delta c_p|_p$ at peak group velocity, with group velocity change less stable.

Mode shapes in a steel rod for the L(0,7), L(0,9), and L(0,12) modes, identified in the dispersion curves from Figure 7.3, are shown in Figure 7.6. These are calculated from Equation 7.6, using the constants from Equation 7.4. It should be noted that these modes are chosen somewhat arbitrarily for visualization. However, only modes above L(0,6) are shown, since modes of lower order than this do not have the same degree of convergence to the plateau region shown in Figure 7.4. Under zero axial stress, it may be seen that the mode shapes are concentrated near the core of a rod, which has been noted in previous studies [213]. Furthermore, even under a 400 MPa stress, the mode shapes are shown to remain concentrated near the core. The characteristic of minimal energy leakage into bordering media, which higher-order modes have under zero stress, is related to the displacement concentration near the core [213], [214]. Based on the results in Figure 7.6, this characteristic is taken to apply for stresses as large as 400 MPa as well. The characteristic forms the basis of modeling an individual wire of a strand as a rod with free boundaries.

7.4.2.3. Approximate Theory for Higher-Order Modes

As shown in Figure 7.3, there exist regions in the dispersion curves of higher-order modes in which they asymptote toward the bulk longitudinal velocity, $c_l^0 = [(\lambda + 2\mu)/\rho]^{1/2}$. In particular, c_g^0 peaks near c_l^0 , and c_p^0 plateaus across frequency as it crosses c_l^0 [213], [223]. For illustration, the peak group velocity points for L(0,7), L(0,9), and L(0,12) are identified in Figure 7.3. As the mode number n tends to infinity, the peak c_g^0 values asymptote at c_l^0 , along with the plateaus in c_p^0 becoming more pronounced. In this report, the frequency region in which the plateau behavior occurs for a given mode is termed the plateau region.

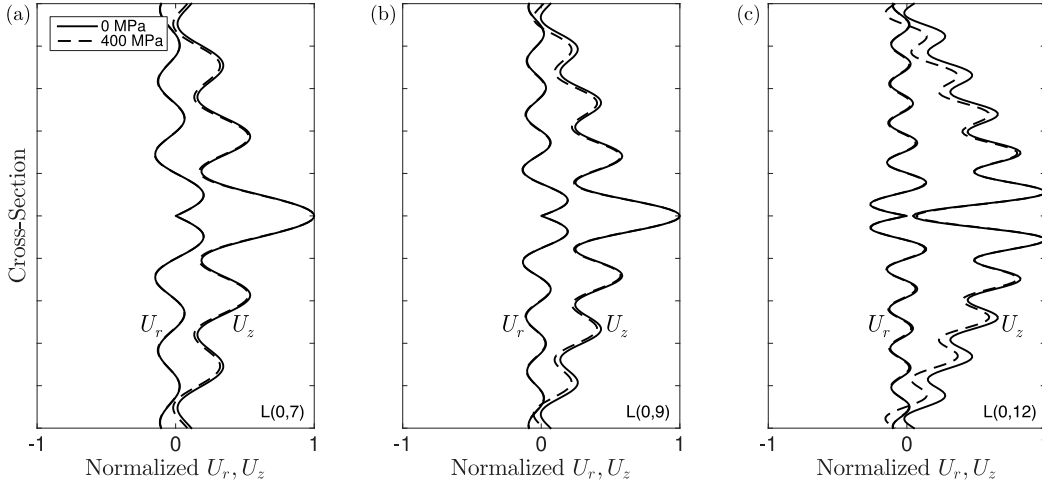


Figure 7.6: Radial U_r and axial U_z modeshapes over a rod cross-section for (a) L(0,7) at 22.6 MHz-mm, (b) L(0,9) at 30.2 MHz-mm, and (c) L(0,12) at 41.7 MHz-mm. Mode shapes at two stress levels overlain, showing concentration of displacements near the core.

Since the unstressed phase velocity c_p^0 tends to the bulk longitudinal velocity c_l^0 , the effect of stress on the bulk velocity is presented. The phase velocity c_l of a bulk longitudinal wave propagating along a principal stress is related to the strain and material properties according to [224]

$$\rho c_l^2 = \lambda + 2\mu + (\lambda + 2l)I_E + (2\lambda + 6\mu + 4m)e_z$$

where e_z is the strain along the propagation direction. The strain may be expressed in terms of a uniaxial stress σ applied along the propagation direction. By neglecting higher-order terms, the bulk phase velocity change $\Delta c_l = c_l - c_l^0$ may then be written as a linear function of stress,

$$\Delta c_l = \kappa \sigma$$

Equation 7.8

where κ is an acoustoelastic constant, which is a function of the material properties:

$$\kappa = \frac{(\lambda + 2l)\mu + (2\lambda + 6\mu + 4m)(\lambda + \mu)}{2(3\lambda + 2\mu)\mu[(\lambda + 2\mu)\rho]^{1/2}}$$

The bulk velocity change under a stress of $\sigma = 400$ MPa is overlain in Figure 7.4. As discussed in the previous section and shown in Figure 7.4, the guided mode velocity change asymptotes to Δc_l in the plateau region, denoted $\Delta c_p|_p$. Therefore, using Equation 7.8, an approximation for the phase velocity change of higher-order modes in this region is proposed as

$$\Delta c_p|_p \approx \kappa \sigma$$

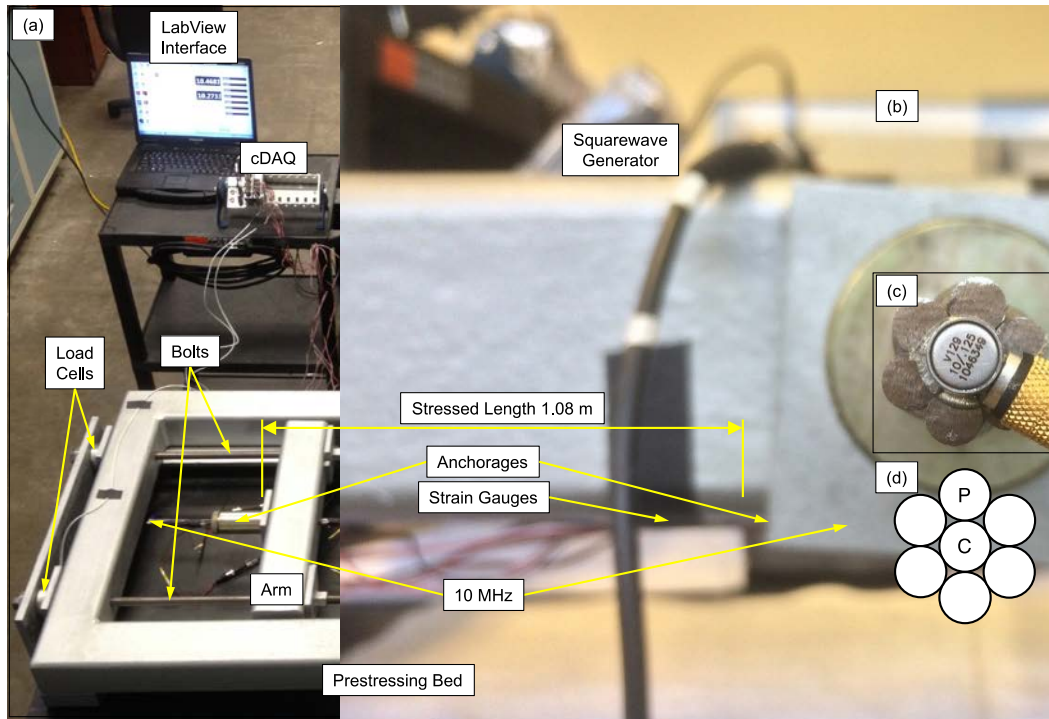
Equation 7.9

In this way, $\Delta c_p|_p$ may be approximated in an explicit manner, without the need to solve for dispersion curves.

7.4.3. Experiment

7.4.3.1. Test Setup and Procedure

A prestressing bed was designed to apply tensile load to a seven-wire strand, as shown in Figure 7.7 (a). The strand was fixed with anchorages between the base of the bed and a moveable arm, and load was applied by tightening two bolts running through the arm. The tested strand had core and peripheral wire diameters of $d_c = 5.22$ and $d_p = 5.08$ mm, respectively, and a lay angle of $\beta = 7.9^\circ$. The nominal diameter of the strand was 15.2 mm (0.6 in.). The length of the strand under stress (i.e., within the anchorage zone) was 1.08 m (3.54 ft), which was defined as the distance between the base of each anchorage. The total load was recorded with two load cells (Interface LW25100-20K) placed around the bolts. The axial strain within individual wires was recorded by placing a strain gauge (Micro Measurements C2A-06-250LW-350) on the surface of each of the six peripheral wires, oriented along the axis. The load cells and strain gauges may be seen in Figure 7.7 (a) and (b). Before strain gauges were placed, the installation area was prepared by degreasing, sanding, and applying surface conditioner. A protective polyurethane coating was also applied after the gauges were bonded. Load cell and strain gauge readings were recorded with a National Instruments cDAQ compact data acquisition system, and monitored using LabView.



Source: Images by Authors

Figure 7.7: (a) Prestressing bed experimental setup and data acquisition systems for collecting guided waves measurements on stressed strand. (b) Strain gauges installed on peripheral wires. (c) Higher-order modes excited with 10 MHz transducers. (d) Schematic of strand cross-section, with core (C) and peripheral (P) wires indicated.

Higher-order longitudinal guided wave modes were excited in a pitch-catch configuration using two piezoelectric transducers (Olympus V129-RM) with a center frequency of 10 MHz. The transducers were bonded to each end of an individual wire's cross-section, as shown in Figure 7.7(c). Furthermore, the transducers were moved from the core to the peripheral wire to excite each wire individually. An Olympus 5077PR squarewave pulser/receiver was used to control higher-order mode excitation, while waveforms were recorded on a LeCroy HDO6104 oscilloscope. The squarewave excitation was wideband with a center frequency between 5 and 6 MHz. Since the device was limited to a squarewave excitation, the excitation was limited to wideband as opposed to narrowband. The waveforms were sampled at 250 MHz and averaged 500 times. The higher-order mode signals excited by the squarewave pulser/receiver had a wide range of frequency content. Therefore, in order to study certain higher-order modes at a time, the signals were filtered with a zero-phase-shift butterworth bandpass filter.

Reference waveforms were first recorded at zero load. Load was then applied at nominal steps of 4.5 kN (≈ 1 kip), and held constant at each step while guided wave measurements were taken. The maximum load applied was 98 kN (≈ 22 kips), equal to roughly 50% of yield and 25% of the ultimate tensile strength (UTS). Due to some variability in the strain readings between different peripheral wires, the

values of the six gauges were averaged to obtain the peripheral wire axial strain e_p . In order to quantify the variability, the standard deviation between the readings was also computed, which was normalized by $N - 1$, with N the number of gauges. Since the strain in the core wire was not measured directly, the peripheral wire reading was converted to a core wire reading using the following relation: [225]

$$e_c = e_p / \cos^2(\beta)$$

The stresses in the core and peripheral wires, σ_c and σ_p , were then obtained by converting the axial strain to axial stress through Equation 7.5 (denoted e_z and σ).

7.4.3.2. Approximate Phase Velocity Change

The phase velocity change at a given stress was computed from the time change for a point of constant phase within a waveform, using Equation 7.7. This may be seen in Figure 7.8, which shows the time change of the L(0,9) mode in the peripheral wire at $fd = 30.2$ MHz-mm for stresses of 0 and 18.7 MPa. This mode and fd are identified in Figure 7.3.

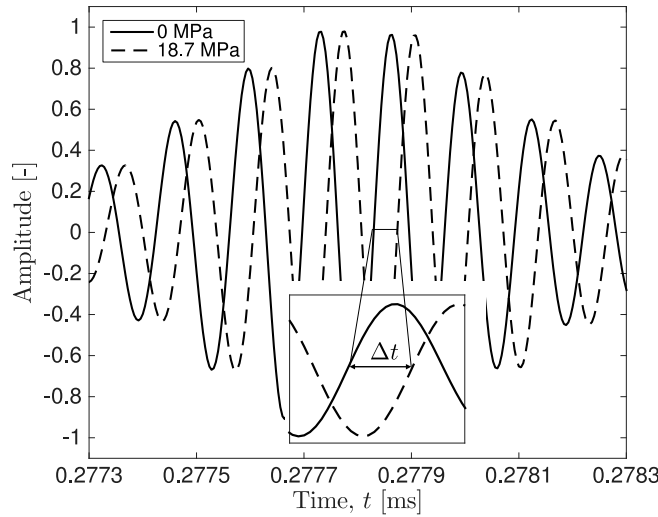


Figure 7.8: Filtered L(0,9) mode waveform at two levels of stress, illustrating time change Δt used for phase velocity change measurement

In addition to the approximate theory from Equation 7.9 for Δc_p in the plateau region, an approximation may also be used to experimentally measure Δc_p . The unstressed phase velocity c_p^0 asymptotes to the unstressed bulk velocity c_l^0 in the plateau region. Therefore, the measurement may be approximated by

$$\Delta c_p|_p \approx - \left[\frac{(c_l^0)^2}{\ell} \right] \Delta t$$

Equation 7.10

In conjunction with Equation 7.9, the phase velocity change of higher-order modes may be (for practical purposes) both theoretically computed and experimentally measured without solving for dispersion curves.

7.4.4. Experimental Results

First, the continuous wavelet transform (CWT) was used to verify that the higher-order modes from the rod theory were recorded by the transducers, which may be seen in Figure 7.9. The power spectrum of the CWT is plotted in this figure, which was computed with a Gabor mother wavelet [226],

$$\Psi = \pi^{-1/4} \left(\frac{\omega_0}{\gamma} \right)^{1/2} \exp \left(-\frac{1}{2} \frac{\omega_0^2}{\gamma^2} t^2 + i\omega_0 t \right)$$

where the parameters ω_0, γ were set to $\omega_0 = 2\pi$ and $\gamma = 80$. The plot corresponds to the signal under the maximum level of applied stress (roughly 400 MPa). Arrival times based on the group velocity of longitudinal modes in a stressed rod are overlain, showing good agreement with the experimental spectrum. The peak group velocity regions (i.e., first arrival waveforms) are clearly defined, although there is some minor mismatch at relatively lower (≈ 15 MHz-mm) and higher (≈ 45 MHz-mm) frequencies. Indeed, this is expected for modes at lower frequencies, since they have more surface motion, thus weakening the assumption of a rod with free boundaries. Additionally, the material properties of the steel strands are not known precisely. This may yield some minor mismatch with respect to the theoretical curves.

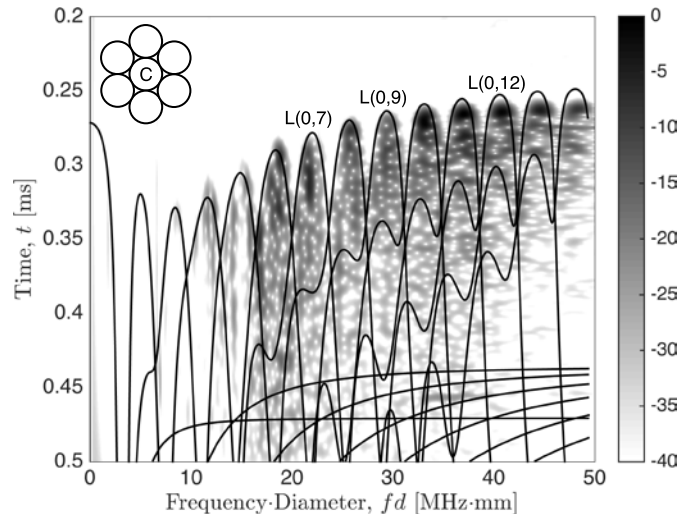


Figure 7.9: Power spectrum [dB] of continuous wavelet transform of unfiltered higher-order mode signal in core (C) wire under 400 MPa axial stress; theoretical group velocity dispersion curves converted to arrival times for steel rod overlain

7.4.4.1. Cross-wire Stability

To validate the application of the acoustoelastic rod theory, the consistency of the phase velocity change between the core (C) and peripheral (P) wires of the strand is first demonstrated in Figure 7.10. This figure plots the experimentally measured phase velocity change for the L(0,9) mode as a function of stress in the C and P wires at $fd = 30.2$ MHz-mm (peak group velocity point). The range shown from 0 to -50 m/s is equivalent to a relative velocity change from 0 to -0.83% , measured with respect to the unstressed velocity. Horizontal error bars in the experimental points are also plotted, based on the standard deviation of the strain gauge readings. It may be seen that the velocity changes in the two wires are very similar at the chosen fd . The similarity between the two wires demonstrates that contact with the anchorages, as well as the grip marks they develop, have a negligible influence on the phase velocity change. Since higher-order modes have minor interaction with a rod surface (see Figure 7.6), the negligibility to grip marks would be expected if the rod idealization was achieved.

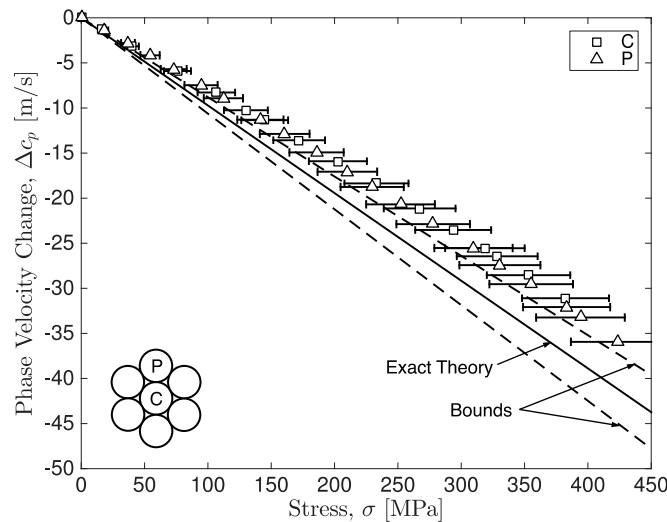


Figure 7.10: Experimental phase velocity change for the L(0,9) mode in the core (C) and peripheral (P) wire at $fd = 30.2$ MHz-mm, with error bars for the variability in strain gauge readings. Theoretical change overlain for a steel rod, including bounds for uncertainty in material constants.

In addition to the experimental points, the theoretical phase velocity change based on dispersion curves from Equation 7.3 is overlain in Figure 7.10. To account for the uncertainty in the elastic constants of Table 7.1, uncertainty bounds for the theoretical velocity change are also shown. The bounds were calculated by determining which combination of the elastic constants, within their respective uncertainties, yielded the greatest and least amount of velocity change. The elastic constants defining the bounds were estimated through a Monte Carlo simulation and are listed in Table 7.2. The simulation was based on one thousand values of (λ, μ, l, m, n) , sampled uniformly within their respective uncertainty bounds (see

Table 7.1). Upper and lower bounds in Δc_p were then determined by computing dispersion curves for each sampled (λ, μ, l, m, n) set, and then recording the extrema of Δc_p across all sets.

Table 7.2: Combinations of Hecla 17 Steel Elastic Constants [GPa] Yielding Upper and Lower Theoretical Bounds in Phase Velocity Change, Determined using Monte Carlo Simulation

Parameter	Lower bound	Upper bound
λ	109.5	111.5
μ	81.5	82.5
l	-358	-298
m	-627	-563
n	-692	-644

The linearity of the velocity change in Figure 7.10 is generally predicted by acoustoelasticity in metals [215]. Additionally, from past studies on the fundamental mode, the linearity is expected to remain for higher stress levels as well, up to at least 1400 MPa (75% UTS) [181], [182], [204]. The slope of the theoretical Δc_p , termed the theoretical acoustoelastic constant, was found to be $\kappa_t = -0.099$ (m/s)/MPa. Measured in terms of the relative velocity change with respect to stress, the slope was $\kappa_t = -0.0017$ %/MPa. Performing linear regression on the C wire velocity change, an experimental acoustoelastic constant was computed as $\kappa_c = -0.083$ (m/s)/MPa (-0.0014 %/MPa). Similarly, an acoustoelastic constant for the P wire was computed as $\kappa_p = -0.084$ (m/s)/MPa (-0.0014 %/MPa). The slight mismatch between the theoretical and experimental slopes ($\approx 15\%$) can be attributed to the use of Hecla 17 to represent the steel strand. Indeed, in testing the theory for various lower Carbon content steels (0.2 to 0.4%, using material properties obtained from [221], [227], it was found that the theoretical slope varied around 10%. For instance, for Hecla 138A [221], Hecla 37 [221], and low Carbon steel [227], respectively, theoretical slopes of -0.107 , -0.111 , and -0.104 (m/s)/MPa were found. Compared to Hecla 17, each of these slopes are farther from the experimental slope of -0.083 (m/s)/MPa, suggesting better agreement with increasing Carbon.

7.4.4.2. Mode and Frequency Stability

In the theoretical results of Sec. 7.4.2, the phase velocity change was shown to plateau across a wide range of modes at different frequencies (see Figure 7.4). The plateau results in a stable velocity change across frequency. This stable behavior is therefore investigated within an individual wire of the strand, and shown in Figure 7.11. Here, the experimental velocity change in the P wire is plotted at $fd = 22.6$ MHz-mm for the L(0,7) mode, and at 41.7 and 40.0 MHz-mm for the L(0,12) mode. The first two fd values correspond to the peak group velocity points shown in

Figure 7.3(b) and Figure 7.9. The third fd corresponds to the low frequency limit of the plateau region for L(0,12). As with Figure 7.10, horizontal error bars are shown based on the standard deviation observed in the strain gauge readings. The theoretical velocity change at the three fd values is also overlain, along with corresponding uncertainty bounds.

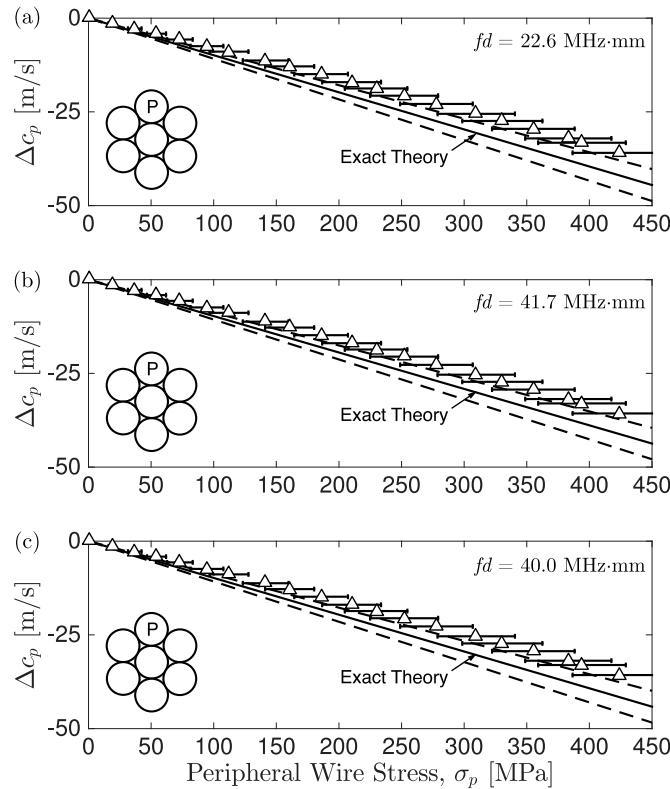


Figure 7.11: Experimental phase velocity change in peripheral (P) wire for (a) L(0,7) mode at $fd = 22.6$ MHz-mm, (b) L(0,12) at 41.7 MHz-mm, and (c) L(0,12) at 40.0 MHz-mm, with error bars for the variability in strain gauge readings. Theoretical change for a steel rod overlain with material uncertainty bounds.

It may be seen that the velocity change (both experimental and theoretical) is nearly identical between the three plots. This is a consequence of the plateaus in phase velocity change near the peak group velocities, shown in Figure 7.4 and Figure 7.5(b), where the change becomes stable across both modes and frequencies. The stability has the potential for reliable stress measurement using the velocity change. Figure 7.11 also demonstrates that different higher-order modes exhibit nearly the same change in velocity. For the two modes studied here (i.e., L(0,7) and L(0,12)), they each appear to be comparable in their advantages for stress measurement.

7.4.4.3. Practical Approximations

In order to demonstrate the approximate phase velocity changes derived from theory and experiment discussed in Secs. 7.4.2.3 and 7.4.3.2, respectively, data for the P wire from Figure 7.10 is used as an example. The experimental points for this

wire are plotted in Figure 7.12 for the exact and approximate phase velocity change (derived from experiment). The exact phase velocity change (derived from experiment) is calculated from Equation 7.7 using the measured time change Δt and the exact dispersion curves c_p^0 from Equation 7.3. Instead, the approximate phase velocity change (derived from experiment) is calculated from Equation 7.10 by using the bulk velocity c_l^0 to approximate the exact dispersion curves in the plateau region. The exact dispersion curves must be obtained by numerically solving an implicit equation, while the bulk velocity may be computed from the explicit equation $c_l^0 = [(\lambda + 2\mu)/\rho]^{1/2}$. It may be seen that using c_l^0 for the approximation yields nearly the same results as using c_p^0 , since c_l^0 approximates c_p^0 with roughly 1% difference in the plateau region (see Figure 7.3(a)).

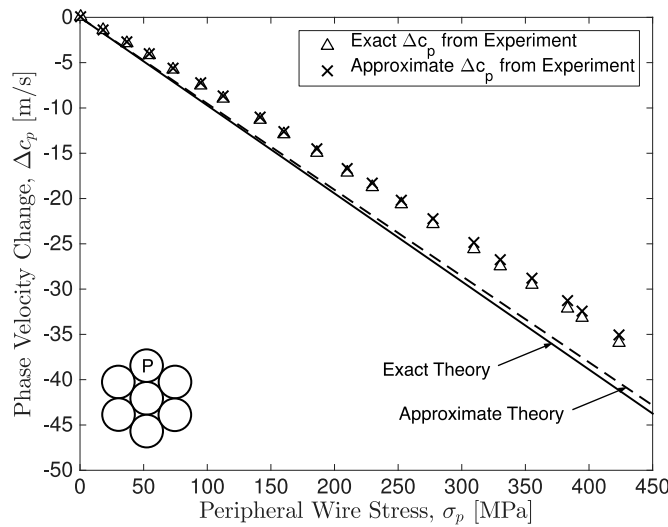


Figure 7.12: Experimental phase velocity change in the peripheral (P) wire for L(0,9) mode at $fd = 30.2$ MHz-mm. Experimental points shown for exact and approximate Δc_p (derived from experiment), using c_p^0 and c_l^0 , respectively. Theoretical changes overlain, showing exact theory (solid line) and the approximate theory (dashed line).

Theoretical phase velocity changes using exact and approximate methods are also overlain in Figure 7.12. In this case, uncertainty bounds are not plotted, in order to emphasize the mean values. The solid line corresponds to the velocity change found through computing the exact dispersion curves for a stressed rod from Equation 7.3. In contrast, the dashed line corresponds to the approximate theory based on the bulk velocity change, which may be calculated through Equation 7.9. It may be seen that the bulk wave-based approximate theory only differs from the exact theory by roughly 2%. For reference, at 1400 MPa (75% UTS) a 2% error corresponds to an error of less than 28 MPa. Although a minor difference in accuracy is introduced through the approximate methods, this may be acceptable in some situations, given the significantly simpler computations.

7.5. Monitoring Corrosion-Induced Stress Redistribution in Strands using Guided Waves

7.5.1. Background and Overview

Prestressed and post-tensioned steel structures have been widely used in bridge construction over the last 40 years. However, from a maintenance and inspection perspective, the evaluation of these structures is technically challenging. Corrosion is one of the most detrimental mechanisms in the load-bearing strands, where resulting stress concentrations can lead to fracture. The value of nondestructive stress monitoring in strands has inspired a variety of structural health monitoring strategies, including vibration [228], electromagnetic [229], and guided ultrasonic wave techniques [201].

Guided ultrasonic wave (GUW)-based approaches are particularly attractive because of their ability to interrogate large areas. A variety of approaches have been taken in the literature for GUW-based stress measurement in strands. They are based on the longitudinal family of GUWs, with the majority using the fundamental mode. Although a number of approaches have proposed using the stress dependence of GUW velocity (i.e., the acoustoelastic effect) to perform stress measurement [181], [182], [203], [204], [230], some have proposed other stress-dependent features as well [205], [207], [231]–[234].

To date, GUW-based stress monitoring approaches have only been validated in undamaged strands. Therefore, it is necessary to study the potential coupling between damage and stress change in order to validate the use of stress measurement approaches. Furthermore, aside from causing stress redistribution due to cross-section loss, corrosion increases surface roughness, which raises the attenuation of GUWs. However, monitoring stress redistribution in an area which is not directly corroding may be able to counteract this effect. Interestingly, it has been found that corrosion in strands takes place primarily in the peripheral wires, while the core remains relatively pristine [188], [235], [236]. Therefore, it may be possible to indirectly monitor corrosion by measuring stress redistribution using GUWs that specifically target the core wire.

Unlike the fundamental mode, higher-order modes have the potential to meet the above-mentioned requirements. This is due to a number of desirable properties, including [210], [213], [237]: (1) small surface displacement, resulting in low influence from surface conditions and low energy leakage (i.e., attenuation) between strand wires; (2) highest group velocity, making them the first arrival at a sensor; (3) low dispersion, allowing stable wave propagation; and (4) linear and stable stress dependence of velocity. A further benefit of higher-order modes (not noted in the literature) is that they may be well suited to data fusion approaches,

which have recently gained attention in GUV-based structural health monitoring [238], [239]. The suitability of higher-order modes in this context is due to the multiplicity of modes, yielding redundant information which may be processed through data fusion.

Motivated by the above considerations, this section exploits the velocity sensitivity of higher-order modes for core-wire stress monitoring in a corroding strand. Particular frequencies of these modes are targeted, which have the ideal properties outlined above. An accelerated corrosion experiment is carried out to demonstrate their stress measurement ability in a corroding strand up to the point of peripheral wire fracture. A modulation technique is proposed for reliably measuring velocity changes by eliminating the influence of artificial phase shifts. By generating several higher-order modes, the technique is used to make redundant estimates of stress change over the course of corrosion. The data fusion approach then combines the redundant information into a single stress change estimate. This estimate is modeled as a stochastic process, whose uncertainty is quantified using Gaussian process regression. The overall flowchart for stress measurement during corrosion is outlined in Figure 7.13.

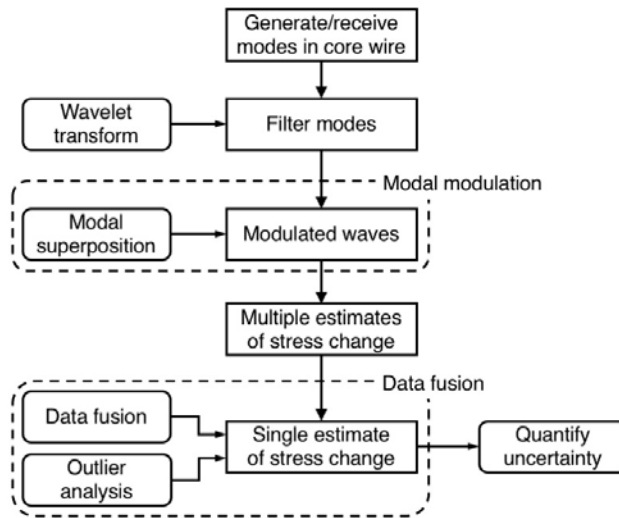


Figure 7.13: Flow chart for stress measurement during corrosion using higher-order modes

This section is organized as follows: First, the estimation of stress change using time change measurements of higher-order modes is reviewed in Sec. 7.5.2. Sec. 7.5.3 details the accelerated corrosion experiment and measurement equipment. Sec. 7.5.4 then describes the resulting corrosion process and the post-processing of measured data. Sec. 7.5.5 presents the results of stress measurement using higher-order modes, as well as the benefits of the modal modulation technique and data fusion approach.

7.5.2. Stress Measurement Using Higher-Order Modes

Higher-order modes are part of the longitudinal family of guided ultrasonic waves (GUWs), and are denoted L(0,2), L(0,3), L(0,4), etc. These modes can remain localized within the core wire of a strand, leading to advantageous properties for structural health monitoring (as mentioned in Sec. 7.3). These properties occur at specific frequencies, referred to here as *plateau frequencies*. However, it should be noted that they only take effect for sufficiently high order modes (roughly L(0,8) and above [237]). Since higher-order modes have little influence from surface conditions, they can be modeled by considering the simplified problem of wave propagation in a rod [237].

The phase and group velocity dispersion curves for longitudinal modes in a 5.22 mm diameter steel rod (representative of a core wire) are shown in Figure 7.14. In terms of the angular frequency ω^0 and wavenumber k^0 , the phase velocity $c_p^0 = \omega^0/k^0$ describes the velocity of a wavefront, while the group velocity $c_g^0 = d\omega^0/dk^0$ describes the velocity of energy transport (superscript 0 denotes an unstressed value). The solution of dispersion curves requires numerical computation, which is implemented here with an in-house code based on [240]. The material properties for steel used in the computation are derived from those in Sec. 7.3. The plateau frequencies for a series of higher-order modes are highlighted in Figure 7.14(a) and (b) in terms of the phase and group velocity. The asymptote toward the bulk longitudinal velocity at these frequencies may be seen in both plots. The true velocity differs from the bulk velocity by less than 1% at these frequencies; this error decreasing with increasing mode number. Additionally, the peaks in group velocity at the plateau frequencies may be seen in Figure 7.14(b), which also asymptote to the bulk velocity.

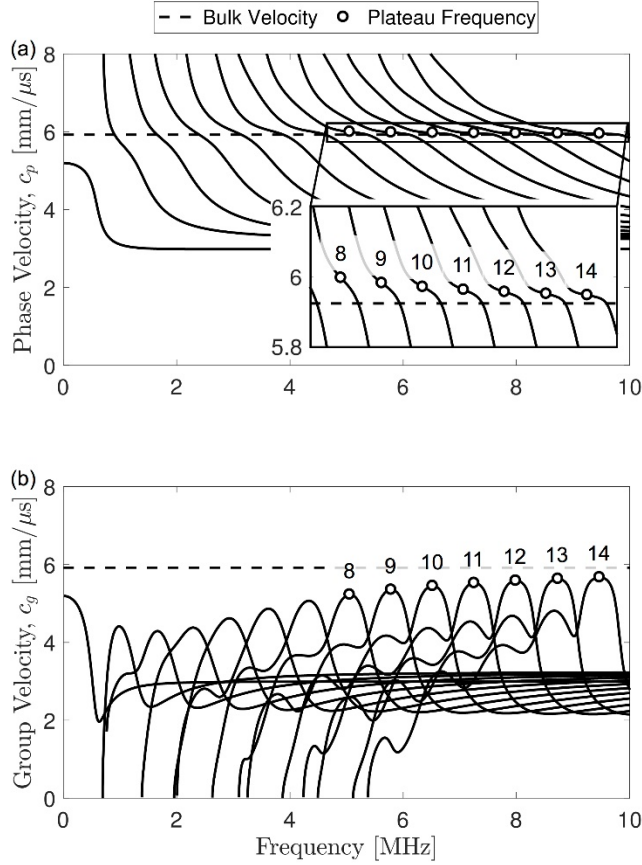


Figure 7.14: (a) Phase velocity and (b) group velocity dispersion curves for longitudinal modes in a (unstressed) 5.22 mm diameter steel rod. Higher-order modes $L(0,m)$ indicated by mode number $m = 8,9, \dots, 14$. Plateau frequencies of higher-order modes highlighted, with bulk longitudinal velocity c_l^0 overlain as dashed line.

In addition to the asymptotic velocity of higher-order modes, an analogous asymptote was demonstrated for the stress dependence of velocity in Sec. 7.3. In particular, a change in axial stress $\Delta\sigma$ changes the phase velocity to $c_p^0 + \Delta c_p$. The stress change is linearly related to the phase velocity change Δc_p through an acoustoelastic constant κ_p ,

$$\Delta c_p = \kappa_p \Delta\sigma$$

Equation 7.11

Although a similar expression may be formed for the group velocity, this section only focuses on the stress dependence of phase velocity, since it was shown to be more stable with respect to frequency in Sec. 7.4.2. At the plateau frequencies, κ_p asymptotes to the acoustoelastic constant κ for a bulk longitudinal wave,

$$\kappa_p \approx \kappa$$

The acoustoelastic constant was calibrated in Sec. 7.3 at $\kappa = -0.083$ (m/s)/MPa, which is the value used in this section.

7.5.2.1. Phase Velocity

Inverting Equation 7.11, a stress change $\Delta\sigma$ may be estimated by measuring the phase velocity change Δc_p . The phase velocity change may be computed by measuring the time change Δt in the phase of a waveform, as in Equation 7.7. Combining Equation 7.7 and Equation 7.11, the stress change may be estimated by measuring the time change,

$$\Delta\sigma = -\frac{(c_p^0)^2}{\kappa\ell} \Delta t$$

At this point, the asymptotic behavior shown in Figure 7.14(a) may be leveraged by inserting the bulk velocity c_l^0 for c_p^0 . This avoids the numerical computation of dispersion curves, which is well suited to field applications where computational resources may be limited. Since the material properties λ, μ, ρ may be obtained with sufficient accuracy (as opposed to l, m), it is not necessary to calibrate c_l^0 . Accordingly, the material properties λ, μ, ρ were obtained from [221] for Hecla 17 steel. Combined with the calibrated acoustoelastic constant κ , the stress change may be estimated as follows:

$$\Delta\sigma = -\frac{(c_l^0)^2}{\kappa\ell} \Delta t$$

7.5.2.2. Modal Modulation

A practical difficulty of implementing higher-order modes for stress measurement is that measurements of phase time changes may be sensitive to artificial phase shifts (e.g., due to sensor reattachment or replacement). In order to eliminate such sensitivity, a technique called modal modulation is introduced here. The main idea is to form a modulated wave through the superposition of two higher-order modes, thus canceling out any phase shift.

Let the displacements u and u' of two higher-order modes propagating along a rod axis z be

$$u = \exp[i(kz - \omega t + \phi)]$$

$$u' = \exp[i(k'z - \omega't + \phi)]$$

Equation 7.12

where ω, k and ω', k' are the angular frequency and wavenumber of the two modes at their respective plateau frequencies, and ϕ is an artificial phase shift. If the phase shift varies while stress is also changing, error will be introduced into the time change measurement. However, this error may be eliminated by superposing the two modes as follows: Without loss of generality, take $\omega' > \omega$ and $k' > k$. Denoting the angular frequency and wavenumber differences as $\Omega = \omega' - \omega$ and $K = k' - k$, the superposition of the two modes in Equation 7.12 yields the displacement

$$u + u' = 2 \cos\left(\frac{Kz - \Omega t}{2}\right) \exp\left[i\left(\frac{k + k'}{2}z - \frac{\omega + \omega'}{2}t + \phi\right)\right]$$

which is composed of a modulation (cosine) and a phase (exponential) term. As opposed to the phase term, it may be seen that the modulation is not influenced by the phase shift ϕ . The modulation term may be extracted by obtaining the envelope of the above as

$$\left|\cos\left(\frac{Kz - \Omega t}{2}\right)\right| = \frac{\mathcal{E}\{u + u'\}}{2}$$

Equation 7.13

where $|\cdot|$ denotes absolute value, and $\mathcal{E}\{\cdot\}$ computes the envelope of a wave according to

$$\mathcal{E}\{\cdot\} = |\cdot + i\mathcal{H}\{\cdot\}|$$

with $\mathcal{H}\{\cdot\}$ denoting the Hilbert transform. Figure 7.15 illustrates the extraction of the modulation term from the superposition of two harmonic waves, where the insensitivity to phase shift is demonstrated.

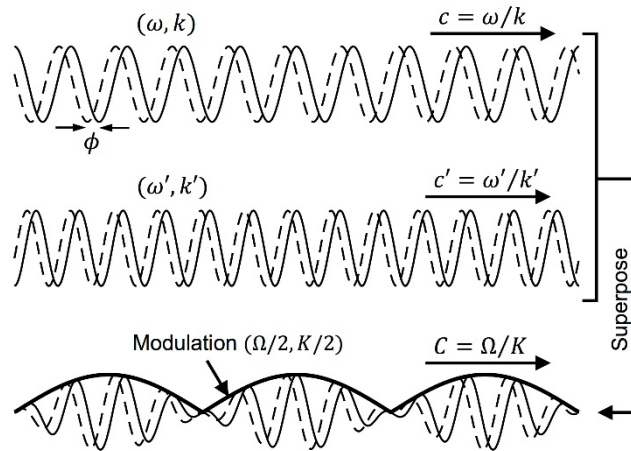


Figure 7.15: Superposition of two harmonic waves to form a modulated wave, where $\Omega = \omega' - \omega$ and $K = k' - k$. Phase velocities c, c' overlap, along with modulation velocity C .

Cases overlain for no phase shift (solid) and phase shift (dashed), showing no influence from phase shift on modulation.

Since higher-order modes asymptote to the bulk velocity at the plateau frequencies, the modulated wave propagates at a (unstressed) velocity C^0 of

$$C^0 = \frac{\Omega^0}{K^0} \approx c_l^0$$

Equation 7.14

The change in modulation velocity ΔC due to stress then approximates the bulk velocity change,

$$\Delta C \approx \Delta c_l = \kappa \Delta \sigma$$

Equation 7.15

Figure 7.16 shows the approximation of (a) the bulk velocity and (b) its stress dependence in terms of the modulation velocity from a series of higher-order mode pairs. It may be seen that the approximations in Equation 7.14 and Equation 7.15 are accurate to within 1% error. Therefore, the stress change may be estimated by measuring ΔC , while using the same acoustoelastic constant κ as is used for the phase velocity. This means that the time change Δt is measured from the modulation wave of a higher-order mode pair.

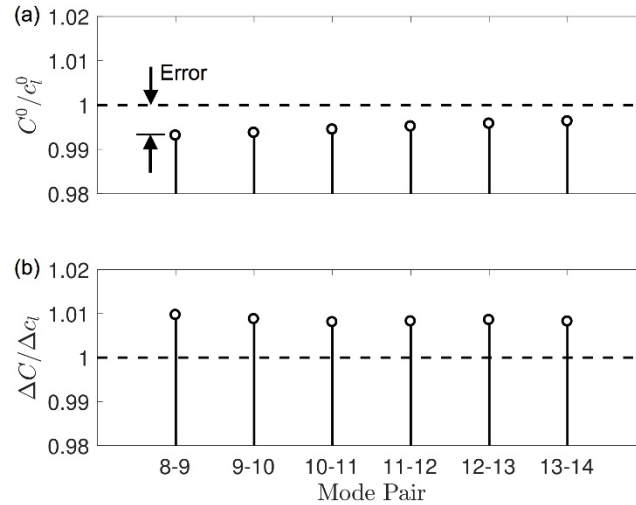


Figure 7.16: (a) Unstressed value and (b) stress dependence of modulation velocity for six higher-order mode pairs $L(0,m)-L(0,m+1)$ for $m = 8, 9, \dots, 13$. Modulation velocity values normalized against bulk velocity values, showing approximation to within 1% error.

7.5.2.3. Data Fusion and Outlier Analysis

The fact that multiple estimations of stress change may be obtained from multiple mode pairs presents the opportunity for combining their information to obtain more

robust estimations. To accomplish this, a data fusion approach is used here to combine the redundant information into a single stress change estimate. Since the data is commensurate, the fused data may be formed as a weighted combination of the original data. This is an intermediate level of data fusion, known as *feature-level fusion* [241].

Denote the estimate of stress change from the n -th mode pair by $\Delta\sigma^{(n)}$. Considering the fusion of N mode pairs, the fused data $\Delta\sigma$ is expressed as a weighted combination of $\Delta\sigma^{(n)}$,

$$\Delta\sigma = \sum_{n=1}^N w^{(n)} \Delta\sigma^{(n)}$$

where $w^{(n)} \in [0,1]$ is the weight of the n -th pair. Here, a two-step process is carried out to assign weights: (1) assign an initial weight based on the amplitude of the pair; (2) detect outlier pairs and set their weight to zero. Step 1 is based on the assumption that mode pairs with higher amplitude have greater reliability for feature extraction (i.e., stress change estimation). Step 2 involves outlier analysis, where the weight is set to zero for pairs that are classified as outliers.

Outlier classification is performed on the deviation statistic $z^{(n)}$ for a given mode pair n , defined [242]

$$z^{(n)} = \frac{|\Delta\sigma^{(n)} - M|}{S}$$

where M and S are the mean and standard deviation of the dataset. These statistics are computed using an *exclusive formulation* [242], where data for the n -th pair is excluded (i.e., M, S are found from the data $\Delta\sigma^{(i)}$ for $i \neq n$). This ensures that the statistics are not influenced by including data for the pair under consideration. A pair is then classified as an outlier if it exceeds two standard deviations,

$$z^{(n)} \leq 2 \quad (\text{non-outlier})$$

$$z^{(n)} > 2 \quad (\text{outlier})$$

Combining Steps (1) and (2) yields the weight assignment for a given mode pair in terms of the amplitude $A^{(n)}$ for that pair,

$$w^{(n)} = \begin{cases} \frac{A^{(n)}}{\sum_{i=1}^N A^{(i)}} & (\text{non-outlier}) \\ 0 & (\text{outlier}) \end{cases}$$

where $A^{(n)}$ is defined as the sum of the two constituent mode amplitudes within the pair.

7.5.2.3.1. Gaussian Process Regression

One of the primary purposes of data fusion is to decrease uncertainty in the estimated values [241]. This section considers estimating stress change over the course of corrosion, with estimates made at a series of corrosion levels. Therefore, the stress change estimate over the course of corrosion is treated as a normally distributed stochastic process (i.e., a Gaussian process). As such, its uncertainty may be quantified by Gaussian process regression (GPR) [243]. GPR is a non-parametric regression method which captures the trend and uncertainty in the data by providing a regression (mean) function along with a standard deviation function. The mean function $R(c)$ denotes the stress change at an arbitrary corrosion level c , which has a corresponding uncertainty defined by the standard deviation function $\Sigma(c)$.

Denoting the stress change data at a series of corrosion levels $\mathbf{c} = (c_1, c_2, \dots)$ by $\Delta\sigma = (\Delta\sigma_1, \Delta\sigma_2, \dots)$, the GPR may be computed as follows [243]:

$$R(c) = \mathbf{k}^T(c)\mathbf{Q}^{-1}\Delta\sigma$$

$$\Sigma(c) = q(c) - \mathbf{k}^T(c)\mathbf{Q}^{-1}\mathbf{k}(c)$$

where \mathbf{Q} is a covariance matrix, $q(c)$ is the covariance at corrosion level c , and $\mathbf{k}(c)$ is a kernel vector measured between the corrosion levels \mathbf{c} and c . To accommodate noisy measurements, the covariance matrix is defined in terms of a kernel matrix \mathbf{K} and a noise hyperparameter s_n as

$$\mathbf{Q} = \mathbf{K} + s_n^2\mathbf{I}$$

The elements K_{ij} of the kernel matrix are defined from a kernel function k , which is based on two hyperparameters s_f and s_l ,

$$K_{ij} = k(c_i, c_j) = s_f^2 \exp\left[-\frac{1}{2}s_l^2(c_i - c_j)^2\right]$$

The covariance at corrosion level c is then

$$q(c) = k(c, c) + s_n^2$$

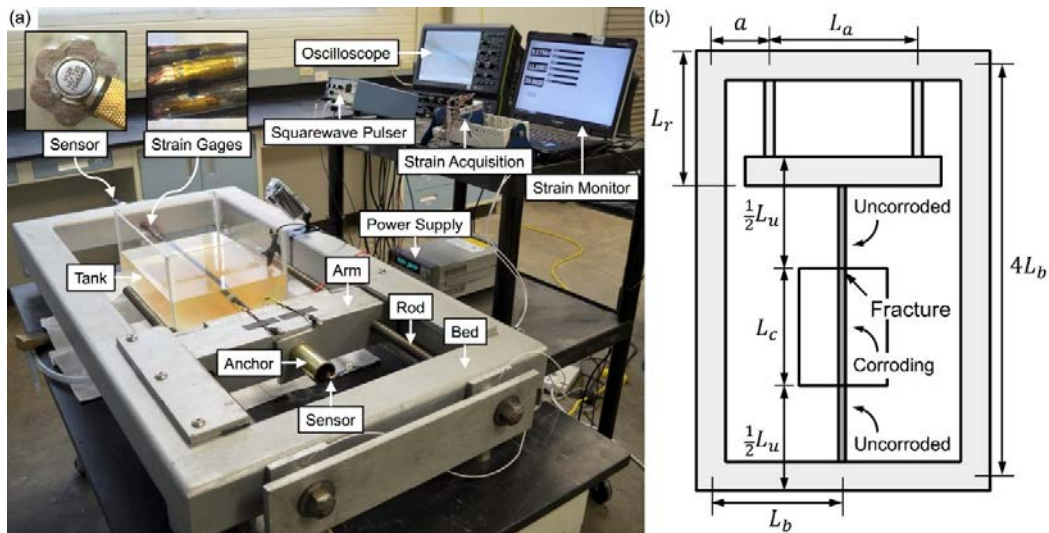
and the elements of the kernel vector $\mathbf{k}(c) = (k_1(c), k_2(c), \dots)$ are

$$k_i(c) = k(c_i, c)$$

GPR relies on numerically tuning the hyper-parameters S_f, S_l, S_n in order to maximize the probability of observing the data $\mathbf{c}, \Delta\sigma$ [243]. The numerical solution is performed here using in-house code.

7.5.3. Experiment

A loading frame was constructed to apply tensile stress to a prestressing strand, as shown in Figure 7.17. This is the same frame that was used in Sec. 7.3. The frame was composed of a bed, an arm, and two threaded rods. The bed and arm were built from square sections (AISC HSS4 × 4 × 1/4), composed of A500 Grade B steel. The square sections had a cross-sectional area of $A_b = 21.7 \text{ cm}^2$ (3.37 in²), and a moment of inertia of $I_b = 325 \text{ cm}^4$ (7.80 in⁴). The arm was reinforced with steel plates, so that its moment of inertia was $I_a = 1170 \text{ cm}^4$ (28.1 in⁴). The threaded rods were composed of corrosion-resistant 316 stainless steel with a 2.22 cm (7/8 in.) diameter.



Source: Images by Authors

Figure 7.17: (a) Experimental setup and data acquisition system for guided wave and strain monitoring of stressed strand under accelerated corrosion. Corrosion applied by impressing current in saltwater tank using power supply. (b) Schematic of loading frame, indicating relevant dimensions. Eventual peripheral wire fracture point near the tank edge shown.

The prestressing strand was composed of Grade 270 steel (UTS of 1860 MPa), with a nominal diameter of 15.2 mm (0.6 in.), and a lay angle of 7.9°. The strand had a yield strength of (at minimum) 90% UTS, or 1670 MPa. The core and peripheral wire diameters were measured at 5.22 and 5.08 mm, respectively. Within the anchors, the strand was composed of uncorroded and corroding segments. The strand length within these segments was $L_u = 0.719 \text{ m}$ (28.3 in.) and $L_c = 0.381 \text{ m}$ (15.0 in.), respectively. The length within the anchors (i.e., under stress) was then $L_u + L_c = 1.10 \text{ m}$ (43.3 in.). The cross-sectional area of the strand (i.e., of the

uncorroded segment) was $A_u = 143 \text{ mm}^2$ (0.222 in²). The dimensions of the frame and strand are depicted in Figure 7.17(b) and collected in Table 7.3.

Table 7.3: Loading Frame and Strand Dimensions

Dimension	Value [m]	Value [in.]
L_a	0.406	16.0
L_b	1.32	52.0
L_c	0.381	15.0
L_r	0.488	19.2
L_u	0.719	28.3
a	0.127	5.0

To record the strand deformation, six strain gages (Micro Measurements) were installed on the peripheral wires in the uncorroded segment, as shown in Figure 7.17(a). These were used to obtain the average axial strain e_u in the peripheral wires. For a strand with a 7.9° lay angle, the peripheral and core wire strains only differ by roughly 2% [182]. Therefore, the strain e_u was taken to describe the axial strain in the strand cross-section as a whole. The strand was initially loaded up to 480 MPa (69.7 ksi), or roughly 25% UTS, with an initial strain value of 2.28×10^{-3} .

7.5.3.1. Accelerated Corrosion Testing

Accelerated corrosion was carried out with the impressed current technique [188], as shown in Figure 7.17(a). In particular, a galvanic cell was constructed in a saltwater tank, through which DC current was applied. The cell was formed by submerging a segment (i.e., corroding segment) of the strand along with a copper mesh in a 5% NaCl saltwater solution within the tank. The strand, copper mesh, and saltwater served as the anode, cathode, and electrolyte, respectively. Current was applied and recorded with a power supply (Keysight), ranging from 1.5 to 3.0 A.

The current was applied in cycles, ranging from 2 to 5 hours in length. A total of 29 corrosion cycles were carried out, resulting in 94 total hours of accelerated corrosion. After each cycle, the tank was drained and the strand was allowed to dry for 24 hours with no applied current. Corrosion products were allowed to build up on the surface of the strand, in order to closely simulate naturally accumulating corrosion. Due to the strong sensitivity of corrosion rate to temperature [244], the temperature of the specimen was controlled at 22 to 24 °C (72 to 75 °F). The accelerated corrosion was terminated when a fracture occurred simultaneously in three adjacent peripheral wires. The fracture point is indicated in Figure 7.17(b), roughly 2 cm from one end of the tank.

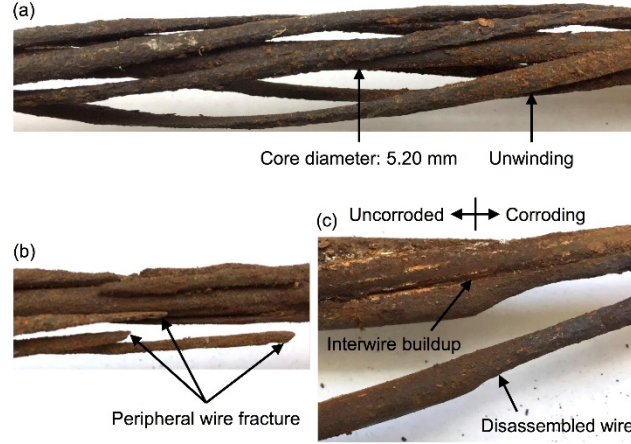
7.5.3.2. Higher-Order Mode Sensing

Higher-order modes were generated and received by piezoelectric transducers (Olympus) installed on either end of the strand, as shown in Figure 7.17(a). The transducers were 5 mm in diameter, nearly identical to the core wire diameter (5.22 mm). The modes were selectively generated in the core wire by installing the transducers (using hot glue) over its cross-section. The transducers were excited by a wideband squarewave pulse using a squarewave pulser-receiver (Olympus). The excitation was tuned to 7.5 MHz, which was used to target modes L(0,8)-L(0,14) from 5 to 10 MHz, as shown in Figure 7.20. High and low pass analog filters at 1 MHz and 10 MHz, respectively, were used to further suppress frequencies outside the target range. The modes were recorded on an oscilloscope (LeCroy), while sampling at 250 MHz and averaging 500 times.

An initial collection of higher-order mode signals was performed before corrosion (i.e., at cycle 0). Subsequently, signals were recorded after each corrosion cycle, following the 24-hour drying period. To investigate the performance of the proposed modal modulation technique, the transducers were reattached before each corrosion cycle, which introduced artificial phase shifts into the waveforms.

7.5.4. Corrosion Progression

The corrosion process in the strand was observed visually after each corrosion cycle. It was found that corrosion products gradually built up on the surface of the strand as the test progressed, and continued until the simultaneous three-wire fracture occurred in cycle 29. The strand was then unloaded and removed from the loading frame for further visual inspection, as shown in Figure 7.18. Due to unloading, the fractured wires further unwound within the corroding segment, as shown in Figure 7.18(a). However, it should be noted that the peripheral wires did not unwind in the uncorroded segment, as seen in Figure 7.18(c). Furthermore, near the edges of the corroding segment, corrosion products built up between the fractured wires and the core wire, which increased interwire friction. It was found that the core wire had a minor amount of corrosion products on its surface. This appears to have been predominantly suffered when the fractured wires unwound and directly exposed the core wire to saltwater. The core wire diameter was measured at 30 locations within the corroding segment, yielding an average value of 5.20 mm and a standard deviation of 0.09 mm. This is nearly the same as its uncorroded value (5.22 mm). In contrast, the peripheral wires suffered diameter losses of roughly 2 to 3 mm. This demonstrates that the large majority of mass loss took place in the peripheral wires [188], [235], [236].



Source: Images by Authors

Figure 7.18: Post-corrosion inspection of unloaded strand: (a) unwinding of peripheral wires, (b) fractured wires, and (c) interwire buildup of corrosion products near fracture point. Core wire diameter (5.20 mm) found to be nearly the same as before corrosion (5.22 mm).

Faraday's law was used to convert the applied current I to cumulative steel mass loss m . Specifically, the mass loss up to cycle c is found as [188],

$$m(c) = \frac{A}{ZF} \sum_{i=1}^c I(i)T(i)$$

where $A = 56$ g is the atomic mass of iron, $Z = 2$ is the ionic charge of iron, $F = 65,000$ A-s is Faraday's constant, and $T(i)$ is the amount of time current $I(i)$ was applied in cycle i . The percentage mass loss in the corroding segment may be calculated as m/M , with M the original mass of the corroding segment. The mass loss reached 45% by the completion of the test.

7.5.4.1. Stress Change Measurement

Structural analysis was carried out to convert the strain in the uncorroded segment to stress in the corroding segment. This was required, since strain gages could not be installed in the corroding segment. To this end, the structural system formed by the strand (i.e., uncorroded and corroding segments) and the loading frame was studied. As corrosion progressed, the strain in the uncorroded segment changed to $e_u = \bar{e}_u + \Delta e_u$. Considering linear elastic beam theory (including axial deformations), the uncorroded and corroding segment stress changes, $\Delta\sigma_u$ and $\Delta\sigma_c$, were found as

$$\Delta\sigma_u = E\Delta e_u$$

$$\Delta\sigma_c = -\left(1 + \frac{k_u}{k_f}\right) \frac{L_u}{L_c} E\Delta e_u$$

where the stiffnesses of the uncorroded segment and the frame are $k_u = 41.9$ kN/mm and $k_f = 66.5$ kN/mm, respectively.

Figure 7.19 shows the measured stress in the strand over the corrosion process. Here, the yield stress and ultimate tensile strength are overlain as dashed lines. The stress in the corroding segment closely approached the yield point in cycle 29, but did not exceed it. The fact that there was a peripheral-wire fracture in the corroding segment at subyield stress may be due to hydrogen embrittlement [245].

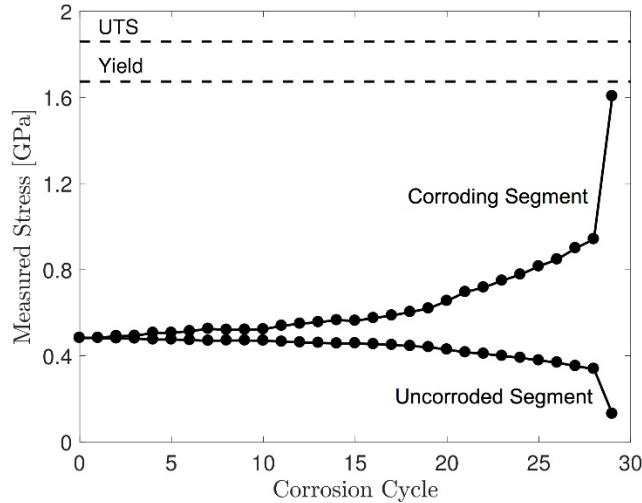


Figure 7.19: Measured axial stress in uncorroded and corroded segments of strand, computed from strain measured in uncorroded segment. Stress increase in corroding segment due to local cross-section loss, with final spike due to fracture.

7.5.5. Higher-Order Mode Stress Measurement

7.5.5.1. Reception and Filtering of Higher-Order Modes

The generation and reception of higher-order modes was confirmed by applying the wavelet transform. The wavelet transform $W(t, \omega)$ was computed using the Gabor mother wavelet, with parameters ω_0, γ set to 2π and 80 (as determined from Sec. 7.4.4). To compare the results to the theoretical dispersion curves in Figure 7.14(b), it is also useful to express the wavelet transform in terms of the group velocity as $W(c_g, \omega)$. This may be done by inverting the time axis and scaling by the propagation distance.

Figure 7.20 shows the scalogram $|W|^2$ of the wavelet transform at four corrosion cycles, as plotted against frequency and group velocity. Seven higher-order modes were generated within the targeted frequency range (5–10 MHz), which are highlighted in the figure. These modes were L(0,8)-L(0,14), whose plateau frequencies are 5.05, 5.80, 6.50, 7.25, 8.00, 8.80, and 9.50 MHz, respectively. For comparison with Figure 7.14(b), the dispersion curves for longitudinal modes are

overlain in Figure 7.20. As corrosion increased, the only regions of the dispersion spectra that were not significantly attenuated were near the plateau frequencies, as seen from Figure 7.20(a) to (b).

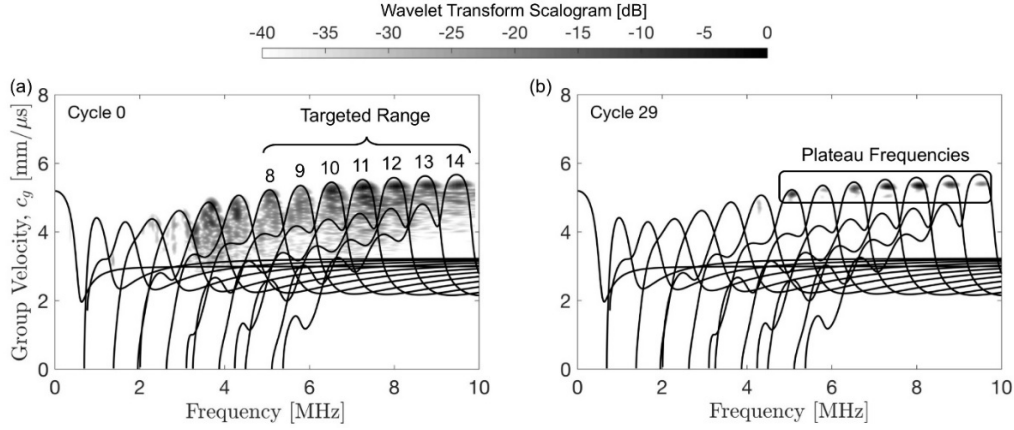


Figure 7.20: Wavelet transform scalogram (–40 to 0 dB) in group velocity-frequency space at two corrosion cycles. Group velocity dispersion curves overlain. Higher-order modes $L(0, m)$, $m = 8, 9, \dots, 14$ generated in frequency range 5–10 MHz are indicated. Due to increasing attenuation, only the plateau frequencies remain by cycle 29.

Aside from visualizing the arrival of each mode, the wavelet transform may also be used as a narrowband filter. This was used to extract signals of higher-order modes at their plateau frequencies. Denoting the plateau frequency of the m -th mode as $\omega^{(m)}$, the filtered signal $x^{(m)}$ for that mode was extracted from the wavelet transform as

$$x^{(m)}(t) = \Re W(t, w^{(m)})$$

where \Re denotes the real part.

7.5.5.2. Modal Modulation-Based Stress Measurement

The proposed modal modulation technique was carried out as follows (see Figure 7.21): First, consecutive higher-order modes $L(0, m)$, $L(0, m + 1)$ were grouped into pairs. Their filtered signals $x^{(m)}(t)$ and $x^{(m+1)}(t)$ were then computed, which were normalized to give each a unit amplitude and then superposed. The envelope of the superposition was then obtained using Equation 7.13, which corresponds to the modulation wave of the two modes.

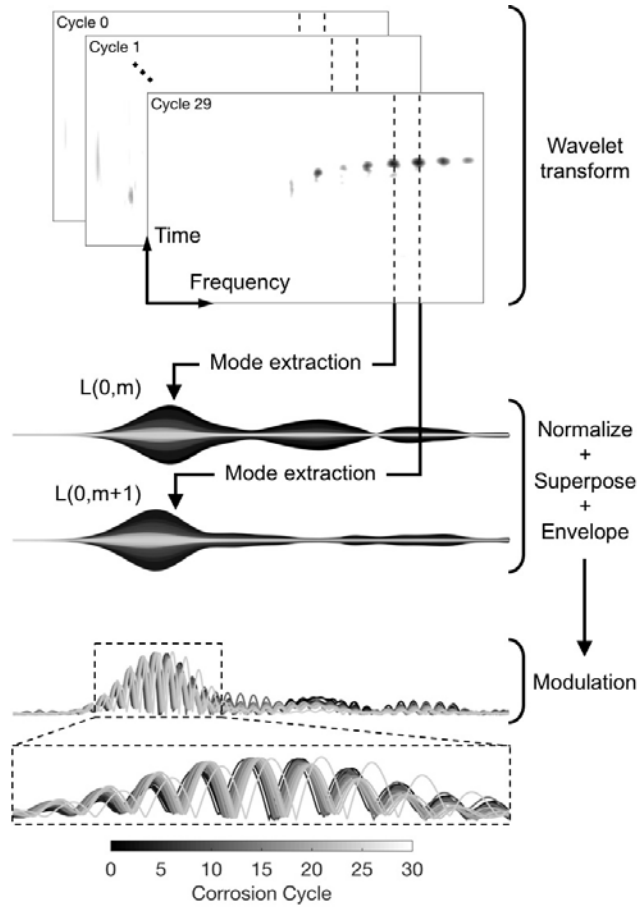


Figure 7.21: Extraction of modulation waves used for stress measurement. Consecutive higher-order modes $L(0, m)$ and $L(0, m + 1)$ extracted in pairs and superposed to form modulations.

Once the modulation waves were obtained, their time change over the corrosion process was measured. This was performed by tracking a peak in the modulations as follows: First, the peak in the cycle 0 modulation wave was obtained, which served as a reference. The change in this peak was then tracked in the modulation waves for subsequent cycles, from which the time change was measured. The time change Δt was then converted to the stress change $\Delta \sigma$ as

$$\Delta \sigma = -\frac{(c_l^0)^2}{\kappa(L_u + L_c)} \Delta t$$

Equation 7.16

Since the propagation path contained both the uncorroded and corroding segments, the estimated stress change from Equation 7.16 represents the average stress change along the strand. In order to compare this to the measured values, the average stress change $\Delta \sigma$ was obtained from the changes in the uncorroded and corroding segments,

$$\Delta\sigma = \left(\frac{L_u}{L_u + L_c}\right)\Delta\sigma_u + \left(\frac{L_c}{L_u + L_c}\right)\Delta\sigma_c$$

Equation 7.17

Figure 7.22 shows the stress change estimates using Equation 7.16 for six higher-order mode pairs, with the measured change from Equation 7.17 overlain. It may be seen that the estimation of stress change using higher-order modes shows good agreement with the measured values. The initial slow rate in stress change up to cycle 20 may be seen in the estimates, as well as the subsequent increasing rate beyond this cycle. Importantly, the spike in stress change caused by peripheral wire fracture in cycle 29 is revealed from each mode pair. In particular, the largest cycle-to-cycle change in the estimated data is from cycle 28-29, where the fracture occurred. To quantify the uncertainty in the estimates, Gaussian process regression (GPR) was computed and overlain in Figure 7.22. Some variation in the uncertainty may be seen between different mode pairs, with the standard deviation of the GPR ranging from 27 to 41 MPa.

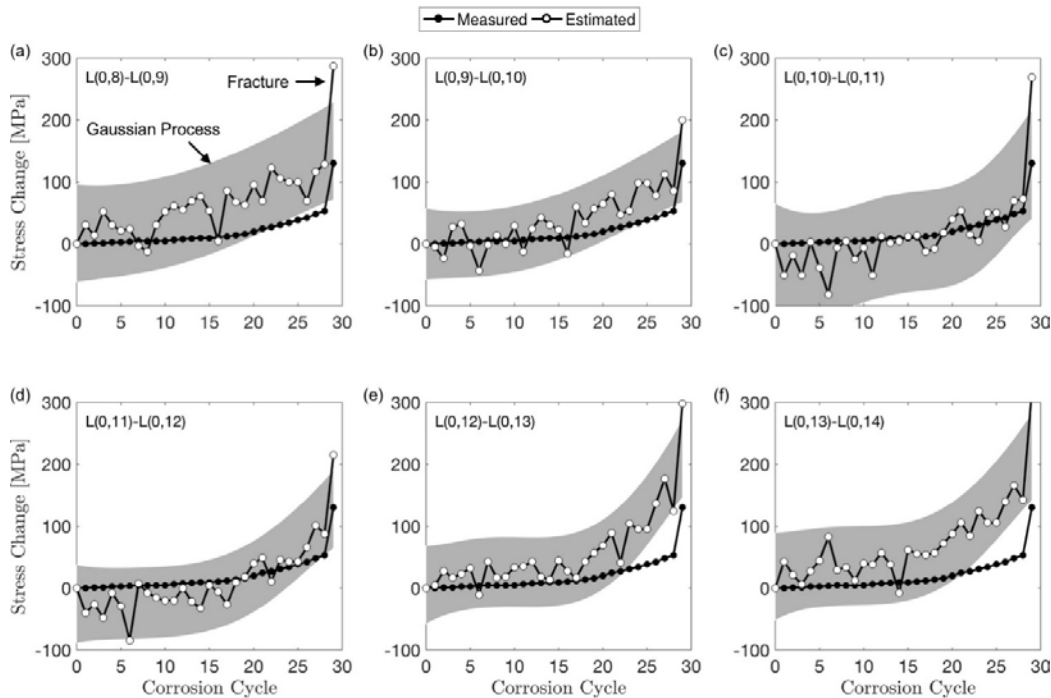


Figure 7.22: Stress change estimated using velocity change for six higher-order mode pairs, shown in (a)-(f), respectively. Velocity change measured at plateau frequency for each mode. Shaded area overlain as 95% confidence interval from Gaussian process regression. Stress change measured based on strain gages overlain.

7.5.5.3. Data Fusion

The previous subsection demonstrated that multiple higher-order mode pairs yield redundant estimations of stress change. Therefore, a data fusion approach is taken in order to combine the data shown in Figure 7.22 into a single stress change

estimate. In particular, data fusion was performed by at each corrosion cycle. The amplitudes input to the weight assignment were obtained from the wavelet transform at each cycle, as shown in decibels in Figure 7.20.

Figure 7.23 shows the estimated stress change using data fusion, with the measured stress change overlain. It may be seen that the initial period up to 17% mass loss (cycle 1–15), which had a slow rate of stress change, was accurately captured by the data fusion estimate. Although there was considerable mass loss, the estimates were able to capture that the strand had not yet significantly lost load-carrying capacity. These estimates were achieved even with significant surface roughness and corrosion products building up on the surface of the strand. It demonstrates the advantage of using higher-order modes in the core wire, which diminishes the influence of surface effects. This may be contrasted to the fundamental mode, which is more sensitive to geometrical effects like surface roughness [201]. Although there was a slight divergence from the measured stress change after cycle 20, the major spike caused by peripheral wire fracture at cycle 29 was well identified. GPR was also performed to quantify the uncertainty of the fused data, which is overlain in Figure 7.23. It may be seen that the uncertainty of the estimated stress change was lower for the data fusion results than for any of the original mode pairs. Specifically, the standard deviation of the fused data was 25 MPa (defined as the average standard deviation of the GPR). In contrast, the standard deviation for the original data ranged from 27 to 41 MPa. Greater confidence was therefore found when using data fusion to estimate the stress change, as opposed to using a single mode pair.

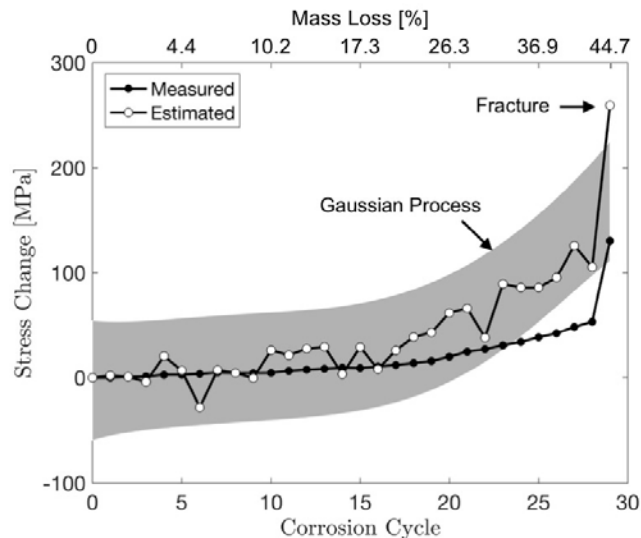


Figure 7.23: Stress change estimated using data fusion of six higher-order mode pairs, ranging from $L(0,8)$ - $L(0,14)$. Shaded area overlain as 95% confidence interval from Gaussian process regression. Stress change measured based on strain gages is overlain.

7.6. Corrosion Monitoring in Prestressed Concrete using Acoustic Emission

7.6.1. Background and Overview

Prestressed concrete members have been widely used in bridge construction over the last fifty years. In these types of structures, corrosion of the steel strands has become of increasing concern for designers, owners, and regulators. Currently, corrosion damage assessment of prestressed concrete members is performed using some form of periodic visual inspection (VI) procedure involving, among other items, the examination of cracking or spalling of concrete. While VI procedures are well-established and can be used to provide a great deal of information pertaining to the performance of a structure, these inspections are time consuming and their findings often depend on the experience and judgment of the inspectors. Moreover, the general inaccessibility of the strands makes the evaluation difficult, costly, and often inconclusive. There is a pressing need to transition from periodic VI established on the basis of limited-to-no-knowledge of likely damage to an automated real-time condition-based inspection method that could be performed on a daily basis. This paradigm shift can be achieved by equipping structures with sensing and analysis systems to enable real-time awareness. An effective monitoring strategy shall not only prevent catastrophic failures but also flag warnings of early deterioration to reduce the costs associated with mitigation strategies. Structural health monitoring strategies based on networks of piezoelectric sensors, which have the capability of receiving acoustic emission (AE) signals, are among the most promising candidates. Acoustic emission is based on continuously “listening” to the sudden releases of energy within a medium due to damage progression, with successful applications demonstrated in a variety of civil structures (e.g., masonry [246], strands [247], steel-concrete shear walls [248], and pipelines [249]). The continuous aspect of AE allows for large amounts of data to be collected, from which a wealth of information may be strategically extracted.

A wide range of AE studies have been investigated for evaluating corrosion in prestressed and reinforced concrete [250]–[264]. These have largely used feature-based AE, with most considering features related to AE activity and frequency content. Acoustic emission activity may refer to the cumulative amount of AE energy recorded, for instance, while frequency content may refer to peak frequency. In particular, numerous researchers have found that the onset of corrosion produces a definitive spike in AE activity [252], [254], [257], [260]–[262]. This feature was also found to indicate concrete cracking due to corrosion buildup, which results in additional AE activity spikes [250], [251], [262]–[264]. Other researchers have found the overall trends in AE activity to be correlated with the extent of corrosion [255], [256], [258], [259], [262]. On the other hand, studies have shown that

considering frequency content may allow for different corrosion mechanisms to be distinguished [253], [265].

With prevalent AE sensors continuously collecting and recording massive amounts of information, there is no doubt this is an era of data deluge. Making sense of and learning from the massive-scale data will constitute a crucial step to facilitate rational decision-making regarding the safety and reliability of a structure. Fortunately, such a large collection of data points (i.e., a datacloud) brings about the possibility of gathering new types of information about corrosion. This includes the shape (i.e., topology) of an AE datacloud itself. Topological data analysis (TDA) has emerged as a quantitative computational method for studying the topology of dataclouds [266]. It is a form of data science based on algebraic topology, with noteworthy applications in time series analysis [267], classification of breast cancer subtypes [268], and natural image statistics [269]. Through TDA, it has been demonstrated that meaningful information can be embedded in a datacloud's topology [267]–[269]. However, to the best of the author's knowledge, no prior studies have been carried out on applying TDA within AE, let alone within a nondestructive testing or structural health monitoring framework.

This section proposes that meaningful information (particularly related to corrosion) may be embedded within the topology of an AE datacloud. To evaluate this proposition, an experimental corrosion study is carried out on a prestressed concrete specimen. Since real corrosion may span years to decades, accelerated corrosion testing of the specimen is conducted in a laboratory setting, using chloride penetration in particular. To gain a benchmark understanding of the induced corrosion, the test incorporates visual inspection, mass loss measurements, and traditional feature-based AE monitoring. Informed by these methods of the physical significance behind the AE data, TDA is then investigated for the extraction of additional corrosion indicators. In particular, the evolution of the AE datacloud's topology over the corrosion process is studied.

This section is organized as follows: First, the process of chloride-induced corrosion in prestressed concrete and the associated AE is briefly overviewed in Sec. 7.6.2. Afterward, the theoretical application of TDA to an arbitrary datacloud is presented in Sec. 7.6.3. Section 7.6.4 describes the accelerated corrosion experiment conducted on two prestressed concrete specimens, with a benchmark corrosion assessment formed in Sec. 7.6.5. The results of TDA are then presented and discussed in Sec. 7.6.6.

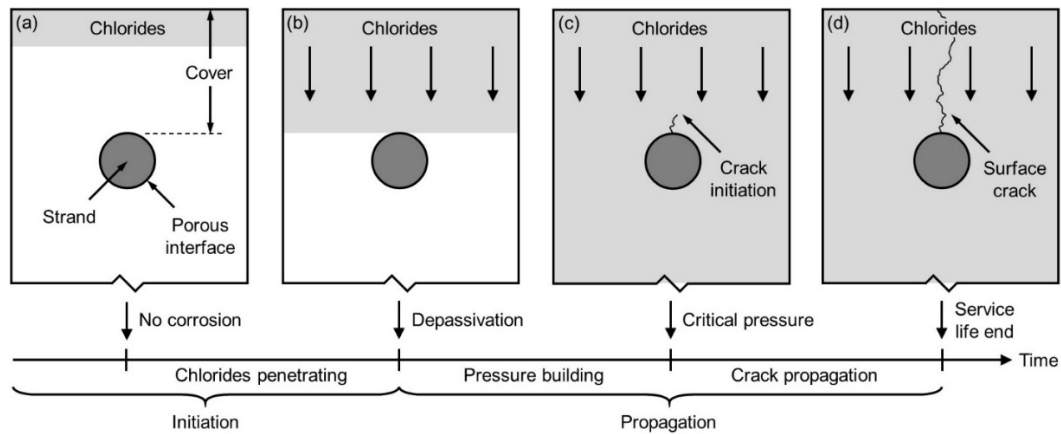
7.6.2. Corrosion Process and Acoustic Emission

In order to aid in the benchmark assessment of corrosion and interpretation of results, this section briefly outlines the process of corrosion in prestressed concrete.

In addition, corrosion-induced acoustic emission (AE) is described in terms of the primary AE features considered in this report.

A widely accepted model of chloride-induced corrosion in concrete is that of Tuutti [270], [271]. The model divides the service life of corroding concrete into two stages: (1) initiation; and (2) propagation. The initiation stage is the time required for chlorides to penetrate to the strand, at which time corrosion onsets and the propagation stage begins. The end of the propagation stage is based on the definition of service life, which is usually taken as the point when visible surface cracks emerge in the concrete [272], [273].

Schematics of four major points in the corrosion process are shown in Figure 7.24. First, an arbitrary point during the initiation stage is shown in Figure 7.24(a), where chlorides are penetrating through the concrete cover but have not yet reached the strand.



Source: Images by Authors

Figure 7.24: Illustration of chloride-induced corrosion in prestressed concrete cross-section. (a) No corrosion before chlorides reach strand. (b) Depassivation when chlorides penetrate to strand. (c) Corrosion products have expanded into porous interface, reaching critical pressure for crack initiation. (d) End of service life when crack reaches surface.

Therefore, no corrosion is taking place during this stage. The end of the initiation stage is shown in Figure 7.24(b), where chlorides reach the strand. At this point, the chlorides begin to break down the passive layer surrounding the strand [260], thus depassivating it and increasing the corrosion sensitivity. It has been demonstrated that AE activity can be used to detect depassivation (i.e., corrosion onset) [257], [260], [261], as indicated by the first spike in AE activity. Between depassivation and concrete crack initiation, corrosion products accumulate in the thin (roughly 10–20 μm thick) porous interface between the strand and the concrete [274], [275]. Once the porous interface is saturated, however, pressure due to corrosion buildup can increase beyond the capacity of the concrete cover. The point

at which a critical pressure is reached may be seen in Figure 7.24(c), resulting in crack initiation through the cover. Such crack initiation has been demonstrated to produce additional AE activity spikes [251]. With further corrosion buildup, the crack may propagate until it reaches the surface, marking the end of service life, as shown in Figure 7.24(d). Again, the propagation of cracks may also cause additional AE activity spikes [251]. For a 45 mm (1.8 in.) cover, such surface cracking can be caused by as little as 4 to 6% mass loss in the strand [276]. In addition, the surface cracking can raise the corrosion rate due to the freer penetration of chlorides [272]. From work on prestressing strands [265] and reinforced concrete [253], it has been demonstrated that different corrosion mechanisms produce AE with different frequency content. Therefore, studying frequency content in addition to AE activity can provide a greater depth of corrosion information. In this report, the considered AE features are cumulative energy, cumulative number of hits, and peak frequency, as illustrated in Figure 7.25 for a typical AE hit.

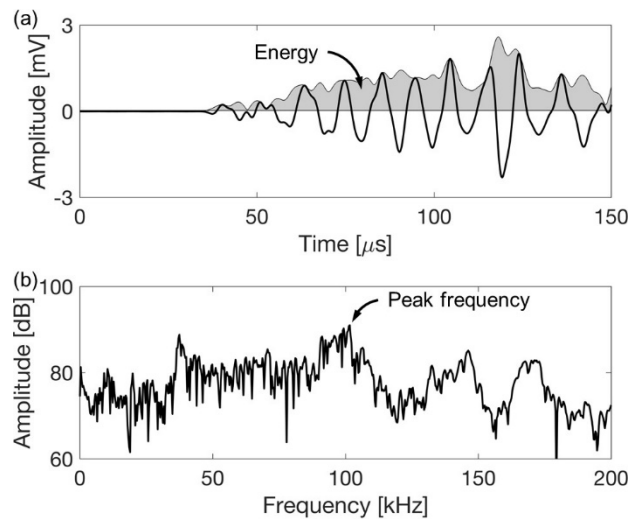


Figure 7.25: Features derived from typical acoustic emission hit, including energy and peak frequency. Hit shown in (a) time domain and (b) frequency domain.

7.6.3. Topological Data Analysis

The main idea motivating topological data analysis (TDA) is that a collection of data points (i.e., a datacloud) has shape, and its shape has meaning [269]. The concept of data having shape (i.e., topology) is illustrated in Figure 7.26(a) for a 2D datacloud with the topology of an annulus. Indeed, in this example the datacloud consists of 25 points randomly sampled from the annulus outlined in Figure 7.26(a). It should be noted that a datacloud itself does not directly disclose its topology, since topology is associated with continuous objects (e.g., the outlined annulus). What is therefore required is a sophisticated method of analyzing the datacloud in order to extract its underlying topology.

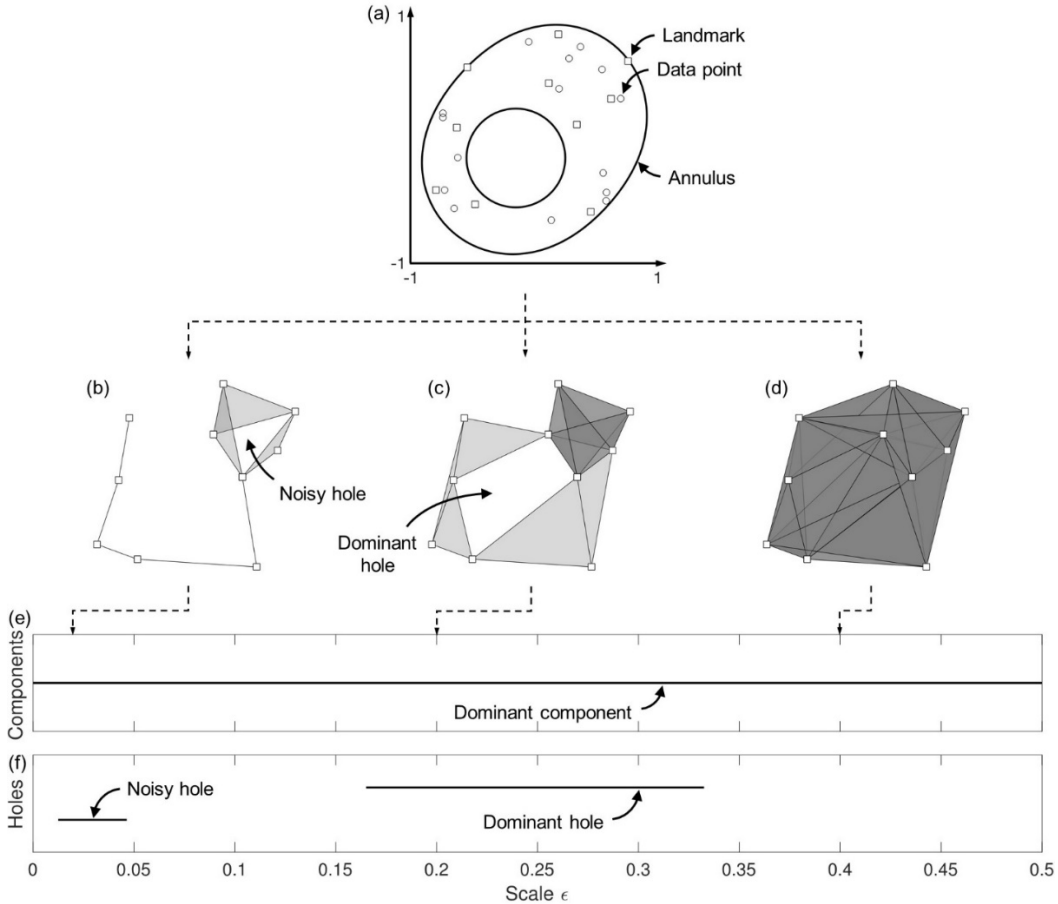


Figure 7.26: Example of topological data analysis for (a) randomly sampled datacloud from a 2D annulus (one component, one hole) with landmarks indicated by squares. (b)–(d) Witness complexes constructed from landmarks, corresponding to three values of ϵ (0.02, 0.20, 0.40). Barcodes for number of (e) components and (f) holes, revealing one component and one hole (the true topology of the annulus).

TDA is designed to meet this purpose by using the relative positions of data points to transform the datacloud into a topological object, from which topological characteristics may be measured. The topological object is a collection of simplices (termed a simplicial complex), which is constructed by “viewing” the datacloud at a given scale ϵ and measuring the connectivity between data points. Here, an n -D simplex is defined as the convex hull of $n + 1$ data points [277]. For instance, a 0-simplex is a point, a 1-simplex is a line, and a 2-simplex is a triangle, with the data points forming the vertices of the simplex in each case. Different forms of simplicial complexes may be adopted, such as the Cech and Rips complexes [266]. However, these complexes may become computationally expensive for large dataclouds. In such cases, the witness complex serves as a computationally efficient alternative [278].

The witness complex achieves computational efficiency by being constructed on only a small subset of data points, known as *landmarks*. Given a selection of

landmarks from a datacloud, a p -simplex of the witness complex is defined as follows: let a subset of the landmarks be denoted $\mathbf{l}_0, \dots, \mathbf{l}_p$, and an arbitrary point in the datacloud be \mathbf{z} (the witness). Further, denote the distance from the $(p + 1)$ -th nearest landmark to \mathbf{z} as $d_p(\mathbf{z})$. For a given ϵ , the p -simplex $\{\mathbf{l}_0 \cdots \mathbf{l}_p\}$ belongs to the witness complex \mathcal{W} if there exists a witness point \mathbf{z} satisfying

$$\|\mathbf{l}_i - \mathbf{z}\|_2 \leq d_p(\mathbf{z}) + \epsilon \quad \text{for } i = 0, \dots, p$$

as well as if each of the $(p - 1)$ -simplices $\{\mathbf{l}_0 \cdots \hat{\mathbf{l}}_i \cdots \mathbf{l}_p\}$, $i = 0, \dots, p$ belong to \mathcal{W} [279], with a hat $\hat{}$ indicating that the data point is absent from the simplex. For the special case of $p = 0$, the 0-simplices are the landmarks themselves. It has been suggested that the landmarks be selected using the *maxmin* algorithm [278]. However, it should be noted that the number of landmarks is a user-specified parameter, and there is no definitive optimal value for a given datacloud. Examples of the witness complex applied to the datacloud in Figure 7.26(a) may be seen in Figure 7.26(b)-(d), corresponding to three values of ϵ . For illustration, ten landmarks are selected from the datacloud and are indicated by squares.

The witness complexes shown in Figure 7.26(b)-(d) each provide a topological description of the datacloud at a particular scale ϵ . However, since there is no single best value of ϵ , a holistic representation of the datacloud's topology may be obtained by studying the witness complex's topology from small to large ϵ [280]. Thus, "true" topological characteristics are identified as those that exist over a wide range of ϵ . Conversely, those which only appear over a brief range of ϵ may be treated as noise [269]. In the n -D case, the relevant topological characteristics are the *Betti numbers*, denoted $\beta_0, \dots, \beta_{n-1}$, where β_i represents the number of i -D holes. As special cases, β_0 and β_1 are also termed, respectively, the number of connected components (termed components here) and the number of loops (termed holes here) [269]. For instance, the 2D annulus considered in Figure 7.26(a) has one component and one hole, as indicated.

Determining the Betti numbers of a simplicial complex (e.g., witness complex) involves breaking it up into a series of simpler complexes [277], as visualized in Figure 7.27.

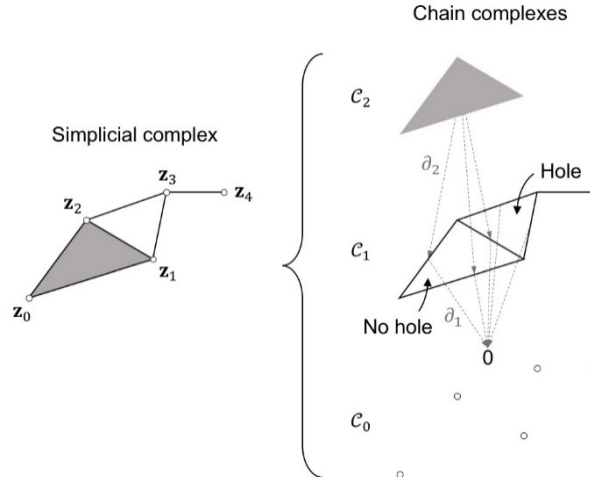


Figure 7.27: Determining the number of holes (first Betti number) in a simplicial complex using its associated chain complexes $\mathcal{C}_0, \mathcal{C}_1, \mathcal{C}_2$. Certain mappings of the boundary operators ∂_1, ∂_2 are shown as dashed arrows. Only one of the cycles in \mathcal{C}_1 has a hole, since the other is “filled in” in \mathcal{C}_2 .

These are termed *chain complexes*, and are denoted $\mathcal{C}_0, \dots, \mathcal{C}_n$, where \mathcal{C}_i contains only the i -simplices in the original simplicial complex. The chain complexes then have boundary operators $\partial_0, \dots, \partial_n$, which map elements in one complex to those in the next lowest dimension. This mapping operates as follows: for a given i -simplex $\{\mathbf{z}_0 \cdots \mathbf{z}_i\}$ in \mathcal{C}_i , the boundary operator ∂_i yields a linear combination of $(i - 1)$ -simplices in \mathcal{C}_{i-1} [277],

$$\partial_i\{\mathbf{z}_0 \cdots \mathbf{z}_i\} = \sum_{j=0}^i (-1)^j \{\mathbf{z}_0 \cdots \hat{\mathbf{z}}_j \cdots \mathbf{z}_i\}$$

Examples are shown in Figure 7.27 of the boundary operator mapping between chain complexes. It may be seen that the simplicial complex in this figure has one hole, which may be determined by studying the boundary operator. For example, as shown in Figure 7.27, the 2-simplex $\{\mathbf{z}_0 \mathbf{z}_1 \mathbf{z}_2\}$ is mapped using ∂_2 to the element $\{\mathbf{z}_1 \mathbf{z}_2\} - \{\mathbf{z}_0 \mathbf{z}_2\} + \{\mathbf{z}_0 \mathbf{z}_1\}$. In other words, this element is in the image of ∂_2 (denoted $\text{img}\{\partial_2\}$), and is termed a *boundary* [277]. It may be seen that this element appears to have a hole, along with the element $\{\mathbf{z}_2 \mathbf{z}_3\} - \{\mathbf{z}_1 \mathbf{z}_3\} + \{\mathbf{z}_1 \mathbf{z}_2\}$, both of which are mapped to 0 using ∂_1 . These elements are thus in the kernel of ∂_1 (denoted $\text{ker}\{\partial_1\}$), and are termed *cycles* [277]. The holes in \mathcal{C}_1 are then those cycles which are not also boundaries (i.e., those cycles which are not “filled in” in \mathcal{C}_2 [281]). Therefore, only the cycle $\{\mathbf{z}_2 \mathbf{z}_3\} - \{\mathbf{z}_1 \mathbf{z}_3\} + \{\mathbf{z}_1 \mathbf{z}_2\}$ has a hole, and there is then one hole in the simplicial complex. This procedure generalizes to an arbitrary dimension: the i -D holes in \mathcal{C}_i are those cycles which are not also boundaries from \mathcal{C}_{i+1} . The Betti number β_i , counting the number of independent i -D holes, is then [280]

$$\beta_i = \text{rank}\{\ker\{\partial_i\}\} - \text{rank}\{\text{img}\{\partial_{i+1}\}\}$$

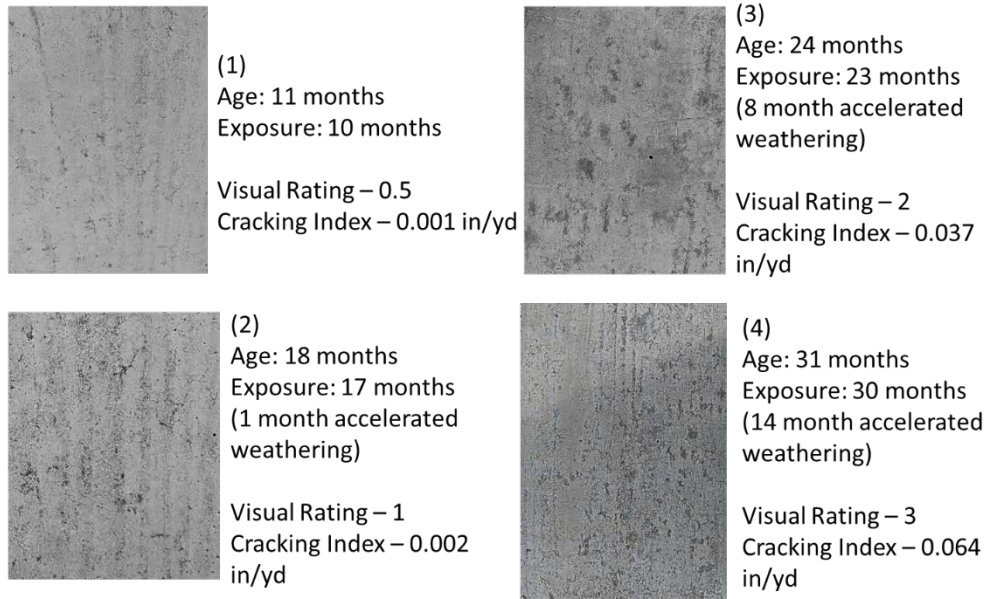
The evolution of the Betti numbers over a range of ϵ provides a holistic topological representation of a datacloud; it is commonly visualized in the form of a *barcode* [266], [269], as shown in Figure 7.26(e) and (f) for components and holes, respectively. Here, the barcode represents each component (or hole) as a line extending over the range of ϵ for which it exists. Those that are truly characteristic of the datacloud therefore have longer lines (i.e., exist longer) than those which may be noise. For this example, the Betti number computation is performed using the javaPlex software [279]. Here, one component and two holes are identified in the barcodes. However, the barcode for one of the holes is significantly shorter than the other (roughly one-quarter of the length), suggesting that it may be noise. The observation of one dominant component and one dominant hole captures the true topology of the annulus from which the datacloud was sampled. Analyzing the barcodes therefore allows the topology of a datacloud to be measured.

7.6.4. Experiment

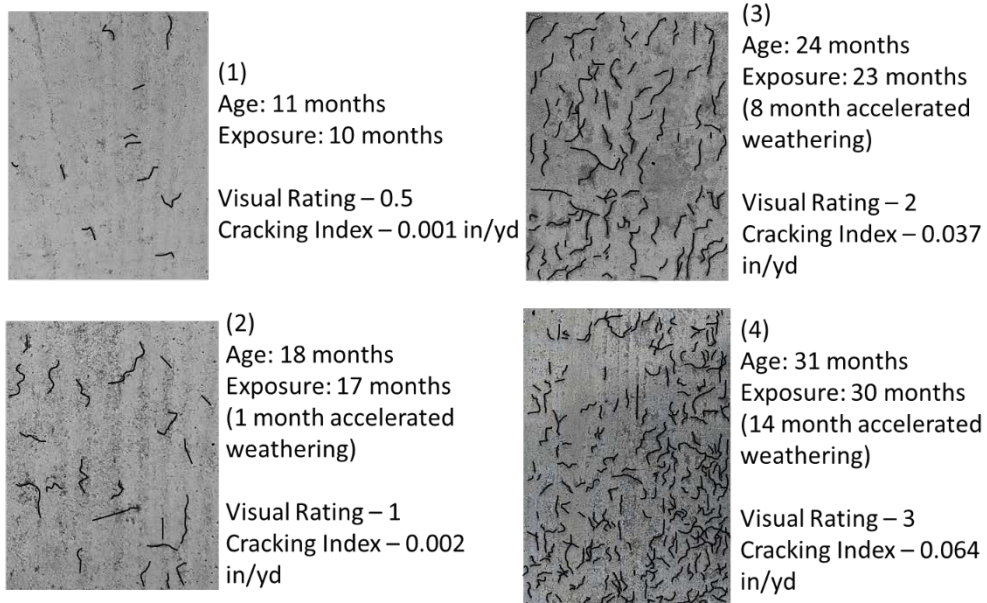
7.6.4.1. Test Specimens

A prestressed specimen was designed with the goal of mimicking a girder specimen. The specimen was reinforced with a pre-stressing strand with a 2-inch cover. The selection of mix proportions is discussed in Section 5.5.2.3.2. The mixture proportions are provided in Table 5.1. Two prestressed concrete test specimens were considered for corrosion testing in this task:

- Specimen A (control): Placed indoors at 73°F to perform as a control specimen. The block was 8 months old when the test began.
- Specimen B (with microcracking): Exposed to the atmosphere after 28 days of curing until the specimen exhibited surface microcracking. The block did not show signs of adequate surface microcracking with just exposure to the environment. Thus, to accelerate the cracking, the block was exposed to accelerated weathering by subjecting the block to four cycles of surface wetting and drying each day. The progression of microcracking is shown in Figure 7.28. Testing on specimen began at 31 months when the specimen had a surface microcracking of 0.064 in./yd or a visual rating of 3.



(a) Progression of Microcracking



(b) Microcracking Highlighted

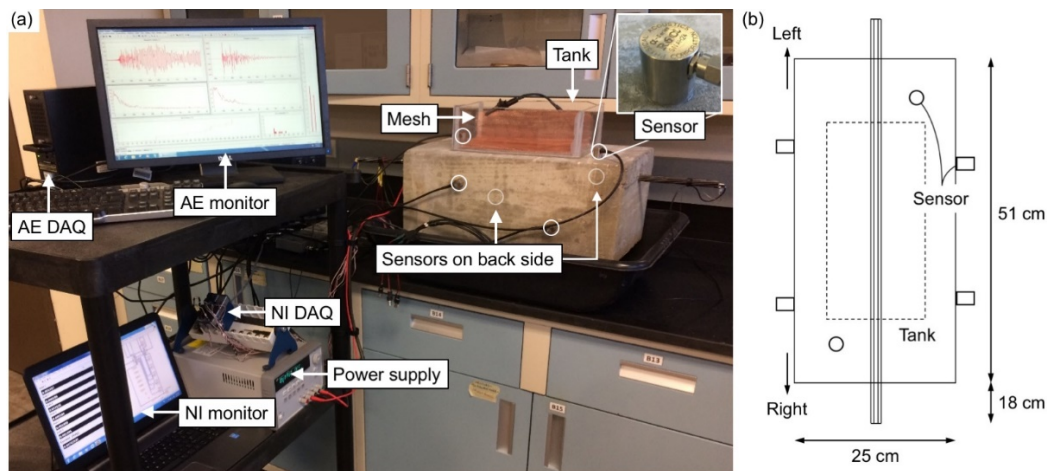
Source: Images by Authors

Figure 7.28: (a) Progression of microcracking in Specimen 2 and (b) microcracking highlighted (CI-Cracking Index and VRI-Visual Rating Index)

7.6.4.2. Accelerated Corrosion and Acoustic Emission Sensing

Accelerated corrosion was carried out on each of the two specimens using the impressed current technique [252], [260]. An example of this may be seen in Figure 7.29(a) for Specimen A. In this technique, chlorides were penetrated into the concrete by ponding 5% NaCl saltwater in a tank on the upper concrete surface.

This tank position on the upper surface was chosen in order to simulate the natural downward seepage of water and chlorides in a real-world specimen. The tank was constructed from acrylic panels and adhered to the concrete using e6000 ceramic epoxy. A galvanic cell was then formed between the strand and a copper mesh inserted in the saltwater tank. In this way, the strand, copper mesh, and saltwater served as the anode, cathode, and electrolyte, respectively. A constant potential of 20 V was applied to the galvanic cell using a DC power supply (Keysight). The resulting current ranged from 20 to 70 mA (at an average of 35 mA) and was recorded with a Labview code, a shunt resistor, and a NI-DAQ system.



Source: Images by Authors

Figure 7.29: (a) Experimental setup and data acquisition system for accelerated corrosion testing. Acoustic emission sensors are highlighted, with those hidden from view also indicated. (b) Schematic of instrumented specimen, as viewed from above, with rightward and leftward ends indicated

The current was applied in cycles (i.e., corrosion cycles), ranging from 4 to 8 hours at a time, with a gap of 1 to 4 days between consecutive cycles. For Specimen A, this pattern was repeated for 118 cycles (spanning 206 days), until the surface cracking limit state in the concrete was reached, as discussed in 7.6.2. For Specimen B, the repetition was carried out for 104 cycles until the same level of surface cracking was observed. To control for the effect of temperature on corrosion [244], the laboratory environment was held relatively constant throughout the test at 22 to 25 °C (72 to 77 °F).

Acoustic emission was continuously recorded during each corrosion cycle using a Mistras Micro-Express DAQ system, as shown in Figure 7.29. To record AE, six Physical Acoustics Corp. (PAC) R6 α sensors were bonded to the concrete surface using hot glue. The sensors were 19.1 mm (0.75 in.) diameter, with a peak response near 60 kHz. The sensors were bonded to three sides of the concrete surface, with two sensors per side.

Recorded waveforms were preamplified by 40 dB using 2/4/6 preamplifiers (PAC). A fixed threshold of 50 dB was used for triggering the DAQ, which was determined prior to the test by measuring the ambient noise level and adding roughly 10 dB. Highpass and lowpass analog filters at 1 kHz and 1 MHz were applied to the sensors. In addition, the hit lockout time (HLT) was set to 2.5 ms. Lastly, the recorded signals were sampled at 5 MHz.

7.6.5. Benchmark Corrosion Assessment

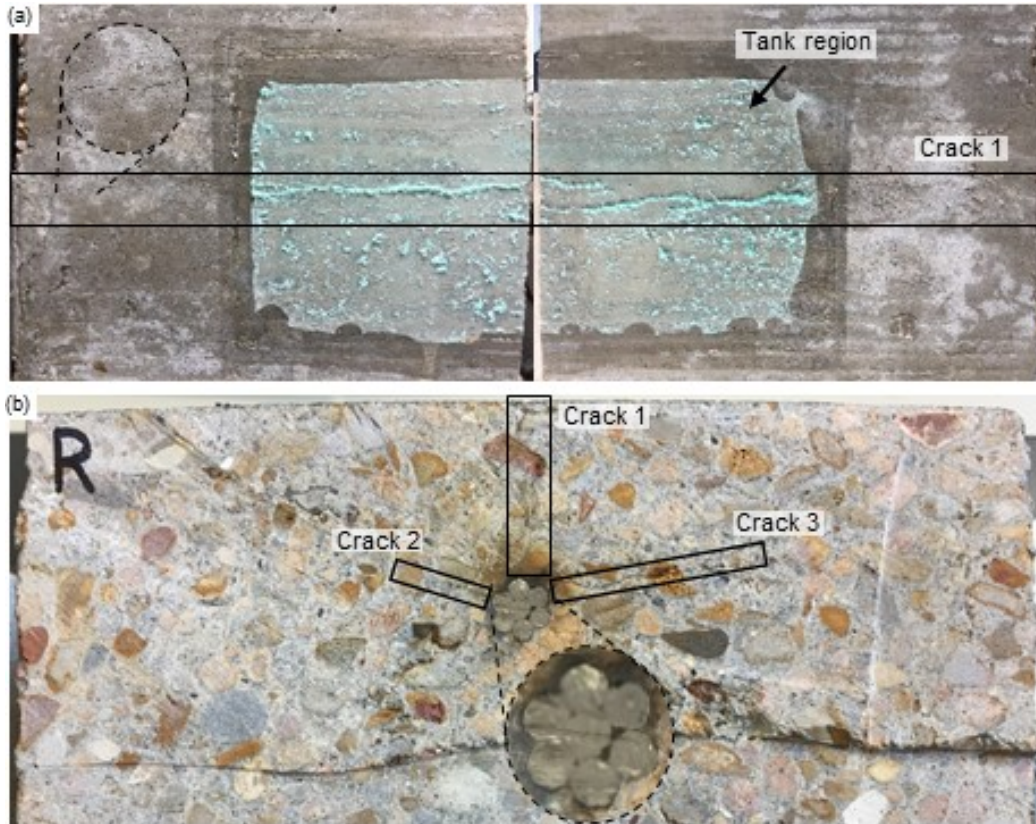
This section uses a combination of established and traditional methods to form a benchmark assessment of corrosion over the course of the experiment. The methods include visual inspection, mass loss measurement, and feature-based AE.

7.6.5.1. Visual Inspection

The major signs of corrosion observed in Specimen A during the test are listed in Table 7.4. The first concrete cover crack (≈ 0.05 mm width) was found toward the right end of the specimen at cycle 108, as seen in Figure 7.30(a). This surface crack ran parallel to the strand, and extended from the rightward end of the saltwater tank to the nearby exiting point of the strand. It is possible that this crack opened earlier than cycle 108, along the surface underneath the saltwater tank, but was not noticed due to lack of visibility through the tank. At cycle 115, an analogous crack (≈ 0.1 mm width) was found mirrored on the opposite side of the specimen. All crack widths were in the barely visible range of roughly 0.05 to 0.1 mm, as defined in [272], [273]. The test was terminated a few cycles later at cycle 118, since the observed crack widths corresponded to the surface cracking limit state [270], [272]. After the test was completed, the two cracks on either end of the specimen were found to be connected through the area under the tank, as shown in Figure 7.30(a). There was thus a continuous cover crack extending along the length of the specimen

Table 7.4: Visual Signs of Corrosion in Specimen A and the Cycle at which They Were Observed During Experiment

Cycle	Signs of Corrosion
108	First surface crack observed, extending through rightward end of cover.
115	Surface crack extends through leftward end of cover.



Source: Images by Authors

Figure 7.30: Post-corrosion visual inspection of Specimen A. (a) Image of surface crack extending along the length of specimen, as viewed from above. (b) Right side of cross-section after being cut open, highlighting three cracks propagating radially from strand.

To better understand the interior crack pattern after the completion of the test, a destructive inspection was carried out. The specimen was cut in half perpendicular to the strand, and the right-end cross-section may be seen in Figure 7.30(b). Here, it may be seen that corrosion products primarily built up on the upper surface of the strand, which was in direct contact with downward-seeping saltwater. The accumulation of corrosion on the upper surface caused a buildup of pressure, resulting in the three radial cracks seen in Figure 7.30(b). The crack propagating upward through the concrete cover (i.e., crack 1) was the only one visible from the outer surface. The other two cracks propagated radially at about $\pm 75^\circ$ angles with respect to crack 1, but did not reach the surface.

The major signs of corrosion observed in Specimen B during the test are listed in Table 7.5. These concerned the pre-existing microcracks that were designed to be present in this specimen in particular. At cycle 65, saltwater began to seep through the microcracks near the tank edge. This is believed to be due to tensile stresses building up in the concrete from accumulating corrosion products around the strand. This process continued through cycles 65 through 97, until the surface cracking extended through the entire concrete cover. During this period, the path of

the saltwater seepage increased in length along the direction of the strand (i.e., normal to the perceived tensile stresses).

Table 7.5: Visual Signs of Corrosion in Specimen B and the Cycle at which They Were Observed during Experiment

Cycle	Signs of Corrosion
65	Saltwater seeping from surface microcracks.
65-97	Path of saltwater seeping extends in length parallel to strand.
97	Surface Crack extends through entire cover

7.6.5.2. Mass Loss Measurement

Mass loss measurement was used to provide a metric of corrosion severity, in addition to the notion of corrosion cycles. In particular, Faraday's law was used to convert the impressed current I to mass loss m in the strand, as shown in Figure 7.31.

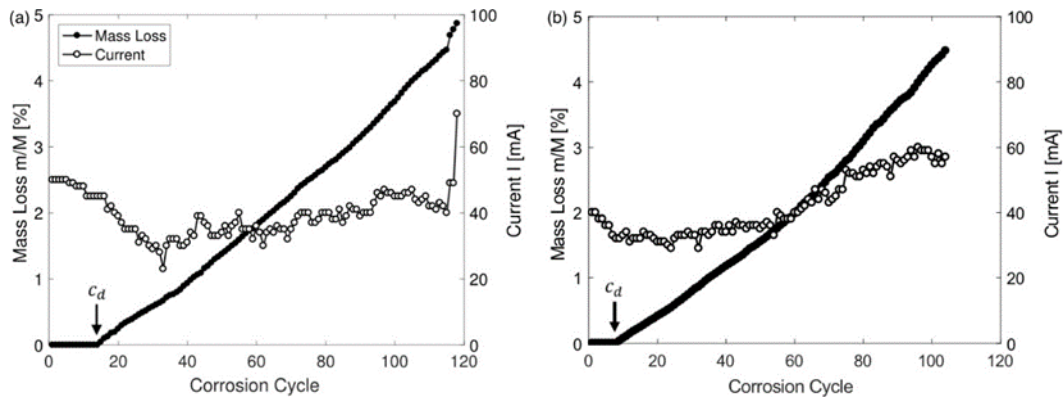


Figure 7.31: Mass loss of strand in (a) Specimen A and (b) Specimen B, normalized against original mass embedded in concrete. Results overlain with impressed current readings.

A modification of the law was applied to account for the fact that no mass loss takes place before the strand is depassivated [260]. The modified Faraday's law converts the impressed current up to cycle c to the cumulative mass loss $m(c)$ according to

$$m(c) = \frac{A}{ZF} \sum_{i=c_d}^c I(i)T(i)$$

with $m(c) = 0$ for $c < c_d$. Here, c_d is the cycle at which the strand was depassivated (determined in Sec. 7.6.5.3), and $I(i)$ is the current applied in cycle i over the cycle's duration $T(i)$. The percentage mass loss may be calculated in terms of the original mass M as m/M , where M is the mass of strand embedded in concrete.

7.6.5.3. Traditional Acoustic Emission Monitoring

The AE activity generated during the corrosion process may be seen in Figure 7.32(a) for Specimen A. This is represented in terms of cumulative energy and number of hits. Depassivation is indicated by the distinct first spike in AE activity [260], beginning at cycle 15. The corresponding onset of corrosion is indicated at this point in Figure 7.32. Minor AE activity spikes appeared around cycles 70 and 90, which may be seen in terms of both energy and hits. The minor spikes near cycles 70 and 90 may respectively be related to initiation and propagation of crack 1 [251]. The next major spike in AE activity occurred at cycle 103. From the time at which it occurred, this spike may be related to near-surface propagation of crack 1, which was found at the surface 5 cycles later. The subsequent increase in the AE activity rate may then be related to gradual propagation of the crack, with it eventually reaching the surface by cycle 108. The final and largest AE activity spike began at cycle 116 and continued in cycle 117. Since this spike occurred after crack 1 extended through the entire length of concrete cover, it may be related to propagation of one (or both) of the angled subsurface cracks (i.e., crack 2 or 3).

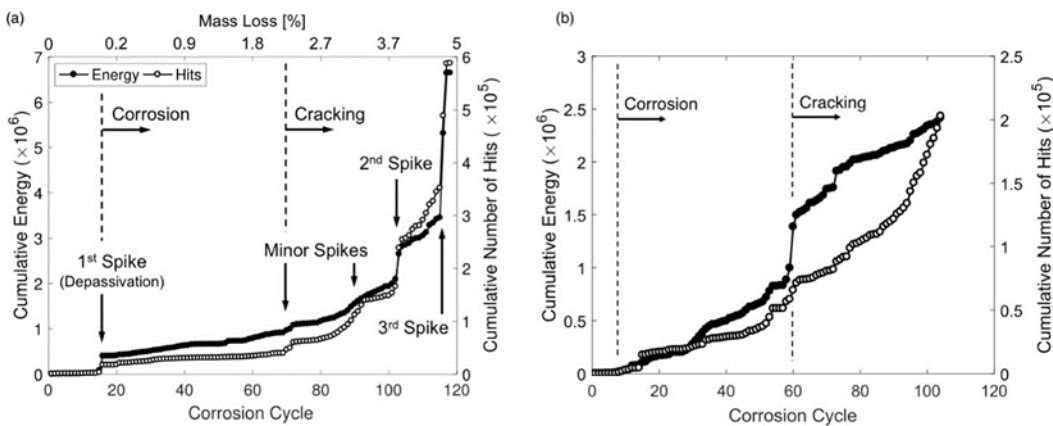


Figure 7.32: Acoustic emission activity recorded over the corrosion process for (a) Specimen A and (b) Specimen B, in terms of cumulative energy and number of hits. Corrosion onset (depassivation) may be seen at cycle 15 where the first activity spike occurred.

Similar conclusions may be drawn for Specimen B from Figure 7.32(b). The first spike in AE activity began at cycle 8, which is marked as the start of corrosion. The fact that corrosion initiated earlier than in Specimen A may be due to this specimen being exposed to aggressive agents prior to accelerated corrosion testing (i.e., being weathered outdoors for 2.5 years). Secondly, the later major spike occurring near cycle 60 strongly correlates with the observed saltwater seepage due to possible microcrack opening.

To further distinguish the various AE activity spikes, the peak frequency for each hit recorded over the entire corrosion process is shown in Figure 7.33. A number of distinct frequency bands may be seen in the datacloud for Specimen A, indicating

that different mechanisms occurred during corrosion [253], [265]. Four main frequency bands may be seen (indicated by arrows in Figure 7.33), appearing at roughly 20, 30–110, 150–170, and 220–260 kHz. It may be seen that these bands did not all emerge at the same point in the corrosion process. The 20 kHz band showed some activity near the start, but did not emerge strongly until around cycle 70, when the first minor spike was observed. The 30–110 kHz band appeared immediately, and remained during the entire process. The 150–170 kHz band appeared slightly later around cycle 20, soon after depassivation. The 220–260 kHz band did not emerge strongly until around cycle 70, again near the first minor spike. Interestingly, there was some degree of fusion within the 30–110 kHz band, causing the opening and closing of holes within the band as corrosion progressed. As indicated in Figure 7.33(a), two dominant holes may be seen in cycles 1–20 and 40–60 (roughly), which are investigated in the next section. The appearance of frequency content between 40 and 90 kHz appeared to be linked to mechanisms during depassivation [253]. The appearance of 150–170 kHz bands near cycle 20 (i.e., shortly after depassivation) suggests that these were associated with corrosion mechanisms occurring prior to crack initiation (such as pitting corrosion in the strand). In combination with the minor spike near cycle 70, the strong emergence of the 20, 220–260 kHz bands near the same cycle points to these being associated with concrete cracking. Along with the observed spike patterns in AE activity, the fact that these bands remained from cycle 70 onward suggests that the crack propagation took place rapidly near cycles 70, 90, 103, and 116–117, and gradually during the intermediate cycles. From these considerations, the deduced start of cracking is indicated in Figure 7.32(a) and Figure 7.33(b) (along with the previously determined start of corrosion).

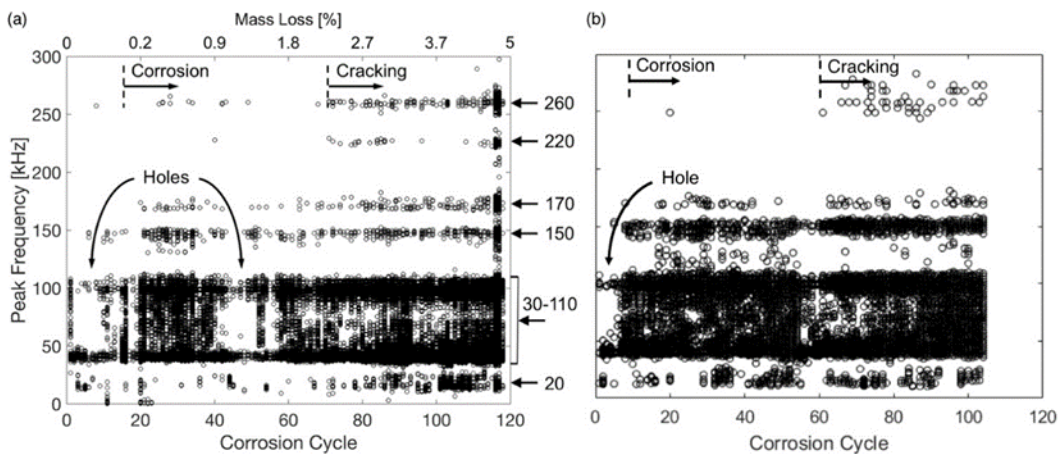


Figure 7.33: Peak frequency datacloud for AE hits over the corrosion process in (a) Specimen A and (b) Specimen B. Several frequency bands observed (indicated by arrows), suggesting the presence of various source mechanisms.

Similar frequency bands may be observed in Specimen B from Figure 7.33(b). Like Specimen A, the closure of a hole in the 30–110 kHz band was correlated with

corrosion onset. This was in addition to the emergence of the 150–170 kHz band around the same point in time. Interestingly, there was no second hole appearance preceding the emergence of the 220–260 kHz band. In fact, the only hole that appeared in the Specimen B datacloud was that marking depassivation. However, the 220–260 kHz band was strongly correlated with an AE activity spike and the appearance of saltwater seepage from microcracks, further suggesting that this band is associated with concrete crack initiation and propagation.

7.6.6. Topological Data Analysis of Acoustic Emission

The AE activity and the various bands in the peak frequency datacloud were used to determine depassivation and cracking in the previous section. However, missing frequency content which formed holes in the 30–110 kHz band may also be related to corrosion. Topological data analysis was therefore used to quantitatively extract the holes from this band, allowing further conclusions to be drawn about their significance.

The extraction of holes using TDA is shown in Figure 7.34 for Specimen A. For reference, the data points in the considered frequency band are shown in black in Figure 7.34(a), with those from other frequency regions shown in light gray. To ensure that the coordinates of the data points had compatible units for TDA, the corrosion cycle and peak frequency axes were normalized from their original ranges of [0,118] and [0,300], respectively, to [0,1]. It was found that 200 landmarks for the witness complex provided a good description of the datacloud, as seen in Figure 7.34(a). Further investigation of the optimal number of landmarks for this datacloud may be found below.

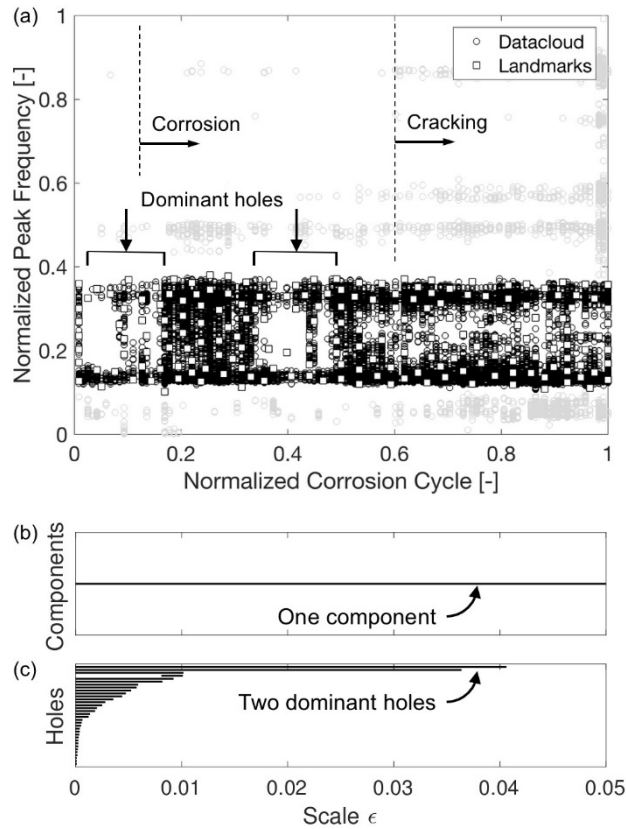


Figure 7.34: Topological data analysis for datacloud of 30–110 kHz frequency band in Specimen A. (a) Datacloud with dominant holes highlighted, with data points from remaining bands overlain in light gray. (b),(c) Barcodes, indicating one component and two dominant holes.

From the given number of landmarks, the barcodes for components and holes may be seen in Figure 7.34(b) and (c). One component was obtained in Figure 7.34(b), representing the observable topology of the single band under consideration. The presence of two dominant holes may be seen in Figure 7.34(c), corresponding to the two holes indicated in Figure 7.34(a). It may be seen in Figure 7.34(c) that various lesser dominant holes were also detected, revealing the relatively small scattered holes seen in the datacloud. However, these may be treated as noise since their barcodes were significantly shorter than those for the two dominant holes.

In order to verify that 200 landmarks accurately captured the topology of the datacloud, the sensitivity of the barcodes with respect to the number of landmarks was investigated. Accordingly, Figure 7.35(b) shows the barcodes for holes obtained from three different numbers of landmarks, including 50, 100, and 200. For visualization, Figure 7.35(a) shows the landmarks for each case overlain on the datacloud. Using only 50 landmarks provided a poor encapsulation of the datacloud, and the resulting barcode shows that only one of the two holes was identified. Using 100 landmarks yielded improved results, where the existence of two dominant holes began to be reasonably identified. By 200 landmarks, the

barcode converged to indicate the two dominant holes. The process confirms that 200 landmarks provided an accurate result for Figure 7.34, and demonstrates that the appropriate number of landmarks may be found by studying the convergence of barcodes.

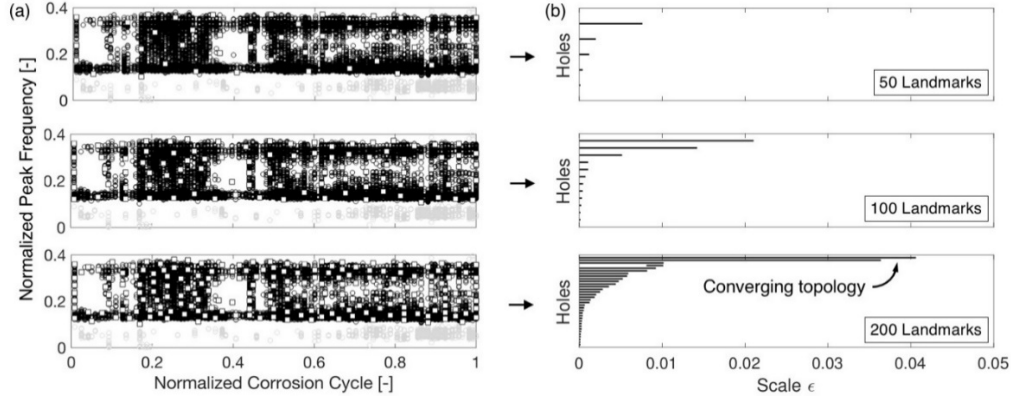


Figure 7.35: Comparison of barcodes obtained from various numbers of landmarks in Specimen A. (a) Landmark selection overlain on the datacloud for 50 (top), 100 (middle), and 200 (bottom) landmarks. (b) Corresponding barcodes for 50, 100, and 200 landmarks. Converging topology of two dominant holes observed by 200 landmarks.

These results demonstrate the ability of TDA to quantify the holes in the datacloud for the 30–110 kHz frequency band. However, this framework is only able to determine the presence of holes, and not their locations within the datacloud (e.g., the corrosion cycles in which they are present). Moreover, the results are only useful for analysis after the entire corrosion process is completed, and is therefore not ideal for real-time monitoring. To overcome these limitations, an on-line cycle-by-cycle framework is proposed below.

7.6.6.1. Cycle-by-Cycle Framework

The cycle-by-cycle TDA framework is visualized in Figure 7.36 for two corrosion cycles, with and without a hole, respectively. The framework involves taking a slice of the datacloud at each cycle and determining hole presence based on the number of components in the slice. First, for simplicity, the peak frequency datacloud for a given cycle is normalized, such that the range [30,110] kHz is mapped to [-1,1]. The presence of a hole at a given cycle is then governed by whether or not there are at least two significantly distanced components (i.e., if the components exist over a sufficient scale). In this report, a hole is said to be present if they exist up to a scale of $\epsilon' = 0.5$ in normalized frequency (i.e., 20 kHz in original frequency). The dependence of the results for various values of ϵ' is studied afterward. Determination of hole presence using this approach may be seen in Figure 7.36(d) and (e). Since the witness complex is only applied to a 1D datacloud (as opposed to 2D), the number of landmarks is set to 15 (i.e., $\approx \sqrt{200}$), as opposed to 200. The

selection of landmarks from slices of the datacloud may be seen in Figure 7.36(b) and (c).

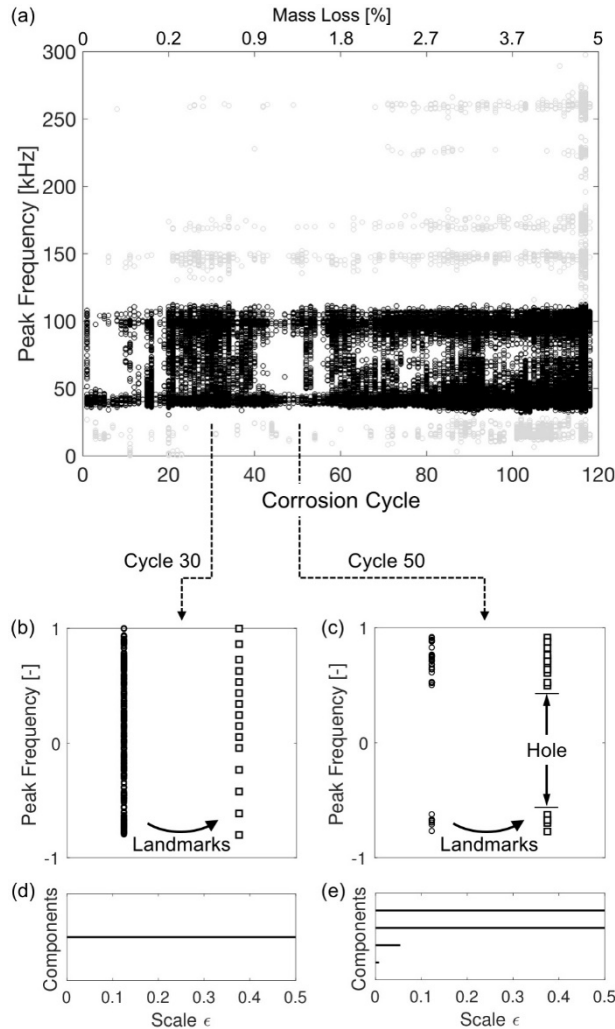


Figure 7.36: Illustration of cycle-by-cycle framework for hole measurement at two cycles based on the number of components. (a) Datacloud for 30–110 kHz frequency band highlighted. (b), (c) Selection of landmarks for cycles 30 and 50. (d), (e) Barcodes for number of components at cycles 30 and 50. Cycle 30 does not have a hole since it has only one significant component. Cycle 50 has a hole since it has at least two components which exist until $\epsilon = 0.5$.

The results of cycle-by-cycle hole measurement using TDA may be seen in Figure 7.37. Here, the datacloud is color-coded based on the presence of holes at given cycles. As in Figure 7.34(a), those data points which are outside the 30–110 kHz band are colored in light gray. In Specimen A, the two main holes from cycles 1–20 and 40–60 are identified, as well as lesser dominant holes around cycle 70–80. However, since the minor hole around cycle 70–80 is less definitive, it is unclear if it is meaningful or simply noise. It may be seen that the closure of the first hole was correlated with depassivation. The presence of a hole before depassivation may point to a lack of variety in source mechanisms. Once depassivation occurs,

however, new mechanisms may take place involving the strand, producing frequency content between 40–90 kHz and closing the hole. From roughly cycle 20–40, immediately after depassivation, the hole remained strongly closed. This correlates with corrosion products building up around the strand from the model in Figure 7.24, involving a greater variety of source mechanisms. Along with the AE activity results, the second hole near cycle 40–60 may be an indication of the corrosion rate slowing due to the buildup of corrosion products (as discussed in [282]), again resulting in less variety of source mechanisms. However, the closing of this hole near cycle 60 appears to serve as an early indication of crack initiation. This may be compared to traditional AE monitoring in Sec. 7.6.5.3, where the emergence of the high-frequency bands was only able to indicate cracking at the point when it occurred near cycle 70. In Specimen B, the main hole from cycle 1–8 was identified, serving as a marker for corrosion onset. Due to their brevity, however, the two later holes near cycles 60 and 70, may only be noise artifacts.

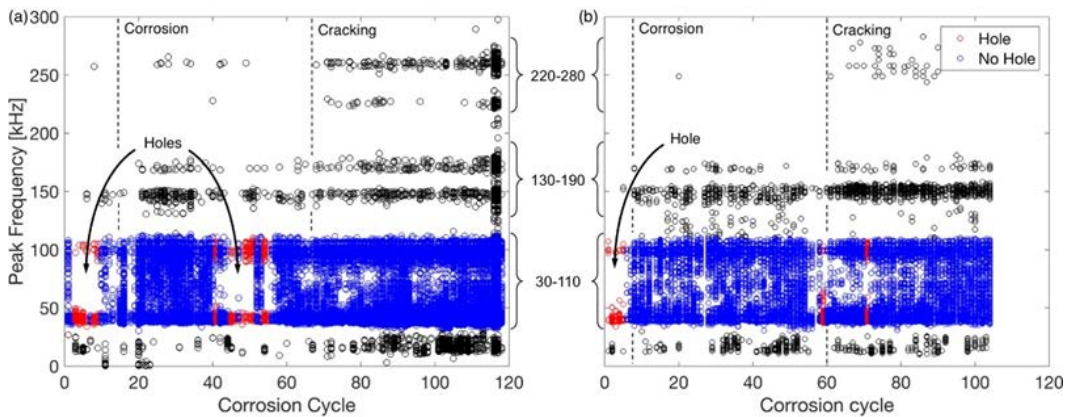


Figure 7.37: Topological data analysis results for hole measurement at each cycle in (a)-(b) Specimen A and (c)-(d) Specimen B.

To study the influence of ϵ' on the cycle-by-cycle framework, analogous results for a variety of ϵ' values were computed for Specimen A, as shown in Figure 7.38. Here, results for four values are shown, within the wide range [0,1]. For a small value of $\epsilon' = 0.25$, it may be seen that the definition of a hole is not sufficiently strict. On the contrary, as the value approaches unity, the definition of a hole becomes overly strict. By studying a wide range of values, it may be seen that the two dominant holes are the only ones present throughout the entire range. The consistency of these holes allows them to be identified as the dominant ones, while showing that a range of ϵ' may be considered in order to identify true holes within this framework.

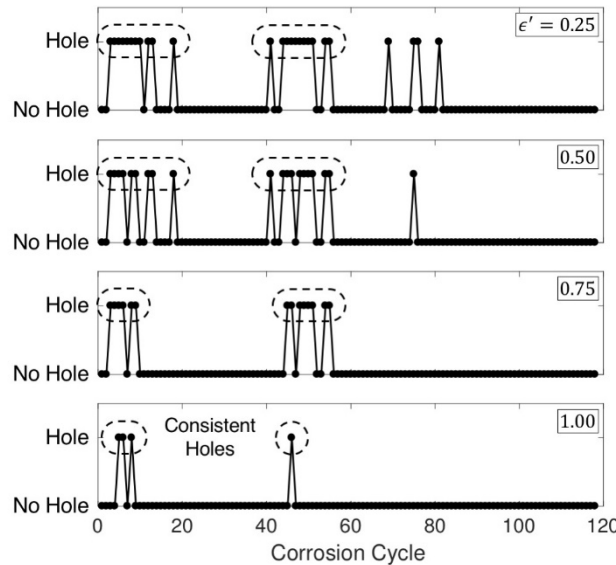


Figure 7.38: Results of cycle-by-cycle framework in Specimen A for various values of ϵ' . Only the dominant holes near cycles 1–20 and 40–60 consistently appear for each ϵ' .

Lastly, to demonstrate the computation time of the cycle-by-cycle framework, the cycle with the largest AE activity rate (i.e., highest hits/time) was selected. This was cycle 116 in Specimen A, which contained 134,078 hits over a time period of 7 hours. In this case, the required computation time was 0.4 sec on a PC, demonstrating that there would be no issue performing TDA in real-time on this data.

7.7. Conclusions

The research team first demonstrated the ability of higher-order GUW modes to estimate corrosion-induced stress change in a strand up to the point of fracture. The estimated stress change closely followed the measured values during the first half of the corrosion process (up to roughly 17% mass loss). The major stress increase caused by fracture was also captured well. Even though the approach was validated on corrosion-induced stress change, it is conceivable that stress change due to non-damage sources may also be monitored (e.g., traffic loading). Moreover, the value of the modal modulation technique for real-world settings was demonstrated, with the transducers being reattached after each corrosion cycle. Secondly, this task considered how topological data analysis (TDA) can aid acoustic emission (AE) in detecting corrosion by quantifying meaningful topology in an AE datacloud. For real-time analysis, a cycle-by-cycle TDA framework was proposed. Across the two specimens, a common dominant hole was quantified using this framework; the closing of which correlated with the point of depassivation. In addition, high-frequency content (> 200 kHz) was found to be related to concrete crack initiation and propagation. Such traditional and topological information may therefore be combined to provide more reliable indications of corrosion onset and concrete crack

growth. Together, there is the potential for gathering early and reliable indications of subsurface cracking, before the serviceability limit state is reached and any visual signs appear from outside. Additionally, detecting the onset of corrosion may provide a reference point for models of time-to-cracking in the concrete and pit depth distribution in the steel.

Lastly, the pre-existing weathering and microcracking in specimen B was found to result in earlier corrosion onset and cracking (by roughly 10 cycles). However, cracking initiated at the surface, as opposed to only at the embedded strand.

Chapter 8. Conclusions

The overarching goals of this research work were to examine the temporal behavior of these microcracks, determine the likelihood of long-term strength and durability issues that might occur due to their presence, and provide recommendations to the maintenance program of these girders, if necessary.

An additional goal was to generate a reasonably reliable service life model that could be used by transportation department engineers in the field to predict the remaining service life of these girders exhibiting microcracking with easily available input variables such as age, material composition, observed cracking index/density, and ultrasonic pulse velocity.

The behavior of these girders with surface microcracks under marine exposure was also observed to determine the effect of the microcracks on chloride-induced corrosion.

The suitability of a monitoring system based on guided ultrasonic waves (GUWs) for detecting the initiation and growth of corrosion damage in prestressed concrete girders was also examined.

The research work was divided into six Tasks. The major conclusions drawn from each study are presented in the following sections, along with the recommendations for modifications in maintenance programs of the girders.

8.1. Task 1: Field Surveys and Selection of Specimens

The team finalized the locations for the field visits. Three types of full-scale girders were selected for the study, discarded cracked girders in TxDOT approved pre-cast yards, in-service projects with cracked girders, and discarded uncracked girders in TxDOT approved pre-cast yards. Five rejected/overcast and six in-service girders with visible microcracking, one rejected/overcast, and two in-service girders with negligible cracking were selected for the study. In addition, one rejected/overcast girder with visible surface microcracking was selected to serve as a validation specimen. The girders tested were selected based on location, accessibility, and extent of cracking. The girders were selected from the information provided by TxDOT engineers on the initial assessment of the extent of visible microcracking. Three rounds of field visits were conducted to each girder, and non-destructive data was collected from all girders, and cores were collected from the rejected/overcast girders. An additional round of field visits was conducted to two rejected/overcast girders to serve as a validation field visit.

8.2. Task 2: In-Situ Examination via Non-Destructive Test Methods

In-situ observation and collection of cracking, strain, ultrasonic pulse velocity, and surface resistivity data from in-service and overcast full-scale girders over two years showed that the girders with surface microcracking exhibited an increase in cracking and shrinkage, and a marginal reduction in the pulse velocity and surface resistivity. The data showed that exposure to environment and presence of pre-existing cracks were major factors affecting the rate of increase in cracking, while external loading has not yet manifested any impact. The study also showed the temporal behavior of average crack width values is heavily dependent on the mechanism of increase in cracking, i.e. whether the change is due to an increase in width of existing cracks or due to the formation of new cracks. When new cracks are formed, this can lead to a decrease in average crack width over time, erroneously indicating that the cracks are growing smaller, whereas this is not the case. Hence, to accurately account for the temporal behavior of cracking, both the growth in cracking index and average crack width should be taken into consideration.

8.3. Task 3: Evaluation of Cores

Laboratory testing showed that the strength, stiffness, and resistivity of the girders did not reduce in a significant manner, while there was a marginal increase in the diffusion coefficients. The increase in diffusion coefficient values was still under serviceability limits.

The effect of exposure and presence of pre-existing cracks was investigated by conducting accelerated weathering tests (alternate wetting and drying) on the extracted cores and measuring the change in cracking, absorption, ultrasonic pulse velocity, bulk resistivity, and chloride diffusion coefficient. The relationships between the number of weathering cycles and initial cracking and the increase in cracking and decrease durability were quantified

At the end of the testing period, the specimens had higher cracking index, average crack width, loss in mass, and absorption. The specimens also exhibited lower ultrasonic pulse velocity and bulk resistivity values. This indicated reduction in overall durability. In addition, the samples undergoing more alternate wetting and drying cycles and samples with higher initial cracking index values exhibited higher loss in durability.

The relationships between the results from the non-destructive tests and the initial cracking index and number of weathering cycles had high multiple regression coefficients, moderate to excellent reliability indices, and standard error under permissible limits. Similarly, the relationship between diffusion coefficient, initial cracking index, and number of wetting and drying cycles moderate multiple

regression coefficients, moderate to excellent reliability indices, and standard error under permissible limits.

8.4. Task 4: Prediction of Remaining Service Life

The effect of increasing degree of cracking (width, depth, and density/index) on the strength, stiffness, and durability properties of concrete was quantified. Compressive and tensile strength, ultrasonic pulse velocity, modulus of elasticity, bulk, and surface resistivity decreased with increased cracking. Carbonation and chloride diffusion coefficient increased with increased cracking. The models generated to quantify the relationship between increasing cracking and decrease in strength, stiffness, and durability had high multiple regression coefficients, moderate to excellent reliability indices, and standard error under permissible limits. The critical cracking values for each test were determined, i.e., the values of crack width, depth, and index at which the test values reach serviceability. The chloride diffusion coefficient was determined to be the critical test parameter, i.e., of all the tests conducted chloride diffusion coefficient had the lowest critical cracking values. A critical crack width of 100 μm (0.004 in.), depth of 7 mm (0.03 in.) and index of 18 mm/m (0.5755 in./yd) was calculated. This translates to 4 cracks with widths of 0.004 inch across one inch of concrete or 18 cracks with widths of 100 μm across 10 cm of concrete.

An empirical model was generated with temporal data collected from 5 overcast girders and 8 in-service girders (see Equation 8.1). This was supplemented with data from the accelerated weathering test conducted on specimens extracted from the overcast girders. The model had a regression coefficient of 0.77, which lies in the “Good” range and moderate to good reliability. A standard error of estimates was calculated to be 359 days, a little less than one year.

$$\text{Age of Specimen} = -8403 - 912 a_1 - 1441 a_2 + 29848 a_3 + 0.2 a_4 + 1330 a_5$$

Equation 8.1

Where,

a_1 = Effect of exposure expressed using a binary code. 0 for samples that were not exposed to the environment and 1 for samples exposed to environment.

a_2 = Effect of pre-existing cracks expressed using the cracking index of girders during the first field visit and the cracking index of accelerated weathering tests before the start of the test.

a_3 = w/cm used to account for variation in material composition.

a_4 = Ultrasonic pulse velocity used to account for variation in material composition.

a_5 = The cracking index observed during subsequent field visits, and at the end of each accelerated weathering test cycle was used.

The service lives of the low w/cm concrete girders were calculated using the generated model. The service life was also calculated using Life-365® and two models for cracked concretes based on modified chloride diffusion coefficients [27], [151]. The remaining service life of the girders, i.e., the amount of time taken to reach a critical cracking index value of 18 mm/m, was calculated using the model generated.

It was seen that the girders have between 50 and 62 years of service life remaining. It was also observed that a girder, when not exposed to the environment, had around two and a half additional years of service life when compared to the same girder when exposed to the environment.

The remaining service life of the girders as predicted by the Life-365® was similar to that predicted by the Kwon et al. (2009) and Pacheco (2019) models [27], [151]. This showed that the two modified models were not sensitive enough to account for the behavior of microcracking. The empirical model under-predicted service life by 4 to 10 years all girders when compared to Life-365®.

8.5. Task 5: Marine Simulation Testing

The change in cracking and corrosion potential of low w/cm concretes with surface microcracking under marine exposure was observed. Three blocks were cast with embedded pre-stressing strands to mimic the real-world conditions of a typical girder. Block A was exposed to the marine environment 28 days after casting, Block B was exposed to marine environment after it exhibited adequate surface microcracking, and Block C performed as a control specimen and was not exposed to the environment. Marine simulation consisted of one unexposed zone, one splash zone that underwent two cycles of exposure to salt-water each day followed by drying, and a submerged zone that was permanently under the waterline. Block A underwent 2000 cycles of wetting and drying, and Block B underwent 348 cycles.

Block A exhibited corrosion-induced cracking in the splash zone within 7 months of marine simulation and in the region between splash and unexposed zones within 24 months of marine simulation. Block B was showed adequate surface microcracking after 26 months of exposure to the environment and was placed in the marine simulation tank. Both blocks showed a greater change in resistivity and half-cell potential in the splash zone, followed by the unexposed zone. The submerged zone did not show any significant changes. Block C did not show any

significant change in resistivity or half-cell potential. None of the blocks have reached serviceability conditions for surface resistivity yet. Block A showed increasing levels of corrosion potential after 8.2 months of marine simulation and higher than 90% corrosion potential after 24 months of marine exposure. Block B showed increasing levels of corrosion potential after 1.7 months of marine simulation. Block C has shown corrosion potential of under 10%.

8.6. Task 6: Monitoring Corrosion of Pre-stressing Strands

The ability of guided ultrasonic waves to estimate corrosion-induced stress change in a strand up to the point of fracture was demonstrated. Trends in stress change were accurately captured under heavy corrosion and cross-section loss. The major stress increase caused by fracture was also captured well. Although validation was focused on corrosion-induced stress change, stress change due to non-damage sources (such as evolving live loads) may also be targeted. The approach was also validated under conditions that may be seen in long-term monitoring using advanced signal processing techniques. This task also considered the topological significance of acoustic emission (AE) in detecting corrosion. Topological data analysis was adapted to quantify meaningful corrosion-related topology in AE data-clouds in real-time. Across control and weathered specimens, a common hole was found to correlate with the point of corrosion onset. Certain high-frequency content was also found to correlate with concrete crack initiation and propagation. These traditional and topological AE features may be combined to provide reliable indications of corrosion onset and concrete crack growth. Together, there is potential for gathering early and reliable indications of corrosion long before any visual signs appear from outside. Additionally, such information of corrosion onset may provide a reference point for models of time-to-cracking in the concrete and pit depth distribution in the steel. Lastly, the pre-existing weathering and microcracking in specimen B was found to result in consistently earlier corrosion onset and cracking. However, in this specimen the cracking initiated at the exterior surface, as opposed to only at the embedded strand.

8.7. Recommendations

Based on the observations of the study, the following recommendations are provided:

- Accuracy of the temporal behavior of cracking can be improved by taking both the growth in cracking index and average crack width into consideration, instead of just the crack width. It is recommended that cracking index of the girders be monitored along with the cracking index.

- The exterior paint coating provided for in-service girders has not prevented the formation of cracks, shrinkage, or loss in resistivity. It, however, prevents the visibility of microcracks. Thus, it is recommended that the surface resistivity and shrinkage of the painted exterior girders be monitored.
- The critical cracking index for the low w/cm concretes used in these pre-cast prestressed girders is 18 mm/m or 0.5755 in./yd. It is recommended that microcracking not exceed this value during their service life to prevent corrosion-related durability concerns.
- As these girders are designed for a service life of 75 years, the present rate of growth in microcracking can reduce the service life of the in-service girders from 2 to 13 years depending on the girder and nature of cracking. On average, the service life reduction was 5 years considering all the girders examined in this study. Further reduction in service life is also possible under fatigue loading as the girders age. Thus, continuous monitoring of the girders, especially in the last two decades of the girder's lives is recommended.
- Exposure to the simulated marine environment led to the formation of microcracks in the low water-cement ratio concrete specimens. However, the presence of microcracks did not significantly impact corrosion potential in the timeframe of the study. It is recommended that this test be continued to observe the behavior of these microcracks under extended marine exposure.
- Guided ultrasonic waves and acoustic emission have been demonstrated to yield quantitative metrics of the corrosion process which may be useful for incorporation into the maintenance program of prestressed concrete bridges. Although the surface microcracking increased corrosion susceptibility, under such conditions there is potential to continuously monitor the onset of corrosion and the resulting opening of such cracks before obvious external signs of corrosion appear. Modeling corrosion as a stochastic process may be an effective way to combine traditional and topological AE analyses for automated diagnostics.

8.8. Future Work

This study involves the observation and collection of data from full-scale girders with temporally evolving surface microcracks and determines the possibility of long-term loss in strength and durability and in turn service life. The study presented a comprehensive report on the behavior of these cracks and their effect

on strength and durability. However, some limitations do exist and can be examined in future studies. These are presented below:

- The bridge girders are relatively young (3 to 12 years at the time of first field visits) while being designed for 75 years of service life. The long-term fatigue and impact loading effects have not yet manifested and might be topics of concern later in the life of these girders. The effect of these factors must also be accounted for.
- The empirical models generated are for concrete mixes with w/cms ranging from 0.28 to 0.36. Widening the range of w/cms and mixture compositions would also allow for broader use of the model.
- The temporal effect of microcracks, with widths ranging from 6 μ m to 100 μ m, observed on the girders are quantified in this study. Larger, macrocracks have not been included. Increasing the range of crack widths and accounting for the three-dimensional effect of cracks, i.e., length and depth, in addition to width and index/density, can also improve the accuracy of the model.
- The effect of harsher exposure conditions, such as marine environments or exposure to deicing chemicals among others, is also a factor that can improve an understanding of the loss in service life due to the presence of cracks.
- Since the presented guided wave approach relied on access to the strand cross-section, it may benefit from future investigations into alternative sensing techniques. Due to attenuation, such research may be necessary in order to transition from laboratory-scale to full-scale specimens.
- The research on acoustic emission only considered small-scale prestressed specimens. It will be beneficial to study large-scale specimens as well, while considering the effect of multiple strands/rebar, etc. Additionally, the work has been conducted within accelerated corrosion settings, where time was measured in corrosion cycles and corrosion severity was measured in strand mass loss. In order to transition to real-world applications, adjustments to “true” time will be necessary.

References

- [1] ASCE, “2017 Infrastructure Report Card,” *Am. Soc. Civ. Eng.*, 2017.
- [2] N. B. Tiburzi, T. Drimalas, and K. J. Folliard, “Evaluation of precast bridge girder cracking: The role of volume change,” *Cem. Concr. Res.*, vol. 101, pp. 55–67, 2017.
- [3] S. Stacey, “Evaluation of ASTM C 494 Procedures for Polycarboxylate Admixtures used in Precast Concrete Elements,” *Univ. Texas Austin*, 2016.
- [4] TxDOT, “Standard Specifications for Construction and Maintenance of Highways, Streets, and Bridges Adopted by the Texas Department of Transportation,” 2014.
- [5] A. (TxDOT) Naranjo, “Service Life of Girders - 75 Years (Source: Andy Naranjo, TxDOT, 03-05-2020).” 2020.
- [6] D. S. Lane, “INVESTIGATION OF BRIDGE DECK CRACKING ON I-95 NORTHBOUND OVER POWELL CREEK. TECHNICAL ASSISTANCE REPORT,” 1994.
- [7] P. D. Krauss and E. A. Rogalla, *Transverse cracking in newly constructed bridge decks*, no. Project 12-37 FY’92. 1996.
- [8] D. Darwin, J. Browning, and W. D. Lindquist, “Control of cracking in bridge decks: Observations from the field,” *Cem. Concr. Aggregates*, vol. 26, no. 2, pp. 148–154, 2004.
- [9] K. V. L. Subramaniam, “Identification of Early-Age Cracking in Concrete Bridge Decks,” *J. Perform. Constr. Facil.*, vol. 30, no. 6, 2016.
- [10] Y. Xia, H. Nassif, M. Asce, and D. Su, “Early-Age Cracking in High Performance Concrete Decks of a Curved Steel Girder Bridge,” *J. Aerosp. Eng.*, vol. 30, no. 2, 2017.
- [11] TxDOT, “Report on Texas Bridges,” *Bridg. Div. Texas Dep. Transp.*, 2018.
- [12] AASHTO, “AASHTO LRFD Bridge Design Specifications,” 2012.
- [13] ACI, “ACI 201.1R - Guide for Conducting a Visual Inspection of Concrete in Service,” 2016.
- [14] NCEI, “www.ncei.noaa.gov,” *National Centers for Environmental Information*, 2017. [Online]. Available: <https://www.ncei.noaa.gov/>. [Accessed: 02-Feb-2018].
- [15] ASTM, “ASTM C494 - Standard Specification for Chemical Admixtures for Concrete,” *Am. Soc. Test. Mater.*, 2017.

- [16] ASTM, “ASTM C150 - Standard Specification for Portland Cement,” *Am. Soc. Test. Mater.*, 2017.
- [17] ASTM, “ASTM C618 - Standard Specification for Coal Fly Ash and Raw or Calcined Natural Pozzolan for Use in Concrete,” *Am. Soc. Test. Mater.*, 2017.
- [18] TxDOT, “Bridge Design Manual-LRFD,” *Texas Dep. Transp.*, 2018.
- [19] F. Benoit, B. Marc-André, F. Kevin, and M. Thomas, “FHWA-HIF-09-004 - Report on the Diagnosis, Prognosis, and Mitigation of Alkali- Silica Reaction (ASR) in Transportation Structures,” 2010.
- [20] ASTM, “ASTM C597 - Standard Test Method for Pulse Velocity Through Concrete,” *Am. Soc. Test. Mater.*, 2016.
- [21] AASHTO, “AASHTO T358 - Standard Method of Test for Surface Resistivity Indication of Concrete’s Ability to Resist Chloride Ion Penetration,” 2013.
- [22] ASTM, “ASTM C823/C823M - Standard Practice for Examination and Sampling of Hardened Concrete in Constructions,” *Am. Soc. Test. Mater.*, 2016.
- [23] TxDOT, “Bridge Project Development Manual,” *Texas Dep. Transp.*, 2018.
- [24] G. H. Cao, S. Zhang, W. Zhang, and X. R. Peng, “Long-term Deflection Test and Theoretical Analysis on Cracked Prestressed Concrete Box Beams,” *KSCE J. Civ. Eng.*, vol. 22, no. 2, pp. 688–695, 2018.
- [25] S. D. Kim, “Prediction of long-term prestress loss in concrete box girder bridges,” 2009.
- [26] M. B. Otieno, M. G. Alexander, and H.-D. Beushausen, “Corrosion in cracked and uncracked concrete – influence of crack width, concrete quality and crack reopening,” *Magazine of Concrete Research*, vol. 62, no. June, pp. 393–404, 2010.
- [27] S. J. Kwon, U. J. Na, S. S. Park, and S. H. Jung, “Service life prediction of concrete wharves with early-aged crack: Probabilistic approach for chloride diffusion,” *Struct. Saf.*, vol. 31, no. 1, pp. 75–83, Jan. 2009.
- [28] X.-H. Wang, D. V. Val, L. Zheng, and M. R. Jones, “Influence of loading and cracks on carbonation of RC elements made of different concrete types,” *Constr. Build. Mater.*, vol. 164, pp. 12–28, Mar. 2018.
- [29] C. Cao, M. M. S. S. Cheung, and B. Y. B. B. Chan, “Modelling of interaction between corrosion-induced concrete cover crack and steel corrosion rate,” *Corros. Sci.*, vol. 69, pp. 97–109, Apr. 2013.

- [30] Z. Yu, Y. Chen, P. Liu, and W. Wang, “Accelerated simulation of chloride ingress into concrete under drying-wetting alternation condition chloride environment,” *Constr. Build. Mater.*, vol. 93, pp. 205–213, 2015.
- [31] G. Malumbela, M. Alexander, and P. Moyo, “Interaction between corrosion crack width and steel loss in RC beams corroded under load,” *Cem. Concr. Res.*, vol. 40, no. 9, pp. 1419–1428, Sep. 2010.
- [32] J. Bao and L. Wang, “Combined effect of water and sustained compressive loading on chloride penetration into concrete,” *Constr. Build. Mater.*, vol. 156, pp. 708–718, Dec. 2017.
- [33] A. Konin, R. Franfois, and G. Arliguie, “Penetration of chlorides in relation to the microcracking state into reinforced ordinary and high strength concrete,” *Mater. Constr.*, vol. 31, pp. 310–316, 1998.
- [34] A. Corina-Maria, S. P. Shah, and A. Karr, “Effect of cracking on water and chloride permeability of concrete,” *J. Mater. Civ. Eng.*, vol. 11, no. 3, pp. 181–187, 1999.
- [35] H.-L. Wang, J.-G. Dai, X.-Y. Sun, X. Zhange, and X.-L. Zhang, “Characteristics of concrete cracks and their influence on chloride penetration,” *Constr. Build. Mater.*, vol. 107, pp. 216–225, Mar. 2016.
- [36] A. Poursaee and C. M. Hansson, “The influence of longitudinal cracks on the corrosion protection afforded reinforcing steel in high performance concrete,” *Cem. Concr. Res.*, vol. 38, no. 8–9, pp. 1098–1105, Aug. 2008.
- [37] I.-S. Yoon and E. Schlangen, “Experimental examination on chloride penetration through micro-crack in concrete,” *KSCE J. Civ. Eng.*, vol. 18, no. 1, pp. 188–198, Jan. 2014.
- [38] S. Alahmad, A. Toumi, J. Verdier, and R. François, “Effect of crack opening on carbon dioxide penetration in cracked mortar samples,” *Mater. Struct.*, vol. 42, no. 5, pp. 559–566, Jun. 2009.
- [39] ACI, “ACI 318 - Building Code Requirements for Structural Concrete,” *Am. Concr. Inst.*, 2017.
- [40] ACI, “ACI 224R - Control of Cracking in Concrete Structures,” *Am. Concr. Inst.*, 2001.
- [41] J. Bisschop and J. G. M. Van Mier, “Drying shrinkage microcracking in cement-based materials,” 2002.
- [42] T. Shiotani, J. Bisschop, and J. G. . Van Mier, “Temporal and spatial development of drying shrinkage cracking in cement-based materials,” *Eng. Fract. Mech.*, vol. 70, no. 12, pp. 1509–1525, Aug. 2003.
- [43] A. Damgaard Jensen and S. Chatterji, “State of the art report on micro-

- cracking and lifetime of concrete—Part 1,” *Mater. Struct.*, vol. 29, no. 1, pp. 3–8, 1996.
- [44] F. Slate, “Microscopic observation of cracks in concrete, with emphasis on techniques developed and used at Cornell University,” *Elsevier Appl. Sci.*, pp. 75–83, 1983.
- [45] P. Okumus and M. G. Oliva, “Evaluation of crack control methods for end zone cracking in prestressed concrete bridge girders,” *PCI J.*, no. Spring, pp. 91–105, 2013.
- [46] TxDOT, “Bridge Design Guide,” *Texas Dep. Transp.*, 2018.
- [47] FHWA, “Load and Resistance Factor Design (LRFD) for Highway Bridge Superstructures,” *Fed. Highw. Adm.*, 2015.
- [48] TxDOT, “DMS-8110 Coatings for Concrete,” *Texas Dep. Transp.*, 2016.
- [49] S. P. Shah and S. Chandra, “Critical Stress, Volume Change, and Microcracking of Concrete,” *ACI J.*, vol. 65, no. 57, pp. 770–780, 1968.
- [50] V. G. Haach, L. M. Juliani, and M. R. Da Roz, “Ultrasonic evaluation of mechanical properties of concretes produced with high early strength cement,” *Constr. Build. Mater.*, vol. 96, pp. 1–10, 2015.
- [51] J. A. Bogas, M. G. Gomes, and A. Gomes, “Compressive strength evaluation of structural lightweight concrete by non-destructive ultrasonic pulse velocity method,” *Ultrasonics*, vol. 53, no. 5, pp. 962–972, Jul. 2013.
- [52] A. Masi, L. Chiauzzi, and V. Manfredi, “Criteria for identifying concrete homogeneous areas for the estimation of in-situ strength in RC buildings,” *Constr. Build. Mater.*, vol. 121, pp. 576–587, 2016.
- [53] F. Saint-pierre, P. Rivard, and G. Ballivy, “Measurement of alkali – silica reaction progression by ultrasonic waves attenuation,” *Cem. Concr. Res.*, vol. 37, pp. 948–956, 2007.
- [54] AASHTO, “AASHTO TP119 - Standard Method of Test for Electrical Resistivity of a Concrete Cylinder Tested in a Uniaxial Resistance Test,” 2015.
- [55] K. Hornbostel, C. K. Larsen, and M. R. Geiker, “Relationship between concrete resistivity and corrosion rate: A literature review,” *Cem. Concr. Compos.*, vol. 39, pp. 60–72, 2013.
- [56] K. R. Gowers and S. G. Millard, “Measurement of Concrete Resistivity for Assessment of Corrosion Corrosion Severity of Steel Using Wenner Technique,” *ACI Mater. J.*, vol. September-, pp. 536–541, 1999.
- [57] P. Ghosh and Q. Tran, “Correlation Between Bulk and Surface Resistivity

- of Concrete,” *Int. J. Concr. Struct. Mater.*, vol. 9, no. 1, pp. 119–132, Mar. 2015.
- [58] A. A. Ramezani-pour, A. Pilvar, M. Mahdikhani, and F. Moodi, “Practical evaluation of relationship between concrete resistivity, water penetration, rapid chloride penetration and compressive strength,” *Constr. Build. Mater.*, vol. 25, pp. 2472–2479, 2011.
- [59] J. Gudimettla and G. Crawford, “Resistivity tests for concrete-recent field experience,” *ACI Mater. J.*, vol. 113, no. 4, pp. 505–512, 2016.
- [60] Kevern *et al.*, “Evaluation of Surface Resistivity for Concrete Quality Assurance in Missouri,” *Transp. Res. Rec. J. Transp. Res. Board*, no. 2577, pp. 53–59, 2016.
- [61] W. Morris, A. Vico, M. Vazquez, and S. R. De Sanchez, “Corrosion of reinforcing steel evaluated by means of concrete resistivity measurements,” *Corros. Sci.*, vol. 44, no. 1, pp. 81–99, 2002.
- [62] R. B. Polder, “Test methods for on site measurement of resistivity of concrete - a RILEM TC-154 technical recommendation,” 2001.
- [63] ACI, “ACI 209R-97: Prediction of Creep Shrinkage and Temperature Effects on Concrete Structures,” *Am. Concr. Inst.*, 1997.
- [64] TxDOT, “Bridge Standards,” *Texas Department of Transportation*, 2017. [Online]. Available: <https://www.dot.state.tx.us/insdot/orgchart/cmd/cserve/standard/bridge-e.htm>. [Accessed: 21-Jan-2018].
- [65] V. M. Malhotra, “Testing Hardened Concrete: Nondestructive Methods,” *ACI Monogr. No. 9*, 1976.
- [66] O. Sengul, “Use of electrical resistivity as an indicator for durability,” *Constr. Build. Mater.*, vol. 73, pp. 434–441, 2014.
- [67] W. J. Weiss and S. P. Shah, “Restrained shrinkage cracking: the role of shrinkage reducing admixtures and specimen geometry,” *Mater. Struct.*, vol. 35, no. 2, pp. 85–91, Mar. 2002.
- [68] W. J. Weiss, W. Yang, and S. P. Shah, “Shrinkage Cracking of Restrained Concrete Slabs,” *J. Eng. Mech.*, vol. 124, no. 7, pp. 765–774, Jul. 1998.
- [69] K. Wiegrink, S. Marikunte, and S. P. Shah, “Shrinkage cracking of high-strength concrete,” *ACI Mater. J.*, vol. 93, no. 5, pp. 409–415, 1996.
- [70] S. P. Shah, M. E. Karaguler, and M. Sarigaphuti, “Effects of shrinkage-reducing admixtures on restrained shrinkage cracking of concrete,” *ACI Mater. J.*, vol. 89, no. 3, pp. 291–295, 1992.

- [71] P. Jia, L. Li, J. Dong, Q. Wang, and Z. Guan, "Determination of the crack initiation stress, elastic modulus and ultimate crack length in TPBT concrete beams based on shear deformation theory," *Eng. Fract. Mech.*, vol. 220, p. 106572, Oct. 2019.
- [72] M. Zhao, Z. Nie, K. Wang, P. Liu, and X. Zhang, "Nonlinear ultrasonic test of concrete cubes with induced crack," *Ultrasonics*, vol. 97, pp. 1–10, Aug. 2019.
- [73] M. W. T. Mak, P. Desnerck, and J. M. Lees, "Corrosion-induced cracking and bond strength in reinforced concrete," *Constr. Build. Mater.*, vol. 208, pp. 228–241, May 2019.
- [74] H. Nakamura, T. Nanri, T. Miura, and S. Roy, "Experimental investigation of compressive strength and compressive fracture energy of longitudinally cracked concrete," *Cem. Concr. Compos.*, vol. 93, pp. 1–18, Oct. 2018.
- [75] S. M. Allam, M. S. Shoukry, G. E. Rashad, and A. S. Hassan, "Crack width evaluation for flexural RC members," *Alexandria Eng. J.*, vol. 51, no. 3, pp. 211–220, Sep. 2012.
- [76] A. Katrien, D. S. Geert, and M. Liviu, "The Influence of Cracks on Chloride Penetration in Concrete Structures - Part 1: Experimental Evaluation," *Transp. Mech. Crack. Concr.*, 2007.
- [77] N. J. Carino, J. R. Clifton, and A. Prabhakar, "NISTIR 5634 - Prediction of Cracking in Reinforced Concrete Structures," *Natl. Inst. Stand. Technol.*, 1995.
- [78] L. Chernin and D. V. Val, "Prediction of corrosion-induced cover cracking in reinforced concrete structures," *Constr. Build. Mater.*, vol. 25, no. 4, pp. 1854–1869, Apr. 2011.
- [79] D. C. Darwin, "Submicroscopic Deformation in Cement Paste and Mortar at High Load Rates," 1988.
- [80] A. H. White, V. A. Aagaard, and A. O. Christensen, "Crazing in Concrete and the Growth of Hair Cracks into Structural Cracks," *J. Proc.*, vol. 24, no. 2, pp. 190–201, 1928.
- [81] X. Ye, N. Hani, and S. Dan, "Early-Age Cracking in High Performance Concrete Decks of a Curved Steel Girder Bridge," *J. Aerosp. Eng.*, vol. 30, no. 2, p. B4016003, Mar. 2017.
- [82] I. Ray, Z. Gong, J. F. Davalos, and A. Kar, "Shrinkage and cracking studies of high performance concrete for bridge decks," *Constr. Build. Mater.*, vol. 28, no. 1, pp. 244–254, 2012.
- [83] K. B. and A. M. Fouladgar, "Solutions to Concrete Bridge Deck Cracking," *Concr. Int.*, vol. 19, no. 7.

- [84] V. T. N. Dao, P. F. Dux, P. H. Morris, and L. O'Moore, "Plastic Shrinkage Cracking of Concrete," *Aust. J. Struct. Eng.*, vol. 10, no. 3, pp. 207–214, 2010.
- [85] M. Kayondo, R. Combrinck, and W. P. Boshoff, "State-of-the-art review on plastic cracking of concrete," *Constr. Build. Mater.*, vol. 225, pp. 886–899, Nov. 2019.
- [86] X.-J. Liu, Z.-W. Yu, and L.-Z. Jiang, "Long term behavior of self-compacting reinforced concrete beams," *J. Cent. South Univ. Technol*, vol. 15, pp. 423–428, 2008.
- [87] C. Mazzotti and M. Savoia, "Long-Term Deflection of Reinforced Self-Consolidating Concrete Beams," *ACI Struct. J.*, vol. 106, no. 6, pp. 772–781, 2009.
- [88] ACI, "ACI 365 - Service-Life Prediction — State-of-the-Art Report," *Am. Concr. Inst.*, 2017.
- [89] E. Ringot and A. Bascoul, "About the analysis of microcracking in concrete," *Cem. Concr. Compos.*, vol. 23, no. 2–3, pp. 261–266, Apr. 2001.
- [90] P. Grassl and I. Athanasiadis, "3D Modelling of the Influence of Microcracking on Mass Transport in Concrete," *ACI Mater. J.*, vol. 89, no. 4, pp. 373–376, 1992.
- [91] F. Pedrosa and C. Andrade, "Corrosion induced cracking: Effect of different corrosion rates on crack width evolution," *Constr. Build. Mater.*, vol. 133, pp. 525–533, Feb. 2017.
- [92] M. Sillanpää, "The effect of cracking on chloride diffusion in concrete," Aalto University, 2010.
- [93] L. Wang and T. Ueda, "Mesoscale Modelling of the Chloride Diffusion in Cracks and Cracked Concrete," 2011.
- [94] A. Bascoul, "State of the art report - Part 2: Mechanical micro-cracking of concrete," *Mater. Struct.*, vol. 29, pp. 67–78, 1996.
- [95] Mo Li and Victor C. Li, "Cracking and Healing of Engineered Cementitious Composites under Chloride Environment," *ACI Mater. J.*, vol. May-June 2, 2011.
- [96] S. Jacobsen, J. Marchand, and L. Boisvert, "Effect of cracking and healing on chloride transport in OPC concrete," *Cem. Concr. Res.*, vol. 26, no. 6, pp. 869–881, Jun. 1996.
- [97] K. M. Nemati, P. J. M. Monteiro, and K. L. Scrivener, "Analysis of compressive stress-induced cracks in concrete," *ACI Mater. J.*, vol. 95, no. 5, 1998.

- [98] C. Zhou, K. Li, and X. Pang, “Effect of crack density and connectivity on the permeability of microcracked solids,” *Mech. Mater.*, vol. 43, no. 12, pp. 969–978, Dec. 2011.
- [99] A. Akhavan, S.-M.-H. Shafaatian, F. Rajabipour, Alireza Akhavan, Seyed-Mohammad-Hadi Shafaatian, and Farshad Rajabipour, “Quantifying the effects of crack width, tortuosity, and roughness on water permeability of cracked mortars,” *Cem. Concr. Res.*, vol. 42, no. 2, pp. 313–320, Feb. 2012.
- [100] X.-Y. Wang and L.-N. Zhang, “Simulation of Chloride Diffusion in Cracked Concrete with Different Crack Patterns,” *Adv. Mater. Sci. Eng.*, vol. 2016, pp. 1–11, 2016.
- [101] ASTM, “ASTM C1723-16, Standard Guide for Examination of Hardened Concrete Using Scanning Electron Microscopy,” 2016.
- [102] ASTM, “ASTM C42/C42M - Standard Test Method for Obtaining and Testing Drilled Cores and Sawed Beams of Concrete,” *Am. Soc. Test. Mater.*, pp. 1–7, 2016.
- [103] ASTM, “ASTM C496/C496M - Standard Test Method for Splitting Tensile Strength of Cylindrical Concrete Specimens,” *Am. Soc. Test. Mater.*, 2015.
- [104] P. Turgut and O. F. Kucuk, “Comparative Relationships of Direct, Indirect, and Semi-Direct Ultrasonic Pulse Velocity Measurements in Concrete,” *Russ. J. Nondestruct. Test.*, vol. 42, no. 11, pp. 1061–1069, 2006.
- [105] ASTM, “ASTM C469 - Standard Test Method for Static Modulus of Elasticity and Poisson’s Ratio of Concrete,” *Am. Soc. Test. Mater.*, 2015.
- [106] FDT, “FM 5-578 - Florida method of test for concrete resistivity as an electrical indicator of its permeability,” *Florida Dep. Transp.*, 2004.
- [107] NTBuild, “NT Build 492 - Concrete, mortar and cement-based repair materials: Chloride migration coefficient from non-steady-state migration experiments,” 1999.
- [108] RILEM, “RILEM Concrete Permanent Committee - Measurement of hardened concrete carbonation depth,” *Mater. Struct. Res. Test.*, pp. 435–440, 1984.
- [109] ASTM, “ASTM C39 - Standard Test Method for Compressive Strength of Cylindrical Concrete Specimens,” *Am. Soc. Test. Mater.*, 2016.
- [110] ASTM, “ASTM C1202 - Standard Test Method for Electrical Indication of Concrete’s Ability to Resist Chloride Ion Penetration,” *Am. Soc. Test. Mater.*, pp. 1–8, 2016.
- [111] PCI, “IS536 - Types and Causes of Concrete Deterioration,” *Portl. Cem.*

Assoc., 2002.

- [112] H. Samouh, E. Rozière, V. Wisniewski, and A. Loukili, “Consequences of longer sealed curing on drying shrinkage, cracking and carbonation of concrete,” *Cem. Concr. Res.*, vol. 95, pp. 117–131, May 2017.
- [113] N. Chahal, R. Siddique, and A. Rajor, “Influence of bacteria on the compressive strength, water absorption and rapid chloride permeability of fly ash concrete,” *Constr. Build. Mater.*, vol. 28, no. 1, pp. 351–356, Mar. 2012.
- [114] J.-G. Dai, Y. Akira, F. H. Wittmann, H. Yokota, and P. Zhang, “Water repellent surface impregnation for extension of service life of reinforced concrete structures in marine environments: The role of cracks,” *Cem. Concr. Compos.*, vol. 32, no. 2, pp. 101–109, Feb. 2010.
- [115] G. Trtnik, F. Kavc̃ic, and G. Turk, “Prediction of concrete strength using ultrasonic pulse velocity and artificial neural networks,” *Ultrasonics*, vol. 49, pp. 53–60, 2009.
- [116] Chien-Chih Wang and Her-Yung Wang, “Assessment of the compressive strength of recycled waste LCD glass concrete using the ultrasonic pulse velocity,” *Constr. Build. Mater.*, vol. 137, pp. 345–353, 2017.
- [117] D. J. Olive, *Linear Regression*, 2017th ed. Springer International Publishing, 2017.
- [118] J. D. Brown, *Understanding research in second language learning: A teacher’s guide to statistics and research design*. Cambridge University Press, 1988.
- [119] G. Piñeiro, S. Perelman, J. P. Guerschman, and J. M. Paruelo, “How to evaluate models: Observed vs. predicted or predicted vs. observed?,” *Ecol. Modell.*, vol. 216, no. 3–4, pp. 316–322, Sep. 2008.
- [120] T. K. Koo and M. Y. Li, “A Guideline of Selecting and Reporting Intraclass Correlation Coefficients for Reliability Research,” *J. Chiropr. Med.*, vol. 15, no. 2, pp. 155–163, 2016.
- [121] K. Lin, “Reliability-based minimum life cycle cost design of reinforced concrete girder bridges.,” 1997.
- [122] P. D. Thompson and K. M. Ford, *Estimating life expectancies of highway assets: Guidebook*, vol. 1. Transportation Research Board, 2012.
- [123] A. A. Sohangpurwala, *Manual on service life of corrosion-damaged reinforced concrete bridge superstructure elements*, vol. 558. Transportation Research Board, 2006.
- [124] FHWA, “Performance-Based Practical Design,” 2017. [Online]. Available:

<https://www.fhwa.dot.gov/design/pbpd/>.

- [125] D. Jones and C. B. T.-P. of B. B. M. Brischke, Eds., “8 - Modelling,” Woodhead Publishing, 2017, pp. 483–546.
- [126] L. Gao, Y.-L. Mo, S. Dhonde, D. Saldarriaga, L. Song, and A. Senouci, “TxDOT 0-6938: Synthesis of Service Life Prediction for Bridges in Texas: Final Report,” 2017.
- [127] X. Li *et al.*, “Evaluation of data-driven models for predicting the service life of concrete sewer pipes subjected to corrosion,” *J. Environ. Manage.*, vol. 234, pp. 431–439, 2019.
- [128] F. E. Harrell Jr, K. L. Lee, and D. B. Mark, “Multivariable prognostic models: issues in developing models, evaluating assumptions and adequacy, and measuring and reducing errors,” *Stat. Med.*, vol. 15, no. 4, pp. 361–387, 1996.
- [129] G. Stukhart, R. W. James, A. Garcia-Diaz, R. P. Bligh, J. Sobanjo, and W. D. McFarland, “Study for a comprehensive bridge management system for Texas,” 1990.
- [130] M. Bolukbasi, J. Mohammadi, and D. Arditi, “Estimating the Future Condition of Highway Bridge Components Using National Bridge Inventory Data,” *Pr. Period. Struct. Des. Constr.*, vol. 9, no. 1, pp. 16–25, 2014.
- [131] A. K. Agrawal and A. Kawaguchi, “Bridge element deterioration rates, 2009,” *New York State Dep. Transp.*
- [132] P. Lu, H. Wang, and D. Tolliver, “Prediction of Bridge Component Ratings Using Ordinal Logistic Regression Model,” *Math. Probl. Eng.*, vol. 2019, 2019.
- [133] M. P. Enright and D. M. Frangopol, “Service-life prediction of deteriorating concrete bridges,” *J. Struct. Eng.*, vol. 124, no. 3, pp. 309–317, 1998.
- [134] P. Omenzetter and J. M. W. Brownjohn, “Application of time series analysis for bridge monitoring,” *Smart Mater. Struct.*, vol. 15, no. 1, pp. 129–138, 2006.
- [135] K. Dinh, T. Zayed, F. Romero, and A. Tarussov, “Method for analyzing time-series GPR data of concrete bridge decks,” *J. Bridg. Eng.*, vol. 20, no. 6, p. 4014086, 2014.
- [136] G. Bu, J. Lee, H. Guan, M. Blumenstein, and Y.-C. Loo, “Development of an integrated method for probabilistic bridge-deterioration modeling,” *J. Perform. Constr. Facil.*, vol. 28, no. 2, pp. 330–340, 2012.

- [137] Y. Jiang and K. C. Sinha, "Bridge service life prediction model using the Markov chain," *Transp. Res. Rec.*, vol. 1223, pp. 24–30, 1989.
- [138] S.-K. Ng and F. Moses, "Bridge deterioration modeling using semi-Markov theory," *A. A. Balkema Uitgevers B. V, Struct. Saf. Reliab.*, vol. 1, pp. 113–120, 1998.
- [139] J. Yang, "Road crack condition performance modeling using recurrent Markov chains and artificial neural networks," 2004.
- [140] O. Thomas and J. Sobanjo, "Comparison of Markov chain and semi-Markov models for crack deterioration on flexible pavements," *J. Infrastruct. Syst.*, vol. 19, no. 2, pp. 186–195, 2012.
- [141] E. EuRam III, "DuraCrete final technical report, probabilistic performance based durability design of concrete structures," *Doc. BE95-1347*, 2000.
- [142] M. G. Alexander, J. R. Mackechnie, and Y. Ballim, "Guide to the use of durability indexes for achieving durability in concrete structures, Research Monograph No. 2," *Dep. Civ. Eng. Univ. Cape T.*, 1999.
- [143] L. Tang, "Chloride transport in concrete-measurement and prediction," *Chalmers Univ. Technol. Sweden, Dr. Thesis*, 1996.
- [144] C. Andrade, N. Rebolledo, F. Tavares, R. Pérez, and M. Baz, "Concrete durability of the new Panama Canal: Background and aspects of testing," in *Marine Concrete Structures*, Elsevier, 2016, pp. 429–458.
- [145] O. E. Gjrv, *Durability design of concrete structures in severe environments*. CRC Press, 2014.
- [146] "STADIUM® Technology Portfolio - SIMCO Technologies." [Online]. Available: <https://www.simcotechnologies.com/what-we-do/stadium-technology-portfolio/>. [Accessed: 18-Oct-2019].
- [147] P. Schiessl, S. Helland, C. Gehlen, L.-O. Nilsson, and S. Rostam, *Model Code for Service Life Design*. 2005.
- [148] M. D. A. Thomas and E. C. Bentz, "Computer program for predicting the service life and life-cycle costs of reinforced concrete exposed to chlorides," *Life365 Manual, SFA*, pp. 12–56, 2002.
- [149] K. Y. Ann, S. Pack, J. Hwang, H. Song, S. Kim, and M. Carlo, "Service life prediction of a concrete bridge structure subjected to carbonation," *Constr. Build. Mater.*, vol. 24, no. 8, pp. 1494–1501, 2010.
- [150] M. Otieno, H. Beushausen, and M. Alexander, "Resistivity-based chloride-induced corrosion rate prediction models and hypothetical framework for interpretation of resistivity measurements in cracked RC structures," *Mater. Struct.*, vol. 49, pp. 2349–2366, 2016.

- [151] J. Pacheco, “Incorporating Cracks in Chloride Ingress Modeling and Service Life Predictions,” no. 116, pp. 113–118, 2019.
- [152] VDoT, “VTRC 18-R2 - Design of Artificially Cracked Concrete Specimens for Virginia Department of Transportation Material Evaluation,” *Virginia Dep. Transp.*, 2018.
- [153] B. Šavija, M. Luković, and E. Schlangen, “Lattice modeling of rapid chloride migration in concrete,” *Cem. Concr. Res.*, vol. 61–62, pp. 49–63, Jul. 2014.
- [154] B. Šavija, J. Pacheco, and E. Schlangen, “Lattice modeling of chloride diffusion in sound and cracked concrete,” *Cem. Concr. Compos.*, vol. 42, pp. 30–40, Sep. 2013.
- [155] X. Du, L. Jin, R. Zhang, and Y. Li, “Effect of cracks on concrete diffusivity: A meso-scale numerical study,” *Ocean Eng.*, vol. 108, pp. 539–551, Nov. 2015.
- [156] L. Marsavina, K. Audenaert, G. De Schutter, N. Faur, and D. Marsavina, “Experimental and numerical determination of the chloride penetration in cracked concrete,” *Constr. Build. Mater.*, vol. 23, no. 1, pp. 264–274, Jan. 2009.
- [157] M. Salehi, P. Ghods, and O. Burkan Isgor, “Numerical Study on the Effect of Cracking on Surface Resistivity of Plain and Reinforced Concrete Elements,” *J. Mater. Civ. Eng.*, vol. 27, no. 12, 2015.
- [158] ASTM, “ASTM C33 - Standard Specification for Concrete Aggregates,” *Am. Soc. Test. Mater.*, 2016.
- [159] A. Schwartzenruber and C. Catherine, “Method of the concrete equivalent mortar(CEM)--a new tool to design concrete containing admixture,” *Mater. Struct.*, vol. 33, no. 232, pp. 475–482, 2009.
- [160] S. W. Dean, J. J. Assaad, J. Harb, and E. Chakar, “Relationships Between Key ASTM Test Methods Determined on Concrete and Concrete-Equivalent-Mortar Mixtures,” *J. ASTM Int.*, vol. 6, no. 3, p. JAI101735, 2009.
- [161] C. A. Ross, P. Y. Thompson, and J. W. Tedesco, “Split-Hopkinson Pressure-Bar Tests on Concrete and Mortar in Tension and Compression,” *ACI Mater. J.*, vol. 86, no. 5, pp. 475–481, 1990.
- [162] R. John and S. P. Shah, “EFFECT OF HIGH STRENGTH AND RATE OF LOADING ON FRACTURE PARAMETERS OF CONCRETE.” Soc for Experimental Mechanics Inc, pp. 35–52, 01-Dec-1987.
- [163] F. M. Mellinger and D. L. Birkimer, “Measurements of stress and strain on cylindrical test specimens of rock and concrete under impact loading,”

Ohio River Div Labs Cincinnati, 1966.

- [164] N Swamy and G Rigby, “Dynamic properties of hardened mortar and concrete paste,” *Mater. Constr.*, vol. 4, no. 19, 1971.
- [165] S. Popovics, J. L. Rose, and J. S. Popovics, “The behaviour of ultrasonic pulses in concrete,” *Cem. Concr. Res.*, vol. 20, no. 2, pp. 259–270, Mar. 1990.
- [166] C. C. Yang, “Effect of the Transition Zone on the Elastic Moduli of Mortar,” *Cem. Concr. Res.*, vol. 28, no. 5, pp. 727–736, 1998.
- [167] X. Chen, S. Wu, and J. Zhou, “Experimental and modeling study of dynamic mechanical properties of cement paste, mortar and concrete,” *Constr. Build. Mater.*, vol. 47, pp. 419–430, Oct. 2013.
- [168] T.-C. Hou, V. K. Nguyen, Y.-M. Su, Y.-R. Chen, and P.-J. Chen, “Effects of coarse aggregates on the electrical resistivity of Portland cement concrete,” *Constr. Build. Mater.*, vol. 133, pp. 397–408, Feb. 2017.
- [169] S. Caré, “Influence of aggregates on chloride diffusion coefficient into mortar,” *Cem. Concr. Res.*, vol. 33, 2003.
- [170] X. Shi, Z. Yang, Y. Liu, and D. Cross, “Strength and corrosion properties of Portland cement mortar and concrete with mineral admixtures,” *Constr. Build. Mater.*, vol. 25, no. 8, pp. 3245–3256, Aug. 2011.
- [171] J. Khunthongkeaw, S. Tangtermsirikul, and T. Leelawat, “A study on carbonation depth prediction for fly ash concrete,” *Constr. Build. Mater.*, vol. 20, no. 9, pp. 744–753, Nov. 2006.
- [172] M. Şahmaran, “Effect of flexure induced transverse crack and self-healing on chloride diffusivity of reinforced mortar,” *J. Mater. Sci.*, vol. 42, no. 22, pp. 9131–9136, Nov. 2007.
- [173] A. A. Ramezani pour, S. A. H. Ghoreishian, B. Ahmadi, M. Balapour, and A. M. Ramezani pour, “Modeling of chloride ions penetration in cracked concrete structures exposed to marine environments,” *Struct. Concr.*, vol. 19, no. 5, pp. 1460–1471, 2018.
- [174] W. Shao and J. Li, “Service life prediction of cracked RC pipe piles exposed to marine environments,” *Constr. Build. Mater.*, vol. 64, pp. 301–307, 2014.
- [175] S. J. Jaffer and C. M. Hansson, “The influence of cracks on chloride-induced corrosion of steel in ordinary Portland cement and high performance concretes subjected to different loading conditions,” *Corros. Sci.*, vol. 50, no. 12, pp. 3343–3355, Dec. 2008.
- [176] K. Kobayashi and Y. Kojima, “Effect of fine crack width and water cement

ratio of SHCC on chloride ingress and rebar corrosion,” *Cem. Concr. Compos.*, vol. 80, pp. 235–244, Jul. 2017.

- [177] H. Z. Lopez-Calvo, P. Montes-García, V. G. Jiménez-Quero, H. Gómez-Barranco, T. W. Bremner, and M. D. A. Thomas, “Influence of crack width, cover depth and concrete quality on corrosion of steel in HPC containing corrosion inhibiting admixtures and fly ash,” *Cem. Concr. Compos.*, vol. 88, pp. 200–210, Apr. 2018.
- [178] NOAA, “www.noaa.gov,” *National Oceanic and Atmospheric Administration, U.S. Department of Commerce*. [Online]. Available: <http://www.noaa.gov/>. [Accessed: 13-Jul-2018].
- [179] ASTM, “ASTM C876 - Standard Test Method for Corrosion Potentials of Uncoated Reinforcing Steel in,” *Am. Soc. Test. Mater.*, pp. 1–8, 2019.
- [180] ASTM, “ASTM F2832-Standard Guide for Accelerated Corrosion Testing for Mechanical Fasteners, ASTM International,” 2011.
- [181] F. Lanza di Scalea, P. Rizzo, and F. Seible, “Stress measurement and defect detection in steel strands by guided stress waves,” *J. Mater. Civ. Eng.*, vol. 15, no. 3, pp. 219–227, 2003.
- [182] S. Chaki and G. Bourse, “Guided ultrasonic waves for non-destructive monitoring of the stress levels in prestressed steel strands,” *Ultrasonics*, vol. 49, no. 2, pp. 162–171, 2009.
- [183] F. Shi, J. E. Michaels, and S. J. Lee, “In situ estimation of applied biaxial loads with Lamb waves,” *J. Acoust. Soc. Am.*, vol. 133, no. 2, pp. 677–687, 2013.
- [184] A. Pau and F. Lanza di Scalea, “Nonlinear guided wave propagation in prestressed plates,” *J. Acoust. Soc. Am.*, vol. 137, no. 3, pp. 1529–1540, 2015.
- [185] E. Dehghan-Niri and S. Salamone, “A multi-helical ultrasonic imaging approach for the structural health monitoring of cylindrical structures,” *Struct. Heal. Monit.*, vol. 14, no. 1, pp. 73–85, 2014.
- [186] R. Raisutis, R. Kazys, L. Mazeika, E. Zukauskas, V. Samaitis, and A. Jankauskas, “Ultrasonic guided wave-based testing technique for inspection of multi-wire rope structures,” *NDT E Int.*, vol. 62, pp. 40–49, 2014.
- [187] C. Schaal, S. Bischoff, and L. Gaul, “Damage detection in multi-wire cables using guided ultrasonic waves,” *Struct. Heal. Monit.*, vol. 15, no. 3, pp. 279–288, 2016.
- [188] A. Farhidzadeh and S. Salamone, “Reference-free corrosion damage diagnosis in steel strands using guided ultrasonic waves,” *Ultrasonics*, vol.

57, pp. 198–208, 2015.

- [189] A. Farhidzadeh, A. Ebrahimkhanlou, and S. Salamone, “Corrosion damage estimation in multi-wire steel strands using guided ultrasonic waves,” in *Structural Health Monitoring and Inspection of Advanced Materials, Aerospace, and Civil Infrastructure*, 2015, vol. 9437, p. 94371F.
- [190] M. Legg, M. K. Yucel, V. Kappatos, C. Selcuk, and T.-H. Gan, “Increased range of ultrasonic guided wave testing of overhead transmission line cables using dispersion compensation,” *Ultrasonics*, vol. 62, pp. 35–45, 2015.
- [191] R. A. Toupin and B. Bernstein, “Sound waves in deformed perfectly elastic materials. Acoustoelastic effect,” *J. Acoust. Soc. Am.*, vol. 33, no. 2, pp. 216–225, 1961.
- [192] N. Gandhi, J. E. Michaels, and S. J. Lee, “Acoustoelastic Lamb wave propagation in biaxially stressed plates,” *J. Acoust. Soc. Am.*, vol. 132, no. 3, pp. 1284–1293, 2012.
- [193] M. Mazzotti, A. Marzani, I. Bartoli, and E. Viola, “Guided waves dispersion analysis for prestressed viscoelastic waveguides by means of the SAFE method,” *Int. J. Solids Struct.*, vol. 49, no. 18, pp. 2359–2372, 2012.
- [194] B. Dubuc, A. Ebrahimkhanlou, and S. Salamone, “Effect of pressurization on helical guided wave energy velocity in fluid-filled pipes,” *Ultrasonics*, vol. 75, pp. 145–154, 2017.
- [195] B. Dubuc, A. Ebrahimkhanlou, and S. Salamone, “Helical guided waves in liquid-filled cylindrical shells subjected to static pressurization stress,” in *Health Monitoring of Structural and Biological Systems*, 2016, vol. 9805, p. 98050T.
- [196] F. Chen and P. D. Wilcox, “The effect of load on guided wave propagation,” *Ultrasonics*, vol. 47, pp. 111–122, 2007.
- [197] P. W. Loveday, “Semi-analytical finite element analysis of elastic waveguides subjected to axial loads,” *Ultrasonics*, vol. 49, no. 3, pp. 298–300, 2009.
- [198] E. S. Suhubi, “Small longitudinal vibration of an initially stretched circular cylinder,” *Int. J. Eng. Sci.*, vol. 2, pp. 509–517, 1965.
- [199] G. Mott, “Elastic waveguide propagation in an infinite isotropic solid cylinder that is subjected to a static axial stress and strain,” *J. Acoust. Soc. Am.*, vol. 53, no. 4, pp. 1129–1133, 1972.
- [200] A. E. Green, “Torsional vibrations of an initially stressed circular cylinder,” in *Problems of Continuum Mechanics*, SIAM, 1961, pp. 148–154.

- [201] H. Kwun, K. A. Bartels, and J. J. Hanley, “Effects of tensile loading on the properties of elastic-wave propagation in a strand,” *J. Acoust. Soc. Am.*, vol. 103, no. 6, pp. 3370–3375, 1998.
- [202] H.-L. Chen and K. Wissawapaisal, “Measurement of tensile forces in a seven-wire prestressing strand using stress waves,” *J. Eng. Mech.*, vol. 127, no. 6, pp. 599–606, 2001.
- [203] H.-L. Chen and K. Wissawapaisal, “Application of Wigner-Ville transform to evaluate tensile forces in seven-wire prestressing strands,” *J. Eng. Mech.*, vol. 128, no. 11, pp. 1206–1214, 2002.
- [204] G. A. Washer, R. E. Green, and R. B. Pond, “Velocity constants for ultrasonic stress measurement in prestressing tendons,” *Res. Nondestr. Eval.*, vol. 14, pp. 81–94, 2002.
- [205] P. Rizzo, “Ultrasonic wave propagation in progressively loaded multi-wire strands,” *Exp. Mech.*, vol. 46, pp. 297–306, 2006.
- [206] F. Treyssède and L. Laguerre, “Investigation of elastic modes propagating in multi-wire helical waveguides,” *J. Sound Vib.*, vol. 329, pp. 1702–1716, 2010.
- [207] C. Nucera and F. Lanza di Scalea, “Monitoring load levels in multi-wire strands by nonlinear ultrasonic waves,” *Struct. Heal. Monit.*, vol. 10, no. 6, pp. 617–629, 2011.
- [208] C. Schaal, S. Bischoff, and L. Gaul, “Energy-based models for guided ultrasonic wave propagation in multi-wire cables,” *Int. J. Solids Struct.*, vol. 64–65, pp. 22–29, 2015.
- [209] F. Treyssède, “Investigation of the interwire energy transfer of elastic guided waves inside prestressed cables,” *J. Acoust. Soc. Am.*, vol. 140, no. 1, pp. 498–509, 2016.
- [210] M. D. Beard, M. J. S. Lowe, and P. Cawley, “Ultrasonic guided waves for inspection of grouted tendons and bolts,” *J. Mater. Civ. Eng.*, vol. 15, no. 3, pp. 212–218, 2003.
- [211] L. Laguerre and F. Treyssède, “Non destructive evaluation of seven-wire strands using ultrasonic guided waves,” *Eur. J. Environ. Civ. Eng.*, vol. 15, no. 4, pp. 487–500, 2011.
- [212] L. Laguerre, O. Durand, and R. Colin, “Method for detecting a defect in a metal wire of a set of metal wires, in particular for an anchoring area of a civil engineering structure.” 2016.
- [213] B. N. Pavlakovic, M. J. S. Lowe, and P. Cawley, “High-frequency low-loss ultrasonic modes in imbedded bars,” *J. Appl. Mech.*, vol. 68, no. 1, pp. 67–75, 2001.

- [214] B. L. Ervin, D. A. Kuchma, J. T. Bernhard, and H. Reis, “Monitoring corrosion of rebar embedded in mortar using high-frequency guided ultrasonic waves,” *J. Eng. Mech.*, vol. 135, no. 1, pp. 9–19, 2009.
- [215] D. S. Hughes and J. L. Kelly, “Second-order elastic deformation of solids,” *Phys. Rev.*, vol. 92, no. 5, pp. 1145–1149, 1953.
- [216] F. D. Murnaghan, *Finite Deformation of an Elastic Solid*, 1st ed. New York: John Wiley & Sons, 1951.
- [217] R. S. Rivlin, “The solution of problems in second order elasticity theory,” *J. Ratl. Mech. Anal.*, vol. 2, pp. 53–81, 1953.
- [218] M. Hayes and R. S. Rivlin, “Surface waves in deformed elastic materials,” *Arch. Ratl. Mech. Anal.*, vol. 8, pp. 358–380, 1961.
- [219] R. N. Thurston and K. Brugger, “Third-order elastic constants and the velocity of small amplitude elastic waves in homogeneously stressed media,” *Phys. Rev.*, vol. 133, no. 6A, pp. A1604–A1610, 1964.
- [220] N. Gandhi, “Determination of Dispersion Curves for Acoustoelastic Lamb Wave Propagation,” Georgia Institute of Technology, 2010.
- [221] R. T. Smith, R. Stern, and R. W. B. Stephens, “Third-order elastic moduli of polycrystalline metals from ultrasonic velocity measurements,” *J. Acoust. Soc. Am.*, vol. 40, no. 5, pp. 1002–1008, 1966.
- [222] J. S. Heyman, S. G. Allison, and K. Salama, “Influence of carbon content on higher-order ultrasonic properties in steels,” in *Ultrasonics Symposium*, 1983, pp. 991–994.
- [223] T. R. Meeker and A. H. Meitzler, “Guided Wave Propagation in Elongated Cylinders and Plates,” in *Physical Acoustics*, 1st ed., W. P. Mason and R. N. Thurston, Eds. New York: Academic Press, 1964, pp. 111–167.
- [224] Y.-H. Pao and U. Gamer, “Acoustoelastic waves in orthotropic media,” *J. Acoust. Soc. Am.*, vol. 77, no. 3, pp. 806–812, 1985.
- [225] S. Machida and A. J. Durelli, “Response of a strand to axial and torsional displacements,” *J. Mech. Eng. Sci.*, vol. 15, no. 4, pp. 241–251, 1973.
- [226] L. Gaul and S. Hurlbaas, “Identification of the impact location on a plate using wavelets,” *Mech. Syst. Signal Pr.*, vol. 12, no. 6, pp. 783–795, 1998.
- [227] D. D. Muir, “One-sided Ultrasonic Determination of Third Order Elastic Constants Using Angle-beam Acoustoelasticity Measurements,” Georgia Institute of Technology, 2009.
- [228] A. B. Mehrabi, “In-service evaluation of cable-stayed bridges, overview of available methods, and findings,” *J. Bridg. Eng.*, vol. 11, no. 6, pp. 716–

724, 2006.

- [229] S. Sumitro, S. Kurokawa, K. Shimano, and M. L. Wang, “Monitoring based maintenance utilizing actual stress sensory technology,” *Smart Mater. Struct.*, vol. 14, no. 3, pp. S68--S78, 2005.
- [230] B. Dubuc, A. Ebrahimkhanlou, and S. Salamone, “Stress measurement in seven-wire strands using higher order guided ultrasonic wave modes,” *Transp. Res. Rec.*, vol. 2672, no. 41, pp. 123–131, 2018.
- [231] H. Kwun and K. A. Bartels, “Magnetostrictive sensor technology and its applications,” *Ultrasonics*, vol. 36, no. 1, pp. 171–178, 1998.
- [232] X. Liu, B. Wu, F. Qin, C. He, and Q. Han, “Observation of ultrasonic guided wave propagation behaviours in pre-stressed multi-wire structures,” *Ultrasonics*, vol. 73, pp. 196–205, 2017.
- [233] J. Qian, X. Chen, L. Sun, G. Yao, and X. Wang, “Numerical and experimental identification of seven wire strand tensions using scale energy entropy spectra of ultrasonic guided waves,” *Shock Vib.*, vol. 2018, p. 6905073, 2018.
- [234] I. Bartoli, S. Salamone, R. R. Phillips, F. Lanza di Scalea, and C. S. Sikorsky, “Use of interwire ultrasonic leakage to quantify loss of prestress in multiwire tendons,” *J. Eng. Mech.*, vol. 137, no. 5, pp. 324–333, 2011.
- [235] A. S. Sason, “Evaluation of degree of rusting on prestressed concrete strand,” *PCI J.*, vol. 37, no. 3, pp. 25–30, 1992.
- [236] R. A. Reis, “Corrosion Evaluation and Tensile Results of Selected Post-Tensioning Strands at the SFOBB Skyway Seismic Replacement Project -- Phase III Report,” 2007.
- [237] B. Dubuc, A. Ebrahimkhanlou, and S. Salamone, “Higher order longitudinal guided wave modes in axially stressed seven-wire strands,” *Ultrasonics*, vol. 84, pp. 382–391, 2018.
- [238] Z. Su, X. Wang, L. Cheng, L. Yu, and Z. Chen, “On selection of data fusion schemes for structural damage evaluation,” *Struct. Heal. Monit.*, vol. 8, no. 3, pp. 223–241, 2009.
- [239] J. Moll, L. De Marchi, C. Kexel, and A. Marzani, “High resolution defect imaging in guided waves inspections by dispersion compensation and nonlinear data fusion,” *Acta Acust.*, vol. 103, no. 6, pp. 941–949, 2017.
- [240] B. Dubuc, A. Ebrahimkhanlou, and S. Salamone, “A spectral method for computing the effect of stress on guided modes in plates and rods,” in *Health Monitoring of Structural and Biological Systems*, 2018, vol. 10600, p. 106001Z.

- [241] D. L. Hall and J. Llinas, "An introduction to multisensor data fusion," *Proc. IEEE*, vol. 85, no. 1, pp. 6–23, 1997.
- [242] C. R. Farrar and K. Worden, *Structural Health Monitoring: A Machine Learning Perspective*, 1st ed. John Wiley & Sons, 2013.
- [243] C. E. Rasmussen and C. K. I. Williams, *Gaussian Processes for Machine Learning*. Cambridge, MA: MIT Press, 2006.
- [244] R. E. Melchers, "Modeling of marine immersion corrosion for mild and low-alloy steels--Part 1: Phenomenological model," *Corrosion*, vol. 59, no. 4, pp. 319–334, 2003.
- [245] S. C. Barton, G. W. Vermaas, P. F. Duby, A. C. West, and R. Betti, "Accelerated corrosion and embrittlement of high-strength bridge wire," *J. Mater. Civ. Eng.*, vol. 12, no. 1, pp. 33–38, 2000.
- [246] P. A. Vanniamparambil *et al.*, "A data fusion approach for progressive damage quantification in reinforced concrete masonry walls," *Smart Mater. Struct.*, vol. 23, no. 1, p. 15007, 2014.
- [247] M. Ercolino, A. Farhidzadeh, S. Salamone, and G. Magliulo, "Detection of onset of failure in prestressed strands by cluster analysis of acoustic emissions," *Struct. Monit. Maint.*, vol. 2, no. 4, pp. 339–355, 2015.
- [248] A. Farhidzadeh, S. Epackachi, S. Salamone, and A. Whittaker, "Bayesian decision and mixture models for AE monitoring of steel-concrete composite shear walls," *Smart Mater. Struct.*, vol. 24, no. 11, p. 115028, 2015.
- [249] B. Dubuc, A. Ebrahimkhanlou, and S. Salamone, "Localization of multiple acoustic emission events occurring closely in time in thin-walled pipes using sparse reconstruction," *J. Intel. Mater. Syst. Struct.*, vol. 29, no. 11, pp. 2362–2373, 2018.
- [250] M. S. Weng, S. E. Dunn, W. H. Hartt, and R. P. Brown, "Application of acoustic emission to detection of reinforcing steel corrosion in concrete," *Corrosion*, vol. 38, no. 1, pp. 9–14, 1982.
- [251] S. E. Dunn, J. D. Young, W. H. Hartt, and R. P. Brown, "Acoustic emission characterization of corrosion induced damage in reinforced concrete," *Corrosion*, vol. 40, no. 7, pp. 339–343, 1984.
- [252] J. Mangual, M. ElBatanouny, P. Ziehl, and F. Matta, "Corrosion damage quantification of prestressing strands using acoustic emission," *J. Mater. Civ. Eng.*, vol. 25, no. 9, pp. 1326–1334, 2013.
- [253] M. Di Benedetti, G. Loreto, F. Matta, and A. Nanni, "Acoustic emission historic index and frequency spectrum of reinforced concrete under accelerated corrosion," *J. Mater. Civ. Eng.*, vol. 26, no. 9, p. 4014059,

2014.

- [254] M. K. ElBatanouny, J. Mangual, P. H. Ziehl, and F. Matta, “Early corrosion detection in prestressed concrete girders using acoustic emission,” *J. Mater. Civ. Eng.*, vol. 26, no. 3, pp. 504–511, 2014.
- [255] S. Patil, B. Karkare, and S. Goyal, “Acoustic emission vis-a-vis electrochemical techniques for corrosion monitoring of reinforced concrete element,” *Constr. Build. Mater.*, vol. 68, pp. 326–332, 2014.
- [256] A. Sharma, S. Sharma, S. Sharma, and A. Mukherjee, “Investigation of deterioration in corroding reinforced concrete beams using active and passive techniques,” *Constr. Build. Mater.*, vol. 161, pp. 555–569, 2018.
- [257] A. D. Zdunek, D. Prine, Z. Li, E. Landis, and S. Shah, “Early detection of steel rebar corrosion by acoustic emission monitoring,” in *CORROSION95*, 1995, pp. 1–9.
- [258] Z. Li, F. Li, A. Zdunek, E. Landis, and S. P. Shah, “Application of acoustic emission technique to detection of reinforcing steel corrosion in concrete,” *ACI Mater. J.*, vol. 95, no. 1, pp. 68–76, 1998.
- [259] D.-J. Yoon, W. J. Weiss, and S. P. Shah, “Assessing damage in corroded reinforced concrete using acoustic emission,” *J. Eng. Mech.*, vol. 126, no. 3, pp. 273–283, 2000.
- [260] S. A. Austin, R. Lyons, and M. J. Ing, “Electrochemical behavior of steel-reinforced concrete during accelerated corrosion testing,” *Corrosion*, vol. 60, no. 2, pp. 203–212, 2004.
- [261] M. Ing, S. Austin, and R. Lyons, “Cover zone properties influencing acoustic emission due to corrosion,” *Cem. Concr. Res.*, vol. 35, no. 2, pp. 284–295, 2005.
- [262] M. Ohtsu, K. Mori, and Y. Kawasaki, “Corrosion process and mechanisms of corrosion-induced cracks in reinforced concrete identified by AE analysis,” *Strain*, vol. 47, pp. 179–186, 2011.
- [263] M. Di Benedetti, G. Loreto, F. Matta, and A. Nanni, “Continuous acoustic emission monitoring of reinforced concrete under accelerated corrosion,” *J. Mater. Civ. Eng.*, vol. 25, no. 8, pp. 1022–1029, 2013.
- [264] H. A. Elfergani, R. Pullin, and K. Holford, “Damage assessment of corrosion in prestressed concrete by acoustic emission,” *Constr. Build. Mater.*, vol. 40, pp. 925–933, 2013.
- [265] S. Ramadan, L. Gaillet, C. Tessier, and H. Idrissi, “Detection of stress corrosion cracking of high-strength steel used in prestressed concrete structures by acoustic emission technique,” *Appl. Surf. Sci.*, vol. 254, no. 8, pp. 2255–2261, 2008.

- [266] R. Ghrist, “Barcodes: The persistent topology of data,” *B. Am. Math. Soc.*, vol. 45, no. 1, pp. 61–75, 2008.
- [267] J. A. Perea and J. Harer, “Sliding windows and persistence: An application of topological methods to signal analysis,” *Found. Comput. Math.*, vol. 15, no. 3, pp. 799–838, 2015.
- [268] P. Y. Lum *et al.*, “Extracting insights from the shape of complex data using topology,” *Sci. Rep.*, vol. 3, pp. 1–7, 2013.
- [269] G. Carlsson, “Topology and data,” *B. Am. Math. Soc.*, vol. 46, no. 2, pp. 255–308, 2009.
- [270] K. Tuutti, “Corrosion of Steel in Concrete,” 1982.
- [271] J. G. Cabrera, “Deterioration of concrete due to reinforcement steel corrosion,” *Cem. Concr. Comp.*, vol. 18, no. 1, pp. 47–59, 1996.
- [272] C. Andrade, C. Alonso, and F. J. Molina, “Cover cracking as a function of bar corrosion: Part I-Experimental test,” *Mater. Struct.*, vol. 26, no. 8, pp. 453–464, 1993.
- [273] C. Alonso, C. Andrade, J. Rodriguez, and J. M. Diez, “Factors controlling cracking of concrete affected by reinforcement corrosion,” *Mater. Struct.*, vol. 31, no. 7, pp. 435–441, 1998.
- [274] R. E. Weyers, “Service life model for concrete structures in chloride laden environments,” *ACI Mater. J.*, vol. 95, no. 4, pp. 445–451, 1998.
- [275] T. El Maaddawy and K. Soudki, “A model for prediction of time from corrosion initiation to corrosion cracking,” *Cem. Concr. Comp.*, vol. 29, no. 3, pp. 168–175, 2007.
- [276] B. H. Oh, K. H. Kim, and B. S. Jang, “Critical corrosion amount to cause cracking of reinforced concrete structures,” *ACI Mater. J.*, vol. 106, no. 4, pp. 333–339, 2009.
- [277] A. Hatcher, *Algebraic Topology*, 1st ed. Cambridge: Cambridge University Press, 2001.
- [278] V. de Silva and G. Carlsson, “Topological estimation using witness complexes,” in *Symposium on Point-Based Graphics*, 2004, pp. 157–166.
- [279] H. Adams, A. Tausz, and M. Vejdemo-Johansson, “javaPlex : A research software package for persistent (co)homology,” in *4th ICMS*, 2014, pp. 129–136.
- [280] H. Edelsbrunner, D. Letscher, and A. Zomorodian, “Topological persistence and simplification,” *Discret. Comput. Geom.*, vol. 28, no. 4, pp. 511–533, 2002.

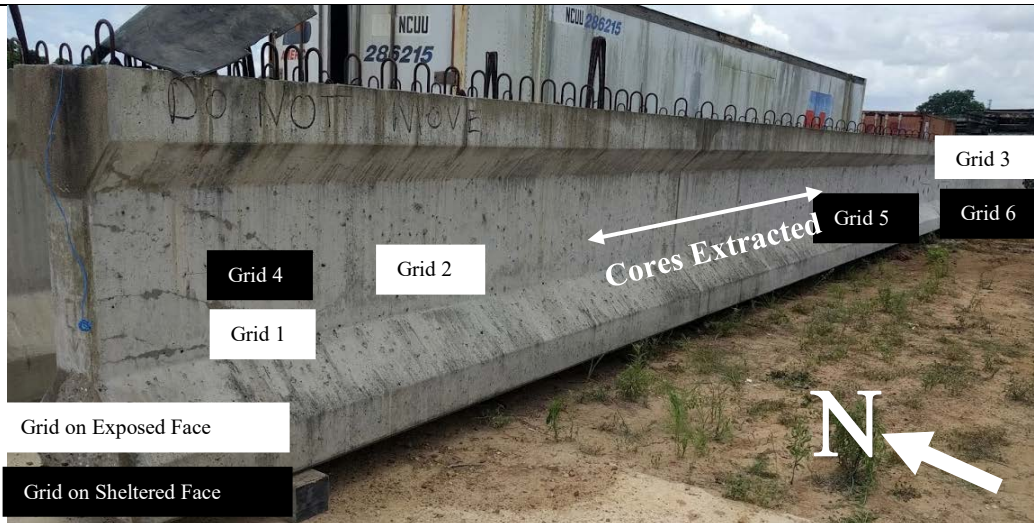
- [281] M. Vejdemo-Johansson and P. Skraba, “Topology, Big Data, and Optimization,” in *Big Data Optimization: Recent Challenges and Developments*, 1st ed., J. Kacprzyk, Ed. Springer, 2016, pp. 147–176.
- [282] R. E. Melchers and C. Q. Li, “Phenomenological modeling of reinforcement corrosion in marine environments,” *ACI Mater. J.*, vol. 103, no. 1, pp. 25–32, 2006.
- [283] A. C. Eringen and E. S. Suhubi, *Elastodynamics*, 1st ed. New York: Academic Press, 1974.

Appendix A. Additional Girder Information

Overcast Girder Information

Table A.1: Girder 1R Additional Information

Girder Notation	1R	Overcast Girder 1
Girder Name: Bexar NH2002(683), 0521-04-223, K-4-02-792		Location: Valley Pre-stress Products, Eagle Lake, Texas
Cast Date: 03/06/2007		In-Service Date: -
Orientation: East-West		Exposure: South Face Exposed



Source: Images by Authors
Figure A.1: Girder 1R

Age		9.6 years
Years in Service		-
Reason for Rejection		N/A
Climate as per NCEI Guidelines [14]	Climate at Storage Yard	Humid
	Climate at In-Service Location	-
Rainfall from NCEI climate data [14]	Average Annual Rainfall at Storage Yard	1115 mm (43.89 in.)
	Average Annual Rainfall at In-Service Location	-
	Total Rainfall from Casting to Visit 1	10541 mm (415 in.)
	Number of Rain Days from Casting to Visit 1	686
Temperature from NCEI climate data [14]	Temperature on Construction Day	28-11 C (69-52 F)
	Temperature during Construction Week	32-25 C (83-77 F)
	Temperature during Field Visit 1	35-25 C (90-72 F)
	Temperature during Field Visit 2	34-25 C (95-77 F)
	Temperature during Field Visit 3	31-21 C (94-70 F)
	Temperature during Field Visit 4	30-22 C (86-71 F)
Mix Proportions	w/cm	0.28
	River Gravel	Fine Aggregate
	River Sand	Coarse Aggregate
	Cementitious Materials as per ASTM C150-2017 and ASTM C618-2017 [16], [17]	Type III Cement + Class F Fly Ash
	Polycarboxylate based High Range Water Reducer as per ASTM C494-2017 [15]	391 ml/100 kg of cement (6 fl. oz./100 cwt)
	Water Reducer and Retarder as per ASTM C494-2017 [15]	196 ml/100 kg of cement (3 fl. oz./100 cwt)
Dimensions	Girder Type according to TxDOT Bridge Design Manual (2018) [18]	Type IV
	Length	30 m (100')
Strength	7-day Strength	69.7 MPa (10110 psi)
	At time of first Field Visit	93.7 MPa (13600 psi)
	Unit Weight	2390 kg/m ³ (149.21 lbs/cft)
Curing	Method	Wet Mat
	Temperature	23.1-59.4 C (79-139 F)
Pre-stressing	Number of Straight Strands according to TxDOT Bridge Design Manual (2018) [18]	44
	Number of Deflected Strands according to TxDOT Bridge Design Manual (2018) [18]	12
	Age at Pre-Stress Release	16 hours







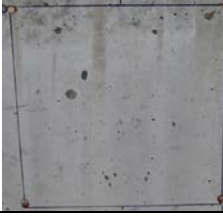

















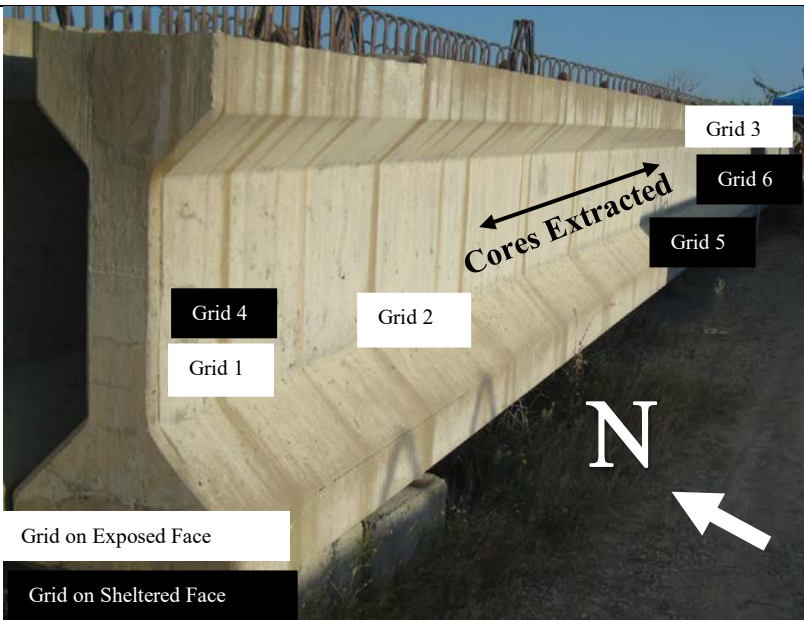
Grid	Visit 1: 10/06/2016	Visit 2: 06/15/2017	Visit 3: 05/17/2018	Visit 4: 05/22/2019
1				
2				
3				
4				
5				
6				

Table A.2: Girder 2R Additional Information

Girder Notation	2R	Overcast Girder 2
Girder Name: 0047-14-063, STP 2008(363) MM, D-A (AA-35), (AA3-10)		Location: Texas Concrete Company, Waco, Texas
Cast Date: 07/24/2009		In-Service Date: -
Orientation: East-West		Exposure: South Face Exposed



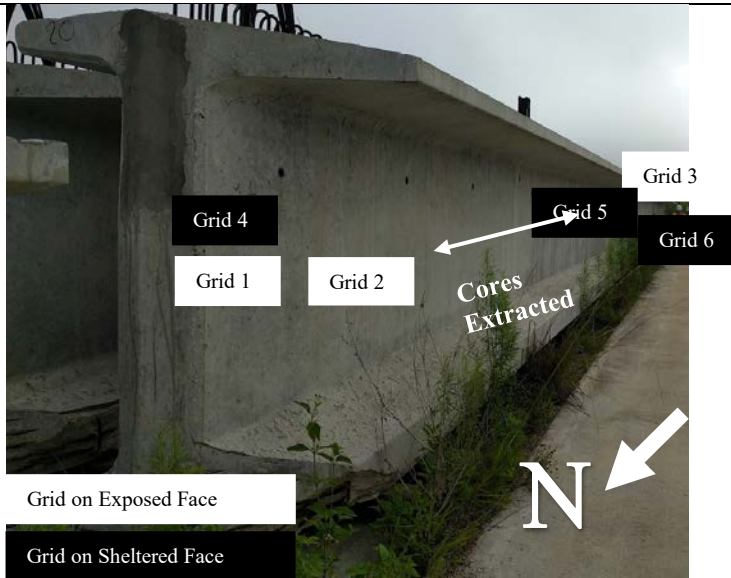
Source: Images by Authors
Figure A.2: Girder 2R

Age		7 years
Years in Service		-
Reason for Rejection		End Spalling
Climate as per NCEI Guidelines [14]	Climate at Storage Yard	Semi-Arid
	Climate at In-Service Location	-
Rainfall from NCEI climate data [14]	Average Annual Rainfall at Storage Yard	924 mm (36.38 in.)
	Average Annual Rainfall at In-Service Location	-
	Total Rainfall from Casting to Visit 1	6722 mm (264.66 in.)
	Number of Rain Days from Casting to Visit 1	312
Temperature from NCEI climate data [14]	Temperature on Construction Day	38-31 C (101-88 F)
	Temperature during Construction Week	37-32 C (103-90 F)
	Temperature during Field Visit 1	32-31 C (100-88 F)
	Temperature during Field Visit 2	32-27 C (89-90 F)
	Temperature during Field Visit 3	37-32 C (99-89 F)
Mix Proportions	w/cm	0.28
	Fine Aggregate	River Gravel
	Coarse Aggregate	River Sand
	Cementitious Materials as per ASTM C150-2017 and ASTM C618-2017 [16], [17]	Type III Cement + Class F Fly Ash
	Polycarboxylate based High Range Water Reducer as per ASTM C494-2017 [15]	391 ml/100 kg of cement (6 fl. oz./100 cwt)
	Water Reducer and Retarder as per ASTM C494-2017 [15]	163 ml/100 kg of cement (2.5 fl. oz./100 cwt)
Dimensions	Girder Type according to TxDOT Bridge Design Manual (2018) [18]	Type IV
	Length	30 m (100')
Strength	7-day Strength	72.8 MPa (10560 psi)
	At time of first Field Visit	80.8 MPa (11726 psi)
	Unit Weight	2416 kg/m ³ (150.80 lbs/cft)
Curing	Method	Wet Mat
	Temperature	31.1-56.7 C (88-134 F)
Pre-stressing	Number of Straight Strands according to TxDOT Bridge Design Manual (2018) [18]	30
	Number of Deflected Strands according to TxDOT Bridge Design Manual (2018) [18]	12
	Age at Pre-Stress Release	14 hours

Grid	Visit 1: 07/21/2016	Visit 2: 06/01/2017	Visit 3: 06/06/2018
Grid 1			
Grid 2			
Grid 3			
Grid 4			
Grid 5			
Grid 6			

Table A.3: Girder 3R Additional Information

Girder Notation	3R	Overcast Girder 3
Girder Name: Q1 TX70-26, Tarrant/Dallas, #3718	Location: Bexar Concrete Works, San Antonio, Texas	
Cast Date: 02/14/2011	In-Service Date: -	
Orientation: North-South	Exposure: West Face Exposed	



Source: Images by Authors

Figure A.3: Girder 3R

Age	5.51 years	
Years in Service	-	
Reason for Rejection	Honeycombing in bottom flange	
Climate as per NCEI Guidelines [14]	Climate at Storage Yard	Humid
	Climate at In-Service Location	-
Rainfall from NCEI climate data [14]	Average Annual Rainfall at Storage Yard	836 mm (32.91 in.)
	Average Annual Rainfall at In-Service Location	-
	Total Rainfall from Casting to Visit 1	4615 mm (181.69 in.)
	Number of Rain Days from Casting to Visit 1	338
Temperature from NCEI climate data [14]	Temperature on Construction Day	25-5 C (77-42 F)
	Temperature during Construction Week	32-5 C (80-42 F)
	Temperature during Field Visit 1	32-23 C (91-74 F)
	Temperature during Field Visit 2	32-27 C (89-80 F)
	Temperature during Field Visit 3	37-32 C (99-89 F)
Mix Proportions	w/cm	0.30
	Fine Aggregate	Limestone
	Coarse Aggregate	River Sand
	Cementitious Materials as per ASTM C150-2017 and ASTM C618-2017 [16], [17]	Type III Cement + Class F Fly Ash
	Polycarboxylate based High Range Water Reducer as per ASTM C494-2017 [15]	342 ml/100 kg of cement (5.3 fl. oz./100 cwt)
	Water Reducer and Retarder as per ASTM C494-2017 [15]	82 ml/100 kg of cement (1.3 fl. oz./100 cwt)
Dimensions	Girder Type according to TxDOT Bridge Design Manual (2018) [18]	Tx70
	Length	53 m (175')
Strength	7-day Strength	67.3 MPa (9765 psi)
	At time of first Field Visit	84.2 MPa (12216 psi)
	Unit Weight	2388 kg/m ³ (149.10 lbs/cft)
Curing	Method	Q-Box
	Temperature	N/A)
Pre-stressing	Number of Straight Strands according to TxDOT Bridge Design Manual (2018) [18]	40
	Number of Deflected Strands according to TxDOT Bridge Design Manual (2018) [18]	10
	Age at Pre-Stress Release	N/A



















Grid	Visit 1: 08/18/2016	Visit 2: 06/29/2017	Visit 3: 07/11/2018
Grid 1			
Grid 2			
Grid 3			
Grid 4			
Grid 5			
Grid 6			

Table A.4: Girder 4R Additional Information

Girder Notation	4R	Overcast Girder 4
Girder Name: Collin Co, 08559 SH21, 05 CNPM, J-4-11-33, DL 1164B		Location: Valley Pre-stress Products, Eagle Lake, Texas
Cast Date: 12/14/2009		In-Service Date: -
Orientation: East-West		Exposure: North Face Exposed



Source: Images by Authors

Figure A.4: Girder 4R

Age		7 years
Years in Service		-
Reason for Rejection		End Spalling
Climate as per NCEI Guidelines [14]	Climate at Storage Yard	Humid
	Climate at In-Service Location	-
Rainfall from NCEI climate data [14]	Average Annual Rainfall at Storage Yard	1115 mm (43.89in)
	Average Annual Rainfall at In-Service Location	-
	Total Rainfall from Casting to Visit 1	6006 mm (236.45in)
	Number of Rain Days from Casting to Visit 1	413
Temperature from NCEI climate data [14]	Temperature on Construction Day	20-11 C (69-52 F)
	Temperature during Construction Week	32-22 C (83-71 F)
	Temperature during Field Visit 1	32-22 C (83-71 F)
	Temperature during Field Visit 2	35-25 C (95-77 F)
	Temperature during Field Visit 3	34-21 C (94-70 F)
	Temperature during Field Visit 4	30-22 C (86-71 F)
Mix Proportions	w/cm	0.30
	Fine Aggregate	River Gravel
	Coarse Aggregate	River Sand
	Cementitious Materials as per ASTM C150-2017 and ASTM C618-2017 [16], [17]	Type III Cement + Class F Fly Ash
	Polycarboxylate based High Range Water Reducer as per ASTM C494-2017 [15]	342 ml/100 kg of cement (5.3 fl. oz./100 cwt)
	Water Reducer and Retarder as per ASTM C494-2017 [15]	98 ml/100 kg of cement (1.5 fl. oz./100 cwt)
Dimensions	Girder Type according to TxDOT Bridge Design Manual (2018) [18]	Type IV
	Length	33 m (116')
Strength	7-day Strength	67.3 MPa (9760 psi)
	At time of first Field Visit	70 MPa (10172 psi)
	Unit Weight	2369 kg/m ³ (147.90 lbs/cft)
Curing	Method	Wet Mat
	Temperature	23.5-59.4 C (74-139 F)
Pre-stressing	Number of Straight Strands according to TxDOT Bridge Design Manual (2018) [18]	40
	Number of Deflected Strands according to TxDOT Bridge Design Manual (2018) [18]	10
	Age at Pre-Stress Release	13 hours

























Grid	Visit 1: 10/06/2016	Visit 2: 06/15/2017	Visit 3: 05/17/2018	Visit 4: 05/22/2019
1				
2				
3				
4				
5				
6				



















Table A.5: Girder 5RC Additional Information

Girder Notation	5RC	Overcast Control Girder 5
Girder Name: Harris Co, C 1.5		Location: Texas Concrete Company, Victoria, Texas
Cast Date: 05/04/2009		In-Service Date: -
Orientation: East-West		Exposure: South Face Exposed



Source: Images by Authors
Figure A.5: Girder 5RC

Age		12.2 years
Years in Service		-
Reason for Rejection		Honeycombing in bottom flange
Climate as per NCEI Guidelines [14]	Climate at Storage Yard	Humid
	Climate at In-Service Location	-
Rainfall from NCEI climate data [14]	Average Annual Rainfall at Storage Yard	1047 mm (41.22 in.)
	Average Annual Rainfall at In-Service Location	-
	Total Rainfall from Casting to Visit 1	13296 mm (523.46 in.)
	Number of Rain Days from Casting to Visit 1	423
Temperature from NCEI climate data [14]	Temperature on Construction Day	25-13 C (78-57 F)
	Temperature during Construction Week	37-32 C (81-73 F)
	Temperature during Field Visit 1	37-22 C (99-81 F)
	Temperature during Field Visit 2	34-33 C (93-91 F)
	Temperature during Field Visit 3	32-31 C (90-88 F)
Mix Proportions	w/cm	0.28
	Fine Aggregate	River Gravel
	Coarse Aggregate	River Sand
	Cementitious Materials as per ASTM C150-2017 and ASTM C618-2017 [16], [17]	Type III Cement + Class F Fly Ash
	Polycarboxylate based High Range Water Reducer as per ASTM C494-2017 [15]	651 ml/100 kg of cement (10 fl. oz./100 cwt)
	Water Reducer and Retarder as per ASTM C494-2017 [15]	196 ml/100 kg of cement (3 fl. oz./100 cwt)
Dimensions	Girder Type according to TxDOT Bridge Design Manual (2018) [18]	Tx54
	Length	33 m (115')
Strength	7-day Strength	55.84 MPa (8100 psi)
	At time of first Field Visit	77 MPa (11115 psi)
	Unit Weight	2373 kg/m ³ (148.14 lbs/cft)
Curing	Method	Wet Mat
	Temperature	33.9-66.1 C (92-151 F)
Pre-stressing	Number of Straight Strands according to TxDOT Bridge Design Manual (2018) [18]	52
	Number of Deflected Strands according to TxDOT Bridge Design Manual (2018) [18]	12
	Age at Pre-Stress Release	14 hours

Grid	Visit 1: 06/29/2016	Visit 2: 06/08/2017	Visit 3: 06/27/2018
Grid 1			
Grid 2			
Grid 3			
Grid 4			
Grid 5			
Grid 6			

In-Service Girder Information






















Table A.6: Girder 6I, 8I, 9I and 12IC Additional Information

Girder Notation	6I 8I and 9I 12IC	In-Service Exterior Girder 6 In-Service Interior Girders 8 and 9 In-Service Control Girder 12
Girder Name:		Location: Inwood and Hampton, Dallas, Texas
Cast Date: March-April 2007		In-Service Date: 2010



Source: Images by Authors
Figure A.6: Girders 6I, 8I, 9I, and 12IC

Age		11.5 years
Years in Service		8 years
Reason for Rejection		-
Climate as per NCEI Guidelines [14]	Climate at Storage Yard	Arid
	Climate at In-Service Location	Humid Sub-Tropical
Rainfall from NCEI climate data [14]	Average Annual Rainfall at Storage Yard	924 mm (36.38 in.)
	Average Annual Rainfall at In-Service Location	1041 mm (40.97 in.)
	Total Rainfall from Casting to Visit 1	8313 mm (327.30 in.)
	Number of Rain Days from Casting to Visit 1	438
Temperature from NCEI climate data [14]	Temperature on Construction Day	25-17 C (77-62 F)
	Temperature during Construction Week	25-12 C (77-53 F)
	Temperature during Field Visit 1	30-13 C (86-55 F)
	Temperature during Field Visit 2	28-21 C (82-69 F)
	Temperature during Field Visit 3	18-9 C (64-48 F)
Mix Proportions	w/cm	0.36
	Fine Aggregate	River Gravel
	Coarse Aggregate	River Sand
	Cementitious Materials as per ASTM C150-2017 and ASTM C618-2017 [16], [17]	Type III Cement
	Polycarboxylate based High Range Water Reducer as per ASTM C494-2017 [15]	587 ml/100 kg of cement (9 fl. oz./100 cwt)
	Water Reducer and Retarder as per ASTM C494-2017 [15]	163 ml/100 kg of cement (2.5 fl. oz./100 cwt)
Dimensions	Girder Type according to TxDOT Bridge Design Manual (2018) [18]	Type IV
	Length	-
Strength	7-day Strength	58.6 MPa (8500 psi)
	At time of first Field Visit	-
	Unit Weight	-
Curing	Method	Steam
	Temperature	18.8-35.5 C (66-96 F)
Pre-stressing	Number of Straight Strands according to TxDOT Bridge Design Manual (2018) [18]	38
	Number of Deflected Strands according to TxDOT Bridge Design Manual (2018) [18]	8
	Age at Pre-Stress Release	14 hours

Grid	Visit 1: 11/07/2016	Visit 2: 11/17/2017	Visit 3: 12/12/2018
6I Grid 1			
6I Grid 2			
8I Grid 1			
8I Grid 2			
8I Grid 3			
8I Grid 4			
9I Grid 1			










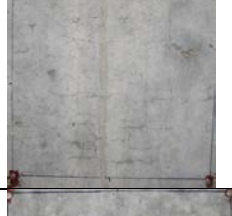

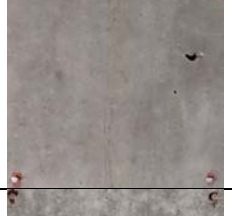


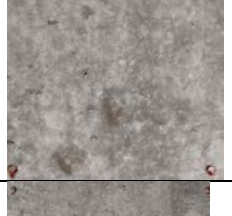




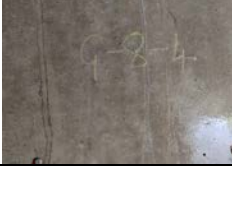




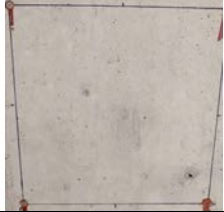



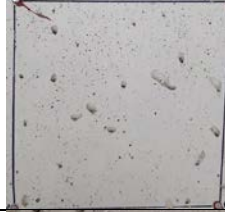








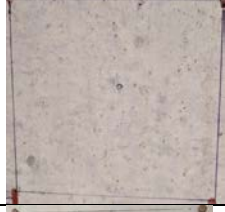

























Grid	Visit 1: 11/07/2016	Visit 2: 11/17/2017	Visit 3: 12/12/2018
9I Grid 2			
9I Grid 3			
9I Grid 4			
12IC Grid 1			
12IC Grid 2			
12IC Grid 3			
12IC Grid 4			

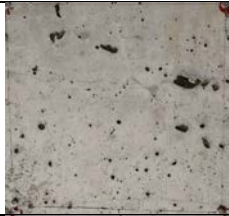





Table A.7: Girders 7I, 10I, 11I, and 13IC Additional Information

Girder Notation	7I 10I and 11I 13IC	In-Service Exterior Girder 7 In-Service Interior Girders 10 and 11 In-Service Control Girder 13
Girder Name: -		Location: I30 and US93, Texarkana, Texas
Cast Date: January – February 2005		In-Service Date: 2008
		
		
<p>Source: Images by Authors</p> <p>Figure A.7: Girders 7I, 10I, 11I and 13IC</p>		

Age		10.8 years
Years in Service	7.	7.8 years
Reason for Rejection		-
Climate as per NCEI Guidelines [14]	Climate at Storage Yard	Arid
	Climate at In-Service Location	Semi-Arid
Rainfall from NCEI climate data [14]	Average Annual Rainfall at Storage Yard	924 mm (36.38 in.)
	Average Annual Rainfall at In-Service Location	1320 mm (51.98 in.)
	Total Rainfall from Casting to Visit 1	9732 mm (383.13 in.)
	Number of Rain Days from Casting to Visit 1	391
Temperature from NCEI climate data [14]	Temperature on Construction Day	19-8 C (66-46 F)
	Temperature during Construction Week	23-9C (73-49 F)
	Temperature during Field Visit 1	12-7 C (54-44 F)
	Temperature during Field Visit 21	17-13 C (63-55 F)
	Temperature during Field Visit 3	16-(-2) C (60-29 F)
Mix Proportions	w/cm	0.36
	Fine Aggregate	River Gravel
	Coarse Aggregate	River Sand
	Cementitious Materials as per ASTM C150-2017 and ASTM C618-2017 [16], [17]	Type III Cement
	Polycarboxylate based High Range Water Reducer as per ASTM C494-2017 [15]	652 ml/100 kg of cement (10 fl. oz./100 cwt)
	Water Reducer and Retarder as per ASTM C494-2017 [15]	163 ml/100 kg of cement (2.5 fl. oz./100 cwt)
Dimensions	Girder Type according to TxDOT Bridge Design Manual (2018) [18]	Type IV
	Length	-
Strength	7-day Strength	64.12 MPa (9300 psi)
	At time of first Field Visit	-
	Unit Weight	-
Curing	Method	Wet-Mat
	Temperature	-
Pre-stressing	Number of Straight Strands according to TxDOT Bridge Design Manual (2018) [18]	42
	Number of Deflected Strands according to TxDOT Bridge Design Manual (2018) [18]	14
	Age at Pre-Stress Release	15.5 hours

Grid	Visit 1: 12/06/2016	Visit 2: 11/16/2017	Visit 3: 12/11/2018
7I Grid 1			
7I Grid 2			
7I Grid 3			
7I Grid 4			
10I Grid 1			
10I Grid 2			
10I Grid 3			

Grid	Visit 1: 12/06/2016	Visit 2: 11/16/2017	Visit 3: 12/11/2018
10I Grid 4			
11I Grid 1			
11I Grid 2			
11I Grid 3			
11I Grid 4			
13IC Grid 1			
13IC Grid 2			

Grid	Visit 1: 12/06/2016	Visit 2: 11/16/2017	Visit 3: 12/11/2018
13IC Grid 3			
13IC Grid 4			

Validation Girder Information

Table A.8: Girder 14V Additional Information

Girder Notation	14V	Validation Girder 14
Girder Name: HEI #123374, Collin, B-4-C-27		Location: Heldenfels Enterprise Inc, San Marcos, Texas
Cast Date: 12/16/2013		In-Service Date: -
Orientation: East-West		Exposure: South Face Exposed



Source: Images by Authors

Figure A.8: Girder 14V

Age		3.5 years
Years in Service		-
Reason for Rejection		
Climate as per NCEI Guidelines [14]	Climate at Storage Yard	Arid
	Climate at In-Service Location	-
Rainfall from NCEI climate data [14]	Average Annual Rainfall at Storage Yard	908 mm (35.75 in.)
	Average Annual Rainfall at In-Service Location	-
	Total Rainfall from Casting to Visit 1	4243 mm (167.06 in.)
	Number of Rain Days from Casting to Visit 1	304
Temperature from NCEI climate data [14]	Temperature on Construction Day	19-(-4) C (67-25 F)
	Temperature during Construction Week	25-16 C (77-61 F)
	Temperature during Field Visit 1	33-27 C (92-81 F)
	Temperature during Field Visit 2	35-22 C (96-72 F)
	Temperature during Field Visit 3	30-21 C (86-71 F)
Mix Proportions	w/cm	0.31
	Fine Aggregate	River Gravel
	Coarse Aggregate	Dolomitic Limestone
	Cementitious Materials as per ASTM C150-2017 and ASTM C618-2017 [16], [17]	Type III Cement + Class F Fly Ash
	Polycarboxylate based High Range Water Reducer as per ASTM C494-2017 [15]	325 ml/100 kg of cement (5 fl. oz./100 cwt)
	Water Reducer and Retarder as per ASTM C494-2017 [15]	65 ml/100 kg of cement (1 fl. oz./100 cwt)
Dimensions	Girder Type according to TxDOT Bridge Design Manual (2018) [18]	Tx54
	Length	23 m (75')
Strength	7-day Strength	67.6 MPa (9800 psi)
	At time of first Field Visit	76.8 MPa (11142 psi)
	Unit Weight	2448 kg/m ³ (152.80 lbs/cft)
Curing	Method	Wet Mat
	Temperature	32-14 C (90.2-57.5 F)
Pre-stressing	Number of Straight Strands according to TxDOT Bridge Design Manual (2018) [18]	28
	Number of Deflected Strands according to TxDOT Bridge Design Manual (2018) [18]	8
	Age at Pre-Stress Release	16 hours

Grid	Visit 1: 06/29/2017	Visit 2: 07/11/2018	Visit 3: 05/30/2019
Grid 1			
Grid 2			
Grid 3			
Grid 4			

Crack Width Distributions

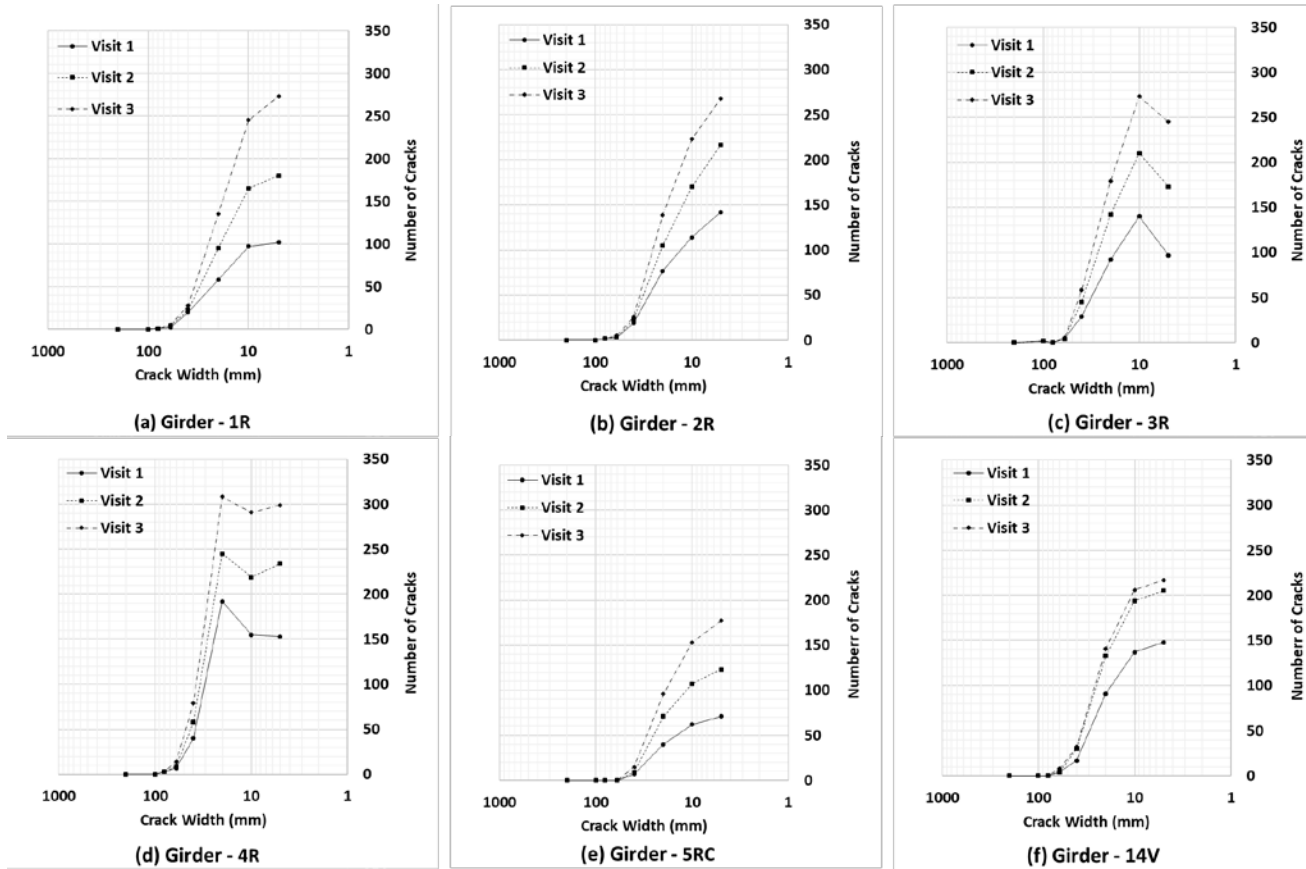


Figure A.9: Crack Width Distribution of Overcast Girders

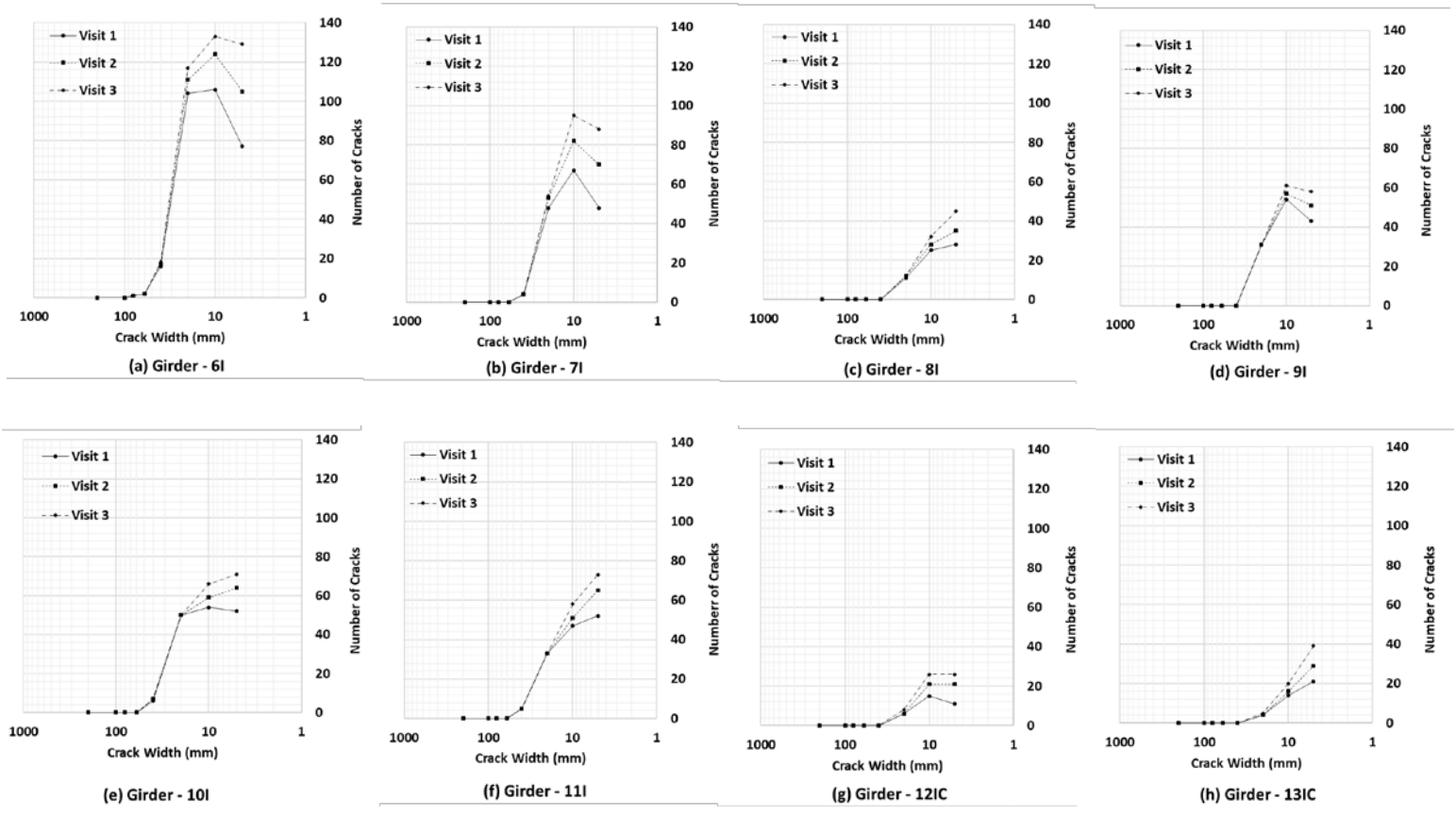
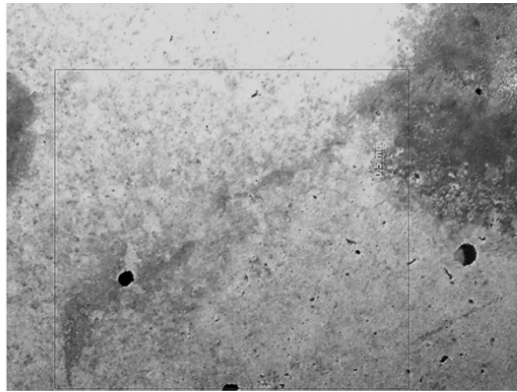
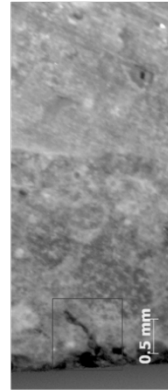


Figure A.10: Crack Width Distributions of In-Service Girders

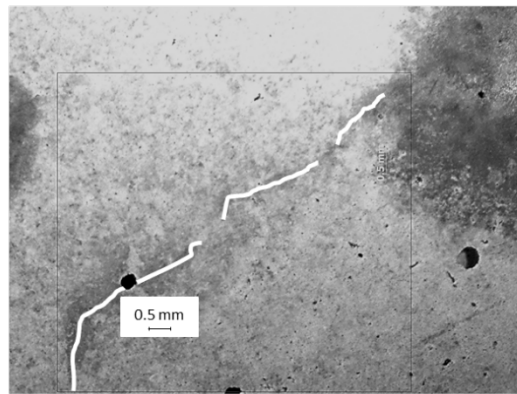
Appendix B. Optical and Scanning Electron Microscopy Images



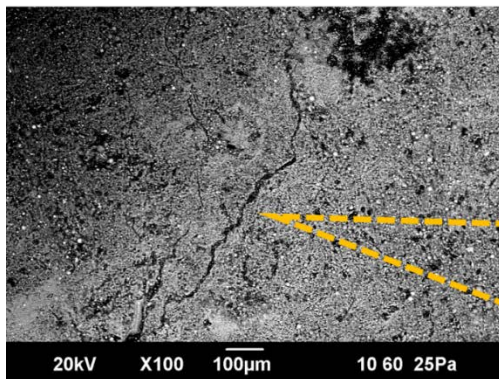
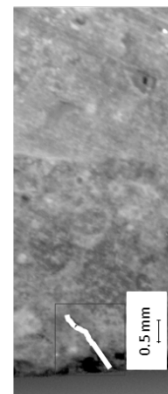
(a) Optical Microscope Images - Core Surface



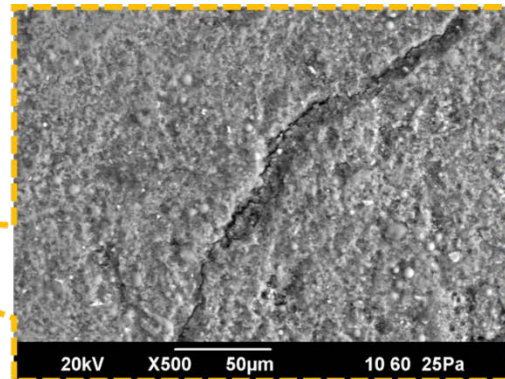
(b) Vertical Sliced Section



(c) Highlighted Microcracks



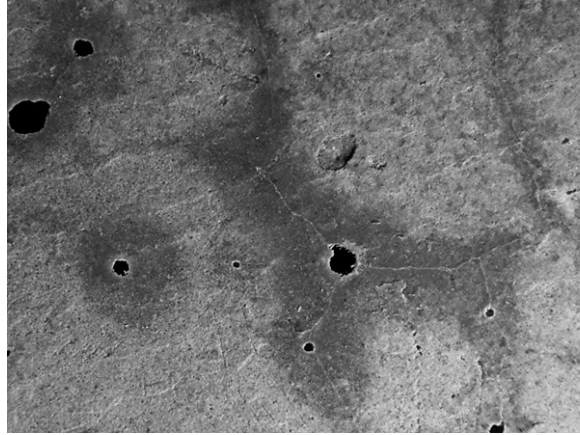
(d) SEM Image of Core Surface (100X)



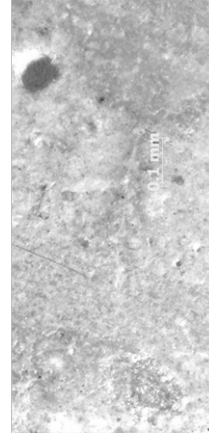
(e) SEM Image of Core Surface (500X)

Source: Images by Authors

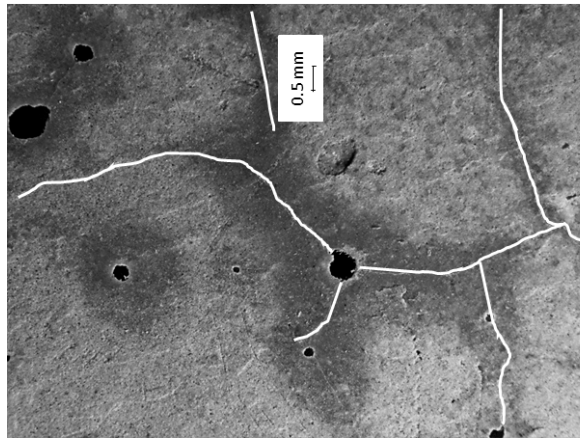
Figure B.1: Microscope Images of Overcast Girder 1R



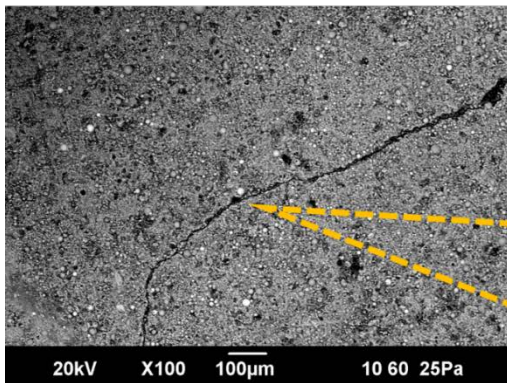
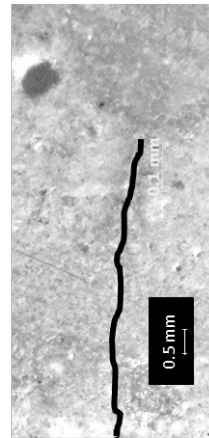
(a) Optical Microscope Images - Core Surface



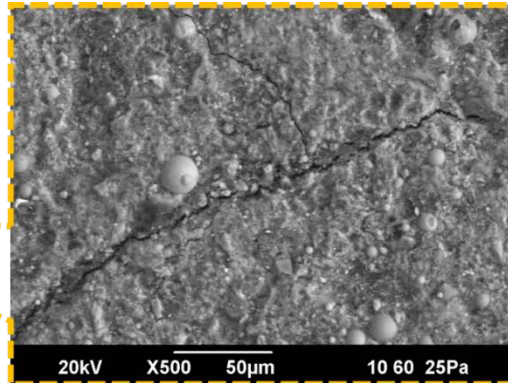
(b) Vertical Sliced Section



(c) Highlighted Microcracks



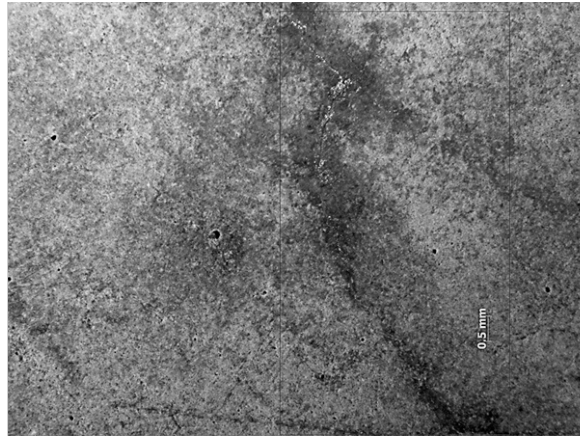
(d) SEM Image of Core Surface (100X)



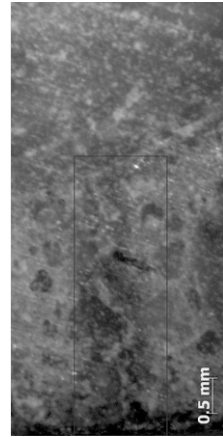
(e) SEM Image of Core Surface (500X)

Source: Images by Authors

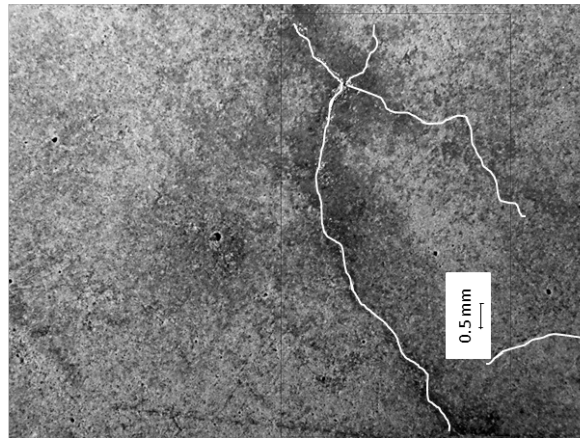
Figure B.2: Microscope Images of Overcast Girder 2R



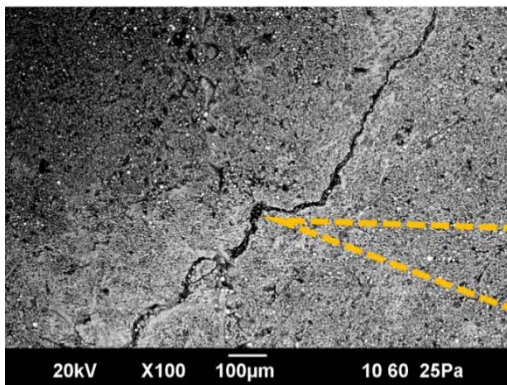
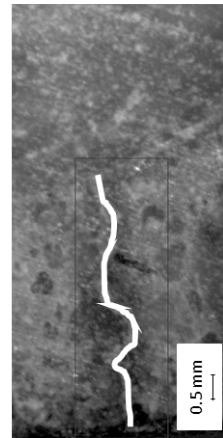
(a) Optical Microscope Images - Core Surface



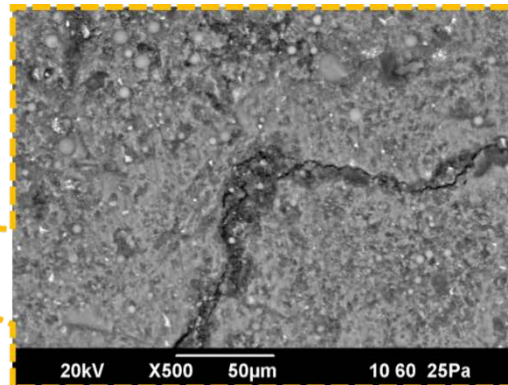
(b) Vertical Sliced Section



(c) Highlighted Microcracks



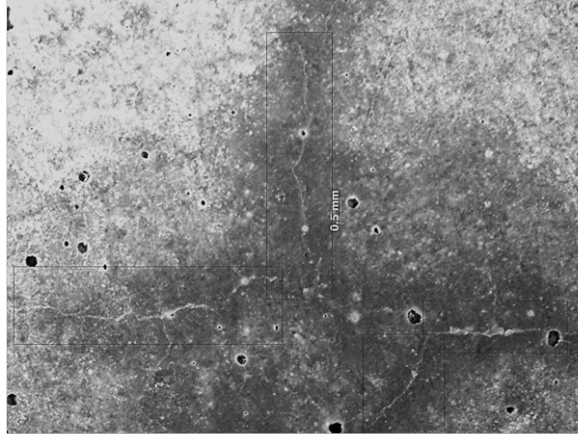
(d) SEM Image of Core Surface (100X)



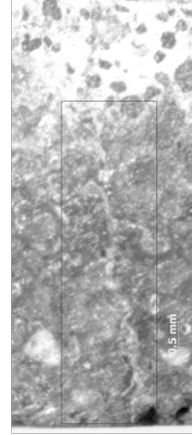
(e) SEM Image of Core Surface (500X)

Source: Images by Authors

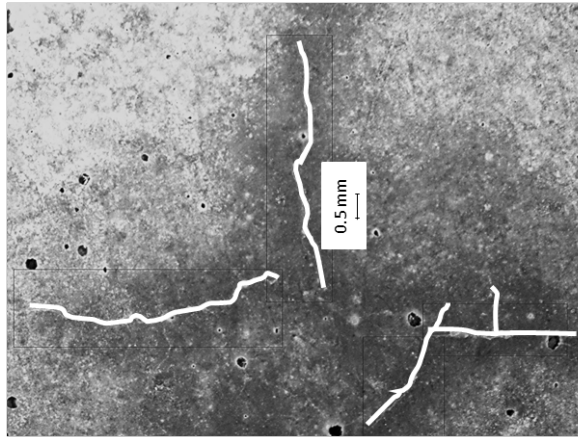
Figure B.3: Microscope Images of Overcast Girder 3R



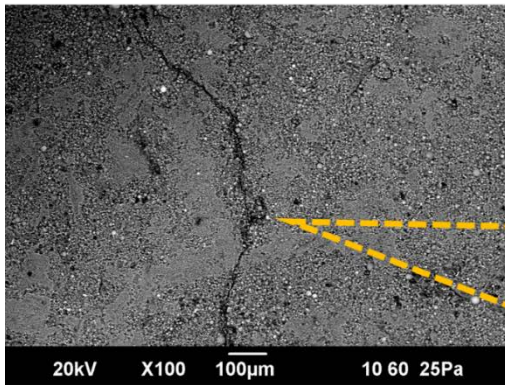
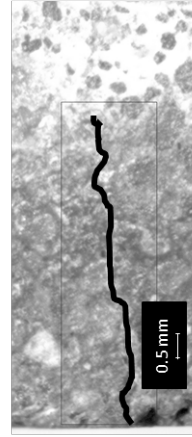
(a) Optical Microscope Images - Core Surface



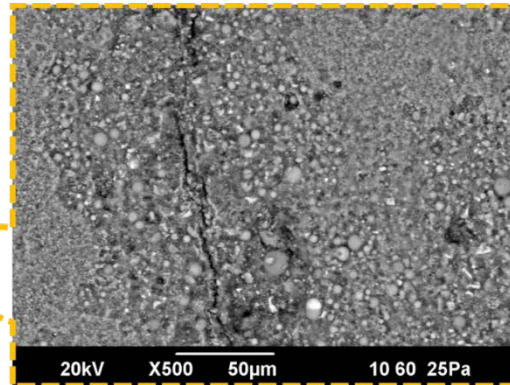
(b) Vertical Sliced Section



(c) Highlighted Microcracks



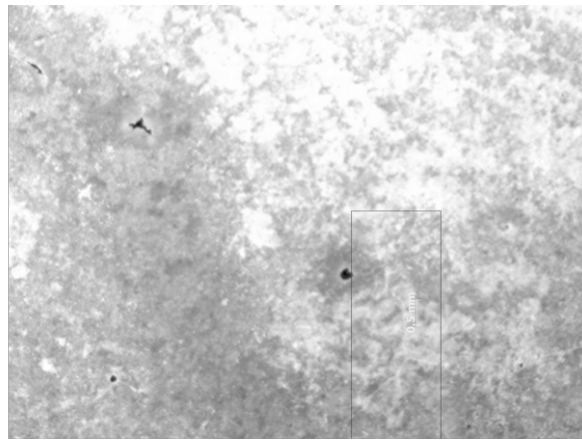
(d) SEM Image of Core Surface (100X)



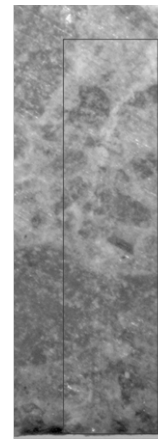
(e) SEM Image of Core Surface (500X)

Source: Images by Authors

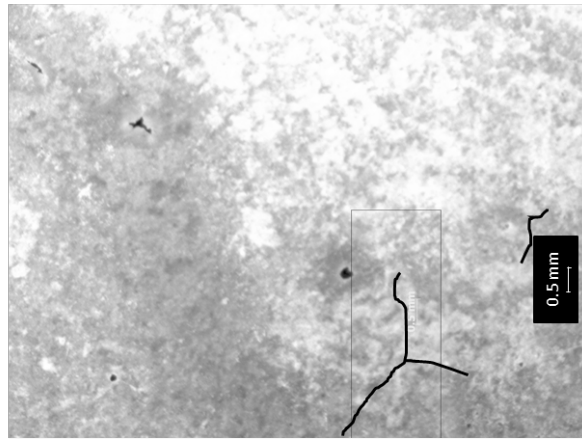
Figure B.4: Microscope Images of Overcast Girder 4R



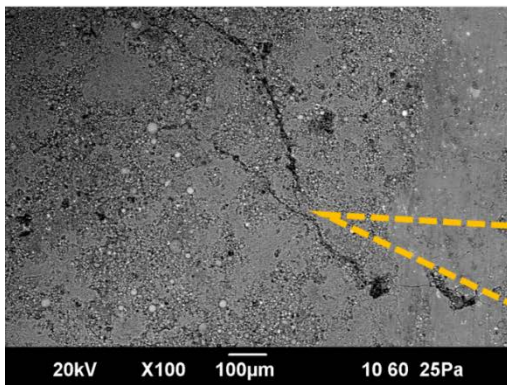
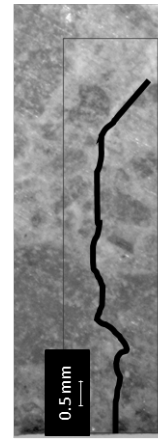
(a) Optical Microscope Images - Core Surface



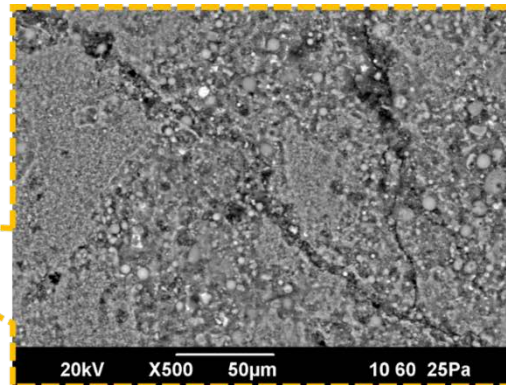
(b) Vertical Sliced Section



(c) Highlighted Microcracks



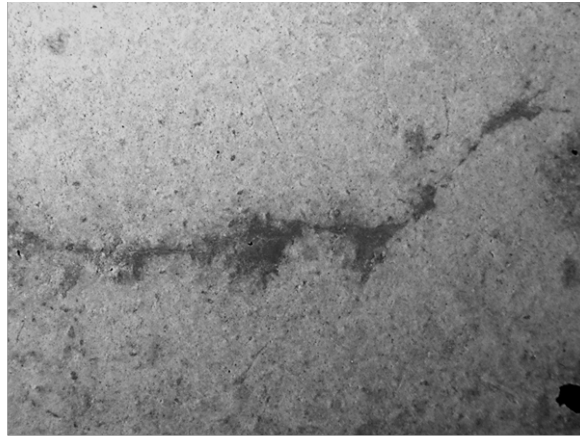
(d) SEM Image of Core Surface (100X)



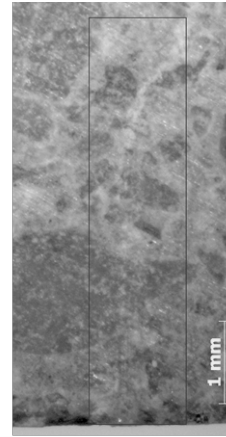
(e) SEM Image of Core Surface (500X)

Source: Images by Authors

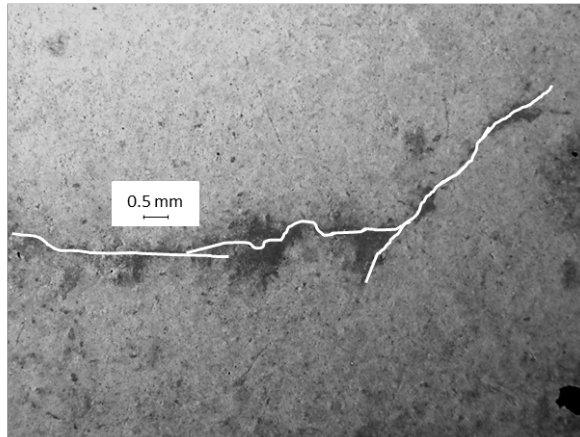
Figure B.5: Microscope Images of Overcast Girder 5RC



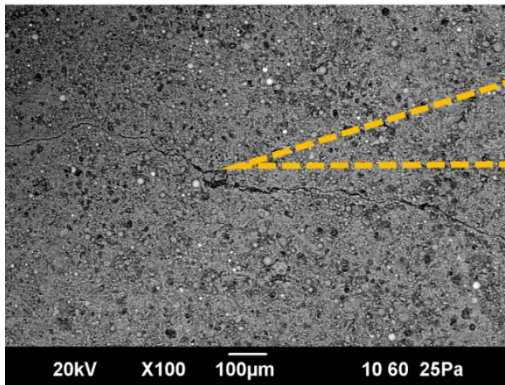
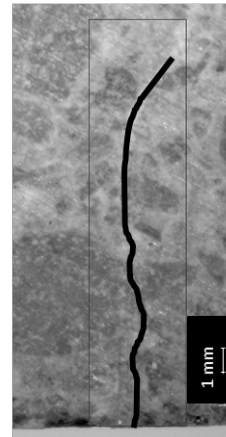
(a) Optical Microscope Images - Core Surface



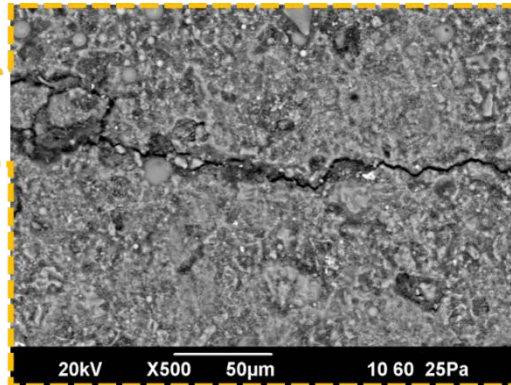
(b) Vertical Sliced Section



(c) Highlighted Microcracks



(d) SEM Image of Core Surface (100X)



(e) SEM Image of Core Surface (500X)

Source: Images by Authors

Figure B.6: Microscope Images of Overcast Girder 14V

Appendix C. Auxiliary Guided Wave Terms

Certain terms appearing in the exact theory for guided wave modes are summarized below from [198]. It should be noted that the factor of 2 appearing in the term $2(\lambda_r^2 + \lambda_z^2)\Phi_{12}$ of the expression for α_1 does not appear in [198]. However, it may be found in [283], pp. 278.

$$\Phi_1 = \frac{2}{\lambda_r^2 \lambda_z} \frac{\partial U}{\partial I_1}$$

$$\Phi_2 = \frac{2}{\lambda_r^2 \lambda_z} \frac{\partial U}{\partial I_2}$$

$$\Phi_3 = 2\lambda_r^2 \lambda_z \frac{\partial U}{\partial I_3}$$

$$\Phi_{ij} = \frac{2}{\lambda_r^2 \lambda_z} \frac{\partial^2 U}{\partial I_i \partial I_j}$$

$$\alpha_1 = 2\lambda_r^4 [\Phi_{11} + (\lambda_r^2 + \lambda_z^2)^2 \Phi_{22} + \lambda_r^4 \lambda_z^4 \Phi_{33} + 2\lambda_r^2 \lambda_z^2 (\lambda_r^2 + \lambda_z^2) \Phi_{23} + 2\lambda_r^2 \lambda_z^2 \Phi_{13} + 2(\lambda_r^2 + \lambda_z^2) \Phi_{12}] - 2\lambda_r^2 [\Phi_1 + (\lambda_r^2 + \lambda_z^2) \Phi_2]$$

$$\alpha_2 = 2\lambda_r^2 \lambda_z^2 [\Phi_{11} + 2\lambda_r^2 (\lambda_r^2 + \lambda_z^2) \Phi_{22} + \lambda_r^6 \lambda_z^2 \Phi_{33} + \lambda_r^4 (\lambda_r^2 + 3\lambda_z^2) \Phi_{23} + \lambda_r^2 (\lambda_r^2 + \lambda_z^2) \Phi_{13} + (3\lambda_r^2 + \lambda_z^2) \Phi_{12}] - 2\lambda_r^2 (\Phi_1 + \lambda_r^2 \Phi_2)$$

$$\alpha_3 = \alpha_2 - (\lambda_z^2 - \lambda_r^2) (\Phi_1 + \lambda_r^2 \Phi_2)$$

$$\alpha_4 = 2\lambda_z^4 (\Phi_{11} + 4\lambda_r^4 \Phi_{22} + \lambda_r^8 \Phi_{33} + 4\lambda_r^6 \Phi_{23} + 2\lambda_r^4 \Phi_{13} + 4\lambda_r^2 \Phi_{12}) - (\lambda_z^2 - \lambda_r^2) (\Phi_1 + \lambda_r^2 \Phi_2)$$

$$\alpha_5 = \lambda_r^2 (\Phi_1 + \lambda_r^2 \Phi_2)$$

$$\beta_1 = \frac{i(\alpha_2 + \alpha_5)}{\alpha_1 - 2\Phi_3} K$$

$$\beta_2 = \frac{i(\alpha_3 + \alpha_5 + \tau)}{\alpha_5} K$$

$$\chi_1^2 = \frac{\gamma\omega^2 - \lambda_z^2 K^2 (\Phi_1 + \lambda_r^2 \Phi_2)}{\alpha_1 - 2\Phi_3}$$

$$\chi_2^2 = \frac{\gamma\omega^2 - K^2 (\alpha_4 + 2\tau)}{\alpha_5}$$

$$\chi_{3,4}^2 = \frac{1}{2} \left[\chi_1^2 + \chi_2^2 - \beta_1 \beta_2 \mp \sqrt{(\chi_1^2 - \chi_2^2)^2 + \beta_1^2 \beta_2^2 - 2\beta_1 \beta_2 (\chi_1^2 + \chi_2^2)} \right]$$